NBSIR 84-2815

Technical Activities 1983 Office of Nondestructive Evaluation

U.S. DEPARTMENT OF COMMERCE
National Bureau of Standards
Center for Materials Science
Office of Nondestructive Evaluation
Washington, DC 20234

December 1983

Prepared for
U.S. DEPARTMENT OF COMMERCE
National Bureau of Standards
Washington, DC 20234

NBSIR 84-2815

TECHNICAL ACTIVITIES 1983 OFFICE OF NONDESTRUCTIVE EVALUATION

Leonard Mordfin, Editor

U.S. DEPARTMENT OF COMMERCE
National Bureau of Standards
Center for Materials Science
Office of Nondestructive Evaluation
Washington, DC 20234

December 1983

Prepared for
U.S. DEPARTMENT OF COMMERCE
National Bureau of Standards
Washington, DC 20234

U.S. DEPARTMENT OF COMMERCE, Malcolm Baldrige, *Secretary*
NATIONAL BUREAU OF STANDARDS, Ernest Ambler, *Director*

TECHNICAL ACTIVITIES

TECHNICAL ACTIVITIES

Table of Contents

LIQUID PENETRANT AND MAGNETIC PARTICLE METHODS

RADIOGRAPHY

NEUTRON METHODS

ULTRASONIC METHODS

ACOUSTIC EMISSION METHODS

EDDY-CURRENT AND ELECTRICAL METHODS

OPTICAL AND THERMAL METHODS

SPECIAL REPORTS

APPENDICES

INTRODUCTION

This report provides brief reviews of the technical activities in nondestructive evaluation (NDE) that were carried out by or for the National Bureau of Standards in fiscal year 1983. Collectively, these technical activities constitute the Bureau's Nondestructive Evaluation Program, which is managed programmatically and administered on a Bureau-wide basis by the Office of Nondestructive Evaluation.

Recognizing that modern NDE must be quantitative, and that NDE measurements must be reproducible, the principal mission of the NDE Program is to provide traceability for NDE measurements, i.e., traceability to national standards of measurement. This mission calls for the development and maintenance of calibration services, reference materials, etc., as well as the formulation of recommended practices to help assure that the means for traceability are implemented properly. The effective accomplishment of this mission -- traceability for NDE measurements -- requires concerted technical activity toward two other objectives as well. First, research must usually be carried out to achieve an adequate understanding of the physical bases of the NDE measurement techniques and processes that need standardization. Second, the results of the Bureau's research and development work on NDE measurements must usually be applied to several specific and meaningful problems in order to demonstrate the validity of the results and to help disseminate them to the user communities. In summary, the technical activities of the NDE Program can be thought of as comprising three tasks; research, standardization, and applications.

A glance at the table of contents will reveal that the technical reviews in this report have been categorized by NDE method. Within some of the larger categories, e.g., ultrasonics, the reviews have been put into an arrangement that reflects the three tasks set forth above, i.e., research first, then standardization and, finally, applications.

Reports such as this one have been issued on an annual basis since 1978 and are commonly referred to as the "NDE annual reports". A parallel series of reports, also issued annually, presents bibliographies and abstracts for the Bureau's technical reports and publications on NDE and its supporting technologies. The purpose of both of these report series is to serve as an introduction to the Bureau's NDE Program. Many readers will want further details on specific aspects of the work or its outputs, and such inquiries are welcomed and encouraged, both by the principal NDE investigators (whose names and affiliations precede each of the articles in this report) and by the Office of Nondestructive Evaluation. Either can be addressed in care of NBS, Washington, D. C. 20234, or reached by telephone via (301) 921-1000. Requests for further information and suggestions for new NDE projects always receive prompt and careful attention.

THIS PAGE IS INTENTIONALLY BLANK

A NEW FLUORESCENT GLASS STANDARD FOR USE IN DYE PENETRANT MEASUREMENTS

R.W. Burke and M.V. Smith

Inorganic Analytical Research Division

Center for Analytical Chemistry

An investigation of a series of materials that were considered reasonable candidates for use as fluorescent standards in dye penetrant testing has resulted in the selection and recommendation of a terbium-doped phosphate glass for this purpose. This glass was specially produced in the Inorganic Materials Division and bulk stock is currently available in rod and bar forms. In making this glass a number of problems had to be solved in order to obtain a product of acceptable optical quality. Particularly troublesome was the severe tendency of this glass to form bubbles in the melts and to develop cracks during the cooling cycle. Ultimately the use of preheated graphite molds was found to offer the best practical solution to both of these problems.

While the doping levels for terbium can exceed 40 percent by weight in phosphate glasses, the glass on which most of the current analytical data have been obtained was prepared by melting a blended mixture consisting of 20% Tb_2O_3, 40% $Al(PO_3)_3$, and 40% $NaPO_3$. The absorption and fluorescence emission spectra of this glass are shown in Figure 1. A strong absorption band is noted in the wavelength range between 330 and 390 nm whereas a strong fluorescence band is observed between 525 and 560 nm. These two spectral regions correspond closely to the absorption and fluorescence wavelength ranges of most of the fluorescent dye penetrants now in common use.

In addition to its spectral characteristics, the unique properties of this glass that enhance its use as a dye penetrant standard are the very small dependence of its fluorescence on temperature and its long-term stability. Based on measurements performed between 15 and 40 °C, the fluorescence was found to decrease 0.05% per degree Celsius increase in temperature. For comparison, the fluorescence temperature dependence of uranyl glass is about 20 times larger. For the stability study, an accelerated test was used in which samples were exposed to radiation that had the same spectral distribution as the fluorescent lighting of the laboratory but was 1000 times more intense. After being subjected to the equivalent of 27,000 hours of continous normal laboratory irradiation, no significant change in fluoresence was measurable (decrease $\leq$ 1.4%).

A portion of the bulk glass is currently being sized and polished to fit adapters that will be used in Turner Models 110, 111 and 112 or Coleman Model 12C fluorometers in pending ASTM round-robin tests on the performance characteristics of dye penetrants. Samples of this glass will be available on request for use in these tests. Later this year this glass will also be available in a form in which a graded series of fluorescent indications of known widths are produced by a combination of masking and overcoating with a nonreflective,

opaque metal film. This type of standard should be particularly useful in improvin the reproducibility and repeatability of comparative crack plate testing of penetrants and for also reducing operator bias in estimating the size of actual surface defects.

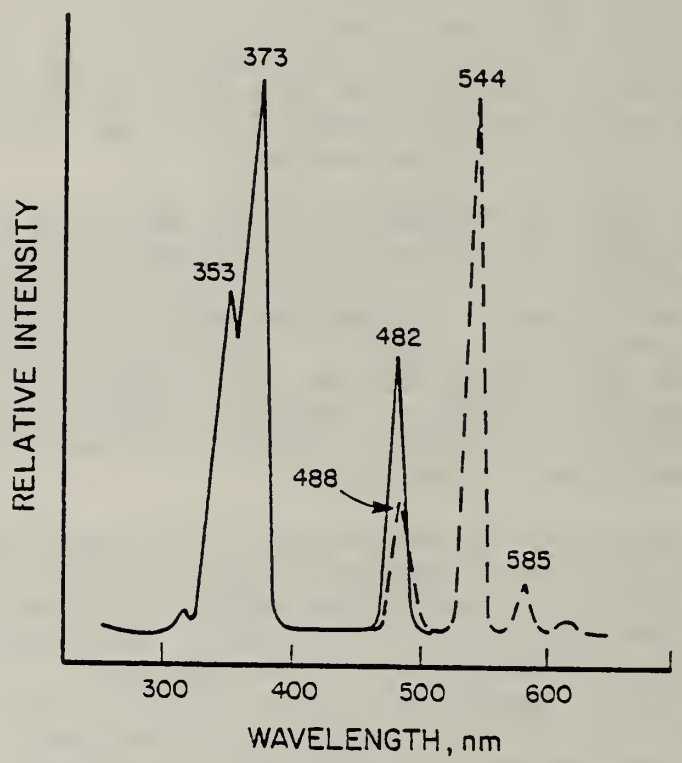

Figure 1. Uncorrected excitation (solid line) and emission (broken line) spectra of proposed terbium phosphate fluorescent glass standard.

MAGNETIC MEASUREMENTS

Lydon Swartzendruber
Metallurgy Division
Center for Materials Science

Magnetic particle NDE is a simple and inexpensive, yet very effective, NDE method and hence is in widespread use. However, the lack of reliability of this method was graphically illustrated by a round robin test reported by Gulley (ref. 1). In that test, eleven laboratories inspected 24 specimens with known defects. Only one laboratory found more than 90 percent of the defects, while the majority found less than 50 percent. The reason for the success of this one laboratory in presence of the failure of the others can be attributed to the technique by which the presence of adequate magnetization of the sample was determined. Our recent results (ref. 2) have shown the basic reason for this and established the following principles:

1) The value of the applied magnetic field, H, in the vicinity of the defect, rather than the B field within the material, is most important for the magnitude of the force exerted on the magnetic particles used in the NDE test.

2) The optimum applied magnetic field to use does not lie at the point of maximum permeability of the material under test, as often assumed, but is considerably larger than this field. The optimum applied field is the largest field which will not cause the magnetic particles to be too sensitive to surface conditions, cause excessive "chaining" of the particles (hence reducing their mobility before they are close to the defect), or give excessively large field gradients due to "flux leakage" caused by sample geometry.

3) An empirical detection criterion can be established from which the detectibility of a crack or defect can be determined. The minimum applied field necessary to detect a defect can then be calculated using suitable computer methods to determine the geometry of the leakage field arising from the defect.

Using these principles it becomes possible to critically inspect the effectiveness of various "rules of thumb" used in magnetic particle inspection. These rules of thumb have, in the past, been based on a combination of what appears to work and what is practical to achieve. These rules are being evaluated and modified according to the principles mentioned above. Use of the current rules established an applied magnetic field of between 1.3 kAm^{-1} (16 Oe) and 11 kAm^{-1} (140 Oe) in the vicinity of the defect. The rationale for this wide range of fields is based on the experience that for very large parts (where the higher fields are difficult to establish with available equipment) defects are of less importance and hence lower fields are required, whereas for smaller parts larger fields are required in order to detect the important smaller defects. Also, the smaller parts generally have a smoother surface and interference effects are not caused by using the larger fields.

Another important aspect of our results (ref. 2) is that they show how a Hall effect magnetometer may be used to determine adequate magnetization in parts of arbitrary geometry. It is necessary that the size of the probe be small in comparison to the rate of change of the H field. It need not be small in comparison to the size of the leakage field from the defects being tested. It also must be arranged to measure the component of H parallel to the surface of the part. This type of determination for adequate magnetization can be expected to be especially useful in the case of alternating current fields whose effects are much more dependent on the magnetic properties of the material under test than are inspections made with direct current.

Another important aspect of magnetic particle inspection relates to the properties of the particles themselves. The optimum particle size for magnetic particle inspection depends on a number of factors but most important are the dimensions of the defect, the field applied to the sample under test, and the surface roughness. To cover as wide a range of situations as possible, a range of particle sizes is desirable and is usually present in most commercial powders. Not only particle size, but also particle shape is important. In this respect, there are two opposing factors. On the one hand particles should be spherical in shape to impart the greatest mobility. On the other hand, needle shaped particles have the greatest response to magnetic field gradient due to their smaller demagnetizing factor (which is in most cases more important than their permeability). There are also two opposing factors for particle size. On the one hand, the smaller particles are the most sensitive to fine cracks and small defects. On the other hand, large particles have higher mobility and are less sensitive to rough surfaces. Current magnetic particle specifications provide for a test of the magnetic particles on a test ring with artificial sub-surface defects and a maximum size for the particles. That this is an inadequate specification can be seen by examination of the three particle distributions shown in Figure 1. The powders represented by the curves A and B represent commercial powders from two different suppliers. Powder C was formulated from comminuted electrolytic iron. All three of these formulations meet the current specifications yet are different in their response to different defect situations. For detecting subsurface defects below a smooth surface, as called for in the particle specifications, powder C was superior to A or B. Yet powder C would be of little use for most magnetic particle NDE situations because of the lack of smaller particles required for fine crack detection and the flake like shape which gives poor mobility on a rough surface. Powder B could be expected to be better than A on a rough surface because the increased amount of larger particles improves the overall mobility of the powder, whereas the opposite situation would apply where fine cracks on a smooth surface were of most interest. Practical tests which could more clearly discriminate between the properties of powders A,B, and C could clearly improve the state of the art in

magnetic particle testing, and provide the nondestructive testing engineer with a more rational choice of particle formulations geared to specific applications.

1. L.R. Gully, "Proceedings of the Interdisciplinary Workshop for Quantitative Flaw Definition", Air Force Materials Laboratory Report AFML-TR-74-238, pp 5-67 (1974).

2. C.L. Oehl and L.J. Swartzendruber, "On the Optimum Applied Field for Magnetic Particle Inspection Using Direct Current", to be published in J. Nondestructive Evaluation, vol. 3, page 125.

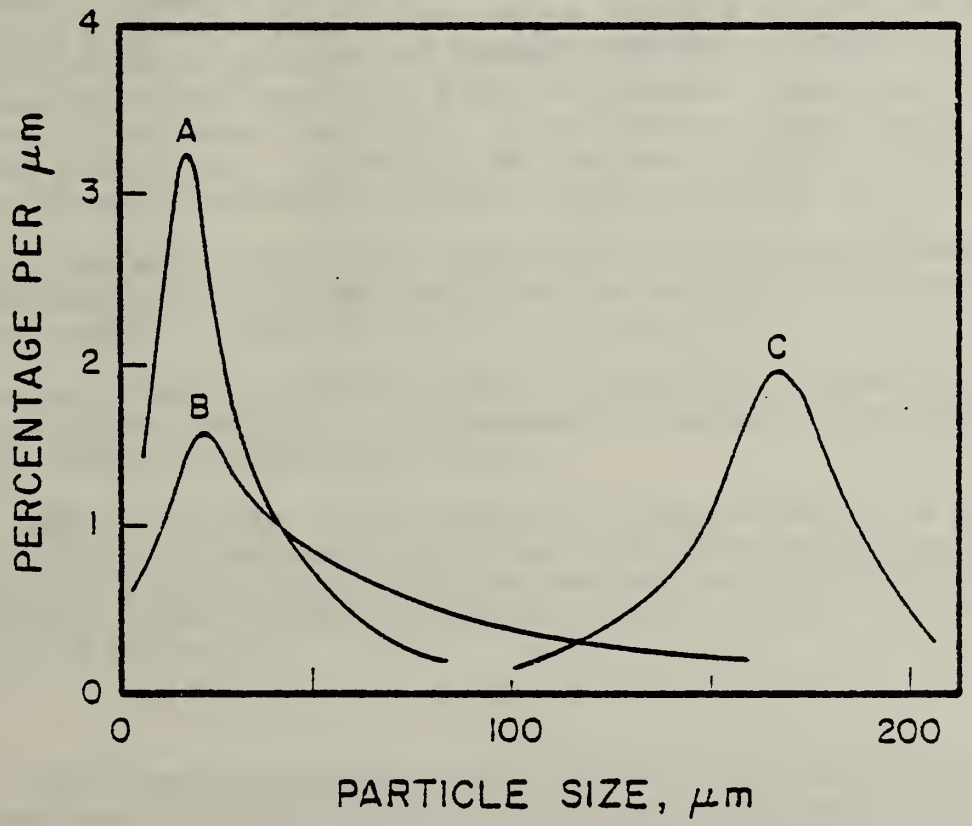

Figure 1. Relative percentage frequency curve for three magnetic particle formulations. For each formulation, the ordinate indicates the percentage of all particles in the formulation that are sized between n and n+1 micrometres.

MAGNETIC PARTICLE INSPECTION STANDARDS

L. Swartzendruber
Metallurgy Division
Center for Materials Science

This project was initiated by the Specifications and Technical Data Branch of the Army Materials and Mechanics Research Center, Watertown, MA. Military specification MIL-M-11472, "Magnetic-Particle Inspection Process for Ferromagnetic Materials", is being reviewed for proposed revision or cancellation and replacement by Military Specification MIL-STD-271, Military Specification MIL-I-6868, or American Society for Testing and Materials Recommended Practice E709-80. The contents of these documents have been compared with current state-of-the-art practice in magnetic particle inspection as revealed by industrial practice, available literature, current applicable Military Standards, Aerospace Materials Specifications, and American Society for Testing and Materials documents. A draft version of a revised MIL-M-11472 has been prepared and circulated for comments by the intended users within the Department of Defense. Comments have been received and the document is currently being revised. In addition, a glossary of terms relating to magnetic particle inspection has been prepared for inclusion in MIL-M-11472.

DEVELOPMENT OF HIGH OPTICAL DENSITY STANDARDS

J. Hsia, C. H. Popenoe, and L. Fink

Radiometric Physics Division

Center for Radiation Research

The anticipated change from the current ISO and ANSI standards (ref. 1) and continuous demands for higher optical density standard materials require proper action from NBS to meet the needs. Optical density standards are used to calibrate densitometers. Densitometers are employed to measure exposed X-ray films which are used for nondestructive evaluation.

The objectives of this project are to develop high optical density standards (up to optical density of 5.8), and to base calibration of master standards on the Inverse Fourth Apparatus through development of hardware and software for the Inverse Fourth Apparatus and characterizations of the apparatus and high optical standards. Some electronic equipment and interface have to be replaced and software developed in order to achieve fully automated measurements. See ref. 2.

HARDWARE

The computer system consists of a 64K microcomputer, two double sided disk drives, a line printer and a CRT. Several interface boards have been designed and constructed. The new high voltage power supply for the photomultiplier has been programmed to change voltages automatically.

The carriage which carries the flexible glass fiber is positioned by a new stepping motor with new power supply and the position of the carriage is read by the computer by counting the moiré fringes.

The current from the photomultiplier is converted to frequency with the current-to-frequency converter. The frequency is counted by the counter and read by the computer as measurement signals.

The integrating sphere for the detector has been fitted with a pressure and vacuum system to create an air gap between the entrance aperture to the integrating sphere and the sample when the sample slider is moving and to press the sample tightly against the aperture when the sample is in the light path during the measurement.

SOFTWARE

Many subroutines have been developed for the Inverse Fourth Apparatus. These subroutines are for positioning the carriage and the sample holder, collecting data, setting high voltages, and initializing the positions for the carriage and sample holder.

Full computer programs have been developed to determine the zero position of the carriage and to determine optical densities of the x-ray and

photographic step tablets.

The optical density measurement procedures are as follows. The sample holder is moved to the area of the sample to be measured. The carriage is moved to a preselected position, d_2, and several signals are measured and averaged (S_2'). The sample is moved out of the light path. The carriage is moved to a position so that the signal is slightly smaller then the average signal S_2'. The carriage is then moved with small interval and the signals at each position are measured. A linear least square fit is performed on the set of data of signals vs positions. The carriage is moved back to distance d_2 and the sample is moved into the light path. Several signals are then measured and averaged (S_2''). The average S_2 of S_2' and S_2'' is calculated. The signal S_2 and the equation of the fitted curve are used to calculate the distance d_1. The transmittance, T, can be calculated by

$$T = \left(\frac{d_2-d_o}{d_1-d_o}\right)^4$$

where d_o is the 'zero distance'. The optical density is then

$$D = -\log T.$$

CHARACTERIZATIONS

Computer simulation has been performed to determine the optimum positions which would give small uncertainty in determining 'zero distance'. These optimum positions were used to perform the measurements and the 'zero distance' has been determined to be 112 mm ±0.5 mm. In determining optical density of a film, the 'zero distance' was purposely varied from 112 mm to 110 mm and 114 mm. The resulting differences in optical densities were within the theoretical predictions.

The uniformity of the power law dependence at different carriage positions was confirmed using the following method. The optical density of a film has been measured at several positions of the carriage. The differences of optical densities were within the random noise of the measurements.

The lamp voltage was varied from 15 to 105 volts. The optical density determinations were independent of voltages from 85 to 105 volts.

Optical densities of a photographic step tablet measured with the Inverse Fourth Apparatus were compared indirectly with that of the Inverse Square Instrument through a transfer densitometer. The results were within one percent of the values.

Preliminary direct intercomparisons on an x-ray step tablet between the

Inverse Fourth Apparatus and the Inverse Square Instrument were performed. The agreements were also within one percent of the values.

Preliminary evaluation of low optical density samples indicated that the receiver using the integrating sphere diffuser yielded higher optical density than using the opal diffuser.

Several high optical density step tablets have been measured. These step tablets, produced by an x-ray company, have seventeen steps. The sixteenth step has 5.45 optical density and the last step has optical density higher than 5.8 and is beyond the measurement capability of the Inverse Fourth Instrument.

Because of some hardware replacements and software development not anticipated in our original plan, this project needs to be extended to the next fiscal year in order to complete the remaining tasks: final intercomparison with the Inverse Square Instrument, intercomparison with other national laboratories, pilot run with selected users, final selection of standard reference materials and preparation of documentation.

REFERENCES

1. "Conditions for Diffuse and Doubly Diffuse Transmittance Measurements (Transmission Density)", American National Standards Institute, PH2.19-1976.

2. D. A. Swyt and J. G. LaRock, "Inverse-fourth apparatus for photometric calibration", Rev. Sci. Instrum. 49 (8), 1083-1089 (Aug. 1978).

RADIOGRAPHIC IMAGE QUALITY EVALUATION AT HIGH ENERGIES

R. C. Placious and D. Polansky

Radiation Physics Division

Center for Radiation Research

The need for measuring x-ray system performance at high energies has led to the design of an image quality indicator (IQI), and test protocol similar to the one developed earlier for low energies (200 kV) (ref. 1). Among the problems in developing a suitable IQI for high-energy x-ray beams is the reduced image contrast per unit specimen thickness that is a property of such beams. In an attempt to produce a viable test object having the required range of contrast sensitivity we have made four modifications to the original design. After each modification it is necessary to provide test exposures using high-energy x-ray sources. Most of these exposures are being provided by private laboratories which are cooperating in this endeavor. The film readers include personnel from these laboratories as well as from NBS. All of the test data are being evaluated here.

To date, exposures have been provided at 4, 7.5 and 8 MeV. Additional exposures are to be made at 2 MeV and 15 or 25 MeV. While it is probable that the test object and protocol will not be applicable over this entire energy range, the inclusion of the latter ranges will allow a decision to be made on where the limitations should be placed. The specimen thickness and the multi-hole plaque used in all exposures are fixed.

REFERENCE

1. ASTM Standard E 746-80 "Standard Method for Determining Relative Image Quality Response of Industrial Radiographic Film" 1982 Annual Book of ASTM Standards, Part 11.

MODULATION TRANSFER FUNCTION MEASUREMENT OF AN IMAGE INTENSIFIED SOLID STATE X-RAY CAMERA

R. D. Spal, H. E. Burdette, W. J. Boettinger and M. Kuriyama

Metallurgy Division

Center for Materials Science

The goal of this work was to develop a simple procedure for measuring the modulation transfer function of an image intensified solid state x-ray camera. This is necessary for precise evaluation of the resolution of the existing camera, and for comparing it to cameras under development. Previous work to specify the camera performance involved one of two procedures, depending on the signal level. A strong signal is defined as one which produces a recognizable image at the standard video rate of 60 fields per second. For strong signals, the resolution was estimated by viewing a test pattern of bars of variable width and spacing. This qualitative method yields a limiting resolution of about 100 microns. For weak signals, the quantum efficiency and resolution were determined by computer processing the image of a uniform beam of known intensity to reveal the number of photon images and their average size. This quantitative method yields an average photo image diameter of about 130 μm. However, it is difficult to extrapolate this result to strong signals, especially since the distribution of photon image diameters is broad and non-Gaussian. The present work uses strong signals.

The camera consists of a thin phosphor screen to convert x-rays to visible light, an image intensifier tube to boost the light intensity, and a solid state camera to convert the image into a video signal. The phosphor screen and solid state camera are coupled to the entrance and exit windows of the image intensifier with fiber optics. The image intensifier has a photocathode deposited on the entrance window, dual microchannel plates, and a phosphor deposited on the exit window. Its luminous gain is adjustable up to 500,000. The solid state camera is a General Electric model TN2500 CID camera, consisting of an area array of 244 by 248 pixels, each measuring 36 by 46 μm. Each pixel is scanned 30 times per second.

The modulation transfer function (MTF) is determined from the image of the edge of a mask in an 8 keV beam. The beam is about 1 mm high, and wider than the camera field of view. The mask is attached to the input phosphor screen, with its edge oriented vertically and centered in the field of view to obscure one half of the beam. The video signal is digitized by a 4 bit frame grabber, and loaded into a buffer memory. An LSI 11/23 microcomputer transfers the data from memory to disk, and later recalls the data from disk for processing.

Since the pixel size is not much smaller than the resolution, Fourier transform techniques are not used to determine the modulation transfer function. Instead, it is assumed that the point spread function is a Gaussian with an unknown standard deviation σ. Convolution of this point spread function with a step function, representing the true mask image, yields the function representing the actual mask image. Besides σ, three adjustable parameters are included in this function, to represent the position of the mask edge, the beam

intensity, and the background intensity. The method of nonlinear least squares is applied to fit the parameters to the data. Each row of pixels is analyzed independently, so that any deviation of the edge orientation from the true vertical is not important.

Data were collected for luminous gains from 20,000 to 300,000. As the gain was increased, the beam intensity was reduced to prevent overload. Some results are presented in Figures 1a through 1c. Figure 1a shows raw and fitted data for a single row of pixels, with a gain of 20,000. The fitted value of σ is 190 μm. It is customary to express resolution in line pairs per mm (lp/mm) at a specified MTF value, usually .05. In these terms, the resolution is 13 lp/mm. The value is nearly independent of gain over the range tested. Figure 1b shows the fitted value of σ for many rows of one image, again with a gain of 20,000. Finally, Figure 1c shows the edge position for many rows of two images, with gains of 20,000 and 150,000. The functional dependence of the edge position on the row number is expected to be linear, with a slope determined by the orientation of the edge. While this holds for the lower gains, it fails for the higher gains. At high gain, the image is distorted, even though the resolution, as determined from σ, is not degraded. The distortion is a bulging of the center of the edge beyond its true position and into the shadow region. This effect is not presently understood, and will be investigated further.

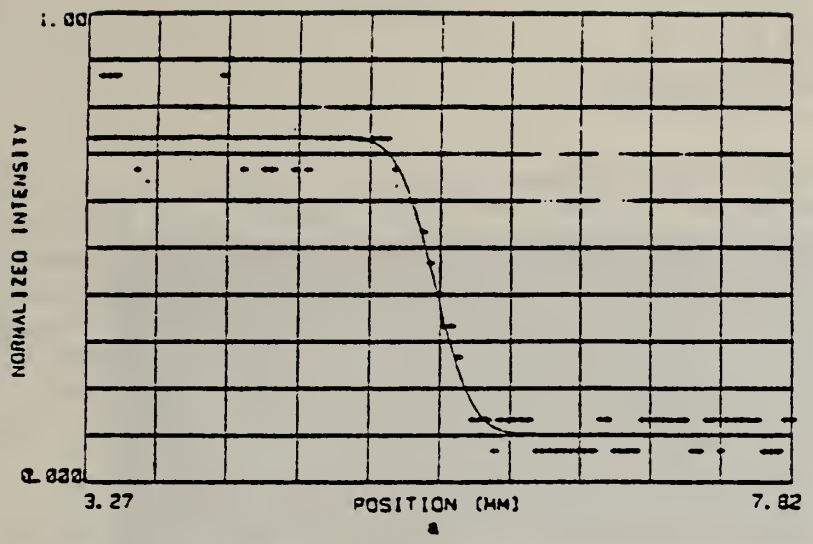

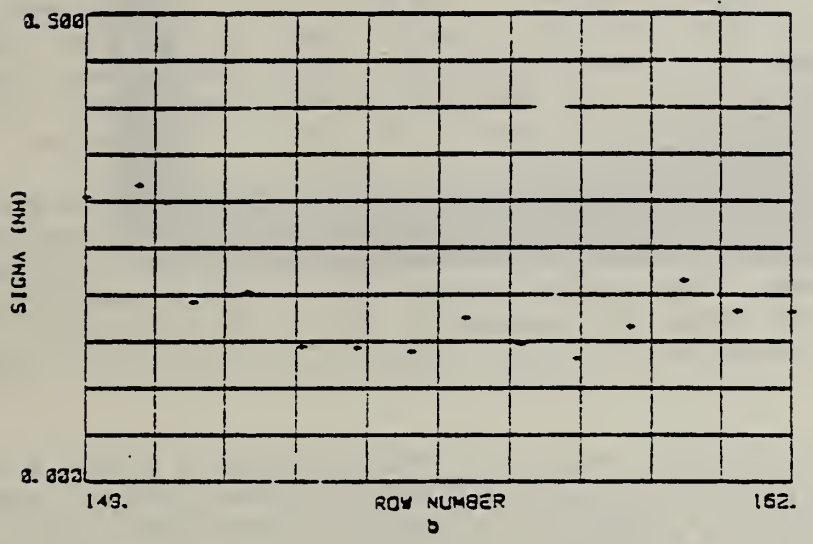

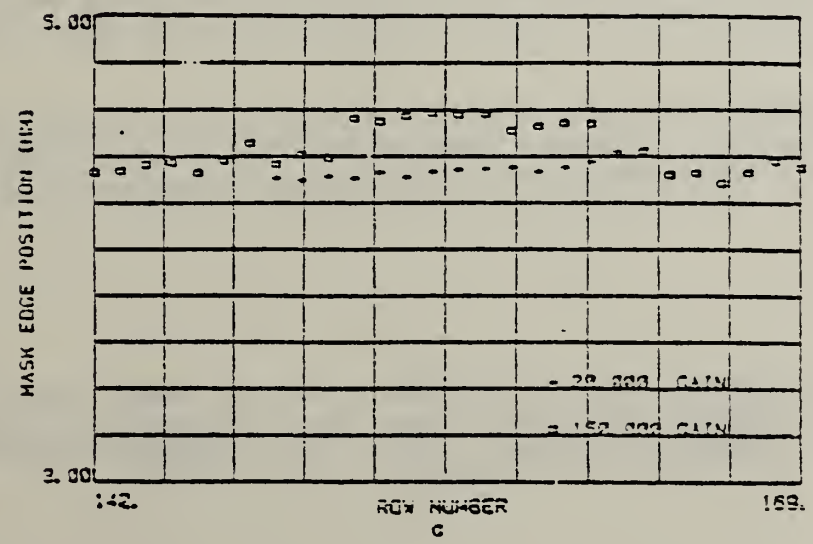

Figure 1 a) Raw and fitted data, b) Fitted SIGMA and c) Mask edge position.

DIGITAL RADIOGRAPHY

R. C. Placious, D. Polansky and J. H. Sparrow

Radiation Physics Division

Center for Radiation Research

Digital imaging technology became feasible in the late 1970's with the advent of fast analog to digital converters coupled with relatively inexpensive random access memory chips and a dedicated microprocessor. Detection equipment for radiography also became more readily available so that it is now possible to take real time images and rapidly execute some processing algorithm or transformation on the image and immediately view the result. Furthermore the displayed image can then have operations performed on it, such as scrolling or zooming, without loss of the original image content.

One of the most useful processing operations is image integration which can be done at TV frame rates. This is analogous to the image integration done by film when exposures are fairly long due to low flux levels. Another useful feature of the digital image processor is the ability to subtract one image from another. This is quite often applied in medical radiology to make changes that occur between two images more readily apparent. Image subtraction is expected to play a major role in a radiologic technique known as dual energy imaging wherein two images are made with different x-ray spectra and compared.

Digital image processing can also be applied to film based radiographs with some degree of success. This is very useful for low contrast radiographic images which can often be improved by a digital transformation which "stretches" the available contrast range. The original radiograph is scanned and digitized in the same way a real-time image is presented to the digital processor. The use of some of these techniques on film based images was discussed in a recent symposium (ref. 1).

Part of the image processor memory is used to provide a graphics capability for the system. In addition to the construction of lines, circles, squares, alphanumeric text, etc., this capability allows for a presentation of histograms which show the gray scale distribution of all pixels in the image of interest. It is often on the basis of this knowledge of the gray scale range that one can construct or select a convolution or transformation which makes the image more amenable to interpretation.

All of the ideas discussed above, along with many others, are being applied to nondestructive inspections. Figure 1 demonstrates the effect of "contrast stretching" applied to a low contrast slit image having a density change of 0.04 or less.

REFERENCE

1. R. C. Placious, D. Polansky and J. H. Sparrow, "Digital Image Processing for Improved Detection and Diagnosis of Hidden Flaws", Proc. 36th MFPG Conference, Phoenix, AZ, Dec. 1982 (Cambridge University Press, NY, in press).

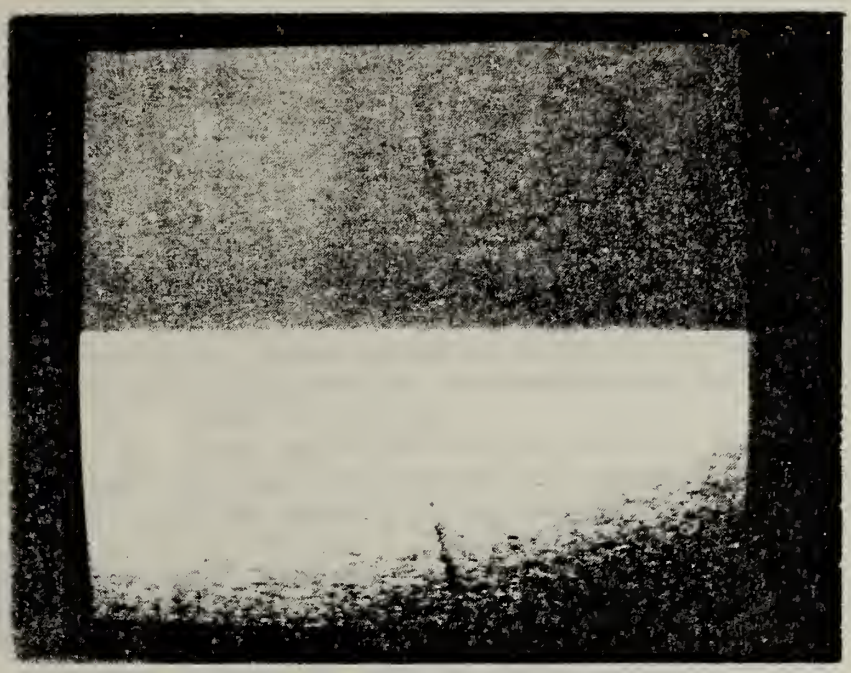

Figure 1. The upper half of this illustration is the original radiograph. The lower half has been enhanced by a digital transformation which greatly "stretches" available contrast.

ADVANCED RADIOGRAPHY

D. Polansky

Radiation Physics Division

Center for Radiation Research

The Test and Inspection Subcommittee of the DoD Manufacturing Technology Advisory Group held a workshop on advanced radiologic programs. The workshop was held December 7-8, 1982 in Phoenix, Arizona with ASTM Committee E-7 as co-sponsor. There were four sessions with papers on real-time imaging, computerized axial tomography, digital enhancement and automatic image analysis. The writer was chairman of the workshop on digital enhancement technology. A summary report* was written and presented to the advisory group.

After lengthy discussion by the workshop participants, the following were identified as vital needs for digital enhancement radiography:

a. The area of reprojection technology should be supported. Tomographic systems that give data in the X-Y plane will require the reprojection of data in the Z plane for analysis.

b. Sensor technology should be supported, and sensors should be studied for optimization at different energy levels.

c. Inspection data should be used for process control.

d. Digital enhancement techniques should be used to promote automatic evaluation of data, to eliminate the operator from decision-making in the inspection process.

e. Develop small-area, high-sensitivity detectors.

The Aracor-Aerojet industry team is developing two computerized axial tomographic systems for the Air Force. One unit is to be used with a 300 kVp x-ray unit for the inspection of low density material up to 70 cm in diameter while the second unit is for the inspection of the Peace-seeker missile for the Air Force.

---

*MTAG Test and Inspection Subcommittee, "Manufacturing Technology Advisory Group, Advanced Radiologic Planning Workshop, 7-9 December 1982," 18 + iii pp (US Army Armament Research and Development Command, Dover, NJ, undated).

NDT SUPPORT FOR THE FLEET MISSILE SYSTEM

D. Polansky and J. H. Sparrow

Radiation Physics Division

Center for Radiation Research

The objectives of this program are to (1) provide technical engineering support to the area of nondestructive testing of Trident missile components, (2) recertify, twice yearly, all facilities involved in x-ray inspections of Trident rocket motors, and (3) evaluate proposed changes in inspection techniques. This work is supported by Strategic Systems Project Office, Department of the Navy.

The two new ballistic missile systems being developed by the Department of Defense are significantly larger than the presently deployed missile. Their nondestructive inspection poses new problems and one avenue being pursued is the use of computer aided tomography (CAT). The NBS task is to follow the technology being developed and advise the Navy Department of its applicability to a specific missile.

The qualification of the real-time inspection systems at all facilities requires a review team. NBS is a member of that team which recently reviewed the quality of inspections at Pomflant.* The team found that some of the inspections did not meet requirements and recommended that corrective action be taken. Another review of this facility is planned in the near future to evaluate their missile inspection performance.

The calibration of the radiation output of the 15 MeV linear accelerator was conducted at two facilities. The x-ray beam profile in the horizontal and vertical directions were measured so that the position of the laser alignment beam relative to the radiation beam could be checked.

Equilibrium caps made of polystyrene will be supplied to all of the facilities for use with their ionization chambers; they can then routinely check the linatron's x-ray output to verify that it remains above the minimum specified for the real-time inspections. The recertification program of all testing facilities is carried out semi-annually by an audit that consists either of visits to the installations or the submittal of test data to the auditors for evaluation. The purchase of a tape recorder on this project, that is the same as those used by the testing facilities, now makes it possible to evaluate real-time inspections at NBS. Copies of magnetic tape recordings of missile inspections will be routinely supplied to NBS for evaluation of the quality level of inspection.

---

* Polaris Missile Facility, Atlantic, located in Charleston, SC.

NONDESTRUCTIVE CHARACTERIZATION OF DISTRIBUTED DAMAGE

E. R. Fuller, Jr., K. Hardman-Rhyne and N. J. Tighe

Inorganic Materials Division

Center for Materials Science

R. J. Fields

Fracture and Deformation Division

Center for Materials Science

INTRODUCTION

In a number of instances, failure of a component results not from the formation and growth of a single macrocrack, but rather from the accumulation of damage, distributed homogeneously throughout the component. An example of such a situation is the nucleation and growth of creep cavities in metallic or ceramic components used in high-temperature applications under stress. An important design consideration for such components is an assessment of the material's creep life. However, of equal importance in service is a nondestructive assessment of the total amount of accumulated creep damage and, hence, of remaining lifetime. Another example of distributed damage might be distributed inhomogeneities (such as, microcracks, impurity phases or porosity) that can develop during or following ceramic processing. Although this damage does not necessarily accumulate during service life, nondestructive assessment of these distributed defects during in-line processing is of importance both for quality control and for early rejection of defective components to reduce later processing costs.

To address these issues, the objective of this research program is to assess nondestructively this accumulation of distributed damage and to correlate that assessment with microstructural defects in the material. As part of this objective various model material systems with distributed defects are being developed. Such "standard" systems allow the comparison of various nondestructive inspection techniques both amongst themselves and with direct observational measurements of size and abundance of defects, thereby increasing the scientific base for these NDE methods. The research effort during the past year has encompassed three such material/damage systems. The first, which is a continuation of research from last year, is a system of distributed creep cavities in metallic specimens at various fractions of their creep life. The second is an analogue damage system in high-temperature, advanced structural ceramics. This ceramic research is supported in part by the Army Materials and Mechanics Research Center, Watertown, MA. The third system is distributed porosity in ceramic materials at various stages of sintering during the processing cycle and is a collaborative effort with a project on green state NDE.

CREEP CAVITATION IN METALS

Research has continued this year in the production of metallic specimens with distributed creep cavities. Two systems are being studied. One, 304 stainless steel, is a commercial alloy of practical importance; the other, OFHC copper (99.99% pure), is a material that is being considered as a model

material/damage system, because it is easily cavitated in a short period of time. These studies are described below. When completed, the results of these studies will be used to assess the correlation between the degree of cavitation at equivalent life fractions in the stainless steel and in the copper, thus establishing a rational basis for nondestructive evaluation of creep damage and other forms of distributed damage in structural metals and alloys.

304 Stainless Steel

304 stainless steel used in high-temperature applications consists of metal carbides in an austenite matrix. The carbide-austenite interface at a grain boundary becomes a preferential site for cavity nucleation, which at elevated temperatures can be readily activated with low applied stresses by creep deformation and/or grain boundary sliding. The resulting cavities then grow, link and ultimately cause failure. The early stages of this process are extremely slow and the creep cavities, due to their small size, are not easily detectable or quantifiable. It is these early stages of nucleation and cavity growth that are examined in this research.

Since carbide precipitates, as well as creep cavities, give rise to neutron scattering, two requirements must be satisfied for a quantitative evaluation of cavitation damage: (i) The volume fraction of carbide precipitates should not change significantly during creep; and (ii) A reference sample with equivalent carbide structure should be measured and subtracted from the scattering spectrum of the crept sample. The first condition was achieved in the present study by a "stabilizing" heat treatment of approximately 40 hours at 775°C prior to initiation of the creep experiments at temperatures of 600°C and below. This allowed a complete precipitation of carbide and thereby stabilized the volume fraction of carbides. The second condition was satisfied by using a reference specimen, which was only heated (and not stressed), along with the crept specimen.

A number of specimens have been crept thus far in this study. Most of these experiments have been conducted at 600°C with applied stresses from 124 to 262 MPa and with accumulated times under stress from 50 to 2300 hours. A list of the nominal stress levels and the times under stress is given in Table 1. Some of these specimens are being studied using small angle neutron scattering (SANS) by researchers in the Reactor Radiation Division. Results of this work will be reported by that group.

A few specimens listed in Table 1 fractured under load. These have been examined metallographically. As shown in Figure 1, these specimens exhibit abundant creep cavitation. Therefore, the assumption in last year's work that the small angle neutron scattering is due to cavitation appears to be justified. The lack of such evidence earlier in this project was viewed as a potential limitation of the work. However, this difficulty is now eliminated. We are now ready to begin density measurements and a sonic resonance determination of the elastic properties of selected bars from these tests.

Pure Copper

A large quantity of OFHC copper (99.99% pure) has been acquired. Creep specimens having dimensions suitable for both SANS and ultrasonic measurements

have been fabricated, and testing has begun. We have determined that this material fails at 600°C in vacuum in approximately 24 to 30 hours under an applied stress of 7.7 MPa (1100 psi). As shown in Figure 2, these specimens are full of distributed damage.

A series of interrupted tests are currently in progress. These tests will be conducted at nominal applied stresses of 7.7 MPa (1100 psi) and 5.8 MPa (840 psi). In all cases an unstressed control specimen is exposed at temperature along with the creep specimen. The density of the 50 mm gage section will be determined as a function of elongation and time under stress, and compared with that of the control specimen. These specimens will then be reduced to 8 mm long cylinders for SANS studies, ultrasonic elastic modulus determinations and internal friction studies.

DISTRIBUTED DEFECTS IN STRUCTURAL CERAMICS

Advanced ceramics, such as silicon nitride, silicon carbide, SiAlON's, etc., are being considered for a number of high-temperature applications because of their excellent high-temperature properties (high strength, corrosion resistance, and thermal conductivity, for example). These applications include heat exchangers and heat engines to mention only two, where numerous components (turbine blades and rotors, combustor chambers, diesel cylinder liners and piston caps, etc.) are being fabricated from ceramics. Long-term reliability of these components will most likely be governed by the same type of creep cavitation failure as for metals. In addition, distributed defects, such as impurity phases, microcracks and porosity, which enter these ceramics during the processing cycle, can also influence reliability. To characterize nondestructively these distributed defects in ceramics two research studies have been undertaken this year. One study examines distributed, submicrometer impurity phases and microcracks in nonoxide ceramics. Small angle neutron scattering (SANS) in the diffraction regime and transmission electron microscopy (TEM) are used for this study. The other study extends SANS techniques to the multiple refraction regime to elicit information about distributed porosity in the size range from micrometers to tens of micrometers. In the coming year both of these SANS techniques and TEM will be applied to elucidate the nature of creep cavities in ceramic materials over an extended size regime.

Inclusions and Microcracks in Nonoxide Ceramics

Small angle neutron scattering (SANS) in condensed matter is a nondestructive technique that can measure distributed defects approximately 2 to 100 nm in size. Defects and impurities that lead to detrimental structural reliability in advanced silicon nitride and silicon carbide materials are generally submicrometer in size and difficult to measure until they have reached an advanced stage of growth, which often leads to failure of the material. SANS techniques are being explored as a nondestructive probe for characterizing these distributed defects, with TEM observations being used to verify the microstructural nature of these defects.

A previous study (ref. 1), using SANS to characterize a hot-pressed silicon nitride material, concluded that neutron scattering in their material was refractive in nature. This is not necessarily a general conclusion for dense ceramics, but rather indicates that the nature of the neutron scattering

needs to be determined for each material system, and if possible verified by alternate techniques. In the present studies, which were supported in part by the Army Materials and Mechanics Research Center, two high-temperature, advanced ceramics [magnesia-doped, hot-pressed silicon nitride (NC 132) and a pressureless sintered silicon carbide (Hexoloy SA)] were examined with SANS and by transmission electron microscopy (TEM).

For the silicon nitride material SANS measurements were made for scattering vectors, Q, in the range of 0.005 $\mathring{A}^{-1}$ to 0.17 $\mathring{A}^{-1}$ and at wavelengths of 5.45, 7.6 and 9.0 $\mathring{A}$. Figure 3 shows the scattering data for Si_3N_4 plotted as the logarithm of intensity versus scattering vector, Q, in reciprocal angstroms. Two regions are particularly useful in analyzing the data. Region 1, shown in Figure 3 and expanded in Figure 4, is the Guinier region where the logarithm of the intensity has a Q^2 behavior. The intensity in region 2, called the Porod region, has a Q^{-4} dependence, and is shown expanded in Figure 5.

A Guinier fit to region 1 yields a radius of gyration of 18.6 nm, which is related to the average radii of the iron and tungsten inclusions in this material, as confirmed by TEM. In this scattering region the neutron intensity is limited by the larger dimensions of the scattering particles. In particular, scattering by large pores or extensive porosity (on the order of 0.8 to 10 μm) could be easily measured, but no such evidence was seen for this high-density material either by SANS or TEM. The SANS results are shown in Figure 6 by comparing the direct beam scattering (blank sample) with the scattering from the Si_3N_4 sample at several wavelengths. If large pores were present there would be significant broadening of these scattering patterns (compare with Figure 10 below).

The Porod region is more sensitive to the smaller dimensions of the scattering centers, and results in a characteristic Porod length which measures a volume to surface ratio. The ratio obtained for this material was 21.2 nm. This result in conjunction with the Guinier analysis suggests an average inclusion radius of 11 to 14 nm.

Data have also been collected for two samples of a sintered alpha silicon carbide. One sample is as-received and the other has been treated at 1370°C for 3500 hours. Initial results indicate microcracks or microvoid healing during the heat treatment, however, analysis is still in progress. TEM observations confirm the presence of microcracks in the as-received samples (Figure 7).

Porosity in $YCrO_3$

Porosity is a critical aspect in the densification process of a sintered ceramic material. To elucidate the extent of such porosity, a quantitative study is being conducted with small angle neutron scattering (SANS) to determine average pore size. Rather than restricting the SANS measurements to the typical submicrometer size regime of neutron diffraction, this study has explored multiple neutron refraction as a means of extending the SANS characterization into the tens of micrometer size regime. Although this study

is conducted jointly with a project to characterize neutron scattering and a project to characterize "green-state" NDE (see articles by N. Berk et al. and T. Negas et al. in this report), similar techniques are expected to apply to creep cavities and other forms of distributed damage. This extension of SANS techniques to larger sizes is an important result because it allows a greater overlap of SANS characterization with other NDE techniques.

In the present study, two samples of $YCrO_3$ were fabricated from pure powders by isostatic pressing at 207 MPa (30,000 psi); one sample was then sintered. The density of the "green" compact was approximately 55% of theoretical density and that of the sintered material was approximately 93%. To explore multiple neutron refraction, SANS measurements were taken at five wavelengths: 5.45, 6.25, 7.0, 8.0 and 9.0 Å. The results revealed a striking difference between the two samples as illustrated in Figures 8 and 9, which are SANS spectra for the "green" compact and sintered specimens, respectively.

In particular, a strong dependence on wavelength is seen in the data for the "green" compact. This dependence is illustrated in Figure 10 by plotting the normalized intensity versus scattering vector, Q, for all five wavelengths. By fitting these data to a Gaussian distribution, the full width at half maximum, FWHM, could be determined and was found to increase linearly with wavelength, Figure 11. This behavior is characteristic of multiple neutron refraction from large particles or voids and is consistent with the porosity of the "green" ceramic compact. The sintered material shows no wavelength dependency indicating either the lack of pores or voids, or that they are very large and beyond the detection limits of our instrument.

Although the qualitative aspects of the data clearly demonstrate a strong effect of ceramic processing on the population of neutron scatterers in these materials, quantitative measures of the void size and void size distribution are less straightforward. If one assumes that the neutron scattering is described by multiple refraction and edge diffraction of voids, the estimate of the average pore radius is approximately 2.5 μm which is physically reasonable for the green compact of $YCrO_3$. For the wavelengths of these measurements, however, this corresponds to scattering phase shifts well within an intermediate range of values for which the neutron scattering is not expected to be analyzable by multiple refraction behavior alone. Therefore, a generalized theoretical technique is being developed by N.F. Berk of the Reactor Radiation Division to provide a quantitative analysis of the SANS data for densified ceramics, and other distributed defects in this size regime.

REFERENCE

1. P. Pizzi, "Analysis of Microvoids in Si_3N_4 Ceramics by Small Angle Neutron Scattering," in Fracture Mechanics of Ceramics, Edited by R.C. Bradt, D.P.H. Hasselman and F.F. Lange, Vol. 3, pp. 85-98 (Plenum Press, New York, 1978).

Table 1. Nominal stress levels and total elapsed times for creep cavitation tests of 304 stainless steel at 600°C.

Material	Nominal Stress (MPa)	Nominal Stress (10^3 psi)	Elapsed Time (hours)
NBS 304 SS	207	30	102
			312
			2113
			2303
	221	32	335
			1116
	234	34	141
			336
			407
			461
	262	38	50
			100
			166
ORNL 304 SS (Reference-heat)	124	18	1537 (interrupted at 789 hours)
	145	21	1493 (interrupted at 745 hours)

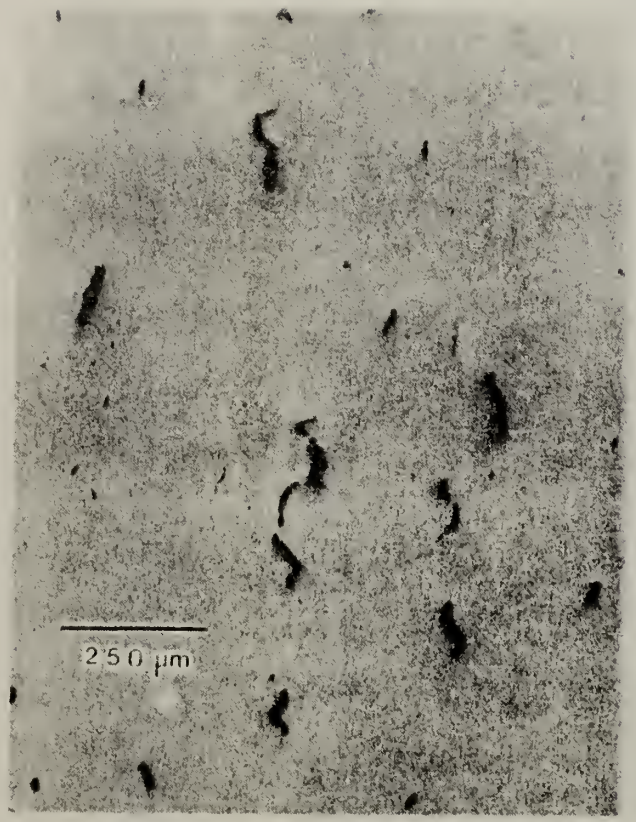

Fig. 1. Creep cavitation in a 304 stainless steel specimen that failed at 600°C in 1116 hours under an applied stress of 221 MPa (32×10^3 psi).

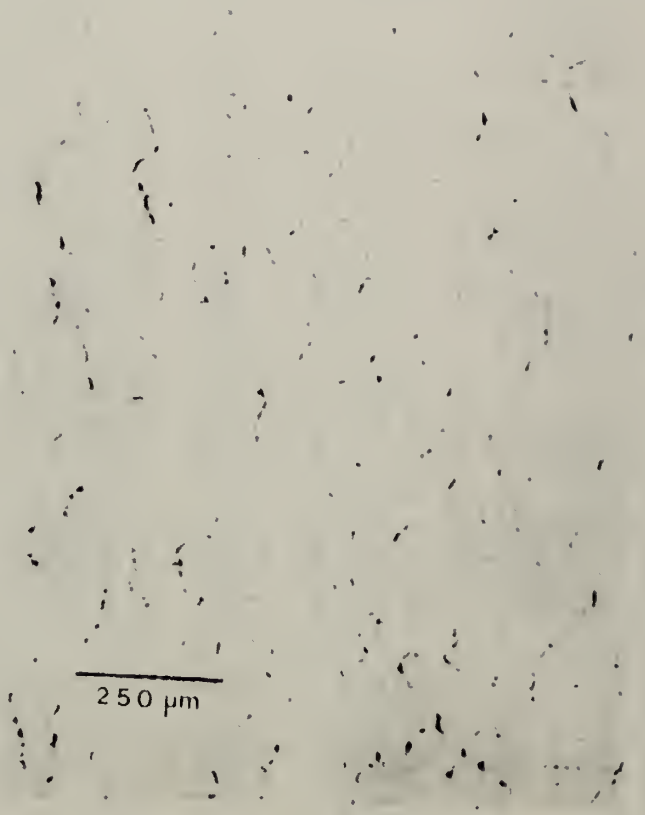

Fig. 2. Creep cavitation in a pure copper specimen that failed at 600°C in vacuum ($<10^{-6}$ torr) after 24 hours under an applied stress of 7.7 MPa (1100 psi).

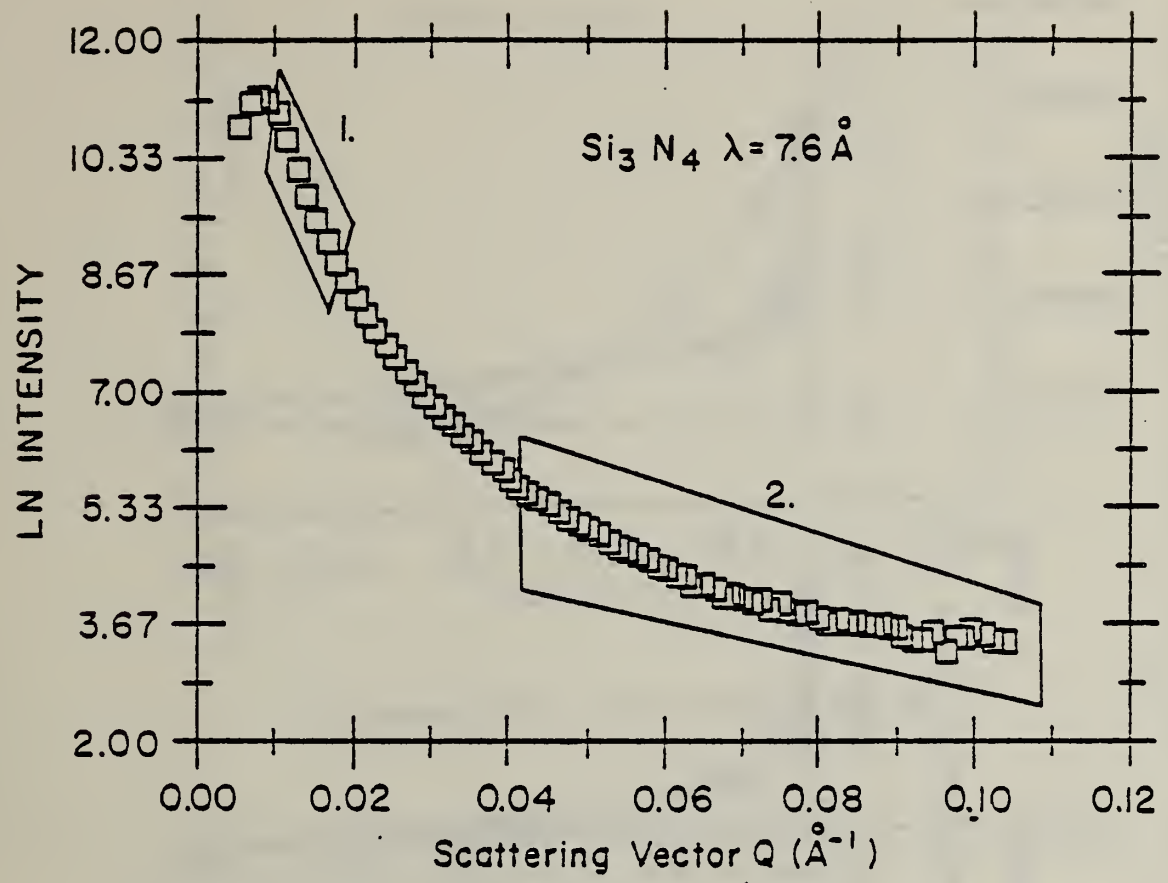

Fig. 3. Logarithm of neutron scattering intensity versus scattering vector, Q, in reciprocal angstroms. The two regions (1. and 2.) denote the Guinier and Porod regions, respectively.

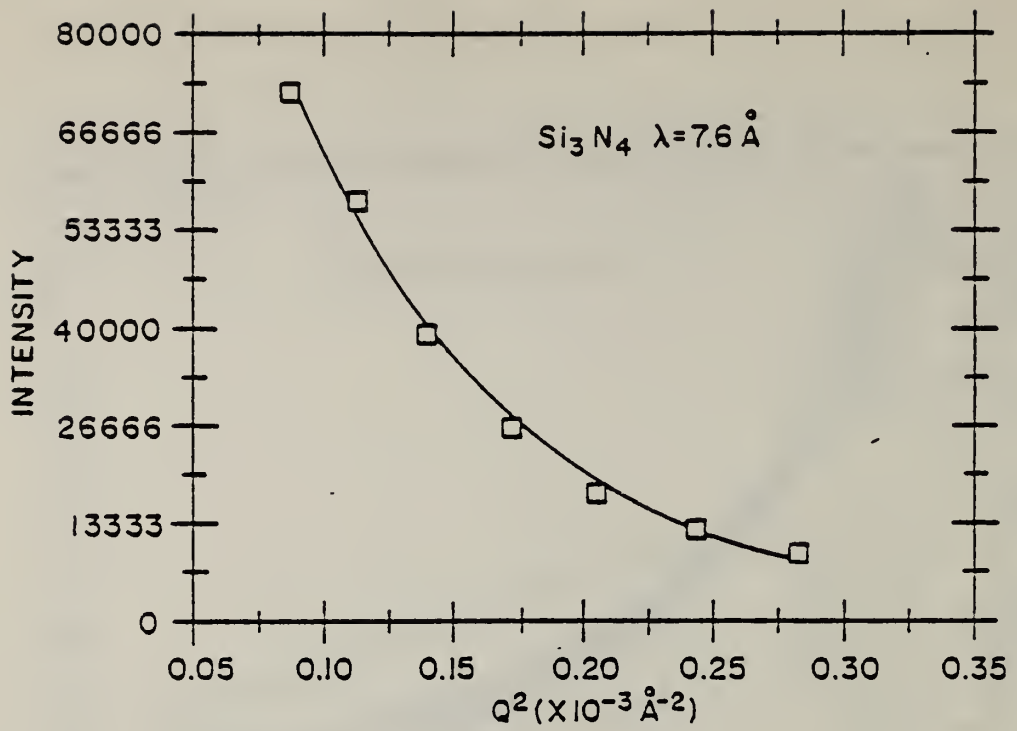

Fig. 4. Plot of the Guinier region from Figure 3.

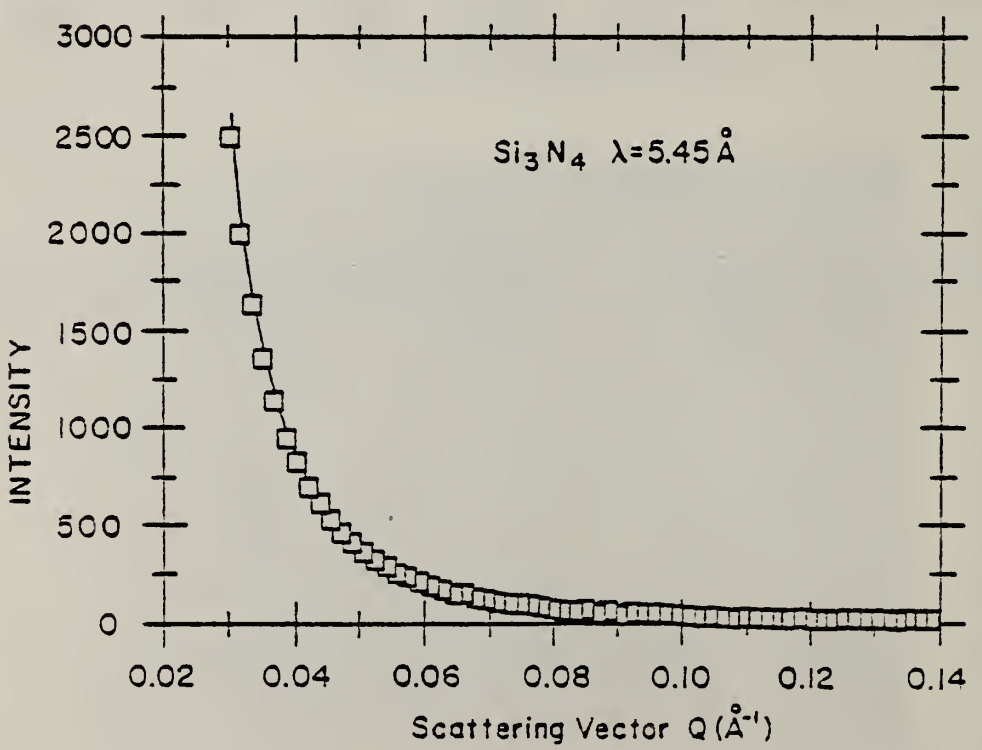

Fig. 5. Plot of the Porod region from Figure 3.

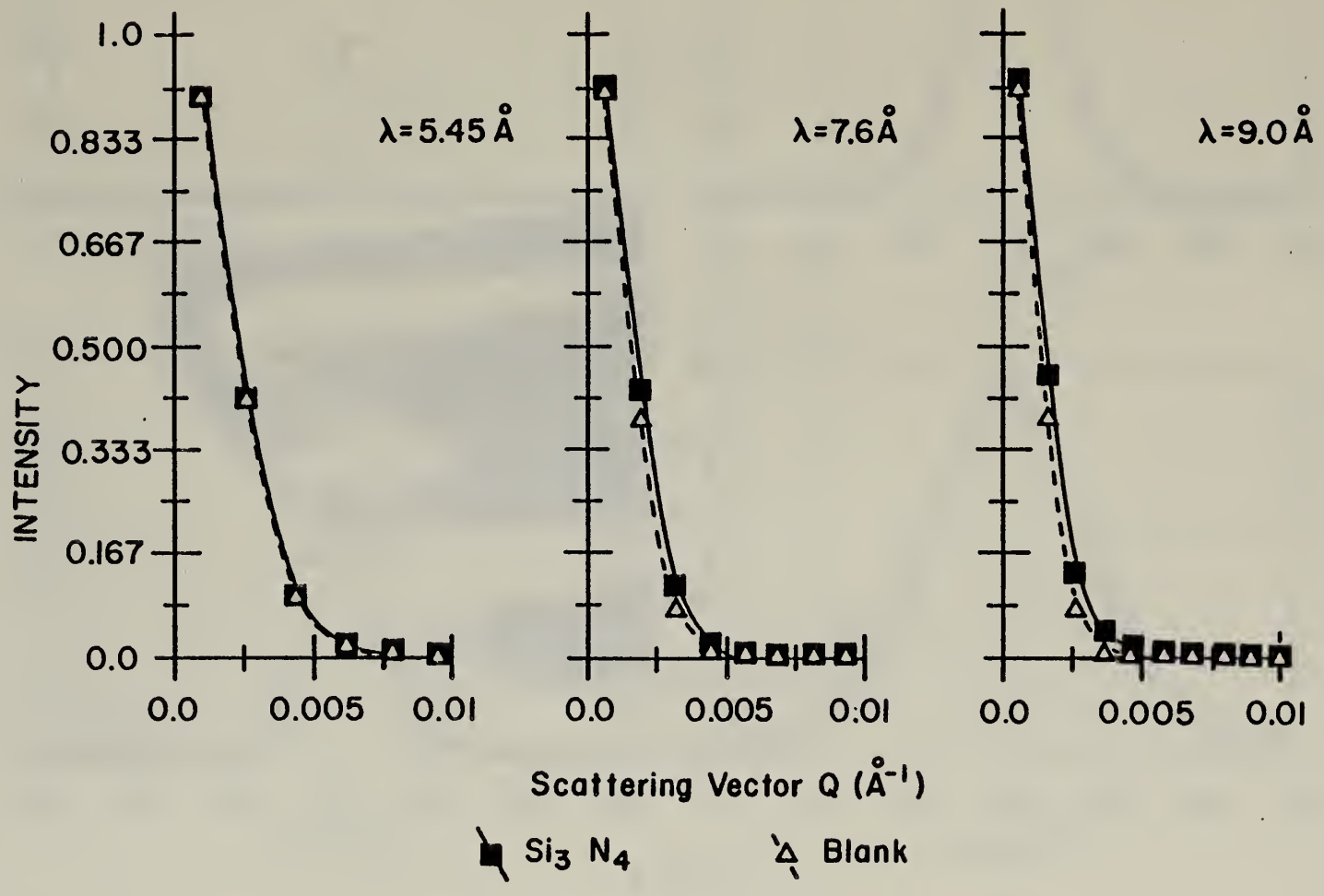

Fig. 6. Comparison of direct beam scattering (blank sample) with the scattering from the Si_3N_4 sample at several wavelengths.

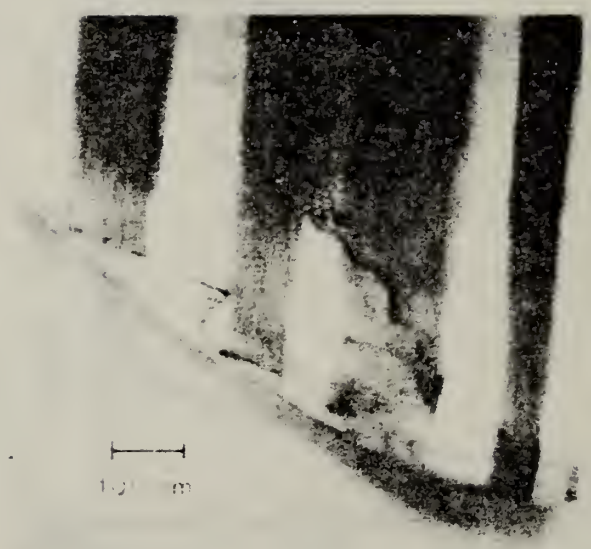

Fig. 7. Transmission electron micrograph of microcracks in the as-received silicon carbide material. Cracking occurs at the intersection of faults in the silicon carbide grains with the grain boundary.

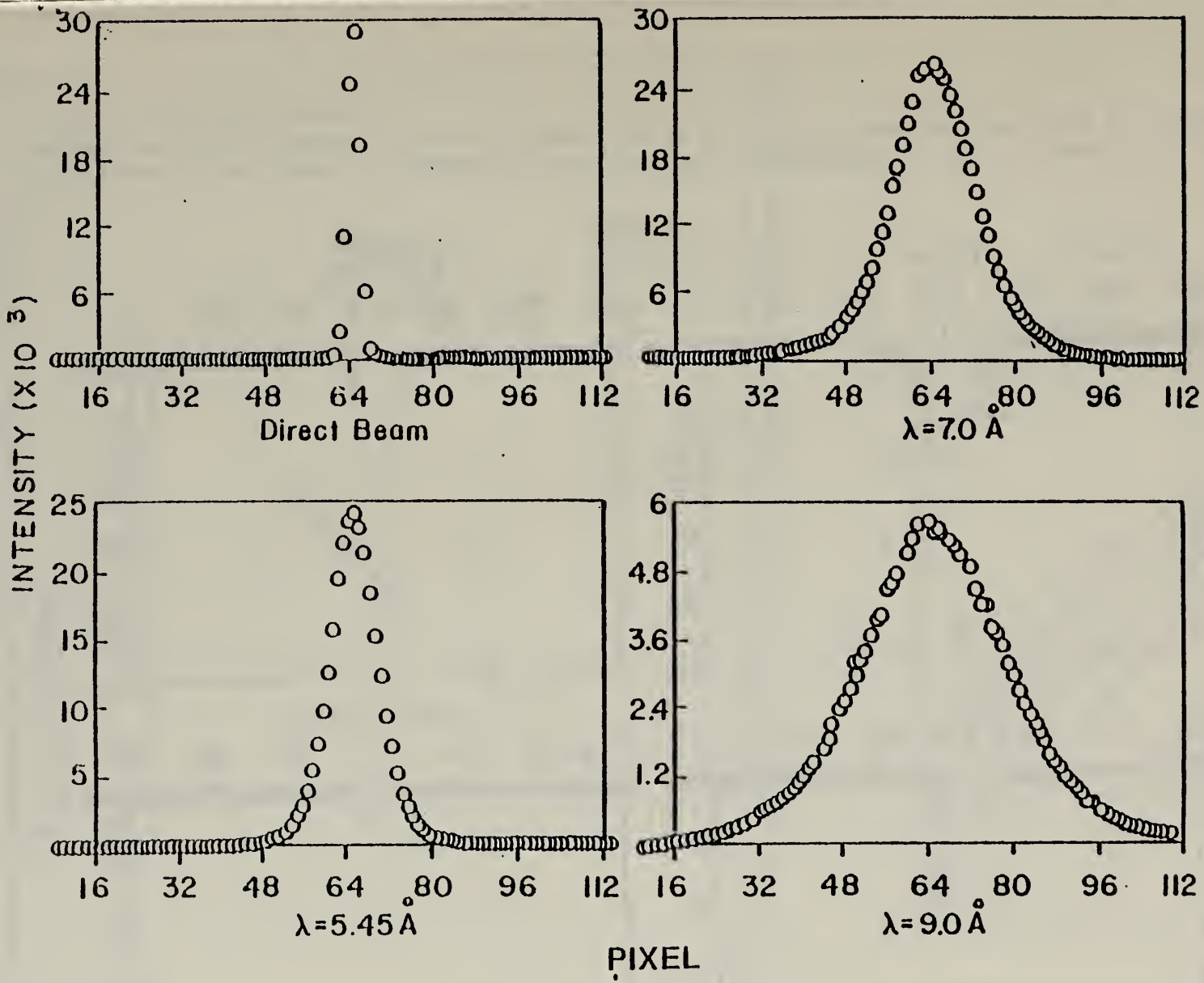

Fig. 8. SANS spectra for a "green" compact of $YCrO_3$ at three wavelengths: 5.45, 7.0 and 9.0 Å. Plotted is the scattering intensity versus a linear slice through the neutron scattering plane (as indicated by pixel number).

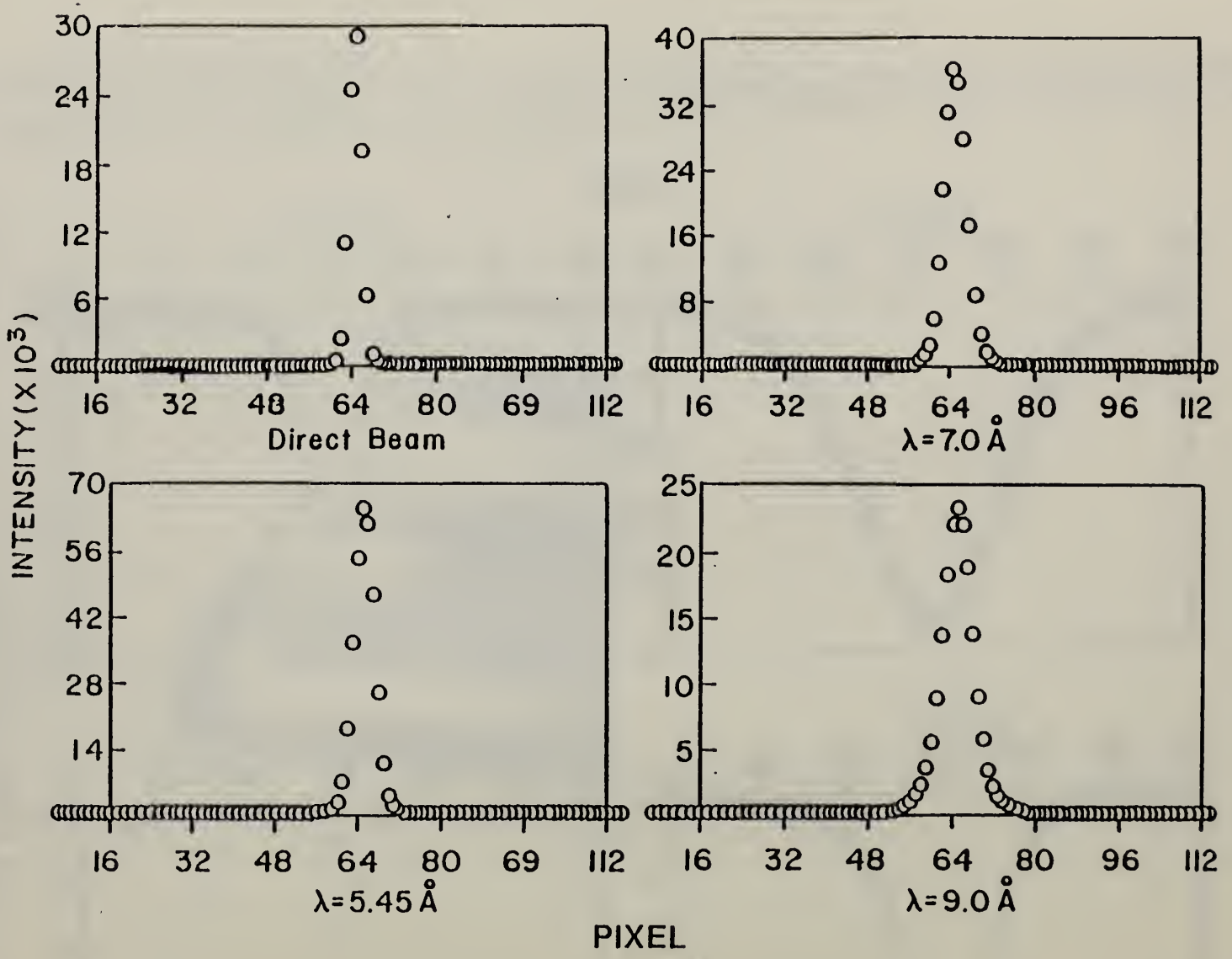

Fig. 9. SANS spectra for a sintered compact of $YCrO_3$ at three wavelengths: 5.45, 7.0 and 9.0 Å. Plotted is the scattering intensity versus a linear slice through the neutron scattering plane (as indicated by pixel number).

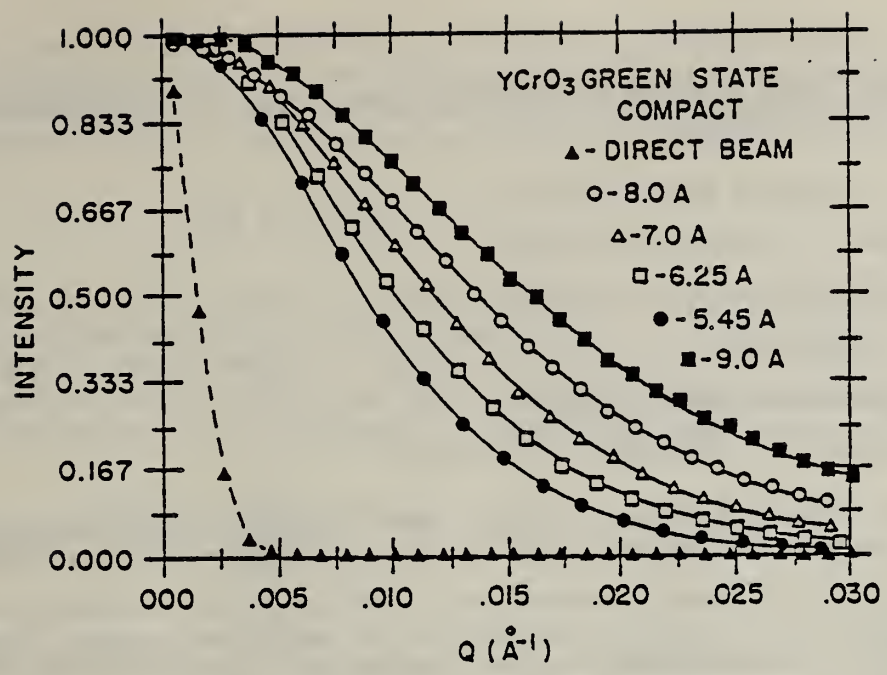

Fig. 10. Normalized scattering intensity versus scattering vector Q, for neutron scattering from a "green" $YCrO_3$ compact at five wavelengths.

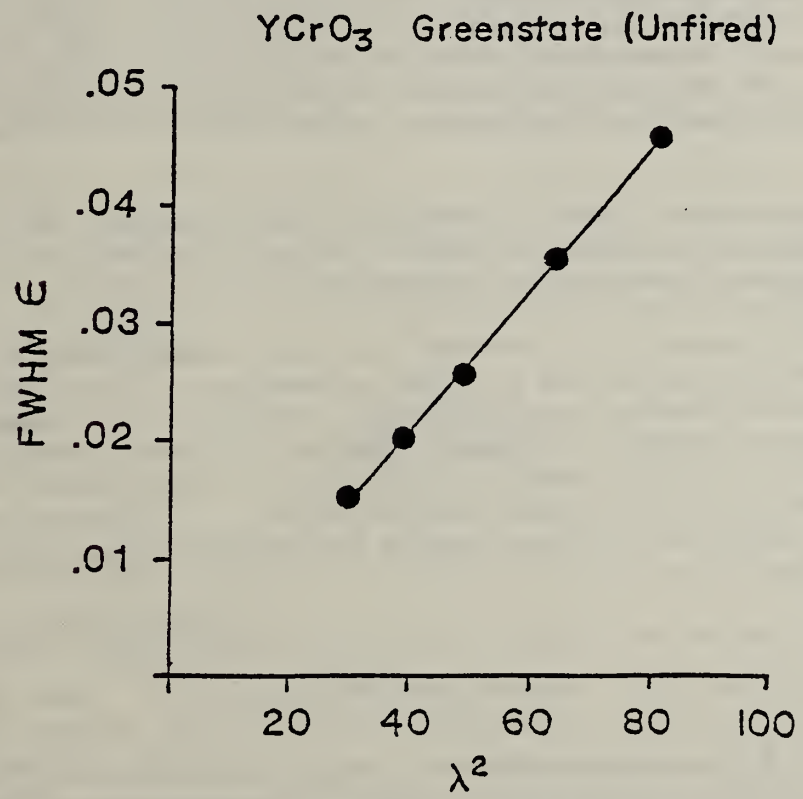

Fig. 11. Full width at half maximum, FWHM, versus wavelength squared for a "green" $YCrO_3$ compact. The FWHM is characterized by the scattering angle $\varepsilon = \arcsin [\lambda Q/2\pi]$ for scattering vector Q.

SMALL ANGLE NEUTRON SCATTERING (SANS) STUDY OF CREEP DAMAGE IN 304 STAINLESS STEELS

S. P. Singhal and B. Mozer

Center for Materials Science

Reactor Radiation Division

R. J. Fields

Center for Materials Science

Fracture and Deformation Division

304 stainless steel used in high-temperature applications consists of $M_{23}C_6$ (M stands for Cr and other metallic elements in the carbide) type of carbides at the grain boundaries. The carbide-austenite interface is a preferential site for the nucleation of cavities during high-temperature degradation--a phenomenon called cavitation. The structure after cavitation consists of three phases; namely, austenite, carbide, and cavities. The attempt to use SANS as a reference method to nondestructively evaluate the evolution of creep cavities from very early stages of cavity growth (inaccessible to conventional methods) requires that the creep induced changes in volume fraction, size distribution, and spacial distribution of carbides do not contribute significantly to the scattered intensity. At this point there is no theoretical or experimental study to indicate that this limitation is not important, yet by adapting special experimental procedures, the effects due to such changes could be minimized. The following two procedures were employed:

a. All samples were given a stabilizing heat treatment of 100 hours at 600 °C prior to the initiation of creep thereby precipitating out the entire volume fraction of carbides.

b. A control sample (undeformed) was heat treated along with the crept samples over the period of creep deformation. SANS spectra from the undeformed sample were used as a baseline to delineate the cavity contribution from the deformed samples. The creep parameters of two samples (x-6, x-8), which fulfilled these requirements in this and a previous study, are described in Table 1. This report describes recent results on these samples and compares them with the previous study (ref. 1).

The SANS studies were carried out on the NBS reactor facility using a converging collimation and a neutron wavelength of 6.25 Å. With the choice of collimation and wavelength parameters, a scattering vector (Q) range of 0.005 $Å^{-1}$ to 0.15 $Å^{-1}$ could be measured in these experiments. This Q range measures the scattering contribution of the inhomogeneities in the size range of approximately 40 Å to 1200 Å. By using converging collimation we have been able to measure the scattering intensity at Q values about a factor of three lower than a previous preliminary study (ref. 1).

Detailed theory and procedures for analyzing the SANS data have been described by Kostorz (ref. 2). A few salient features will be discussed here. If scattered intensity is denoted by Z, then the macroscopic differential scattering cross section of the scattering entities is given by

$$\frac{d\varepsilon}{d\Omega} = CZ/tMT \tag{1}$$

In this equation, t is the sample thickness, M is the total monitor count, T is the sample transmission, and C is a combination of experimental constants for the instrument. Creep damage as related to the evolution of cavities and changes in carbide size, shape, and spacial distribution is measured by the difference in the $d\varepsilon/d\Omega$ for the deformed (D) and undeformed sample (U), i.e.,

$$\left(\frac{d\varepsilon}{d\Omega}\right)_{damage} = \left(\frac{d\varepsilon}{d\Omega}\right)_D - \left(\frac{d\varepsilon}{d\Omega}\right)_U = C[Z_D/t_D M_D T_D - Z_U/t_U M_U T_U] \tag{2}$$

In further discussion, we have assumed that contribution to $\left(\frac{d\varepsilon}{d\Omega}\right)_{damage}$ comes predominantly from creep cavities. Figures 1 and 2 show scattering patterns for the deformed and undeformed samples of x-6 and x-8, respectively. We can see that in these (also, in all other samples measured) the deformed sample always showed higher scattered intensity than the undeformed, thereby emphasizing cavity contribution to the scattering. Figures 3 and 4 show only cavity contribution, i.e., after substracting the spectra for the undeformed sample from the deformed one. The steep fall of scattering intensity in figure 3 is indicative of very narrow size distribution of cavities.

One parameter of major interest is the growth of average cavity size as a function of creep deformation at constant stress. A Guinier analysis was performed on these spectra (figures 3 and 4) to obtain an average cavity size. Guinier (ref. 2) showed that for a randomly distributed, monosized, spherical heterogeneity, the intensity (Z) and scattering vector (Q) relationship can be described by the equation

$$Z = Z_o \exp\left(\frac{-Q^2 \cdot R_g^2}{3}\right) \tag{3}$$

Here R_g is the radius of gyration of the particles and is related to their diameter (D) by the equation

$$D = \sqrt{10/3} \cdot R_g \tag{4}$$

Z_o is the constant related to the volume and number density of the cavities. If heterogeneities are not monosized, then the utility of Guinier approximation is limited to only a very small Q range near zero. Figures 5

and 6 represent Guinier plot [Log Z vs. Q^2] for cavities in samples x-6 and x-8. It is clear from these plots that cavities must have a size distribution as a straight line in these plots can be fitted only in the narrow Q region near the peak. The cavity diameter obtained by this procedure normally overestimates the contribution of large cavities, yet it is a very useful parameter to study cavity growth as a function of creep time while degradation is in progress. Using a least square fit subroutine, equation (3) was fitted to the data points in the relevant Q range of figures 5 and 6. The experimental data points and the fit line are shown in figures 7 and 8. A reasonably accurate fit was obtained in the selected Q range for both cases. The average cavity sizes derived from these fits for the two samples are

$$\langle D_{cavity} \rangle \approx 770 \text{ Å for x-6}$$

and

$$\langle D_{cavity} \rangle \approx 763 \text{ Å for x-8.}$$

Table 1 shows that doubling the creep time at the same stress has the effect of doubling the average cavity size for sample x-6. Figure 9 shows the growth of cavity size as a function of creep time in the two samples assuming that at the initiation of creep, the cavity size is negligible. If we include the point at the origin, there appears to be a linear time dependent size growth of the cavities in x-6; but in the absence of more data points, only a limited significance can be attached to the trend in figure 9. In the previous report (ref. 1), we concluded that x-6 has higher average cavity size despite the longer creep time because x-6 was stressed at 21 ksi as opposed to 18 ksi for x-8, therefore resulting in the enhanced stress induced coarsening of cavities. In this study we find that average cavity size in the two samples is not very different. This indicates that for longer creep times the size growth of cavities is perhaps less sensitive to the small changes in applied stress. This is because the stress difference between these two samples is only about 3 ksi. The other possibility as debated by Weertman (ref. 3) is that when a large fraction of cavities grow large enough to scatter at the Q values below minimum Q in the experiments, the average size and volume fraction parameter from the standard SANS analysis are highly underestimated and also the Guinier region is inaccessible. The confirmation that this has taken place at a certain stage of the creep requires the void size and volume fraction determinations by TEM and density measurements, respectively. Such measurements are currently in progress. To refine the general application of SANS as a reference method to quantify creep cavity growth in alloys, further work must be performed on simpler metals or model alloys to absolutely identify the contribution of interacting microstructures and defects in structural alloys.

REFERENCES

1. E. R. Fuller, Jr., R. J. Fields, E. D. Case, S. Singhal, and C. J. Glinka, "Nondestructive Evaluation of Distributed Damage," Annual Report, Reactor Radiation Division, NBS (1983).

2. G. Kostorz, "Neutron Scattering in Materials Science," Chapter 5 in Treatise in Materials Science and Technology 15, ed. G. Kostorz, (Academic Press, New York, 1979).

3. J. R. Weertman, M. Yang, and M. Roth, "Grain Boundary Cavitation in Copper Subjected to High Temperature Creep," Annex to Annual Report, Institut Laue-Langevin, Grenoble, France, p. 263 (1982).

Table 1. Growth of creep cavities as a function of time at constant stress in 304 stainless steel.

Sample #	Creep Parameters	Average Cavity Diameter from Guinier Approximations	
		(Å)	(nm)
x-6	745 at 21 ksi (144.8 MPa)	346	34.6
	1493 at 21 ksi (144.8 MPa)	770	77.0
x-8	789 at 18 ksi (124.1 MPa)	266	26.6
	1537 at 18 ksi (124.1 MPa)	763	76.3

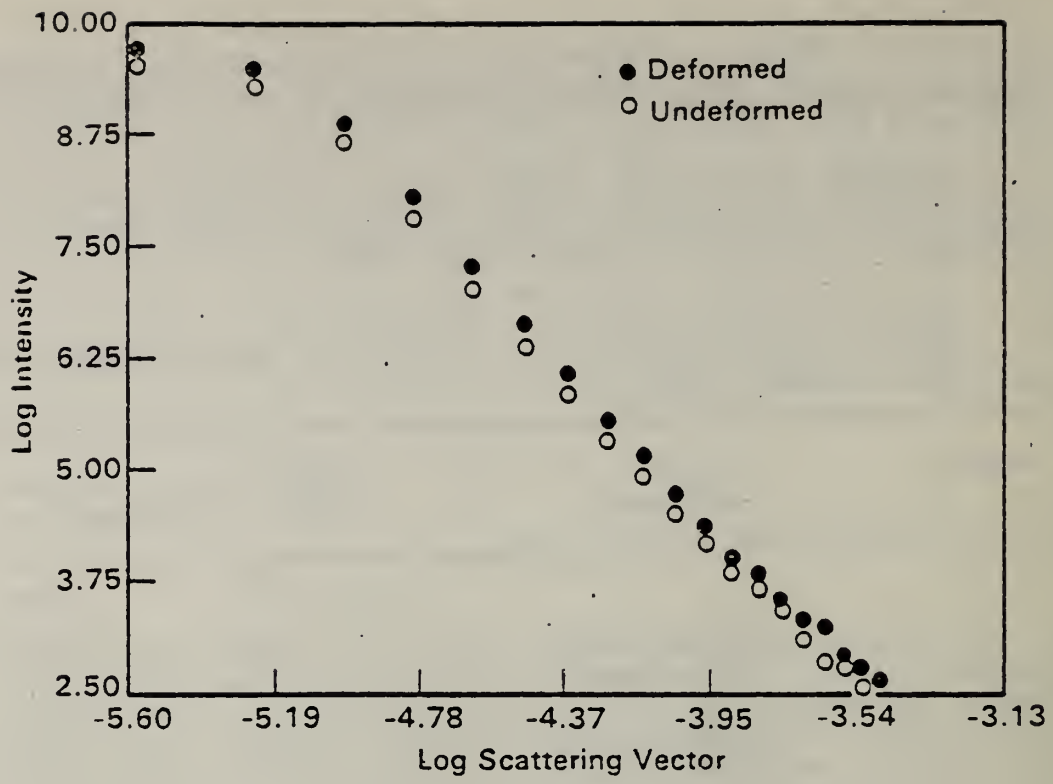

Figure 1. SANS spectra on deformed and undeformed x-6. Deformation under 21 ksi stress was carried out at 600°C for 1493 hours.

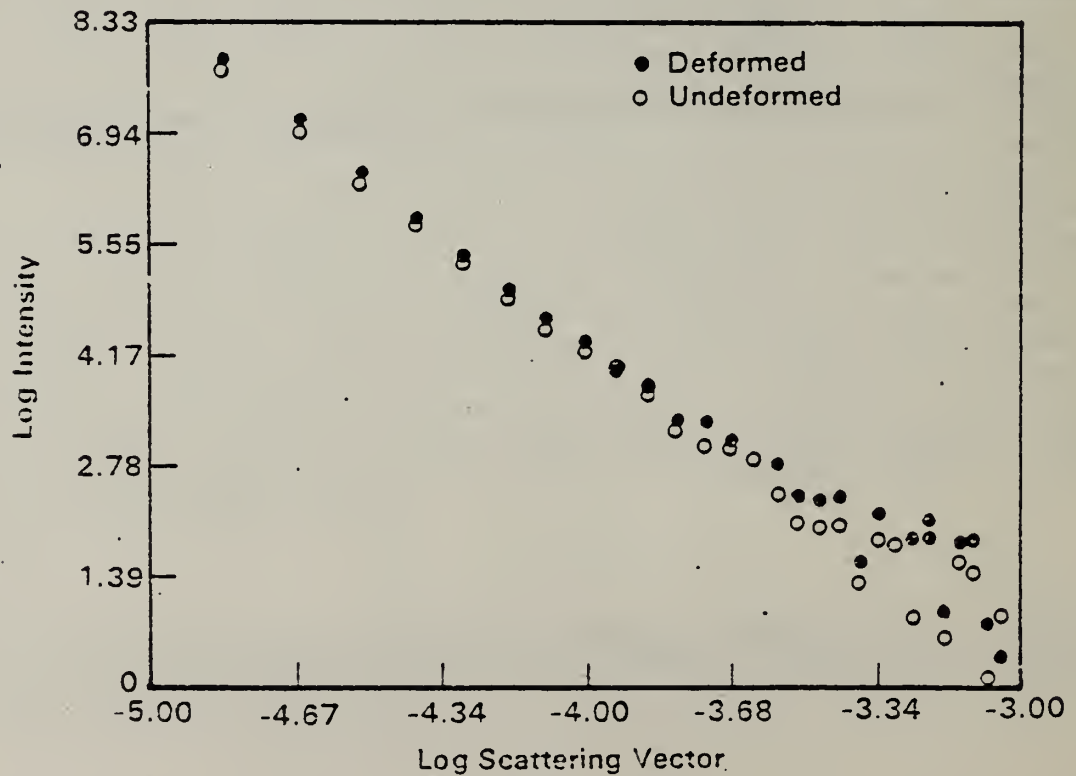

Figure 2. SANS spectra on deformed and undeformed x-8. Deformation under 18 ksi stress was carried out at 600°C for 1537 hours. The undeformed sample was heat treated at 600°C for 1537 hours.

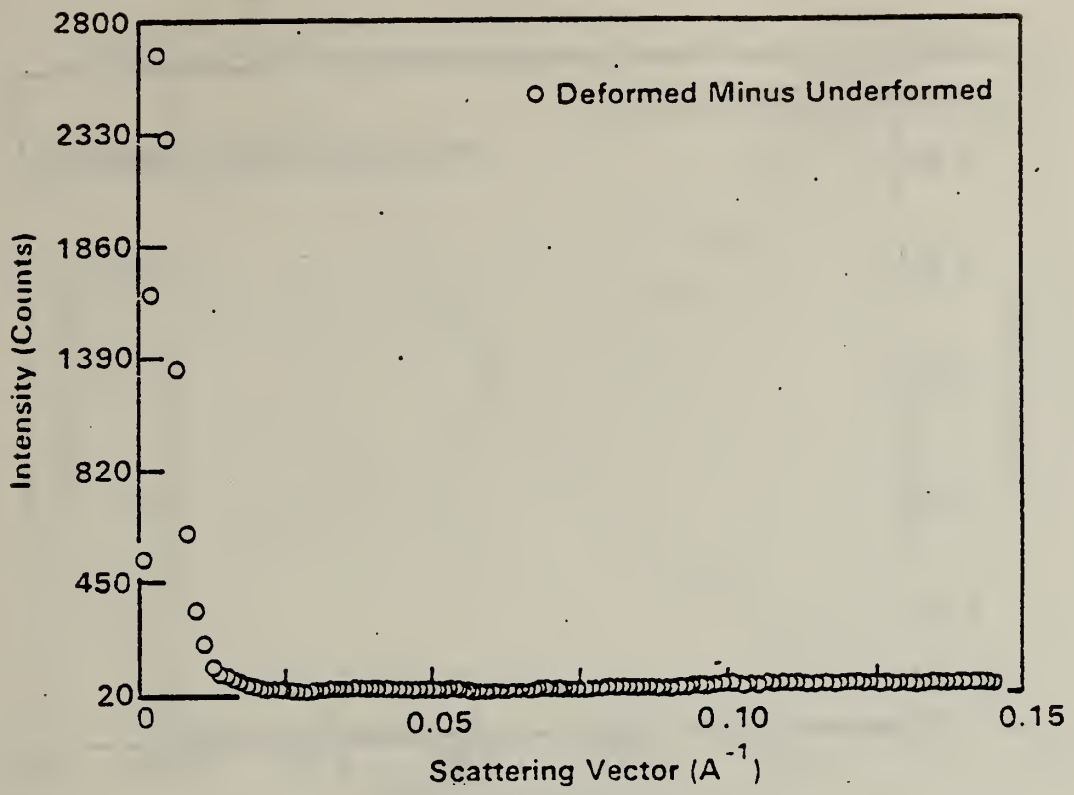

Figure 3. SANS spectra showing the scattering due to creep-induced cavities for x-6.

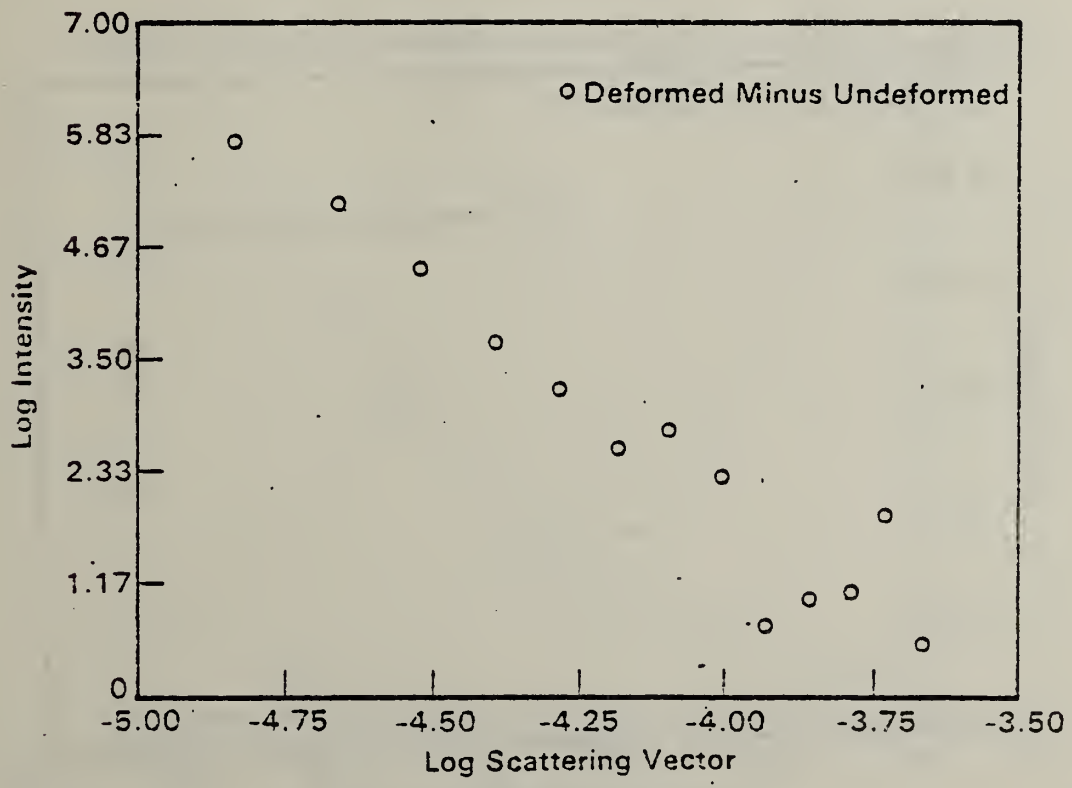

Figure 4. SANS spectra showing the scattering due to creep-induced cavities for x-8.

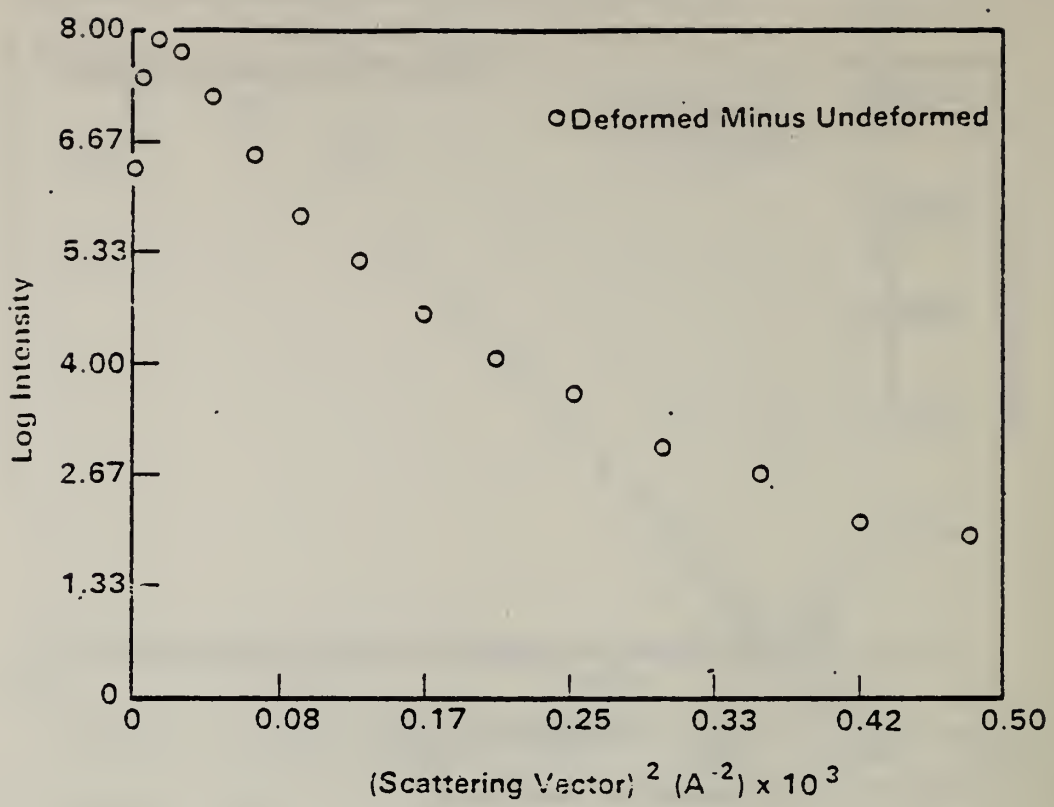

Figure 5. Guinier plot showing the scattering contribution of creep cavities in sample x-6.

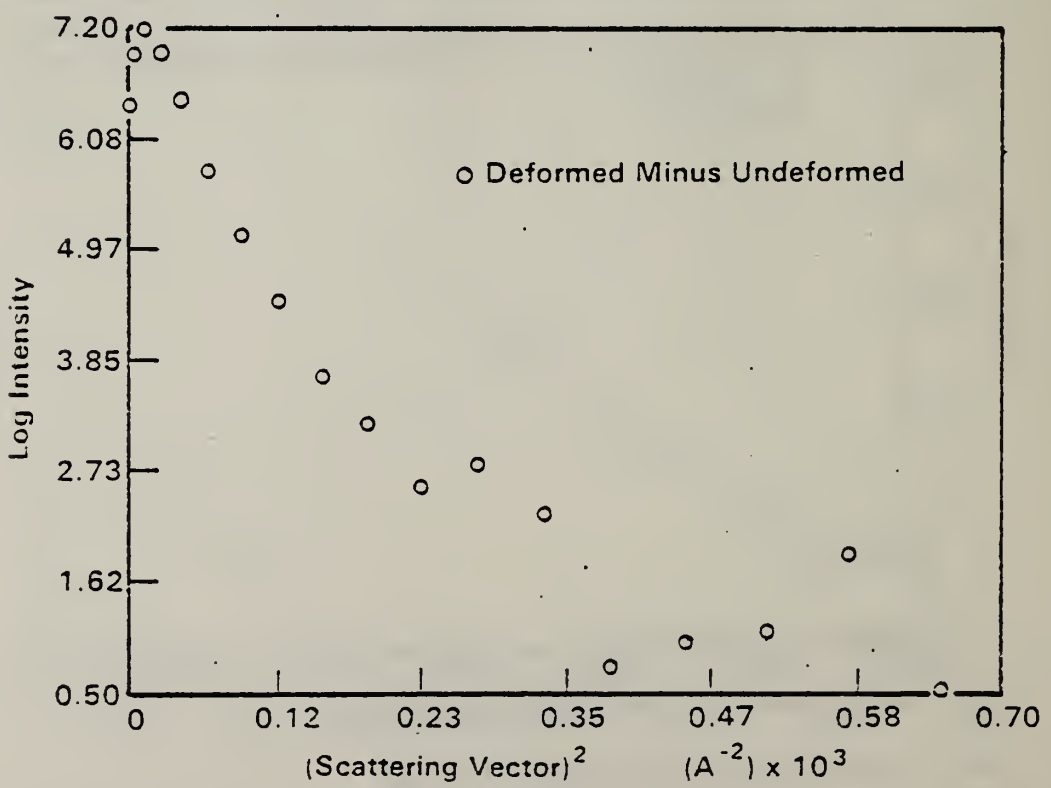

Figure 6. Guinier plot showing the scattering contribution of creep cavities in sample x-8.

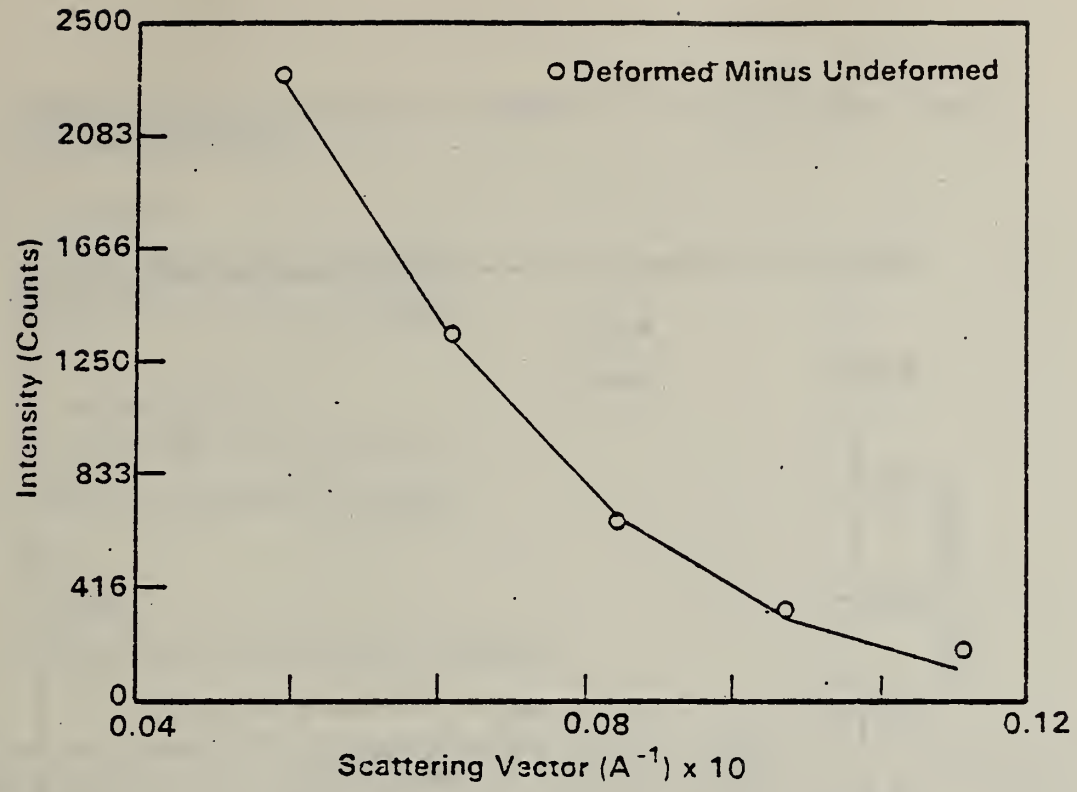

Figure 7. Least square fit of the Guinier function of the data in the selected range of figure 3 for sample x-6.

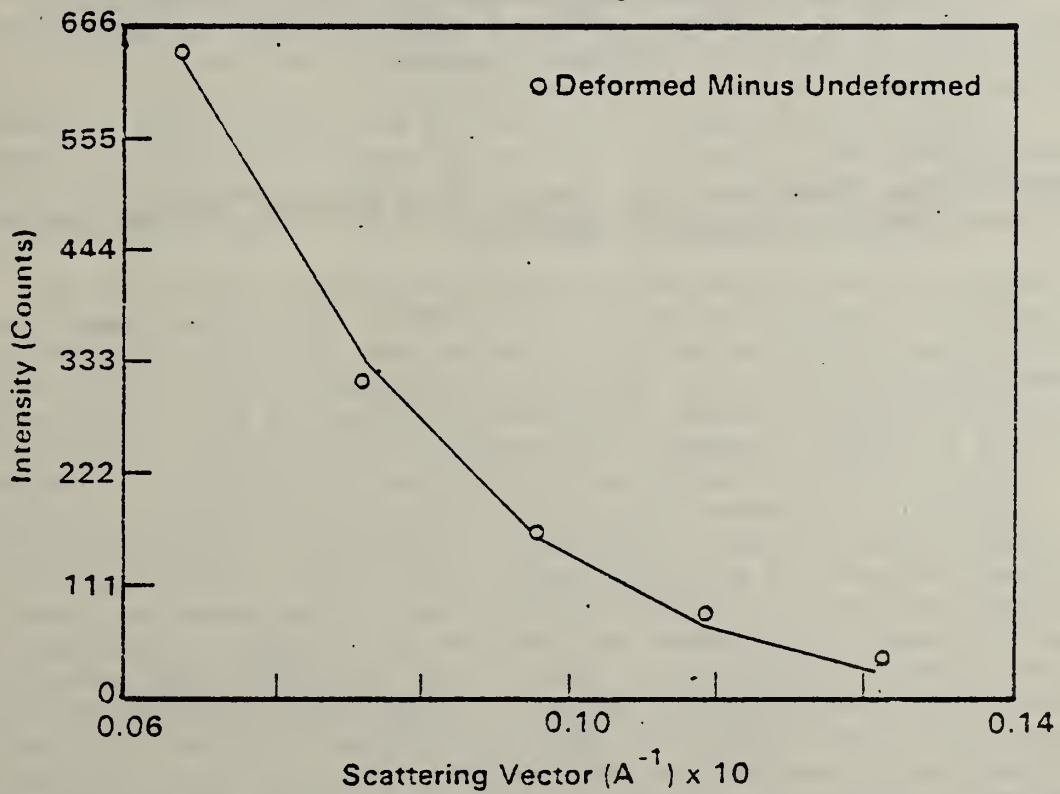

Figure 8. Least square fit of the Guinier function to the cavity scattering data in the selected Q range for the sample x-8.

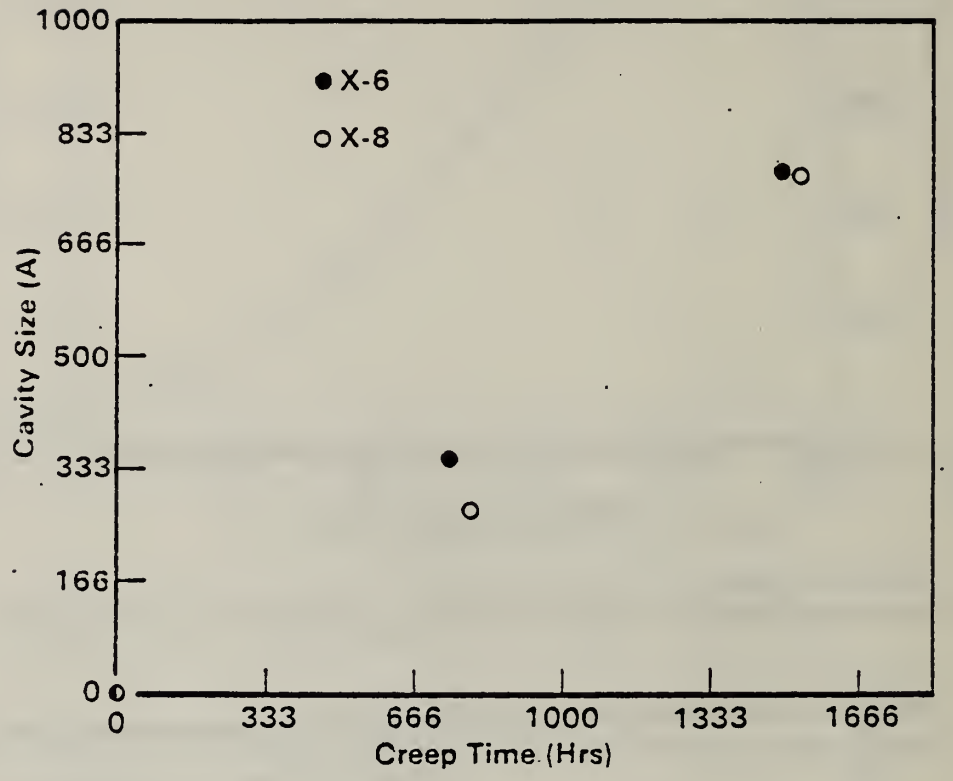

Figure 9. Size growth of creep cavities as a function of creep time at 600°C for samples x-6 and x-8.

NONDESTRUCTIVE EVALUATION OF POROSITY IN $YCrO_3$ BY SMALL ANGLE NEUTRON SCATTERING

N. F. Berk
Reactor Radiation Division
Center For Materials Science
and
K. Hardman-Rhyne
Inorganic Materials Division
Center for Materials Science
and
E. Case
University of California, Berkeley

We are undertaking a quantitative study of porosity in $YCrO_3$ and other ceramics using small angle neutron scattering (SANS). The goal of the investigation is to provide reliable data on average pore size in ceramic materials at different stages of densification, including the highly porous green state compact. Detailed understanding of the densification process is vital to the ceramics industry since the strength and refractory behavior of the final product depend on properties of its microstructure and especially on the distribution of pores and defects. While large pores are visible by electron microscopy of suitably prepared thin sample specimens, scattering methods generally provide the best means of obtaining statistical information from the bulk and may be the only technique available for fragile or otherwise difficult-to-handle materials. Moreover, the interaction of thermal neutrons with condensed matter is so weak that the method, unlike electron microscope techniques, is totally nondestructive, even in the green state.

The usefulness of SANS for nondestructive evaluation of ceramics has already been demonstrated at NBS by an innovative application to the study of microcracking in $YCrO_3$ made recently by Case and Glinka, who were able to subtract the intrusive background scattering from voids and other defects by combining data from samples having different thermal histories. The study of scattering produced by pores themselves, however, requires a different technique. In particular, multiple scattering and refractive effects become increasingly important as average void size increases. This entails qualitative changes in the nature of the SANS intensity which alone can signal significant alterations in the distribution of pores as density is increased, as shown below. Quantitative determination of pore size is less straightforward, however, and requires the comparison of measured intensities with theoretical predictions over a range of parameters for which practical theory has generally been lacking. The derivation and numerical implementation of appropriate multiple scattering theory applicable over a wide range of average pore sizes and neutron wavelengths has thus been stimulated by these researches and has become an important component of the overall program to obtain dependably quantitative SANS characterizations of densification.

In the preliminary phase of the experimental study we have obtained SANS data from two samples of $YCrO_3$ which were similarly prepared pure powders, isobarically pressed at 3^3TPa (30,000 kbar). One, a green state compact has 55% theoretical density; the other, a sintered sample, has 93% theoretical density. Measurements were made at several neutron wavelengths and are shown for the green state compact as a function of scattering wavevector in Fig. 10 on page 33. The full widths at half maximum of these curves were determined by approximate Gaussian fits and increase linearly with wavelength in the range shown, a behavior characteristic of multiple refraction from large particles and thus consistent with the evident porosity of the green state. In contrast, the scattering from the sintered sample (not shown) exhibits no wavelength dependence on this scale, indicating the absence of comparably large pores. Clearly, even a qualitative analysis of such data reveals a strong effect of processing on the population of neutron scattering in these materials. Moreover, if the scattering in Fig. 10 on page 33 is assumed to be describable only as multiple refraction and edge diffraction by voids then an estimate of average pore radius gives a value of approximately 2μm, which appears to be physically reasonable for the green state compact. This estimate is based on a fit of a preliminary version of the theory to experiment at several wavelengths. As example is shown below; the curve is approximately Gaussian except in the tail. The extent to which the whole shape of measured intensity curves can be accounted for by theory will be a crucial factor in setting the limits of dependable void size determinations using SANS.

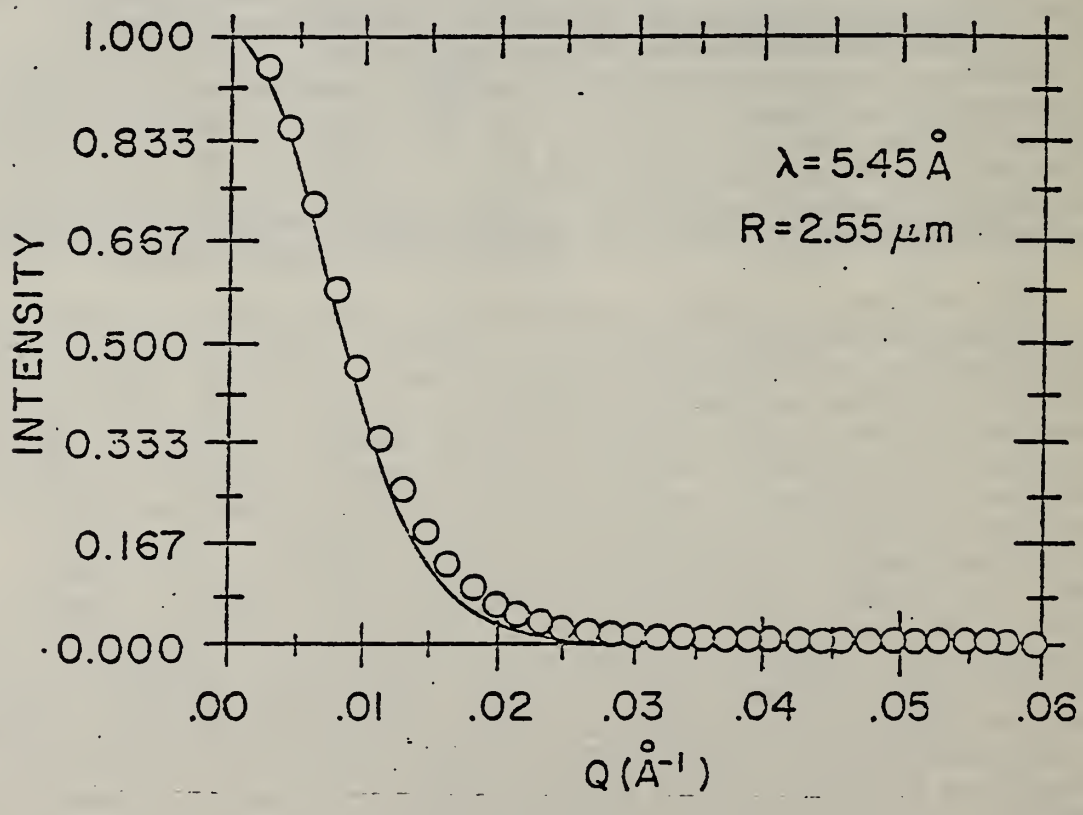

Figure 1. Comparison of preliminary theory (solid line) with experimental data (open circles).

GREEN STATE CERAMICS

T. Negas, E. Fuller, K. Hardman-Rhyne, and C. Robbins

Inorganic Materials Division

Center for Materials Science

INTRODUCTION

Rejection of ceramics after densification, and their failure in-service, are due primarily to defects that influence the physical/chemical properties of the materials. Increased demands for higher-performance advanced materials have imposed more stringent requirements on the processing industry. Proven reproducibility and reliability of ceramic components are needs that can only be accomplished by a combination of processing controls and NDE procedures (ref. 1) together with a fundamental understanding of how defects arise and evolve within the processing cycle. This program focuses on the early stages of ceramic processing, the "green state", which consists of an assemblage of particulates loosely consolidated by forming methods and often containing binders, moisture, and other additives that normally are "burned out" during a preliminary calcination step. The green part, therefore, constitutes a reservoir of accumulated processing flaws and imperfections (voids, pressure or particle packing heterogeneities, fissures, agglomerates, inclusions, etc.) that persist and/or generate new defects during subsequent processing. Ideally, characterization and rejection of parts should begin at this stage, but virtually no work has been done on the properties of green compacts. Reliable methods to detect and relate initial flaws to final structural imperfections, therefore, have not been demonstrated.

This work consists of the following related elements:

(a) processing of generic green ceramics containing flaws of controlled size and distribution;

(b) characterization of these compacts through final microstructural evolution, primarily by microscopy and small angle neutron scattering (SANS); and

(c) evaluation of potential NDE methods cross correlated with characterization measurements.

PROJECT ACTIVITIES

During this year, a cooperative program was established among NBS, Argonne National Laboratory (ANL), and a guest worker, Dr. Eldon Case, Univ. of Calif., Berkeley. NBS is responsible for all aspects of green state processing and pertinent characterization measurements. ANL is conducting exploratory NDE measurements based on ultrasonics, microfocus radiography, and NMR on the green compacts and on those also subjected to binder burnout and final densification.

Processing

Two classes of green ceramics are under investigation. $YCrO_3$-based compacts, when fully densified, provided the first model ceramic materials used to apply diffractive mode, SANS techniques, and theory (see NBS, NDE Annual Report, 1982) to the detection and characterization of finely distributed defects (microfissures) in the 2-200 nm size range. Green compacts of these materials were characterized by NDE (at ANL) and by SANS (at NBS) methods. As a result of promising preliminary results (see below), emphasis was turned to a broad range of generic green state defects that encompass agglomerates, impurity inclusions, and heterogeneous packing of particles. These features can all be simulated in one type of green composite ceramic consisting of a relatively uniform matrix of fine particles containing a distribution of densified, large spheres. $MgAl_2O_4$ (spinel) was selected for both the matrix and "hard" spheres to maintain constant chemistry, thermal expansion, and thermal conductivity for subsequent processing and characterization. Table 1 summarizes the processing cycle for these compacts. Three sets (ten specimens each) of these materials having 0, 2, and 20 percent volume fractions of agglomerates in the 75-100 μm range were fabricated for investigation. In addition, specimens from each set were calcined at 700 °C to remove organic binders and then sintered at 1500-1550 °C to obtain final densification. Measurements on these latter materials permit monitoring of the evolution of flaws from the green state to the finished microstructure. Figure 1A illustrates a typical green composite as processed. After densification, Figure 1B, new flaws (pores) have developed, adjacent to the spherical agglomerates, indicating that the matrix phase detaches due to faster densification (greater shrinkage). The detrimental effect of these defects also is reflected by final bulk density. Without agglomerates, green compacts densify to near 98 percent of theoretical, while the materials loaded with two and 20 percent attain approximately 94 and 85 percent, respectively.

Characterization by SANS

Small angle neutron scattering from materials is characterized by two dominant regimes, diffractive (DS) and multiple refractive scattering (MRS). The DS mode yields microstructural information for the 2-200 nm size range. However, the MRS mode is potentially more useful for the green state as larger, micron-size defects can be detected. In cooperation with Dr. E. Case and the Reactor Division staff, numerous exploratory measurements have been made on $YCrO_3$ and $MgAl_2O_4$ green compacts (ref. 2). Using six neutron wavelengths (λ = 4.85, 5.45, 6.25, 7.0, 8.0, and 9.0 Å), it has been demonstrated that MRS is the dominant mechanism. The specimens show typical beam broadening (full width at half maximum FWHM) with a linear dependence on λ^2 and a circularly symmetric Gaussian profile. A comparison of neutron scattering data from densified $YCrO_3$ (shown in Fig. 8, page 31) with data from green state $YCrO_3$ (shown in Fig. 9, page 32) illustrates the observed phenomenon and basic differences

between DS and MRS.* Figure 2 shows observed MRS (9.0 Å) for green compacts of $MgAl_2O_4$ with (20 percent) and without hard agglomerates. The data demonstrate remarkable reproducibility and the ability to detect changes in scattering intensity from different samples. Processing history and microstructure evolution also can be followed by these changes in MRS, as shown in Figure 3. Here, the curves display a progressive increase of scattering centers at small scattering vector, Q, for a $MgAl_2O_4$ green compact (no agglomerates, plus binder) after calcination at 700 °C and at 975 °C.

To date, SANS experiments using green compacts are yielding preliminary information that demonstrates differences among materials (ref. 2). Future research will be devoted to a critical analysis of these data combined with an evaluation of existing and new models and theory for MRS, especially linked to the specific type of scattering centers (defects) in green ceramics. A high temperature furnace for SANS also has been constructed to continuously monitor microstructural flaws in-situ throughout the processing cycle. It is recognized that SANS techniques have limited application for in-line process control for manufacturing conditions. However, they provide a powerful laboratory tool to follow defects through processing cycles, and they constitute a unique laboratory standard with which alternate NDE methods can be compared.

NDE Characterization

In collaboration with Dr. D. S. Kupperman, ANL, ultrasonic studies of $YCrO_3$ and $MgAl_2O_4$-based green ceramics are in progress (ref. 3). Two $YCrO_3$ specimens were examined with both longitudinal and shear waves. Surprisingly, no liquid couplant was necessary to propagate these waves, and the shear-wave velocity varied with polarization, indicating elastic anisotropy. The latter observation may be due to the fact that the compacts were first hard-die, uniaxially pressed before isostatic compaction. This result could be most significant if it can be established that density gradients from the former processing step are carried into, and "imprinted" within, the latter. The results of the measurements are:

$$V_l = 1.43 \times 10^3 \text{ m/s}; \quad V_t = \begin{matrix} 0.919 \\ 0.947 \end{matrix} \times 10^3 \text{ m/s}$$

where the two values of V_t show the variation with polarization.

*The profile of the multiply refracted beam should be given by the Fourier convolution of the incident beam with the n-fold refraction. As n is large, detailed information from the main beam profile is lost in the MRS process, leaving only information on scatterers present in the specimen.

Table 2 summarizes data for ultrasonics measurements of $MgAl_2O_4$ green compacts (ref. 3). Five points on each specimen were probed, and sample-to-sample variability is now under investigation. Preliminary results show that the frequency spectrum for these materials is within 0-2.0 MHz and that the spectra, as in SANS, are different for each material measured, suggesting anomalous microstructure. Additional research is necessary to determine sensitivity of ultrasonics using green compacts containing smaller flaw sizes and populations, as well as sintered materials. In addition, microfocus x-radiography techniques will be examined using NASA equipment.

CONCLUSIONS

Generic green ceramic compacts can be processed to contain a variety of controlled flaws and heterogeneities. Preliminary SANS and ultrasonics measurements have shown the ability to detect microstructural anomalies in these materials. The sensitivity and selectivity of these techniques to controlled defects require future research efforts.

REFERENCES

1. A. G. Evans, "Structural Reliability: A Processing-Dependent Phenomenon", J. Am. Ceram. Soc. 65, No. 3, pp. 127-37 (March 1982).

2. K. Hardman-Rhyne and E. Case, "Small Angle Neutron Scattering Measurements on Green Compacts of $YCrO_3$", presentation at TMS-AIME Fall Meeting, Philadelphia, PA, October 1983.

3. W. A. Ellingson, D. S. Kupperman, T. Negas, and E. Fuller, "Initial Results of Nondestructive Evaluation Methods Applied to Green Ceramics", presentation at TMS-AIME Fall Meeting, Philadelphia, PA, October 1983.

Table 1

Processing of $MgAl_2O_4$-Based Green Ceramics

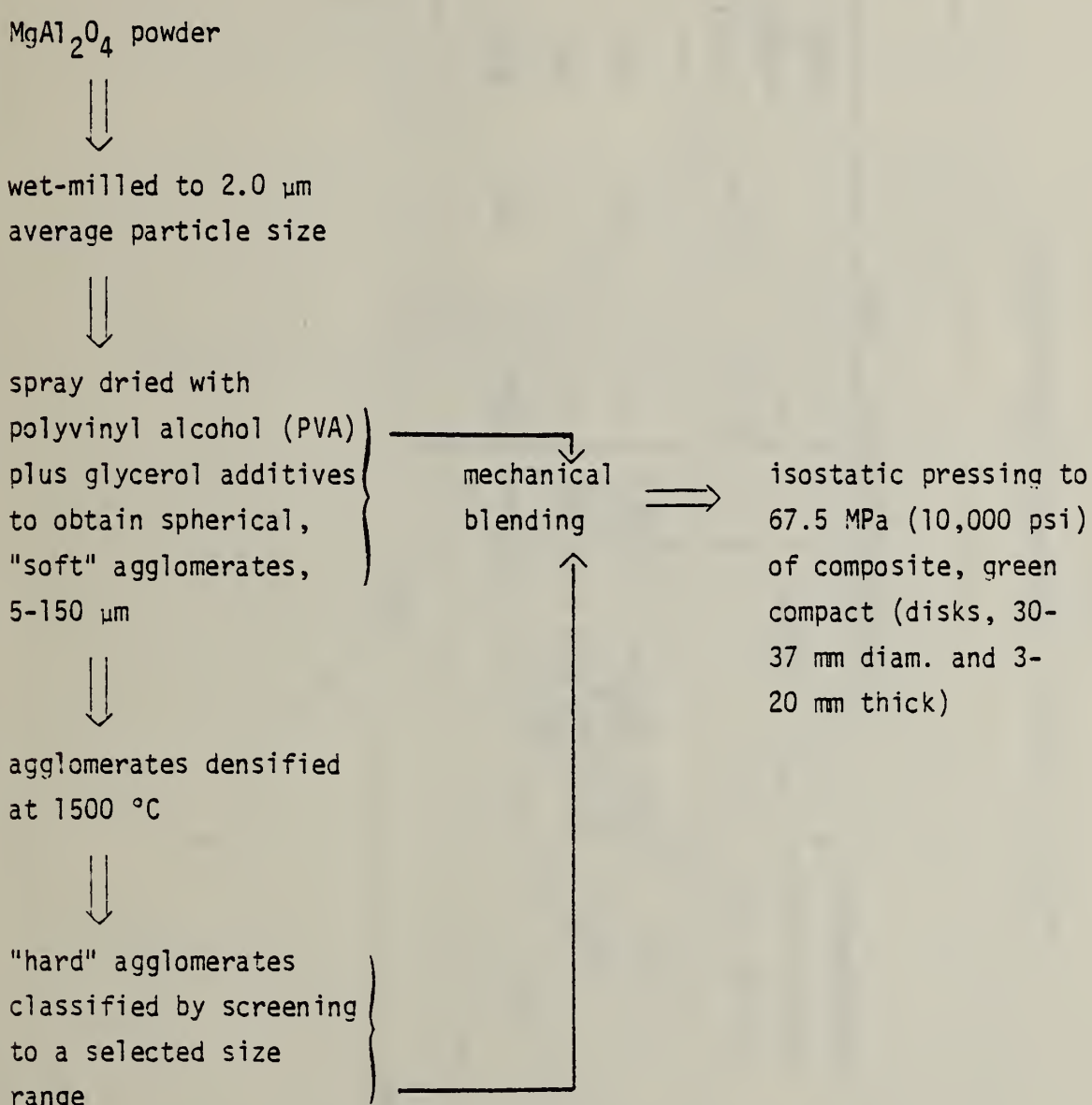

Table 2

Velocity of Sound vs. Agglomerate Concentration

Sample ($MgAl_2O_4$ + PVA Binder) (36 mm dia. X 6 mm thick)	Agglomerate Concentration (75-100 μm)	Longitudinal Velocity* (m/s)							Shear Velocity (m/s)	Poisson's Ratio
		Region					Ave.			
		A	B	C	D	E	(5 pts)	St. Dev.		
NB-2	0%	1343	1334	1355	1333	1315	1336	15	947	0.0
NB-7	2%	1338	1321	1320	1350	1330	1332	13	865	0.1
NB-12[+]	20%	1350	1310	1300	1280	1240	1300	40	871	0.1

*Frequency = 1.0 MHz.

[+]High attenuation.

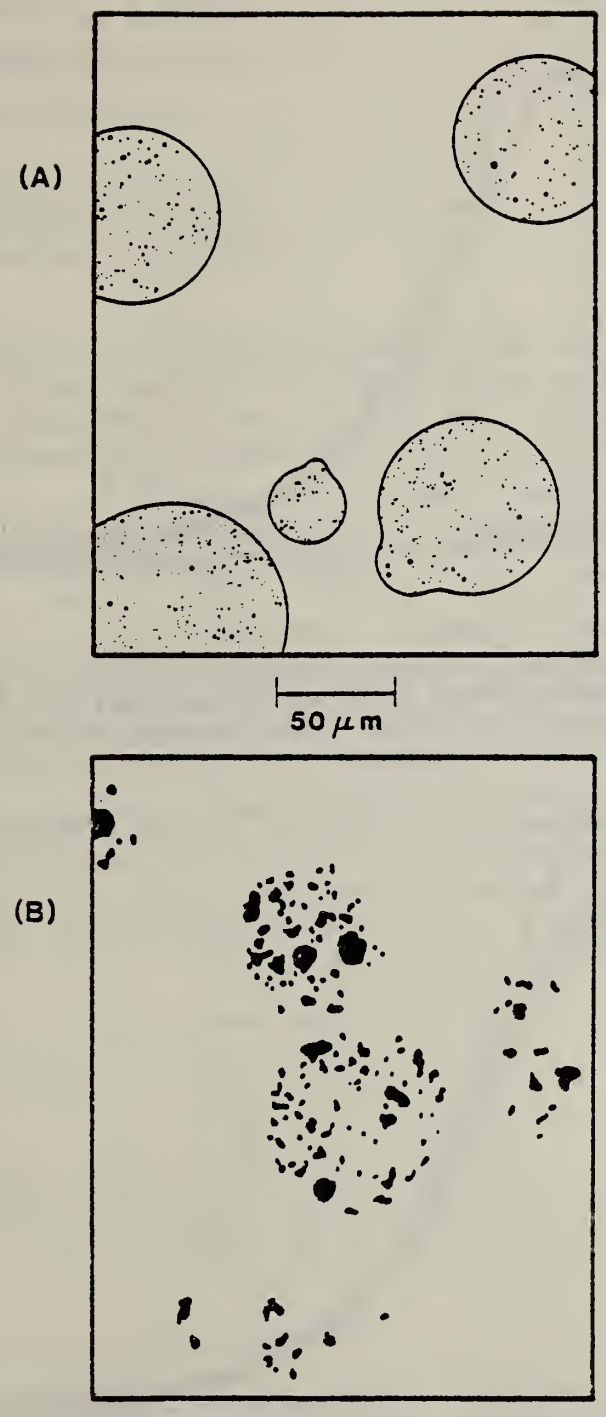

Figure 1 Line reproductions of SEM micrographs illustrating spherical agglomerates in green state $MgAl_2O_4$ (A) and generation of new pores (darkened) after densification at 1500 °C (B).

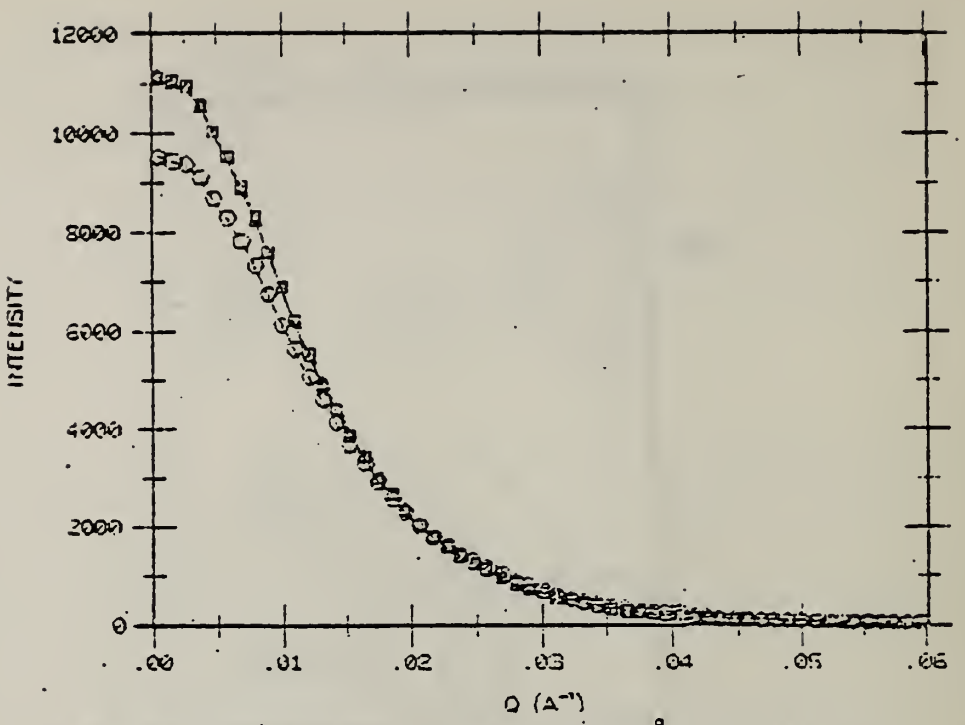

Figure 2 Neutron scattering profiles (λ = 9.0 Å) for green compacts of $MgAl_2O_4$ (lower curve, no agglomerates) and of two specimens of $MgAl_2O_4$ plus 20 percent agglomerates (upper curve).

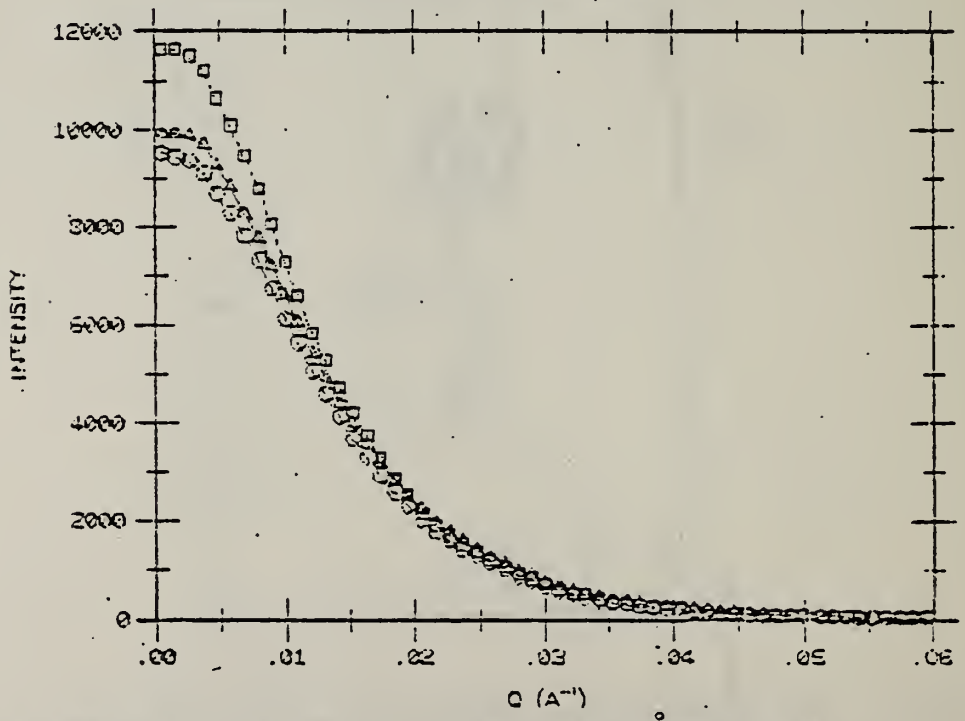

Figure 3 Neutron scattering profiles (λ = 9.0 Å) for a green compact of $MgAl_2O_4$ (lower curve, no agglomerates), fired at 700 °C to remove binders (middle curve), then calcined at 975 °C (upper curve) before fully densifying at higher temperature.

NONDESTRUCTIVE CHARACTERIZATION OF SUBSURFACE RESIDUAL STRESS

H. J. Prask and C. S. Choi
Energetic Materials Division
U. S. AMCCOM, Dover, NJ
and
Reactor Radiation Division
Center for Materials Science

In earlier work it was demonstrated that the precision and reproducibility of the neutron diffraction method were sufficient for residual stress measurements (ref. 1). It was also found, however, that for the differential volumes of interest in technological applications (less than about 20 mm^3 as defined in Figure 1) and employing conventional θ-2θ scans, texture could produce shifts in apparent peak positions greater than any expected from residual stress.

To minimize the role of texture in residual stress measurements we have adopted an energy dispersive approach (ref. 2), utilizing a three-axis spectrometer, in which sample orientation remains fixed with respect to incident and diffracted neutron beam directions, and monochromator and analyzer wavelengths are matched and scanned.

Initial measurements have centered on an aluminum alloy (2024-T351) ring-plug sample fabricated for use as a reference sample for ultrasonic measurements (ref. 3). In this shrink-fit type of cylindrical sample the theoretical stress distribution is given by:

radial stress,
$$\sigma_r = \frac{PR_1^2}{R_2^2 - R_1^2}\left(1 - \frac{R_2^2}{r^2}\right), \qquad r > R_1 \qquad (1)$$

tangential stress,
$$\sigma_\theta = \frac{PR_1^2}{R_2^2 - R_1^2}\left(1 + \frac{R_2^2}{r^2}\right), \qquad r > R_1 \qquad (2)$$

and
$$\sigma_r = \sigma_\theta = -P, \qquad r \leq R_1 \qquad (3)$$

where
$$P = \frac{E(R_2^2 - R_1^2)\delta}{2R_2^2}, \qquad (4)$$

R_1 is the plug radius, R_2 is the ring outer radius, E is Young's modulus, and δ is the differential radial interference. In the aluminum reference sample

E = 73100 MPa, Poisson's ratio is 0.33, R_1 = 12.7 mm, R_2 = 38.1 mm, with a thickness of 25 mm.

The measurements were made using the (200) reflection and a differential volume of 1.5 x 1.5 x 20 mm at a scattering angle of 90°. If the unstressed lattice spacing (d_o) is known, residual stresses for the three principal directions could be obtained directly by three strain measurements at each point of interest in the sample. Alternatively, ($\sigma_r - \sigma_\theta$) can be obtained at each point of interest without a knowledge of d_o (ref. 4). Values for σ_r and σ_θ can then be extracted by application of the overall equations of equilibrium and the use of an analytical model.

In Figure 2, measured $\sigma_r - \sigma_\theta$ values are shown for selected points in the sample. These are compared with $\sigma_r - \sigma_\theta$ values calculated with the use of eqns. (1) - (4) and the measured, pre-assembly dimensions of the sample. We have also calculated a stress distribution in the sample independent of any model except for the assumptions shown in Figure 2. With the application of the local equilibrium conditions, also shown, the adjustable parameters B (= 443 ± 19 MPa·cm^{C-1}) and C (= 3.01 ± 0.1) are evaluated from a fit to the data in the ring region. Finally, applying the overall equilibrium condition for force on a principal plane, P is evaluated to be -122 ± 5 MPa, to be compared with -129 ± 2.4 MPa from measured dimensions and the variance thereof.

In view of the success with the aluminum ring-plug sample, the energy-dispersive neutron diffraction method is being applied to a material which has posed serious difficulties for conventional residual stress measurement techniques; depleted uranium. Initial results on two 25-mm diameter extruded cylinders with quite different thermomechanical histories show markedly different strain distributions. It is anticipated that unstressed lattice spacings and three-dimensional stress profiles will be obtained at selected points in the samples in the very near future with existing instrumentation.

REFERENCES

1. C. S. Choi, et al, in "NBS Reactor: Summary of Activities - July 1977 to June 1978," F. J. Shorten, editor, NBS TN 995, p. 34 (1979).

2. L. Pintschovius, et al, "Determination of Residual Stress Distributions in the Interior of Technical Parts by Means of Neutron Diffraction," Residual Stress and Stress Relaxation, E. Kula and V. Weiss, editors, pp. 467-482 (Plenum Press, N. Y., 1982).

3. N. N. Hsu, T. M. Proctor, Jr. and G. V. Blessing, "An Analytical Approach to Reference Samples for Ultrasonic Residual Stress Measurement," ASTM J. Testing & Evaluation 10, No. 5, pp. 230-234 (Sept. 1982).

4. See, for example, J. B. Cohen, H. Dolle and M. R. James, "Determining Stresses from X-Ray Powder Patterns," Accuracy in Powder Diffraction, S. Block and C. R. Hubbard, editors, NBS SP 567, pp. 453-477 (1980).

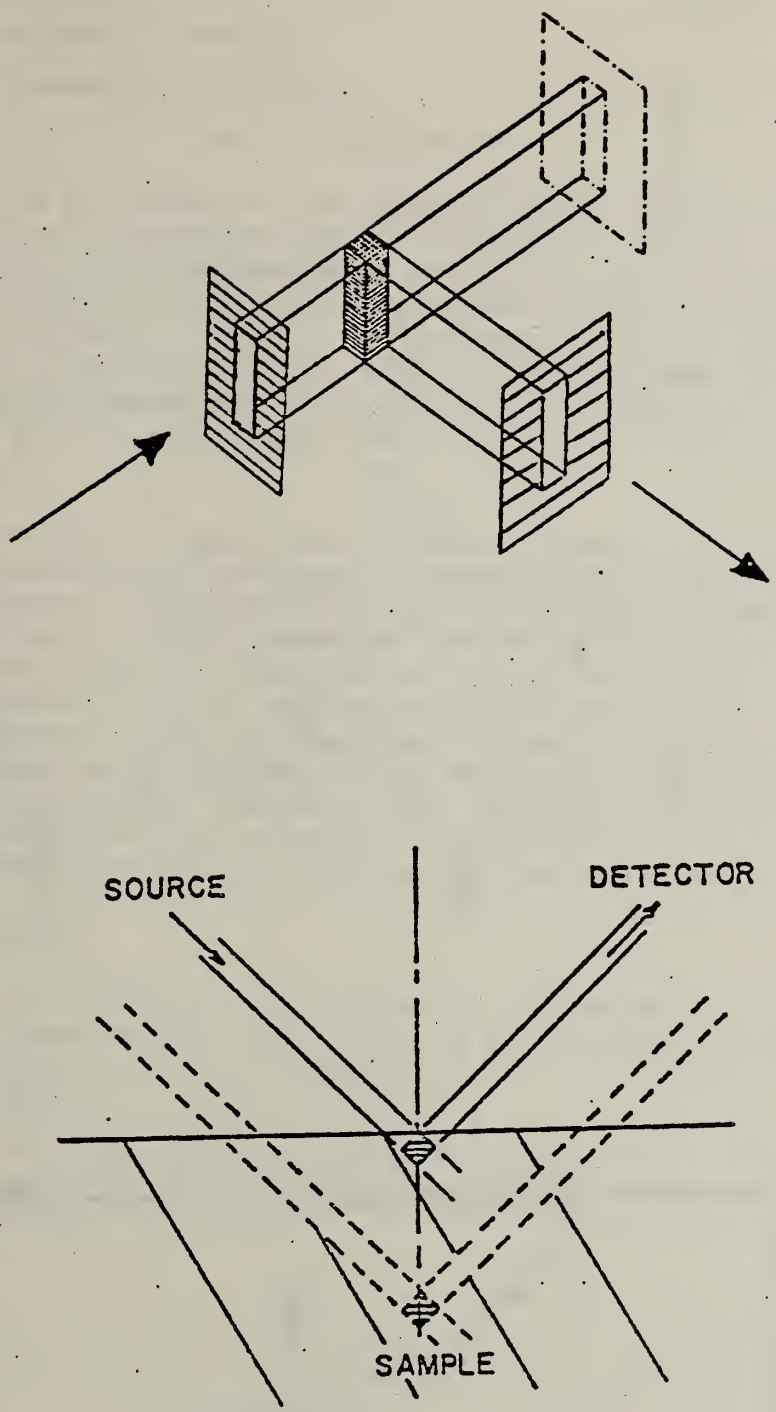

Figure 1. Upper: Perspective schematic of differential volume defined by source-side and detector-side collimation at a scattering angle of 90°.

Lower: Plan view of sample movement in beam for examination of different regions.

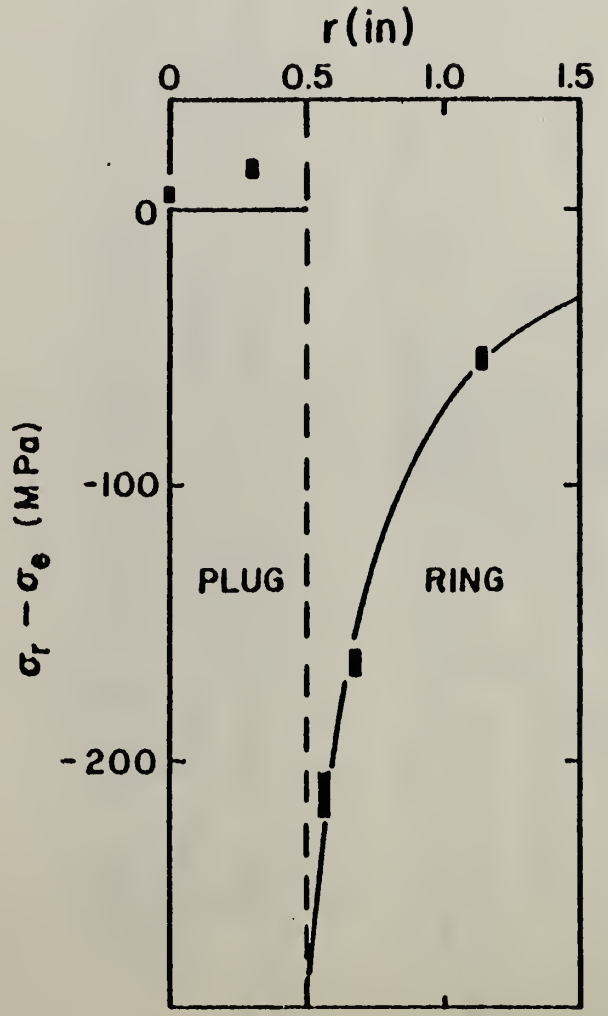

Assume:

$$\sigma_r - \sigma_\theta = 0 \qquad \text{in plug.}$$

$$\frac{d\sigma_r}{dr} = \frac{-B}{r^c} \qquad \text{in ring.}$$

$$\sigma_\theta \neq \sigma_\theta(Z).$$

Apply:

$$\int FdA = 0 = \int_0^{R_2} \sigma_\theta \, dr.$$

$$\sigma_r(R_2) = 0.$$

$$\frac{d\sigma_r}{dr} + \frac{\sigma_r - \sigma_\theta}{r} = 0.$$

In plug:

$P = -129.0 \pm 2.4$ MPa, "theory".

$P = -122 \pm 5$ MPa, neutron diffraction.

Figure 2. Experimental results and equations for ring/plug sample analysis (as described in text).

THEORETICAL STUDY OF ACOUSTIC WAVE SCATTERING

Raymond D. Mountain

Thermophysics Division

Center for Chemical Engineering

The scattering of low frequency sound waves is one way to investigate inhomogeneities in a material. In principle, the details of the scattered wave (relative intensity, polarization, directional variation) contain a great deal of information about the scatterers. Earlier, we developed within the framework of the Born approximation, a formal relation between the intensity of the scattered power and a novel set of moments of the scatterer which provide information about the size and shape of the inhomogeneity, ref. 1.

In order to apply these results to easily realized laboratory situations, it is necessary to reanalyze the scattering problem in the time domain. This has been done along the lines outlined by Rose and Richardson in ref. 2 where the scattering of a unit impulse is examined. Our results may be expressed as follows. From the measured amplitude of the scattered signal, the second and fourth temporal moments may be determined. Then, one immediately obtains the ratio of the fourth to the second moment, which is theoretically shown to be proportional to the square of the "radius" of the scatterer. In order that instrumental effects not obscure the signal, the duration of the incident pulse must be short compared with the transit time across the scatterer.

REFERENCES

1. R.D. Mountain and G. Birnbaum, "Inhomogeneity Size and Shape Determination from Scattering of Low-Frequency Sound Waves", Journal of Applied Physics 53, No. 5, pp. 3581-3584 (May 1982).

2. J.H. Rose and J.M. Richardson, "Time Domain Born Approximation", Journal of Nondestructive Evaluation 3, No. 1, pp. 45-53 (1982).

NDE TERMS AND DEFINITIONS: ULTRASONICS AND ACOUSTIC EMISSION

Donald Eitzen and Marilyn Cadoff

Mechanical Production Metrology Division

Center for Manufacturing Engineering

The Army Materials and Mechanics Research Center (AMMRC) has asked that NBS assist them in developing terms and definitions on general terms and on ultrasonics suitable for use in MIL-Standards. The specific objectives of the current phases of this activity are to:

1. Develop appropriate terminology for the broad NDTI primary terms, including: Nondestructive Testing, Nondestructive Inspection, Nondestructive Evaluation, and Nondestructive Examination.

2. Develop appropriate terminology for some of the general terms associated with nondestructive methods, including: Reference Standards, Calibration Standards, Reference Blocks, and Calibration Blocks. The metrological use and implications of these terms will be taken into account in this terminology.

3. Develop appropriate and precise terminology for ultrasonic test methods and procedures using resources such as ASNT, ASTM, ASME, and military publications with definitions of ultrasonic terms. Also, identify terms that are necessary but not yet defined.

4. Develop additional general terms associated with nondestructive methods. The metrological use and implications of these terms will be taken into account. Also, develop precise terminology for those specific terms for ultrasonic methods identified earlier as needing definition.

In carrying out these tasks well over 30 draft or published documents were reviewed and competing terms and definitions were organized. A number of internal workshops were conducted with NBS experts on metrology and on NDE. As a result, four terms were proposed for the broad NDE primary terminology such as "Nondestructive Testing." General terms such as "reference standards" were studied and, as a result, 28 general terms were proposed. Also 115 terms were proposed for ultrasonic test methods. This phase of the project is essentially complete; however, additional editing of some terms was undertaken in order to maintain consistency between this effort and some recent NBS comments on proposed MIL-STD-1309C, "Definition of Terms for Test, Measurement and Diagnostic Equipment." Input is being received on the terms from the other armed services as the draft MIL-glossary is in the "coordination" phase. Further revisions await receipt of all coordination inputs.

The 115 terms on ultrasonic methods have also been used as the basis for a new ASTM ultrasonics glossary. At the request of ASTM E7.06 and of AMMRC the definitions were reformatted and have been balloted within the ultrasonics subcommittee of ASTM. The terms are currently being revised based on the results of the ASTM ballot.

A further objective relating to terms for acoustic emission (AE) has more recently been defined by AMMRC:

5. Develop acceptable, precise, and consistent terminology for acoustic emission test methods and procedures.

In working on this task over 16 draft or published documents were reviewed and used to develop a data base for terms and for input to definitions. Approximately 37 terms were selected and draft definitions composed. The chairman of ASTM E7.04.01 on AE Glossary has begun reviewing the drafts for input to the MIL-document and for use in the ASTM glossary. A class of terms relating to "source severity" has not been defined because they seem to be application/material dependent. A class of terms on equipment-specific AE parameters has also not been defined to date.

ULTRASONIC REFERENCE BLOCK CALIBRATION METHODOLOGY

G.V. Blessing and D.G. Eitzen

Mechanical Production Metrology Division

Center for Manufacturing Engineering

The NBS, as part of its calibration mission, has an on-going program to evaluate and improve ultrasonic reference block calibrations. A review of the state of the art of those calibration practices, especially as they have been guided by the ASTM, has been recently completed (ref. 1). In that review, the principal system variables of the calibration procedure are identified, and recommendations for reducing their associated measurement errors are presented. Quantitative evaluations of the limitations to improving measurement precision are made in light of present technology. Finally, suggestions for improving present practices are given, and extensive reference to the relevant technical literature is made.

The ultrasonic transducer is identified as a significant variable in the calibration system, even though much effort has been expended to design a reproducible unit. As a result, correction factor approaches have been studied to compensate for the responses between different transducers. In an effort to apply correction factors to a ceramic element transducer in order to bring it into compliance with the ASTM E127 quartz standard (ref. 2), the following tests were performed. A ceramic transducer with like dimensions and fundamental frequency as the quartz standard was used. The center axis far-field responses of two transducers were then compared (Fig. 1), and the necessary correction factors determined. The calibration results on a block set before and after applying these correction factors to the ceramic transducer were then compared with those obtained using the quartz standard. The results are plotted in Figure 2 relative to the quartz data represented by the solid horizontal line. Of special note is the improvement in the agreement between the ceramic and the quartz data by simply using a block target to set system sensitivity.

REFERENCES

1. G.V. Blessing, "An Assessment of Ultrasonic Reference Block Methodology," NBSIR 83-2710 (Jun. 1983).

2. Anon., "Standard Practice for Fabricating and Checking Aluminum Alloy Ultrasonic Standard Reference Blocks", E127-81 in the Annual Book of ASTM Standards, Part 11. Philadelphia, PA: American Society for Testing and Materials, 1982.

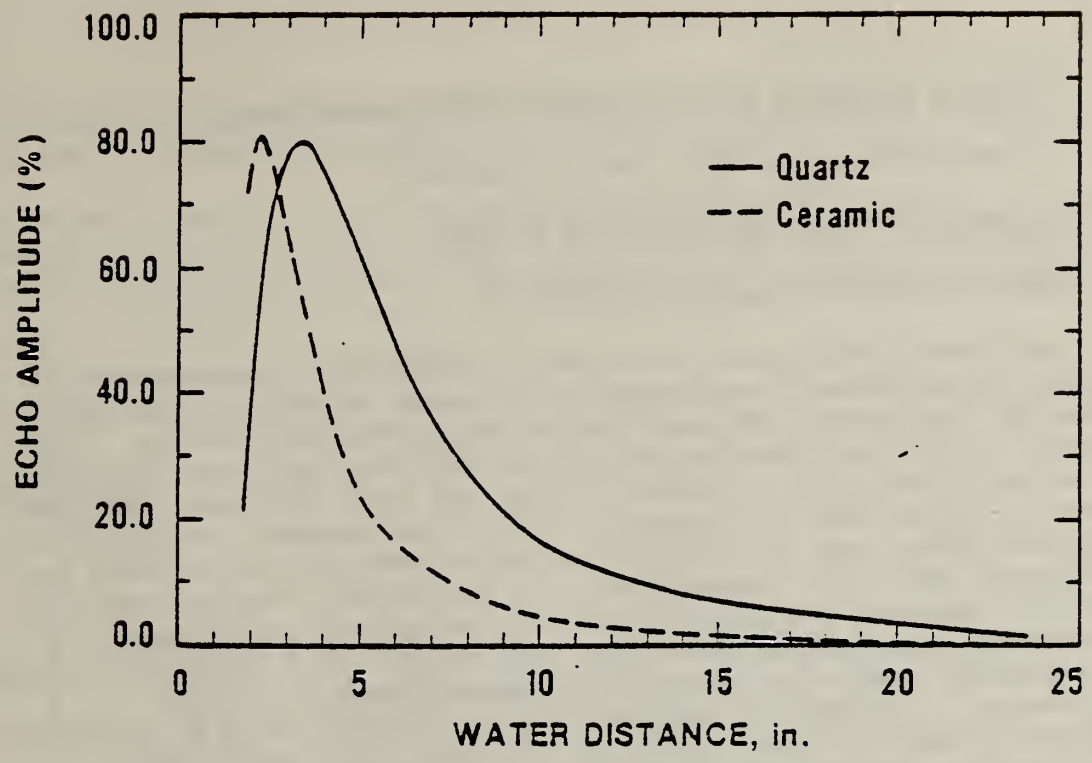

1. Far-field center axis beam profiles of a ceramic (dashed line) and a quartz transducer (solid line).

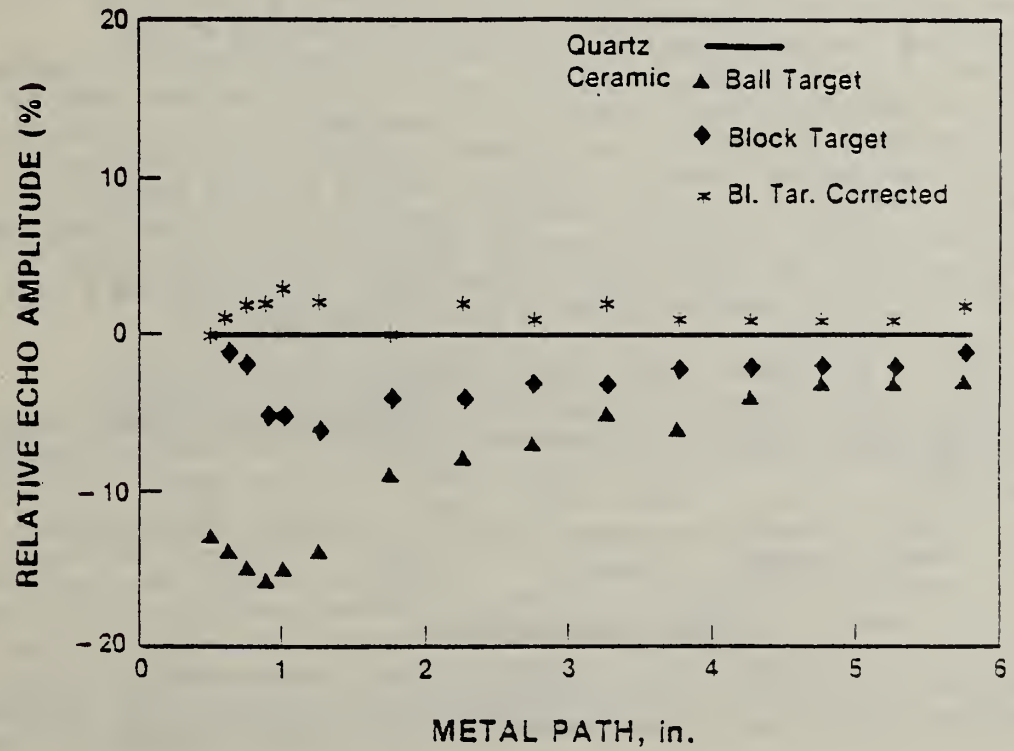

2. Reference-block-echo amplitude data taken with a ceramic transducer (discrete points), relative to that taken with a quartz transducer (solid line), as a function of metal path distance for a No. 5 hole set. Ceramic values using two distinct targets before the application of correction factors (diamonds and triangles), compared with the corrected values (stars) using a block target.

TRANSFER STANDARDS FOR ULTRASONIC POWER MEASUREMENTS

F. Breckenridge, S. Fick, and C. Tschiegg

Mechanical Production Metrology Division

Center for Manufacturing Engineering

The characterization of ultrasonic transducers by measurements of total radiated output power is motivated by the needs of such diverse applications as medical ultrasonics and quantitative nondestructive testing. In the interest of improved transfer of calibrations based on these measurements, a new series of standard ultrasonic sources has been developed. Design criteria included the improvement of overall performance and the elimination of certain operational difficulties often encountered during field use. While proof tests were underway on early prototypes, research was also conducted involving the feasibility of a "universal source" capable of operation at many frequencies. (The availability of a "universal" source would greatly reduce the number of standards needed by client laboratories.) Successful feasibility tests were followed by proof tests now almost complete. Fabrication of the first lot of units to be distributed by the Office of Standard Reference Materials will begin upon delivery of transducer element raw materials.

The principal use envisioned for the new transducers is the transfer of NBS measurements of total radiated ultrasonic power in liquid media. In transfers involving earlier standard sources, errors arising from the use of the sources were significant compared with those of the underlying measurement of ultrasonic power. By allowing elimination of two calculations and two measurements of rf voltage in the transfer procedure, the inclusion of built-in metering circuitry in each transducer reduces this added error to insignificance. Additional advantages of this feature of the new design include reduction of the equipment needed by the user and preclusion of substantial errors sometimes inherent in high frequency rf measurements. Impedance matching networks customized for these transducers will be offered so that optimal use can be made of readily-available 50 ohm rf sources, and to allow operation at higher power levels than are usually possible with matching networks commonly used in the field.

Operation at the higher power levels needed in some medical applications is facilitated by the use of 36-degrees Y-cut lithium niobate in place of the quartz used for transducer elements in earlier designs. By drastically reducing (by 95 percent) the rf drive voltage needed to attain a given level of output power, use of this element material reduces the complexity of the accompanying matching network and allows the use of elements of lower fundamental frequency. The new "universal" sources have a fundamental frequency of nominally 0.5 MHz. Overtone operation is at 1 MHz intervals; this spacing is adequate for most currently-known applications. Shown in Fig. 1 are the results of a swept-frequency measurement of output power. Equipment limitations prevented graphically recording test results for frequencies higher than 30 MHz; manual tests have been successfully made at 78 MHz.

At present, transfer calibrations have been at power levels between 5 mW and 500 mW at frequencies between 1 MHz and 16 MHz.

Continuing research includes studies of the long-term stability of the new transducers (which has so far been indistinguishable from the stability of the earlier quartz units) and of the possibilities of further refinements of mechanical and electrical design.

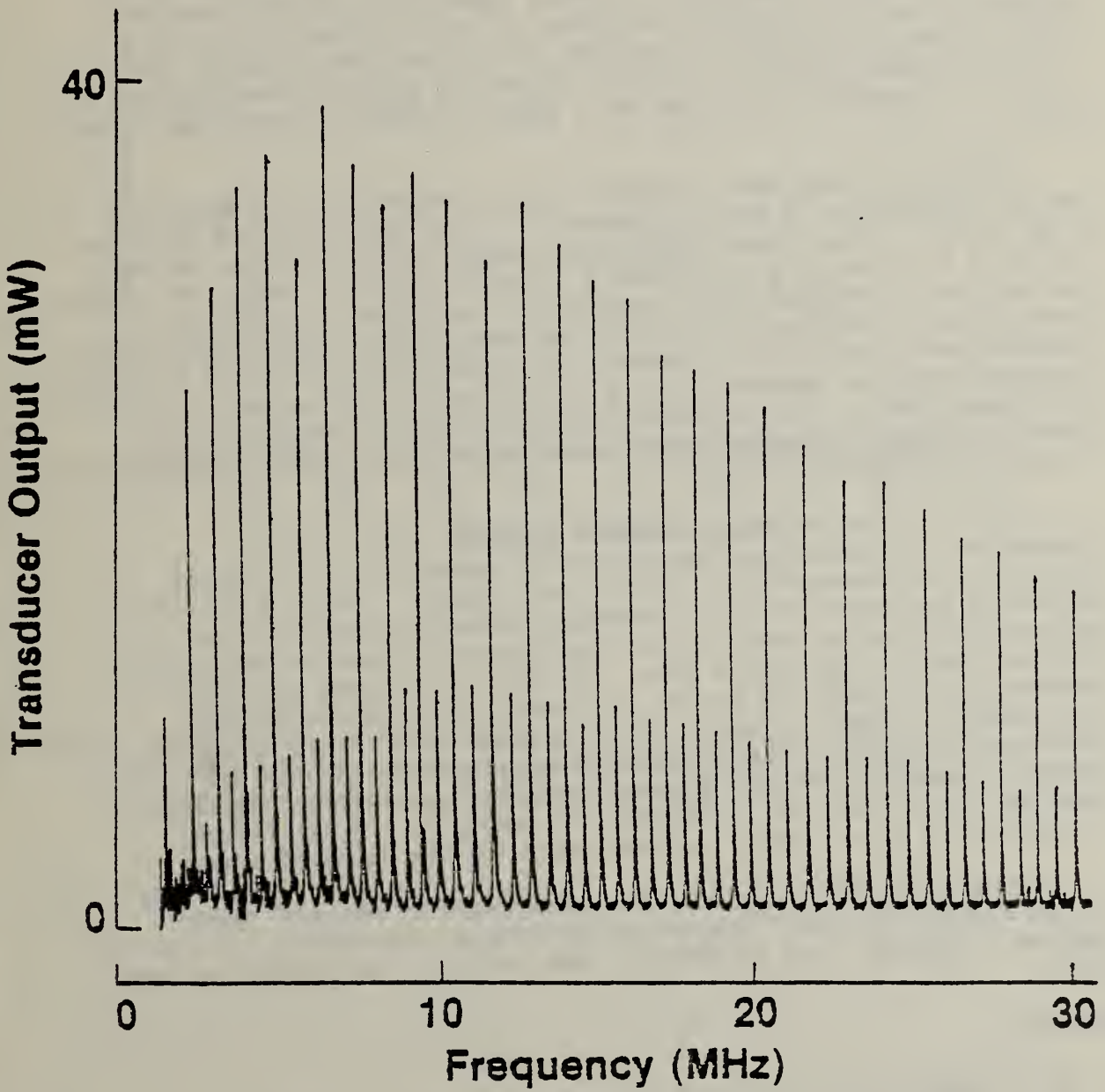

Figure 1. Swept-frequency measurement of ultrasonic output power of new "universal" source.

ULTRASONIC RESIDUAL STRESS MEASUREMENTS

G.V. Blessing, N.N. Hsu, T.M. Proctor

Mechanical Production Metrology Division

Center for Manufacturing Engineering

A reliable means to nondestructively evaluate the residual stress state of an object is of much interest to materials scientists, design engineers, and safety officials. While substantial research has been expended to apply ultrasonic techniques to this problem, practical difficulties of measurement precision and unknown sample stress have limited its application. This work focuses on both of these problems by using new transducer technology on a sample designed with a known stress state.

Ultrasonic shear wave time-of-flight measurements were made at a nominal frequency of 4 MHz on a shrink-fit disk sample of 2024 aluminum alloy (ref 1). The stress state of the sample was produced by shrink-fitting a plug and ring to produce a calculated 130 MPa region of uniform compression in the plug, and a concomitant nonuniform tension and compression in the ring. Time-of-flight measurement scans across sample diameters were made using a piezoelectric shear transducer with a viscous couplant, and were repeated using a contactless electromagnetic acoustic transducer (EMAT). The ultrasonic results were then compared with elasticity theory, assuming the acoustoelastic relationship between sound velocity and material strain.

Figure 1 illustrates the pattern obtained using the EMAT transducer to traverse specimen diameters respectively in stressed (asterisks) and non-stressed (solid line) samples. The time difference relates to the sound velocity difference between orthogonal wave polarizations for one round trip of the ultrasonic wave pulse measured from the first to the second echo. The data are in good qualitative agreement with elasticity theory. Of special note is the dramatic improvement (by about a factor of ten as compared with the piezoelectric transducer scans) that was obtained in measurement precision due to the absence of coupling effects between transducer and sample. Measurement repeatability of the time difference was nominally $\pm$ 1 ns, limited principally by a low signal-to-noise ratio for the observed echoes.

Future plans for the ultrasonic measurement of residual stress include the use of hybrid transducer techniques, fabricating a ring-plug specimen from steel, and fundamental data analysis for the zero stress state.

REFERENCE

1. G.V. Blessing, N.N. Hsu, T.M. Proctor, "Ultrasonic Shear Wave Measurements of Known Residual Stress in Aluminum," Proceedings of the Symposium on Nondestructive Methods for Material Property Determination, Hershey, PA (April 6-8, 1983).

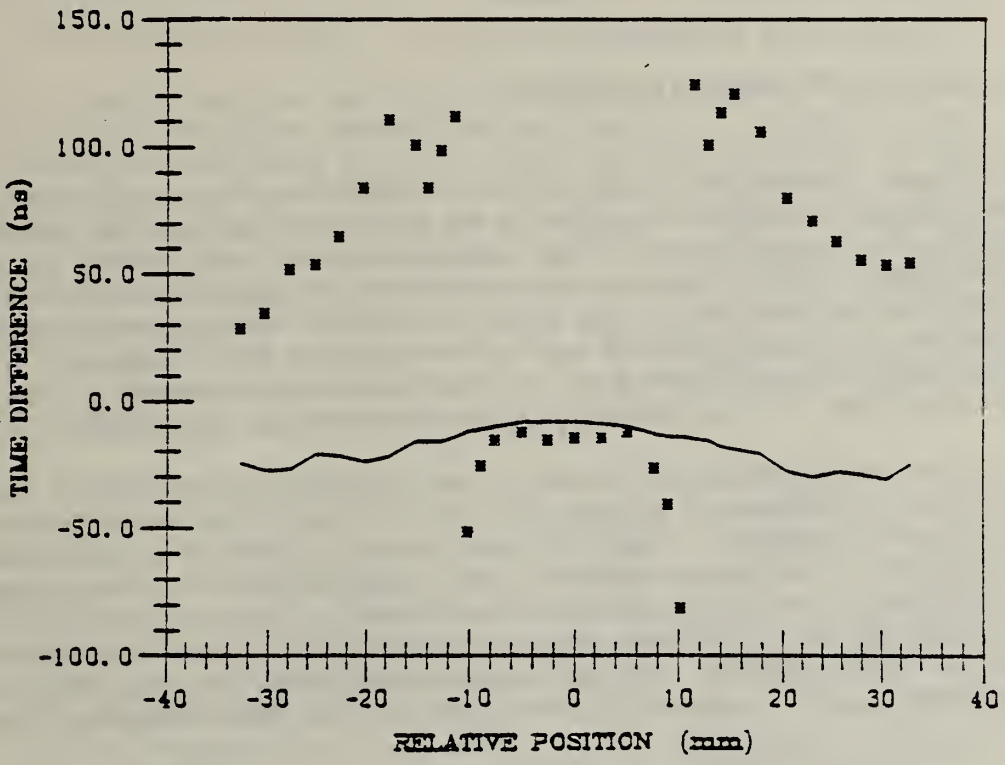

Figure 1. Time-of-flight differences between orthogonal ultrasonic-wave polarizations across a diameter of a standard specimen (asterisks) and an unstressed specimen (solid line).

EVALUATION OF RESIDUAL STRESSES IN INHOMOGENEOUS, ANISOTROPIC MATERIALS USING HORIZONTALLY POLARIZED SHEAR WAVES

R. B. King and C. M. Fortunko

Fracture and Deformation Division

Center for Materials Science

A new acoustoelasticity theory was developed for horizontally polarized shear waves (SH-waves) propagating at arbitrary angles with respect to the normals to the surfaces of plate geometries (ref. 1). Based on this theory a new experimental procedure was developed and experimentally verified. This procedure involves making two sets of relative velocity measurements at two different propagation angles with SH-waves. It was shown that from these measurements the difference of in-plane principal stresses (T_2-T_1) could be evaluated even in the presence of unknown material anisotropy.

The theory presented in ref. 1 was limited to the special case when the principal directions of stress are parallel to the basis vectors which define the material symmetry. While this is valid in certain circumstances (e.g., butt-welded plates with symmetric weld preparations) it is unnecessarily restrictive. The theory was extended in ref. 2 to the case where the principal stress directions are at an arbitrary angle with respect to the material basis vectors. It was demonstrated that the experimental procedure described in ref. 1 was still applicable in the more general situation.

Based on the theory of refs. 1 and 2, it is expected that SH-waves propagating at grazing incidence in a plate are completely insensitive to material anisotropy but are sensitive to the difference of the in-plane stress components (T_{22}-T_{11}). The insensitivity to anisotropy was confirmed using a plate of rolled aluminum alloy 6061-T6. It was found that relative measurements with grazing-incidence SH-waves were approximately fifty times less sensitive to material anisotropy than are conventional birefringence measurements with normally incident shear waves.

REFERENCES

1. R. B. King and C. M. Fortunko, "Determination of In-Plane Residual Stress States in Plates Using Horizontally Polarized Shear Waves," J. Appl. Phys. 54, No. 6, pp. 3027-3035 (1983).

2. R. B. King and C. M. Fortunko, "Evaluation of Arbitrary Plane Residual Stress States in Nonhomogeneous, Anisotropic Plates," Ultrasonics (in press).

DETERMINATION OF THE ELASTIC MODULI OF MELT-SPUN METALLIC GLASSES

M. Rosen, C. L. Friant and H. N. G. Wadley

Metallurgy Division

Center for Materials Science

Metallic glass formation and subsequent crystallization upon annealing has recently become an active research area. Rapidly solidified alloys exhibit a variety of desirable physical, chemical and mechanical properties of particular interest in the electronics and power industries. The enhanced development of rapidly solidified metallic glasses has been accompanied by an extensive body of research concerning both material characterization and processing. Microstructural characterization applying nondestructive techniques, e.g., contact or noncontact (laser) ultrasonics, may be attractive for the contribution to understanding the kinetics and mechanisms of transformations occurring in the melt-spun ribbons, and for its ultimate application for on-line feedback control of materials processing variables.

A novel approach was developed and reported last year for the determination of sound velocity in thin metallic ribbons employing contactless laser generation and either piezoelectric or laser-interferometric detection of the propagating ultrasonic waves (ref. 1). The Young's modulus can be readily calculated from the experimentally-determined sound wave velocity, assuming one-dimensional extensional waves propagating in a homogeneous, isotropic, linearly elastic solid of known density. Determination of the variation of Young's modulus with annealing time and temperature yielded important kinetic information on the stability of the glassy metals, PdCuSi and Cu-Zr alloys, against relaxation processes and crystallization (refs. 2-4).

The present work was concerned with the development of an experimental procedure and theoretical analysis whereby, in addition to the Young's modulus, the second independent elastic modulus (shear modulus) can be derived. By knowing both independent moduli, the others can also be calculated, e.g., adiabatic compressibility, Poisson's ratio, Debye temperature. Several features of guided waves which propagate in bounded elastic media, such as plates, sheets, foils, ribbons, and thin cylinders, distinguish them from bulk waves. Guided waves show dispersion of wave velocity with frequency and plate thickness, or rod diameter. The only nondispersive guided wave is the fundamental horizontally polarized shear wave SH (0). The SH (0) mode can therefore be very useful in the determination of the shear modulus. However experimental difficulties had to be surmounted before the SH (0) velocity could be measured in thin metallic ribbons. Among others, the orientations of the generating and receiving transducers relative to the ribbon proved to be important considerations (ref. 5).

Using a specially developed goniometric device for the determination of the shear wave velocities in thin metallic ribbons, and applying the theoretical considerations mentioned above, both the longitudinal and shear wave velocities in thin ribbons were measured directly for the first time. Table I shows the

velocities, Young's and shear moduli, adiabatic compressibility and Poisson's ratio for PdCuSi, Cu-Zr, "Metglas" 2605-SC and aluminum foil. Noteworthy is the unusually high compressibility and Poisson's ratio for PdCuSi in its glassy state. Work is in progress to analyze the composition dependence of the adiabatic compressibility and shear moduli of Cu-Zr alloys in terms of the relative stability of the glassy state against crystallization.

REFERENCES

1. C. H. Palmer, S. Fick and M. Rosen, "A Dual-Probe Laser Interferometer for Contactless Determination of Ultrasonic Wave Velocities and Attenuation", in preparation.

2. M. Rosen, H. N. G. Wadley and R. Mehrabian, "Crystallization Kinetics Study of Amorphous PdCuSi by Ultrasonic Measurements", Scripta Metall. 15, 1231 (1981).

3. J. C. Chang, F. Nadeau, M. Rosen and R. Mehrabian, "Crystallization Kinetics Study of Amorphous $Cu_{50}Zr_{50}$ by Means of Ultrasonic Measurements and MicroHardness", Scripta Metall. 16, 1073 (1982).

4. M. Rosen and E. Horowitz, "Ultrasonic Nondestructive Characterization (NDC) of Metallurgical Microstructures and Transformations", Johns Hopkins University, Report CMR-NDE-7 (September 1982).

5. C. L. Friant and M. Rosen, "Ultrasonic Materials Characterization of Melt-Spun Metallic Ribbons", Proc. Symposium on Nondestructive Methods for Material Property Determination, April 1983, Hershey, PA (in press).

TABLE I

Alloy	V_E(cm/s)	E(dynes/cm^2)	V_S(cm/s)	G(dynes/cm^2)	V_l(cm/s)	K(dynes/cm^2)	ν
Pd·Cu·Si	2.97×10^5	9.45×10^{11}	1.787×10^5	3.36×10^{11}	4.495×10^5	16.78×10^{11}	0.41
Cu·Zr	3.30×10^5	7.98×10^{11}	1.98×10^5	2.87×10^{11}	4.67×10^5*	12.15×10^{11}	0.39
Metglas 2605·SC	4.64×10^5	15.72×10^{11}	2.86×10^5	5.97×10^{11}	5.56×10^5*	14.56×10^{11}	0.32
Aluminum Foil	5.12×10^5	7.09×10^{11}	3.13×10^5	2.65×10^{11}	6.36×10^5	7.19×10^{11}	0.34

*Longitudinal velocities calculated from experimentally observed extensional and shear velocities.

EFFECT OF COMPOSITION ON THE CRYSTALLIZATION KINETICS AND ELASTIC PROPERTIES OF Cu-Zr ALLOYS

M. Rosen, F. Nadeau and H. N. G. Wadley

Metallurgy Division

Center for Materials Science

As-spun metallic glasses, e.g., Cu-Zr alloys, are not thermodynamically stable. They tend to structurally relax and finally crystallize when the thermomechanical conditions are appropriate (ref. 1). The resulting more stable structures exhibit a drastic reduction of the initially superior mechanical, physical and chemical properties. The factors governing the thermal stability of amorphous alloys and their effects on properties are not well understood. A very prominent change in properties upon crystallization is the increase, by about 40 percent, in the elastic moduli of the material, accompanied by a drastic reduction in the plastic behavior (ref. 1). The objective of the present study was to investigate the compositional dependence of the elastic properties in the Cu-Zr system by means of ultrasonic measurements (ref. 2).

Five Cu_x-Zr_{1-x} alloys (x = 0.3, 0.4, 0.5, 0.6, 0.7) were prepared by melt-spinning in the form of ribbons 2 mm wide, and 25 μm thick. X-ray diffraction indicated no crystallinity. The ribbons were isothermally annealed at different temperatures for different time periods. Some samples were held near the crystallization temperature for more than 24 hours to assure complete crystallization.

The sound wave velocity was determined by measuring the transit time of a single pulse generated by a Nd:YAG laser and detected either by a piezoelectric transducer (ref. 3) or by the dual-laser interferometer described last year. The total estimated error in the calculated value of the Young's modulus was ± 0.2 percent. Ribbon densities were determined by means of a float and wire technique.

The extensional wave velocity, Fig. 1, and the Young's modulus vary in a sigmoidal manner as a function of annealing time, characteristic of a thermally activated process. Crystallization occurs by nucleation and diffusional growth. Analysis of the kinetics of the crystallization yields activation energies of 376 kJ $mole^{-1}$ for compositions up to 50 w/o Cu. For higher concentrations of Cu, the activation energy increases continually up to 451 kJ $mole^{-1}$ (Fig. 2). The increasing activation energy can be related to changes in the configurational entropy of the alloy as the population of the Cu-Cu pairs increases (ref. 4).

Young's modulus of amorphous Cu-Zr varies with composition in the form of a smooth S-curve (Fig. 3). Higher values of the Young's modulus are obtained for higher Cu concentrations. In the present investigation, a functional relationship has been found between the variation of the Young's modulus with composition and that of the glass transition temperature. The behavior of Young's modulus versus composition of the glassy alloys (Fig. 3) was found to be in qualitative agreement with the behavior of the glass

transition temperature, Tg, Fig. 4. This relationship is particularly interesting since it may indicate a connection between variations in the cohesive energy of the alloy and its glass forming capability. The analogous behavior may be due to changes induced in the bonding strength between constituent atoms as the composition is varied. Should such a relationship indeed exist between the elastic properties and the glass transition temperature, then the elastic properties might be a figure of merit of the glass formation ability of the alloy. In this case, a non-destructive ultrasonic capability exists to characterize and predict the glass formation ability. More work is necessary to establish the validity of this assumption.

REFERENCES

1. J. C. Chang, F. Nadeau, M. Rosen and R. Mehrabian, "Crystallization Kinetics Study of Amorphous $Cu_{50}Zr_{50}$ by Means of Ultrasonic Measurements and Microhardness", Scripta Metall. 16, pp 1073 (1982).

2. F. Nadeau, M. Rosen and H. N. G. Wadley, "Effect of Composition on the Elastic Properties of Cu_xZr_{1-x} Glassy Alloys", in preparation.

3. M. Rosen and E. Horowitz, "Ultrasonic Nondestructive Characterization (NDC) of Metallurgical Microstructures and Transformations", Johns Hopkins University Report CMR-NDE-7 (September 1982).

4. M. Rosen, C. L. Friant, F. Nadeau, J. J. Smith and E. Horowitz, "Ultrasonic Nondestructive Materials Characterization of Rapidly Solidified Microstructures", Johns Hopkins University Report CMR-NDE-8 (August 1983).

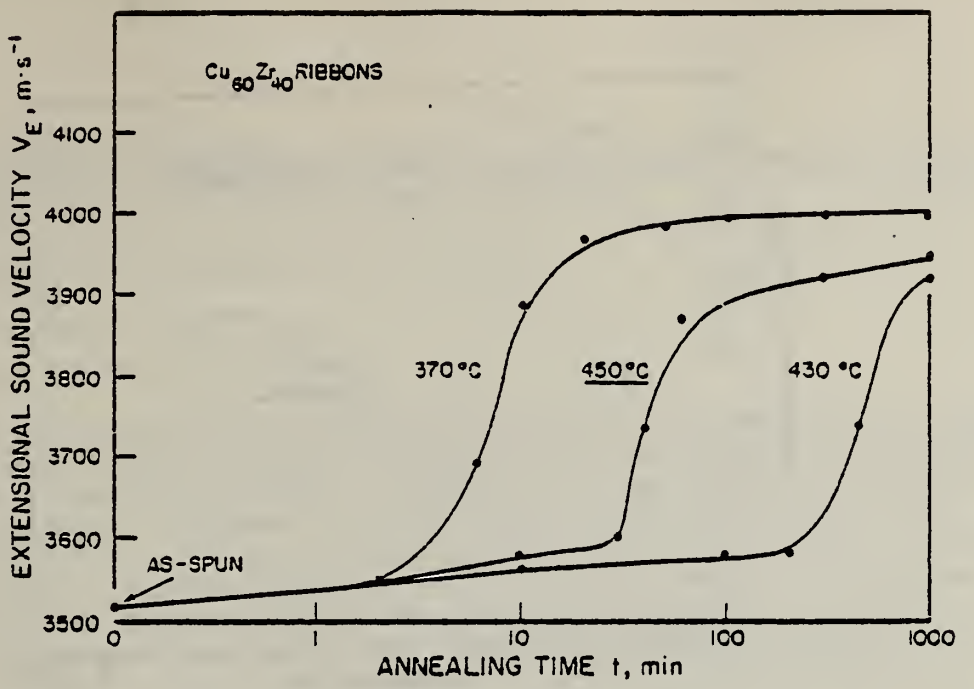

Figure 1. Variation of the extensional sound wave velocity as a function of time at three isothermal holding temperatures during recrystallization of $Cu_{40}Zr_{60}$ glassy metallic alloy.

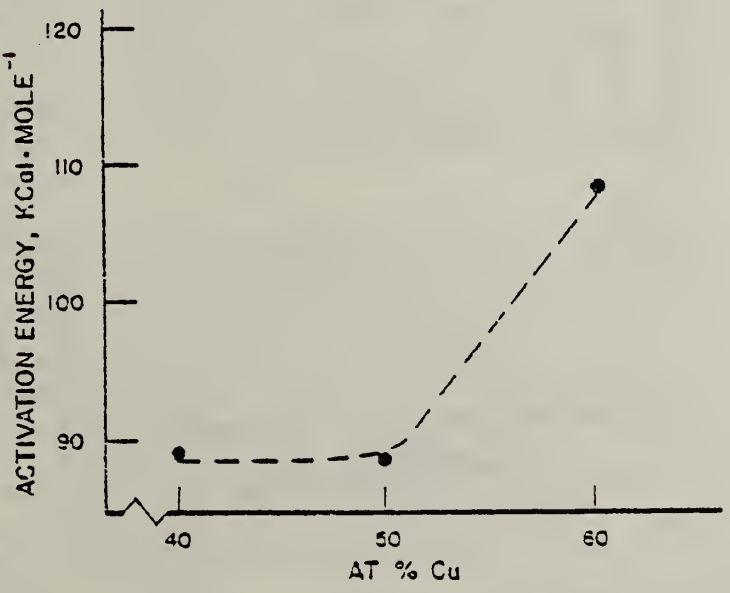

Figure 2. Effect of composition on the activation energy of crystallization in Cu-Zr amorphous alloys.

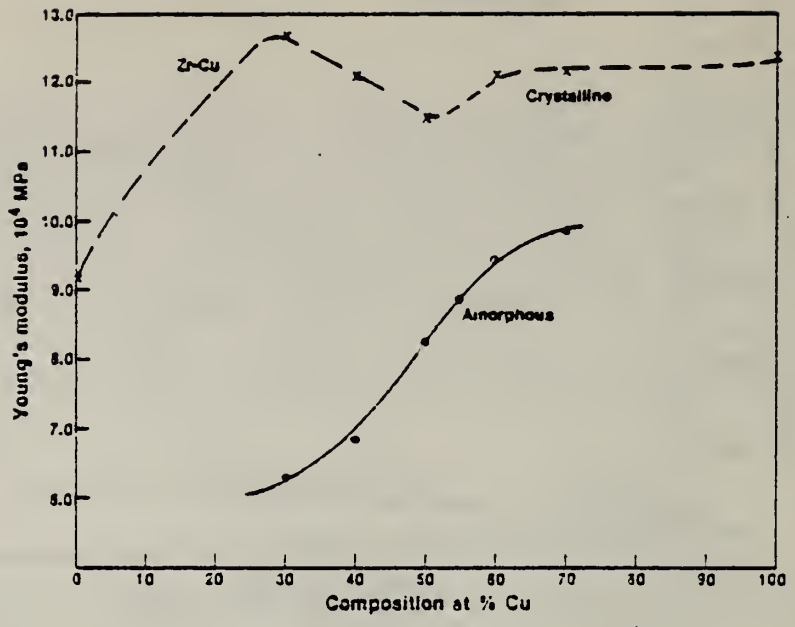

Figure 3. Variation of Young's modulus with copper content in amorphous and crystalline Cu-Zr alloys.

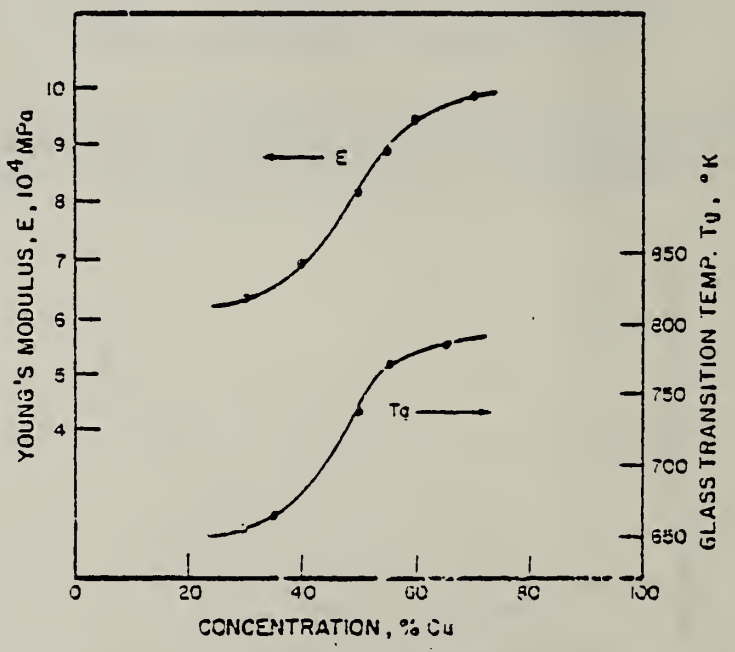

Figure 4. Variation of the Young's modulus and glass transition temperature with copper content in amorphous Cu-Zr alloys.

NONDESTRUCTIVE CHARACTERIZATION OF MICROSTRUCTURALLY MODIFIED SURFACE LAYERS BY MEANS OF RAYLEIGH SURFACE WAVES

M. Rosen, B. Elkind and H. N. G. Wadley

Metallurgy Division

Center for Materials Science

Directed energy source irradiation by means of high power lasers and electron beams is being extensively applied for the modification of surface properties of metallic surfaces. Significantly improved wear, corrosion and fatigue properties have been achieved by rapid melting and quenching of peripheral surfaces of metals. Modification of surfaces may also involve incorporation of alloying elements into the surface layer, or localized thermomechanical treatment of the desired characteristics. In nearly eutectoid steels, the martensitic layer at the irradiated and rapidly-quenched surface will be followed by layers of bainite and pearlite. Control of the developing microstructures and their nondestructive characterization are crucial in understanding the operating mechanisms. However, the modified surface zones are not readily amenable to conventional nondestructive ultrasonic characterization. The objective of the present research task is to develop a nondestructive characterization method using Rayleigh surface waves that enables the determination of the elastic moduli of the modified layer and the depth of penetration of the heat-affected zone into the bulk.

The present report provides preliminary results of the effect of electron beam glazing on aluminum alloys and steel samples. The nondestructive method involves generation of Rayleigh surface waves and their detection by means of a specially designed device based on piezoelectric transducers, as well as laser generation and laser-interferometric detection of the Rayleigh waves (refs. 1,2). Choice of an appropriate frequency range enables determination of the elastic properties of the microstructurally modified layers. From the frequency analysis of the "apparent" Rayleigh wave velocities, it is feasible to determine the depth of penetration of a homogeneously modified surface layer into the bulk of the sample.

Electron beam glazing has been applied in the course of this research to develop modified metallurgical microstructures on PdCuSi, Fig. 1, age hardened aluminum alloys 2024, 5052 and 6061, as well as formation of martensitic and bainitic layers on pearlitic steel substrates, Fig. 2. In all the steel samples the Rayleigh wave velocity of the modified layers was lower than the bulk values, by about 2 percent (ref. 2). In PdCuSi the Rayleigh velocity of the amorphous layer was found to be 30 percent smaller than in the crystalline substrate (ref. 1). The results in aluminum can be explained in terms of annealing of the surface age hardened layer. This assumption is corroborated by the lower hardness values of the glazed aluminum surfaces. The results of this investigation are being analyzed in terms of the elastic properties of the specific phases involved.

Work is in progress to measure the apparent Rayleigh velocity as a function of frequency, thus enabling thickness gauging of the layer affected by the electron beam irradiation.

REFERENCES

1. M. Rosen and E. Horowitz, "Ultrasonic Nondestructive Characterization (NDC) of Metallurgical Microstructures and Transformations", Johns Hopkins University Report CMR-NDE-7 (September 1982).

2. M. Rosen, C. L. Friant, F. Nadeau, J. J. Smith and E. Horowitz, "Ultrasonic Nondestructive Materials Characterization of Rapidly Solidified Microstructures", Johns Hopkins University Report CMR-NDE-8 (August 1983).

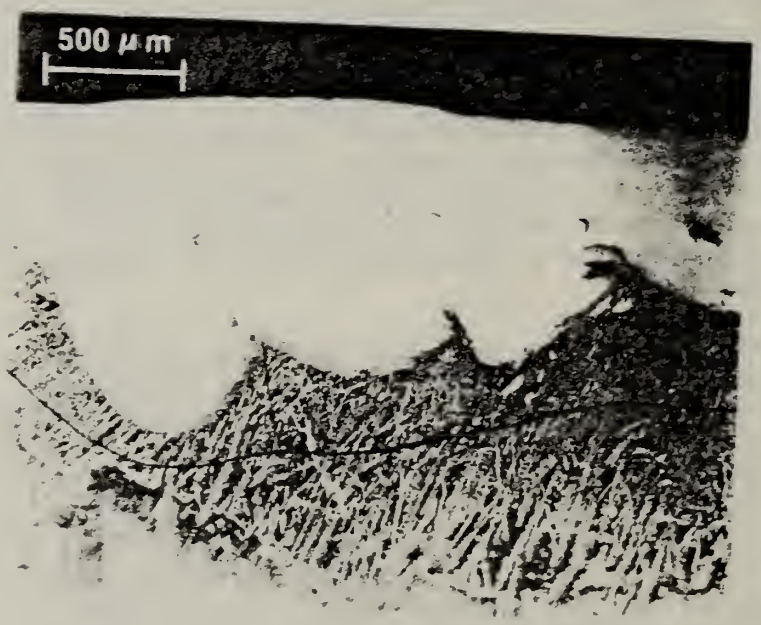

Figure 1. Modified metallurgical microstructure on PdCuSi.

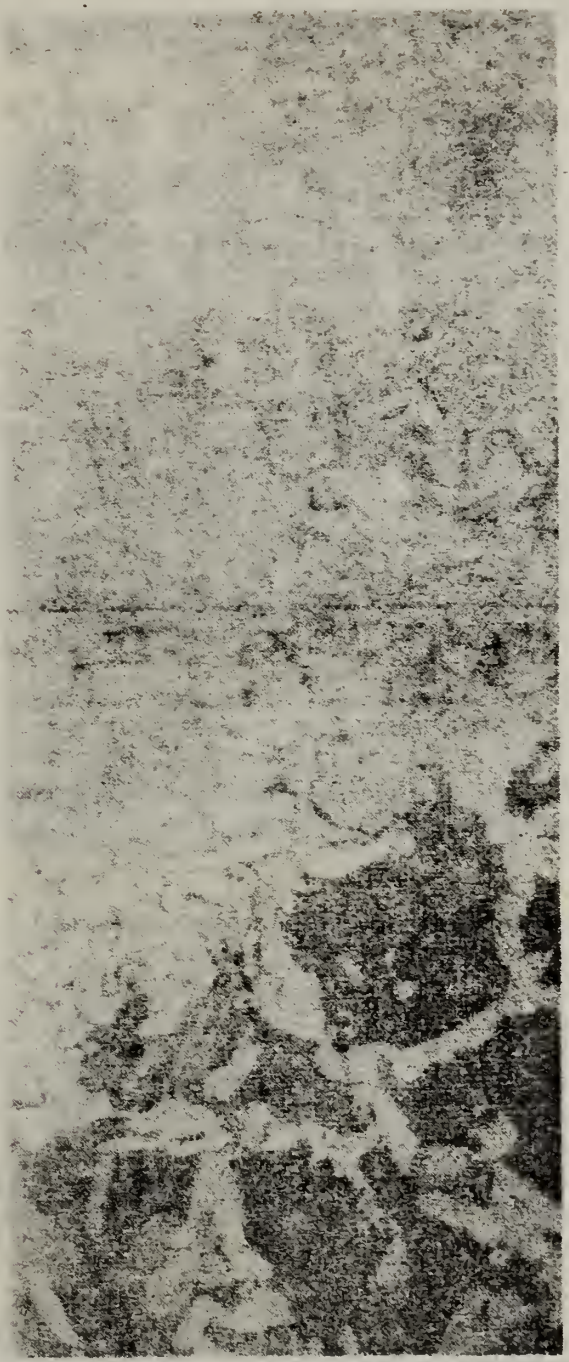

Figure 2. Martensitic and bainitic layers on pearlitic steel substrate.

DETERMINATION OF PHASE STABILITY CRITERIA OF EXTENDED SOLID SOLUTIONS BY MEANS OF NONDESTRUCTIVE CHARACTERIZATION

M. Rosen, R. J. Schaefer, J. J. Smith and H. N. G. Wadley

Metallurgy Division

Center for Materials Science

Extension of the solid solubility of alloys under nonequilibrium conditions by means of rapid cooling has great scientific and technological potential in terms of the ability to predict and design the metallurgical properties of alloy systems. Extended solid solutions of aluminum with transition metal additions have been shown to possess excellent mechanical properties, corrosion resistance and improved fatigue life. At the present time, there is no widely accepted model or set of criteria that permits predictions to be made concerning the amount of extension of the solubility as a function of quenching conditions. By attaining the necessary supercooling, suppression of the decomposition of the alloy can be controlled, thus preventing segregation, solute clustering or subsequent aging. The objective of the research is to undertake a systematic investigation of aluminum-base alloys that are known to possess extended solid solubilities upon rapid cooling from the melt. These aluminum systems include additions of first row transition metal elements such as Cr, Mn and Fe. Nondestructive evaluation techniques, e.g., sound velocity, ultrasonic attenuation, compressibility, and electrical resistivity, will be used to characterize the physical properties of the alloys as related to the heat treatments of the alloys. The NDE data can be correlated with the mechanical properties and thermal stability of the alloys. Corroborating evidence from x-ray analysis, optical and electronic microscopy, and strength and hardness measurements provides additional aspects that cannot be covered by nondestructive ultrasonic methods.

The first phase of the research program dealt with the Al-Mn system (refs. 1-3). Samples were prepared in ribbon form by melt spinning and by electron beam surface melting of bulk samples. The samples were evaluated by several experimental techniques in the as-quenched condition and after annealing for different times at 450°C. The measurements gave consistent indication of the high degree of supersaturation attained in the rapidly-solidified materials and showed changes in several physical properties as decomposition of the supersaturated phase progressed. At low supersaturations, the precipitates were localized at the grain boundaries. At high manganese concentrations, the precipitates were abundantly dispersed through the matrix, and the lattice supersaturation decreased more rapidly.

The maximum equilibrium solubility of Mn in Al is 1.82 w/o. In the supersaturated condition the aluminum lattice accommodates up to 13 w/o, as found by x-ray diffraction of the as-spun Al-Mn ribbons. At 15 w/o Mn, x-ray diffraction showed that additional peaks appear. The electrical resistivity

of the ribbons, determined by means of a standard four-probe potentiometric method, shows a strong increase in resistivity with increasing concentration of manganese, Fig. 1. Annealing at 450°C strongly affects the resistivity. By means of a nucleation and diffusion controlled growth process, Al-Mn particles are formed, thus diminishing the number of effective electron scatterers from the aluminum matrix.

The velocity of ultrasonic waves, Fig. 2, was determined by measuring the transit time of a single pulse generated by a Nd:YAG laser and detected by a piezoelectric transducer (ref. 4). Rayleigh surface waves were used to characterize the supersaturated solid solution generated by electron beam-surface melting of a slab of Al-7 w/o Mn. The 2 percent difference in Rayleigh velocity, with that of the untreated face being the greater one, is due to the presence of Al-Mn precipitates in the equilibrium structure.

The elastic moduli of both annealed and unannealed ribbons exhibit a prominent minimum at 2.5 w/o Mn. It is believed that the minimum in the elastic moduli is of intrinsic importance, and is related to changes in the bonding strength as manganese is added to the aluminum lattice. The behavior of the lattice parameter, Fig. 3, and electrical resistivity, Fig. 1, as a function of manganese concentration, corroborates the significance of the minimum in the elastic properties. Work is in progress to investigate the behavior of the elastic properties, electrical resistivity and lattice parameter of aluminum-base alloys with Cr and Fe.

The present phase of the research also indicates a measurable difference in the sound velocity between annealed and unannealed samples. The difference increases with increasing manganese content. The difference in sound velocity indicates that nondestructive measurements are feasible for in-process dynamic monitoring and determination of the supersaturation range of rapidly-solidified alloys.

REFERENCES

1. R. J. Schaefer, M. Rosen, J. J. Smith, D. Shechtman and R. Mehrabian, "Nondestructive Characterization of Rapidly Solidified Al-Mn Alloys", Proc. 3rd Conf. on Rapid Solidification Processing, R. Mehrabian, M. Cohen and B. Kear, editors (in press).

2. M. Rosen, C. Friant, F. Nadeau, J. J. Smith and E. Horowitz, "Ultrasonic Nondestructive Materials Characterization of Rapidly Solidified Microstructures", Johns Hopkins University Report CMR-NDE-8 (August 1983).

3. J. J. Smith, M. Rosen and H. N. G. Wadley, "Effect of Composition on the Elastic Properties of Rapidly Solidified Al-Mn Alloys of Extended Solid Solubility", in preparation.

4. M. Rosen and E. Horowitz, "Ultrasonic Nondestructive Characterization (NDC) of Metallurgical Microstructures and Transformations", Johns Hopkins University Report CMR-NDE-7 (September 1982).

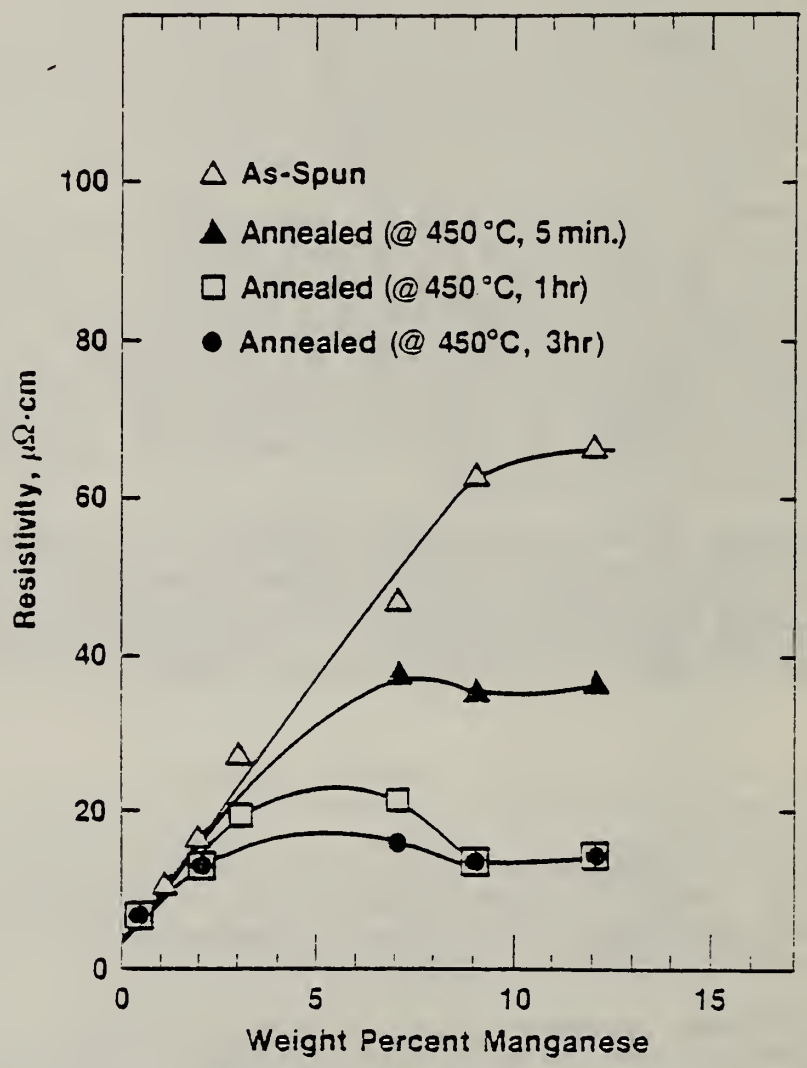

Figure 1 Variation of the electrical resistivity in rapidly solidified Al-Mn alloys as a function of Mn concentration in the as-spun and annealed conditions.

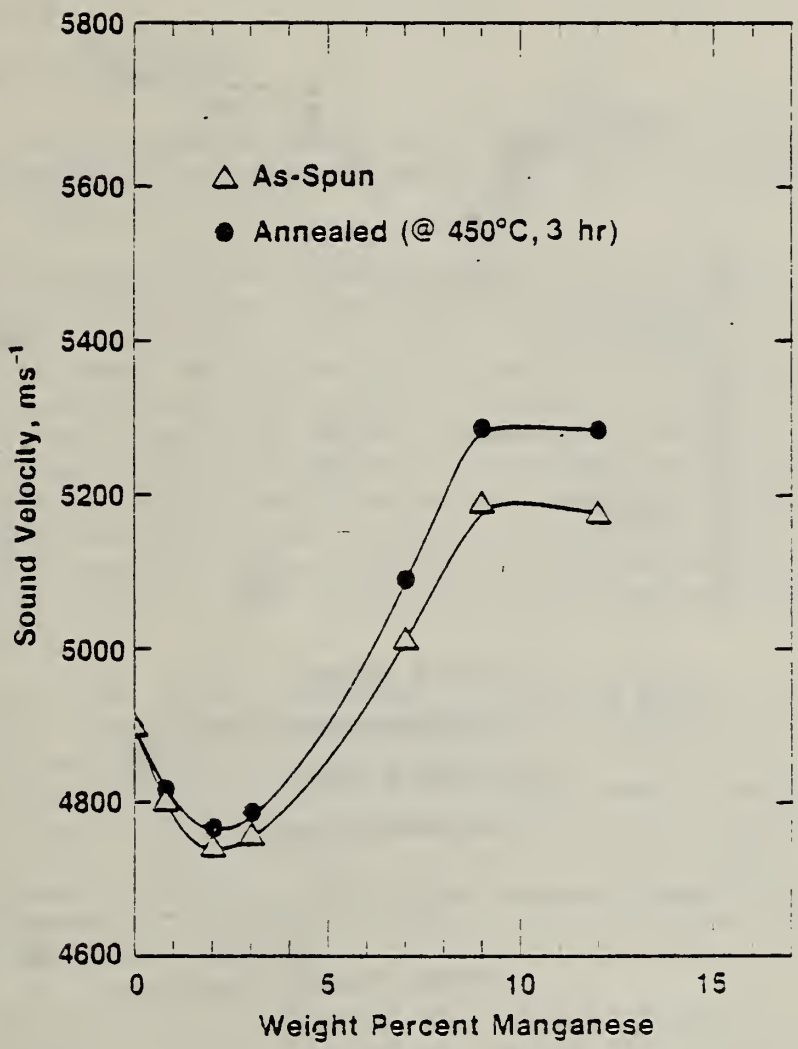

Figure 2 Variation of the extensional sound wave velocity in rapidly solidified Al-Mn alloys as a function of Mn concentration in the as-spun and annealed conditions.

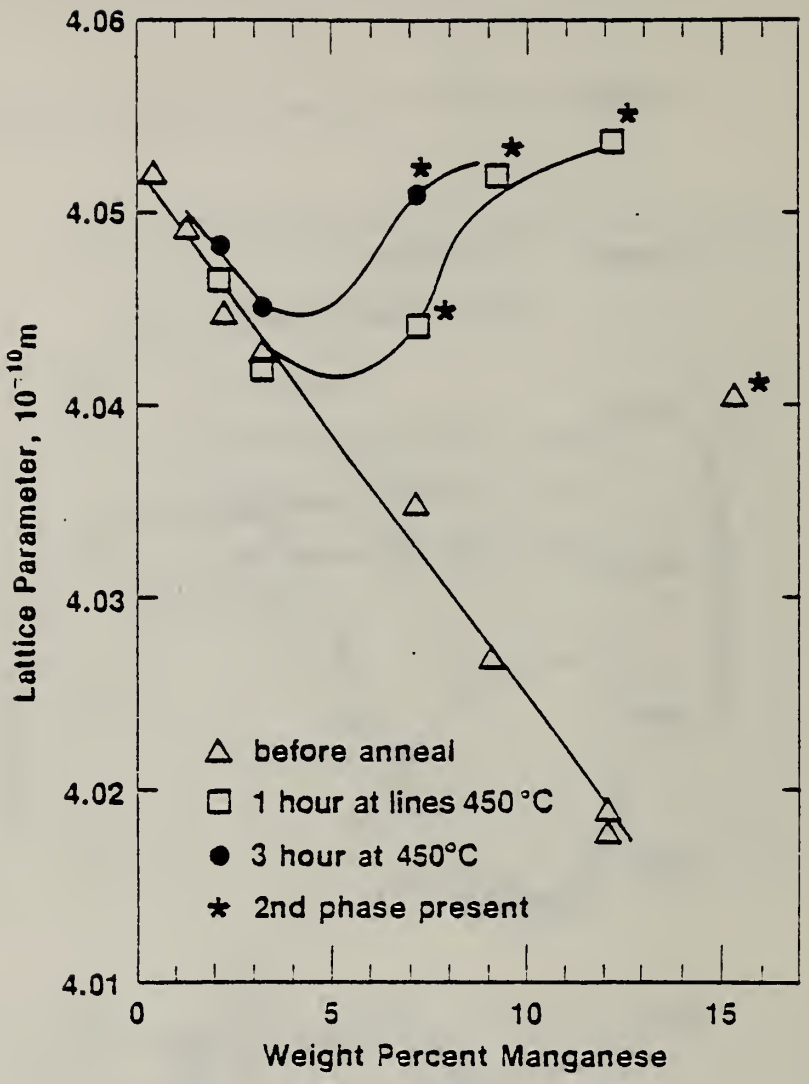

Figure 3 Variation of the lattice parameter in rapidly solidified Al-Mn alloys as a function of Mn concentration in the as-spun and annealed conditions.

ULTRASONIC MEASUREMENT OF SOLID/LIQUID INTERFACE POSITION DURING SOLIDIFICATION AND MELTING OF METALS

R. L. Parker and J. R. Manning

Metallurgy Division

Center for Materials Science

Ultrasonic techniques are being developed to provide real-time in-situ, nondestructive measurement of the position, motion and shape of solidification interfaces in opaque materials.

The use of pulse-echo ultrasonic flaw detectors to detect the presence and location of cracks, voids, and other flaws in metals and non-metals is well known. The solid-liquid interface in a melting or freezing metal should also produce a reflected echo, in that there is a measurable difference in both sound velocity and density across the interface. For normal incidence of longitudinal waves, about 10% of the pressure amplitude, or 1% of the energy, would be expected to be reflected from a planar solid-liquid interface in a pure metal. Such a technique would be useful for feedback and closed-loop process control of solidification to achieve improved quality control and productivity--such as in warning of potential breakouts in continuous casting of steel, ref. 1. The technique can be regarded as real-time ultrasonic metallography.

A paper on this subject (ref. 2) was presented at the Army Research Office Tri-Service Conference on Manufacturing Research held at Leesburg, Virginia May 31 - June 2, 1983, and appears in the Proceedings of that meeting. It summarizes our earlier work in this area, including measurements on solid-liquid tin in a resistance-heated Bridgman furnace; the use of computer spatial averaging in room-temperature modelling tests on large-grain stainless steel, in order to improve signal/noise ratios in the presence of strong Rayleigh scattering; a survey of earlier tests by others; and current NBS tests on hot steel and iron.

The tests on hot steel have been made with an RF induction furnace in the Bridgman geometry, in argon, with the transducer coupled to the cool end of the 12 cm long specimens. Using 1 MHz longitudinal waves, we have made measurements of the solid-liquid interface location and motion in pure iron rods 2 cm OD by 12 cm long, and in 304 stainless rods 3 cm OD by 12 cm long, in the presence of substantial grain growth. These are the first such measurements on these materials. This grain growth both attenuates the incoming beam and introduces back-reflected noise signals. In the case of alloys, the changes in acoustic impedance as the beam enters the mushy zone are much less abrupt than is the case for a pure metal, and therefore the reflected signal is further reduced. Thus, digital signal processing is necessary for reliable test results with alloys, using spatial averaging. In the Bridgman geometry, this can be accomplished by rotating the transducer followed by signal averaging. Rotation alters the interference patterns from the grains (much as in the parallel translation case) because there are variations in the cylindrical symmetry of the sound field produced by variations in the PZT element. A stepper motor, computer-controlled, provides the rotation.

To develop a reliable pulse-echo system for determining skin thickness in continuous casting of steel, it is essential to determine the degree of transmission through bulk, hot steel and the degree of reflection from the solid-liquid interface. These quantities are frequency dependent, and can be time-dependent in the case of grain growth and interface motion. An apparatus has been constructed to do this, and measurements are underway on iron and steel. Computer signal processing is necessary to improve signal/noise ratios in the case of alloys.

1. R. L. Parker, "Ultrasonic Measurement of Solid/Liquid Interface Position during Solidification and Melting of Metals," AIP Conference Proceedings No. 84 (Physics in the Steel Industry), New York, 1982.

2. R. L. Parker, "Ultrasonic Measurement of Solid/Liquid Interface Position During Metal Solidification," Proc. Army Res. Off. Conf. on Mfg. Res., June 2, 1983.

ULTRASONIC STEEL TEMPERATURE SENSORS

S. J. Norton, M. Linzer, H. N. G. Wadley, C. Turner, F. S. Biancaniello and S. D. Ridder

Metallurgy Division

Center for Materials Science

An investigation was undertaken of the feasibility of determining the internal temperature distribution within a cylindrical steel billet from ultrasonic time-of-flight measurements along different paths penetrating the billet. From these measurements, the internal sound-velocity distribution can be reconstructed by tomographic techniques. Using an empirical relationship between sound velocity and temperature, the velocity profile can then be converted to a map of the internal temperature distribution.

Heat flow modelling was included in the study to investigate the spatial and temporal characteristics of the internal temperature distribution in a cooling cylindrical billet. As a first step in measuring temperature, a tomographic algorithm was developed for reconstructing the internal sound velocity distribution from time-of-flight measurements along a minimum number of paths penetrating the billet. By representing the unknown velocity distribution in a suitable orthogonal basis set, only a minimum number of terms in the basis expansion need be retained for a sufficiently accurate representation of the velocity distribution. The basis set can also be chosen to satisfy automatically the geometric constraints of the boundary, as well as any boundary conditions known a priori, such as surface temperature. In this way, a proper choice of basis functions can greatly reduce the number of measurements required for an adequate representation of the velocity. The reconstructed velocity distribution is then converted directly into a temperature distribution using the known velocity-temperature relationship for steel.

To test the reconstruction theory, time-of-flight measurements were simulated by computing the transit times of pulses along particular paths through an assumed temperature distribution in a cylinder, where the temperature profile was obtained from heat flow theory. The simulated time-of-flight data were then used as input to the tomography algorithm and a velocity reconstruction generated. The velocity distribution was in turn converted to temperature, and finally compared to the assumed temperature distribution. In the absence of measurement errors, the simulated reconstructions closely matched the original temperature profile when only three or four transit-time measurements were used.

Preliminary reconstructions were also obtained using actual time-of-flight measurements through a hot six-inch steel cylinder. When the number of terms in the basis expansion of the sound velocity is kept small, the reconstruction was found to compare to within 10 percent of the measured temperature distribution (Fig. 1). When more terms are included, which are responsible for higher

spatial resolution, the reconstruction process becomes increasingly sensitive to measurement errors, and as a consequence, the reconstructed temperature was in poorer agreement with the measured temperature profile. The effects of measurement errors and their relationship to spatial resolution and accuracy in the reconstructed temperature distribution are now being investigated.

An investigation of transducer technology suitable for ultrasonic detection at high temperatures was undertaken. It was concluded that piezoelectric devices, such as PZT, would be much more sensitive than electromagnetic transducers (EMATs) and many orders of magnitude more sensitive than laser interferometer detectors. A scheme for coupling piezoelectric transducers to surfaces at high temperatures was devised, using a fused silica buffer rod and a glass couplant between the rod and hot surface. This coupling scheme, combined with the use of a 500 kHz ultrasound frequency, allowed very sensitive detection of ultrasonic energy propagating through steel up to 1320°C, the highest temperature obtainable in our furnace.

A first-order mathematical theory of the inverse dimensional resonance problem was also developed. Dimensional resonance represents another approach to reconstructing internal temperature in steel by measuring ultrasonic resonances in slabs of rectangular geometry. In this approach, sound-velocity inhomogeneities arising from spatial temperature variations are reconstructed by exciting the resonance modes in the steel slab and measuring the resultant shifts in the resonance frequencies. When the inhomogeneities are relatively small, the theory shows how the perturbed resonance frequencies can be used to reconstruct the velocity variations within the slab. Again, exploiting the known temperature-velocity dependence, the internal temperature distribution may then be recovered.

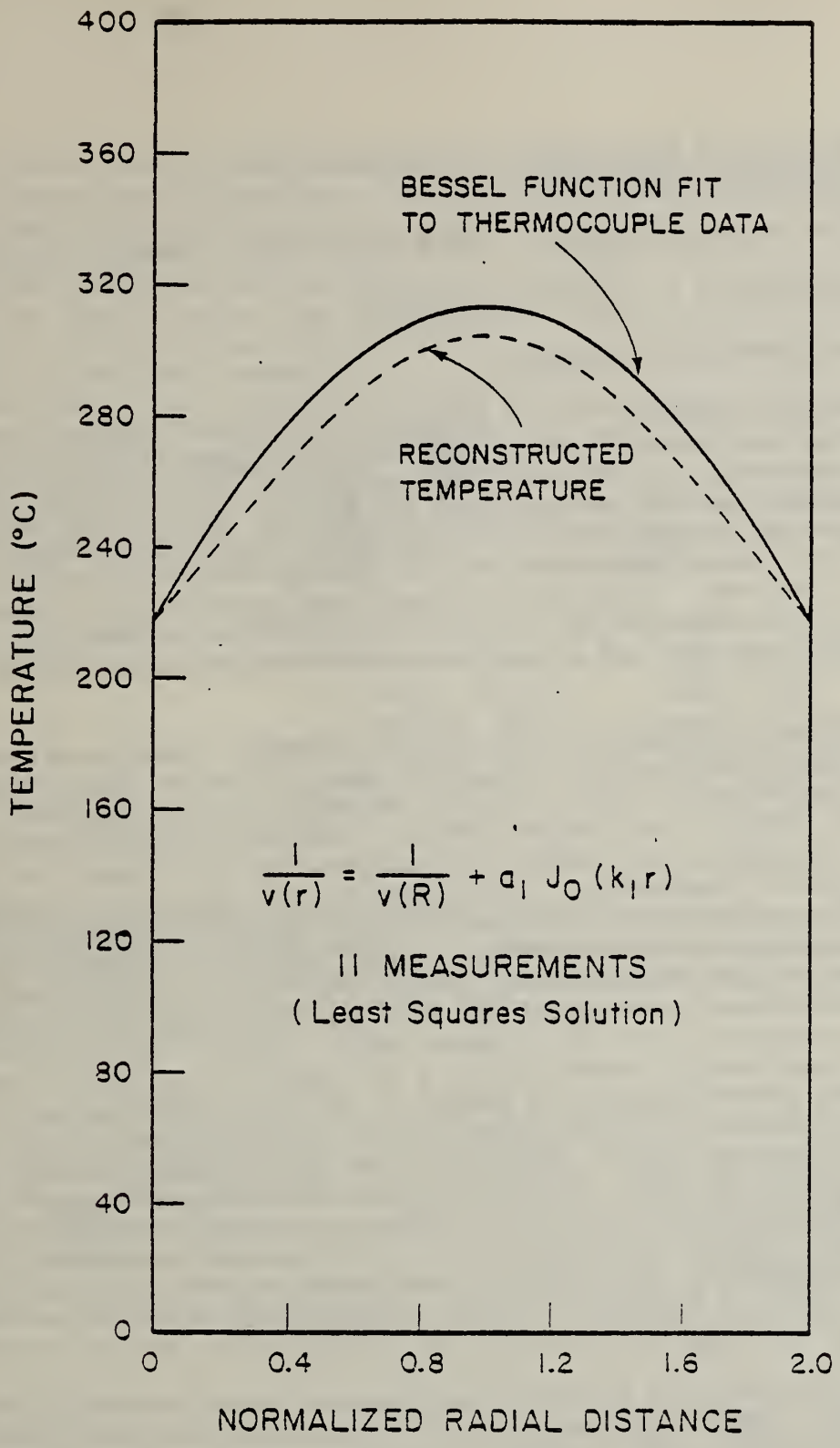

Figure 1 Temperature profiles in hot cylindrical billet. The solid line is a Bessel function fit to the true internal temperature measured with thermocouple probes. The dashed line is a reconstruction of the temperature computed by estimating the parameter a_1 in a least squares sense from 11 time-of-flight measurements. The surface temperature is assumed known.

CURE MONITORING IN POLYMERS AND COMPOSITES VIA NONDESTRUCTIVE TECHNIQUES

Donald L. Hunston, Bruno M. Fanconi, and Fred I. Mopsik

Polymer Science and Standards Division

Center for Materials Science

The rapidly expanding use of polymers in structural applications has generated much interest in the new field of polymer processing with chemically reacting (i.e. polymerizing) materials. The commercial importance of these polymer systems combined with the general lack of knowledge in this area has produced an urgent need to investigate the basic science of processing with reacting polymers and to develop nondestructive test methods to explore this area. These needs include both laboratory test techniques which permit the study and optimization of the processing reactions and on-line techniques that can be used to monitor and adjust processing variables.

A fundamental approach to this problem, however, requires a variety of measurement techniques since important events occur on the molecular level, the morphological level, and the mechanical properties level. The approach taken in the program currently underway in the Polymers Division is addressing this difficulty by combining techniques from three different areas: spectroscopy, dielectrometry, and mechanical characterization. The spectroscopic technique (Fourier transform infrared measurements) have the potential to examine curing (polymerization) reactions at a molecular level indicating what the reactions are and how rapidly they proceed. The mechanical characterization technique involves the ultrasonic test method developed previously in the NDE program, refs. 1 and 2. In this method an ultrasonic shear wave is propagated in a thin quartz strip that is coated with the sample to be tested. By measuring the wave in the quartz, information related to the mechanical properties of the coating can be obtained. Consequently, this method provides data directly relevant to processing and performance. The dielectric experiments, which utilize the unique NBS time domain dielectric spectrometer, provide information on mobilities at a morphological level, i.e., a size scale intermediate to the other two methods. By combining these three techniques, it will be possible to obtain a much more complete understanding of the transformations that occur during reactive processing of polymers.

During the past year a feasibility study was conducted to determine if all three of these techniques could be used to monitor cure in similar chemically reacting polymer systems. These tests confirmed that such measurements could be made and thus demonstrated that an in-depth development of each technique as a cure monitoring tool would be advantageous. In

previous years the ultrasonic technique has been shown to be a valuable cure monitoring device which has a unique capability to nondestructively follow changes that occurred during the curing of polymers in thin films or restricted layers. In addition to this the technique has the potential for quantitatively determining mechanical properties. Over the past year this latter capability has been implemented. Since no other technique can provide equivalent measurements the only way to validate this capability for highly viscoelastic materials is to compare the results from the ultrasonics test with extrapolated values obtained by applying time-temperature superposition to low frequency data from torsional oscillation experiments on a thermorheologically simple material. Such tests were conducted using a polyvinyl chloride plastisol and the results are shown in Table I. In light of the large extrapolations involved (5 decades), the agreement between the two sets of results is excellent.

Table I: Validation of Ultrasonic Technique

Method	Shear Storage Modulus (MPa)	Shear Loss Modulus (MPa)
Ultrasonic Tests	0.70	1.8
Estimate from Superposition	0.78	2.1

The successful development of this technique has led to a desire by a number of other groups to implement a similar device for addressing their particular problems. For example, NBS is currently constructing such a device for the Bureau of Engraving and Printing so they can use it to study drying of printing inks, ref. 2.

Future work in this program will focus on the development of the time domain dielectric spectrometer as a cure monitoring device. This instrument, which was developed at NBS, has the capability to measure the dielectric constant of a material over a very wide range of times (or frequencies) in a single experiment. Preliminary studies on the latter phases of cure have shown that this capability makes it possible to follow changes in molecular mobilities that would otherwise be very difficult to detect because they appear only in the very low frequency range. This is illustrated in Figure 1 which shows the complex dielectric constant (real part minus a background level of 100 pF, $\Delta C'$, and the imaginary part, C'') for an epoxy-derivative solid film before and after a post cure heat treatment. This type of information is particularly useful since the final degree of cure is often a critical parameter in processing. As a result further development of this technique is highly desirable and will be a major goal next year.

REFERENCES

1. D. L. Hunston, "Cure Monitoring of Thermosetting Polymers by an Ultrasonic Technique, Review of Progress in Quantitative Nondestructive Evaluation, Vol. 2, D. O. Thompson, ed., pp. 1711-1730 (Plenum Pub. Corp., 1983).

2. D. L. Hunston, "Relationship between Mechanical Properties and Performance of Inks as the Basis for Quality Control Techniques", NBSIR-83-2691 (April, 1983).

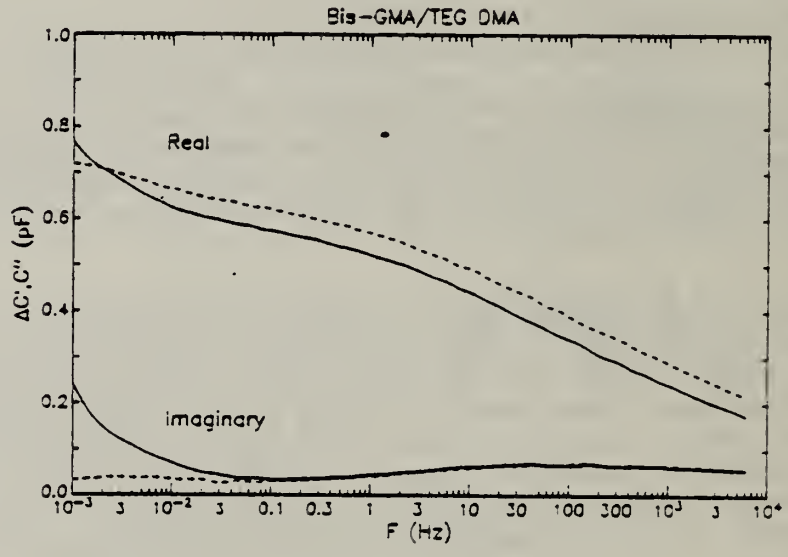

Figure 1. The real part of the complex dielectric constant minus a background level, $\Delta C'$, and the imaginary part, C", as a function of frequency for an epoxy-derivative solid film before, ———, and after, - - - -, a post cure thermal treatment.

ULTRASONIC APPLICATIONS TO NDT AND MATERIALS EVALUATION

G. V. Blessing

Mechanical Production Metrology Division

Center for Manufacturing Engineering

Miscellaneous small projects were performed in response to other agency requests and committee round-robin efforts.

1. Ni Alloy Bond Defects: A diffusion-bonded nickel alloy sample possessing unbond artifacts was evaluated using ultrasonic C-scan and continuous amplitude scan techniques for Pratt & Whitney, West Palm Beach, FL.

2. Residual Stress Round-Robin: The elastic anisotropy of both stainless steel and carbon steel samples were evaluated as part of a round-robin effort for residual stress standard development sponsored by the Society for Experimental Stress Analysis (SESA).

3. Fused Quartz Sound Speed: The transit times of shear and longitudinal waves were precisely measured in a fused quartz disk. This disk is being evaluated as a candidate for an ASTM round robin effort for making sound speed measurements.

4. Metal Matrix Composite Scans: Several sample sheets of graphite-reinforced metal matrix composites, developed by the Army, were ultrasonically scanned for their scattering amplitude profiles.

5. Carbon/Carbon Turbine Composite: A variable thickness carbon/carbon composite sample was ultrasonically scanned for possible delaminations. The turbine material was developed by the Vought Corp., Texas, for a DARPA-sponsored project.

6. DOT Steel Support Weldments: The welded regions of failed support rods were ultrasonically evaluated using a surface wave technique. These specimens were taken from the scene of the highway ramp support failure which occurred in Chicago, 1982.

ULTRASONIC IMAGING FOR MEDICAL APPLICATIONS

Melvin Linzer and Stephen J. Norton

Metallurgy Division

Center for Materials Science

Work for this program in the past year consisted of theoretical analysis and development of imaging techniques, organization of the "Eighth International Symposium on Ultrasonic Imaging and Tissue Characterization" and editing of the journal Ultrasonic Imaging.

In the imaging area, a proof of convergence of the iterative reconstruction-from-projections algorithm was derived (ref. 1). This proof, for the first time, separates rates of convergence for different spatial frequency components in the image. An inverse-scattering approach for generating separate high-resolution, quantitative images of the variations in density and compressibility in tissue was also developed (ref. 2).

The Eighth International Ultrasonic Symposium attracted 225 attendees, one of our largest audiences to date. Seventy-seven papers were presented, covering a wide variety of ultrasonic imaging and characterization techniques. The journal Ultrasonic Imaging has become recognized as the leading journal concerned with ultrasonic techniques. Subscribers now exceed 500 for the first time. A large increase in the number of submitted papers occurred last year and we are planning to increase the number of pages by 25 percent in 1984. The subject most widely discussed in the journal in 1983 was the development of techniques for measuring attenuation in reflection.

In the accounts that follow, the theoretical work on imaging is reviewed:

1. Iterative Reconstruction Techniques: Convergence as a Function of Spatial Frequency

   The convergence of two well-known iterative reconstruction-from-projections algorithms, ART (algebraic reconstruction technique) and SIRT (simultaneous iterative reconstruction technique) was analyzed. The analysis reveals how individual spatial frequency components in the image converge at different rates to their respective object components. The functional form of this convergence is also revealed. The analysis proceeds by considering the continuous versions of the ART and SIRT algorithms in the limit of continuous sampling along the projections and in angle. From the continuous versions, explicit convergence formulas are derived which show that the continuous ART and SIRT algorithms indeed converge to the correct solutions, that the convergence is geometric, and how the rate of convergence varies with spatial frequency. The rate of convergence as a function of spatial frequency could well represent information of practical importance in establishing stopping criteria

for these iterative techniques (ART and SIRT), particularly when prior information about the inherent bandwidth of the projection data is known. Once these limits are given, the number of iterations needed to achieve a given amount of error reduction for a particular spatial frequency could, in principle, be estimated in advance.

2. A Method for Imaging Separately Density and Compressibility Variations in Tissue

A method was developed for reconstructing separate images of the variations in density and compressibility in the same tissue sample. The images can be obtained from near-field scattering measurements using only two long, rectangular transducer elements. As in diffraction tomography, 180° access around the region of interest is required. This approach differs from conventional diffraction tomography, however, in that no transducer arrays are required and broadband illumination is used. A flat transducer, assumed long relative to the extent of the object, is used as a source of broadband, plane-wave illumination, and as a receiver of the backscattered sound. A second transducer, oriented at a different angle with respect to the first, is used as a receiver only. The two transducers are rotated together 180° around the object directly, backscattering measurements are performed during the rotation. This arrangement can be shown to sample the plane-wave spectrum of the object directly and provides sufficient information to reconstruct independent images of the variations in both the density and compressibility of the scattering medium. Image resolution is limited by the bandwidth of the illuminating sound.

REFERENCES

1. S. J. Norton, "Iterative Reconstruction Techniques: Convergence as a Function of Spatial Frequency", in preparation.

2. S. J. Norton, "A Method for Imaging Separately Density and Compressibility Variations in Tissue", Ultrasonic Imaging 5, No. 3, p. 240-252, 1983.

ACOUSTIC EMISSION THEORY DEVELOPMENT

J. A. Simmons and H. N. G. Wadley

Metallurgy Division

Center for Materials Science

Theoretical efforts on acoustic emission during the past year have concentrated on two main areas: 1) completion of the deconvolution program required for tranducer calibration and underlying multichannel acoustic emission inversion. The results of this research have been submitted to the IEEE Journal on Acoustics, Speech and Signal Processing (ref. 1).

A new concept of causal boundary roots was developed using the roots of a slightly modified Z-transform of a time series (called the Y transform) obtained from new programs which can solve polynomials in excess of degree 800. If a causal time series has non-zero elements a_1, a_2, a_3, ... one considers the roots of the polynomials

$$\sum_{n=1}^{N} a_n y^n = 0$$

As N becomes large (typically in excess of 100) the roots with absolute value less than 1 of this series become fixed and can serve as a recognizable signature for the initial or transient part of the time series.

The roots of the Y transform also provide a powerful new technique for deconvolution in the presence of noise. The most advanced methods hitherto available for treating deconvolution treat it as an ill-conditioned but well-posed problem in linear algebra. This approach was applied here previously using a new and efficient singular valued decomposition (SVD) technique. However, that technique was not particularly robust and it was often difficult to guess which candidate estimate to the deconvolved inverse was best. By modifying the formulation of the deconvolution problem to give a well-conditioned but ill-posed problem, it has been possible to develop a completely new method based on Y transform roots in which "a priori" information can be used to produce comparable noise reduction to that obtained by SVD techniques while providing more accurate frequency information about the deconvolved inverse.

However, this method, too, suffers from lack of robustness. By combining the SVD and the Y transform root methods in a cross-cutting algorithm in which each method is used to refine the errors of the other, a new level of robustness and accuracy was achieved for deconvolution which finally appears to be powerful enough to deal with typical transducer calibration and multichannel AE inversion problems. An example applied to a model deconvolution problem is shown in the accompanying figures. The transducer response taken from an empirical waveform filtered at 2.5 MHz upper frequencies is shown in Figure 1. The model transducer response is shown in Figure 2 and the composite data

with added noise is shown in Figure 3. No conventional methods we have found can be applied to even approximately deconvolve the curve in Figure 1 from that in Figure 3 to obtain the curve in Figure 2. The estimate from the cross-cutting algorithm overlaid with the correct answer is shown in time representation in Figure 4 and in frequency representation in Figure 5. As can be seen in Figure 5, the recovery of frequency information up to 1 MHz is almost exact. Only above 2.5 MHz is there essentially no information about the answer, as would be expected due to the low frequency content of the curve in Figure 1.

The second area of effort in the theory of AE has centered on detailed forward modelling of the thermoelastic emission from laser heating with diffusion effects and comparison with acoustic emission to be expected from vertical cracking at and near the plate surface (ref. 2).

Because of the large flat surfaces of the plate, the dynamic Green's functions for motion due to a monopole force function are characterized by Heaviside and logarithmic jumps occurring at discrete arrival times associated to multiple wave reflections. The Green's functions associated to the force dipoles characteristic of thermoelastic and crack sources then have delta function components and cannot be accurately modeled using ordinary moment expansions without proper filtering either in space or time. However, because of the presence of these discrete components for the Green's function in a plate, it becomes possible to resolve certain dynamic near-surface aspects of material processes. For instance, Figure 6 shows the predicted AE from a half-penny crack growing in a self-similar mode at 1 mm/μs for one microsecond in a 22.25 cm plate of stainless steel. The first moment corrections associated to the particular crack growth model clearly differentiate it from the model-insensitive zeroth moment curve. Similar calculations have been carried out for predicting the AE to be expected from the heating due to thermal expansion from a laser pulse. Figure 7 shows the predicted AE versus an experimentally measured AE waveform on 37.46 mm thick 2024-T6 aluminum plate. The effects of thermal diffusion are too slow, even in aluminum, to be detected in the AE signal. Thus AE from a laser pulse tends to be model independent, although there are some small discrepancies which are still being investigated.

REFERENCES

1. J. A. Simmons, "New Results for Deconvolution and Signature Analysis of One-Sided Time Series", in press.

2. H. N. G. Wadley, J. A. Simmons and C. Turner, "Predictive Modelling of Quantitative Acoustic Emission Waveforms", Review of Progress in Quantitative NDE, Plenum Press, 1983.

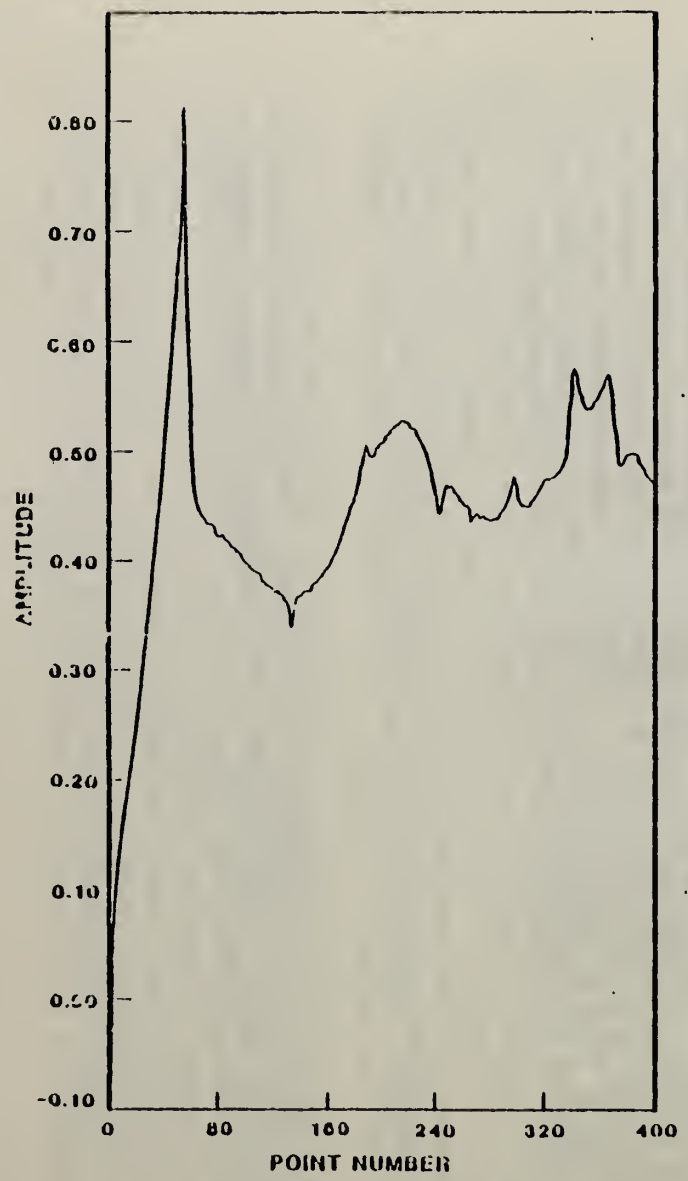

Figure 1. Reference transducer response for model deconvolution problem.

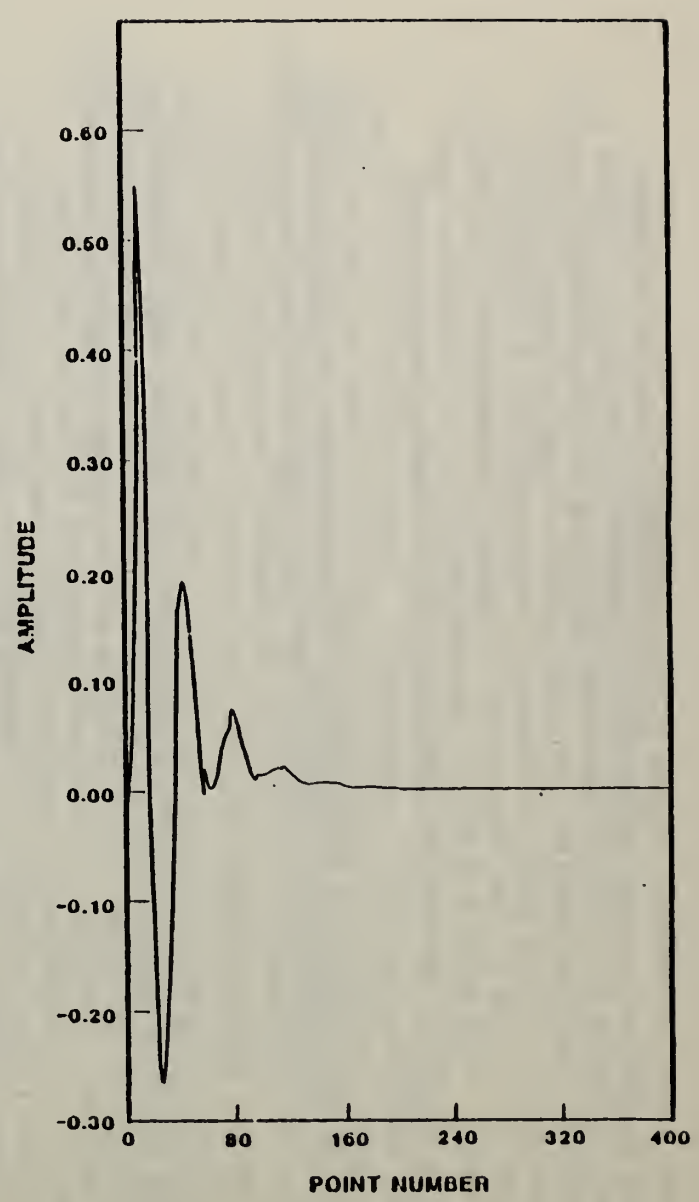

Figure 2. "Unknown" transducer response for model deconvolution problem.

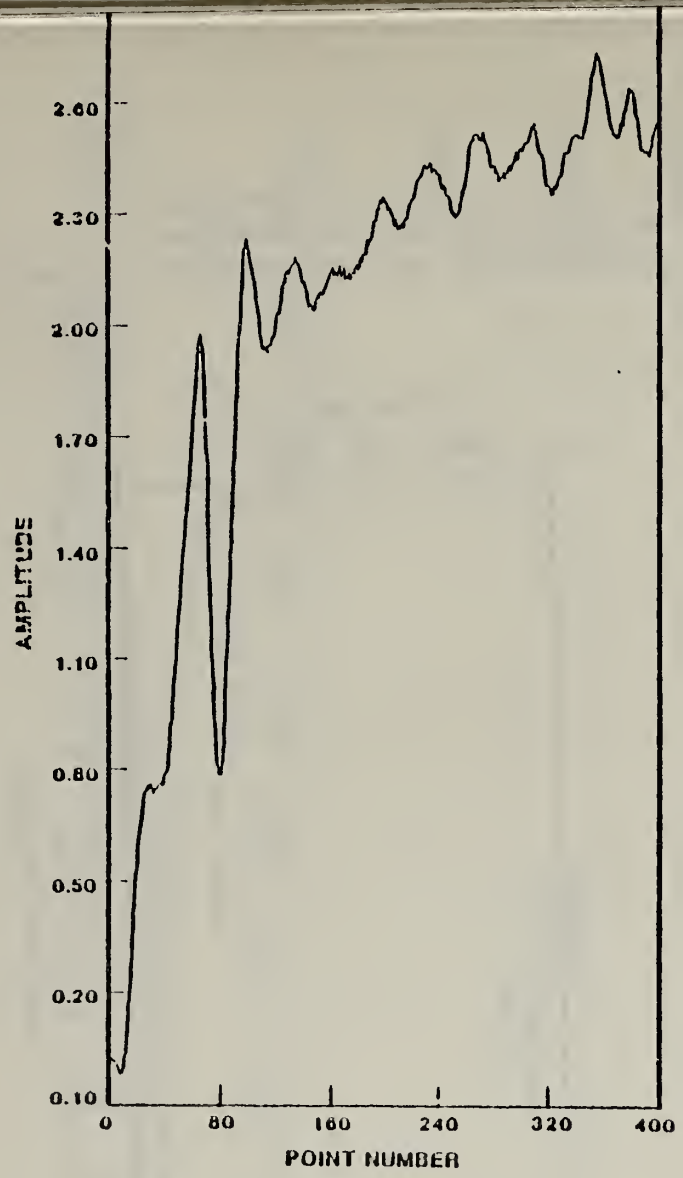

Figure 3. Output data with noise for model deconvolution problem.

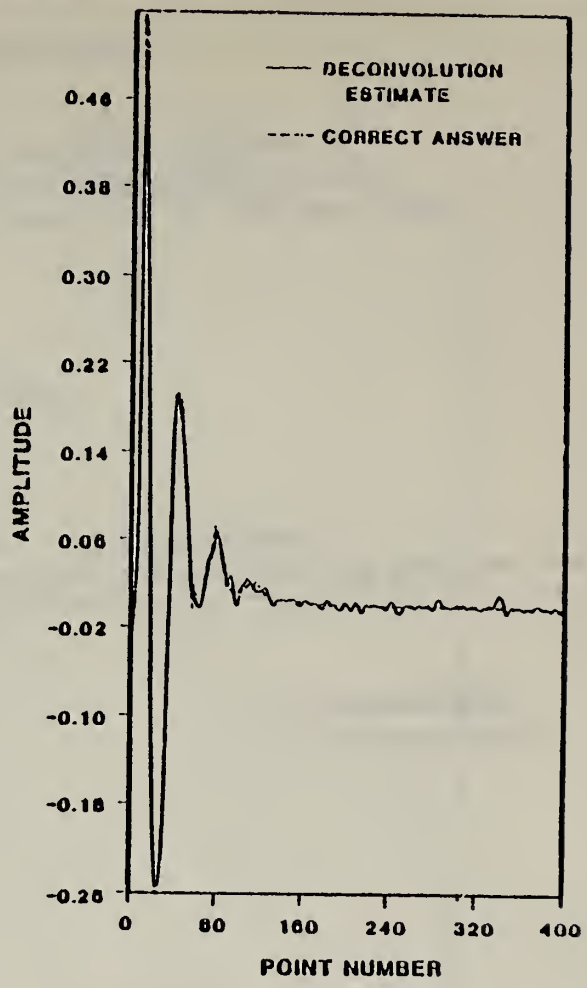

Figure 4. Deconvolution estimate for "unknown" transducer response as produced from cross-cut algorithm.

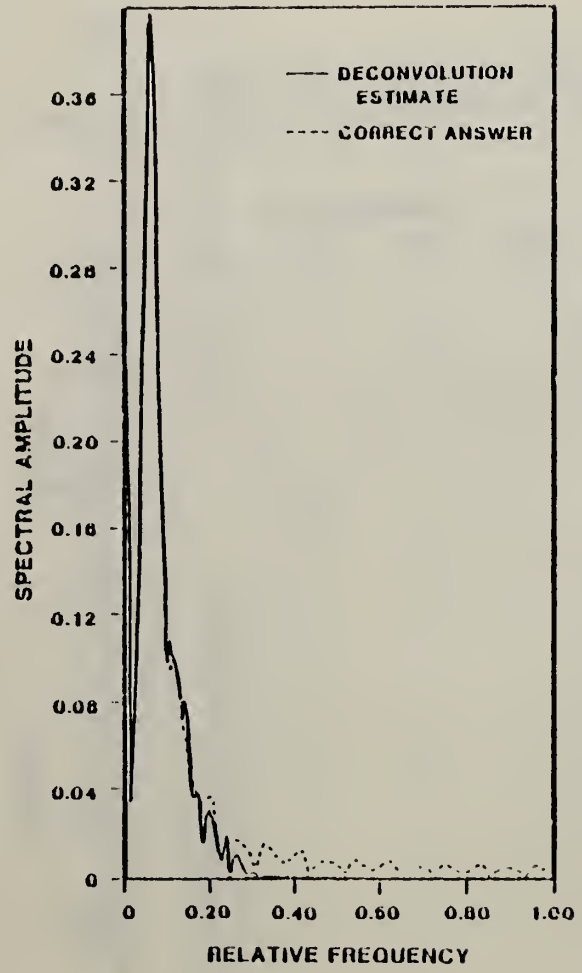

Figure 5. Spectral plot for deconvolution estimate in model deconvolution problems.

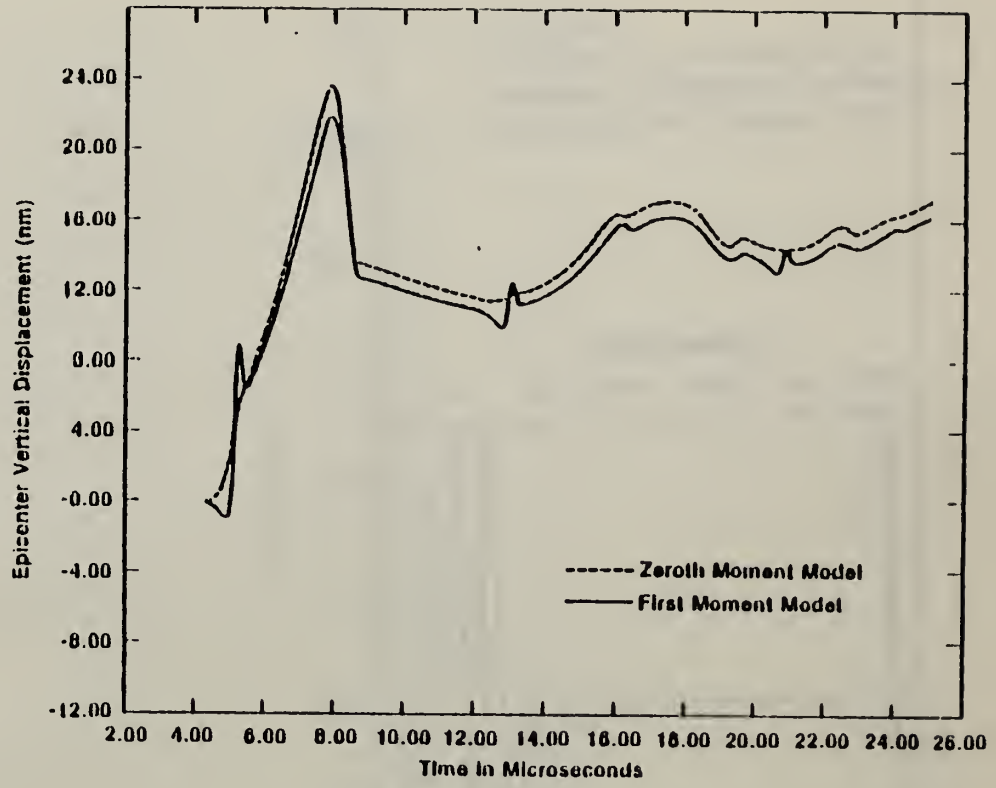

Figure 6. Predicted AE from half-penny crack showing effects of moment corrections.

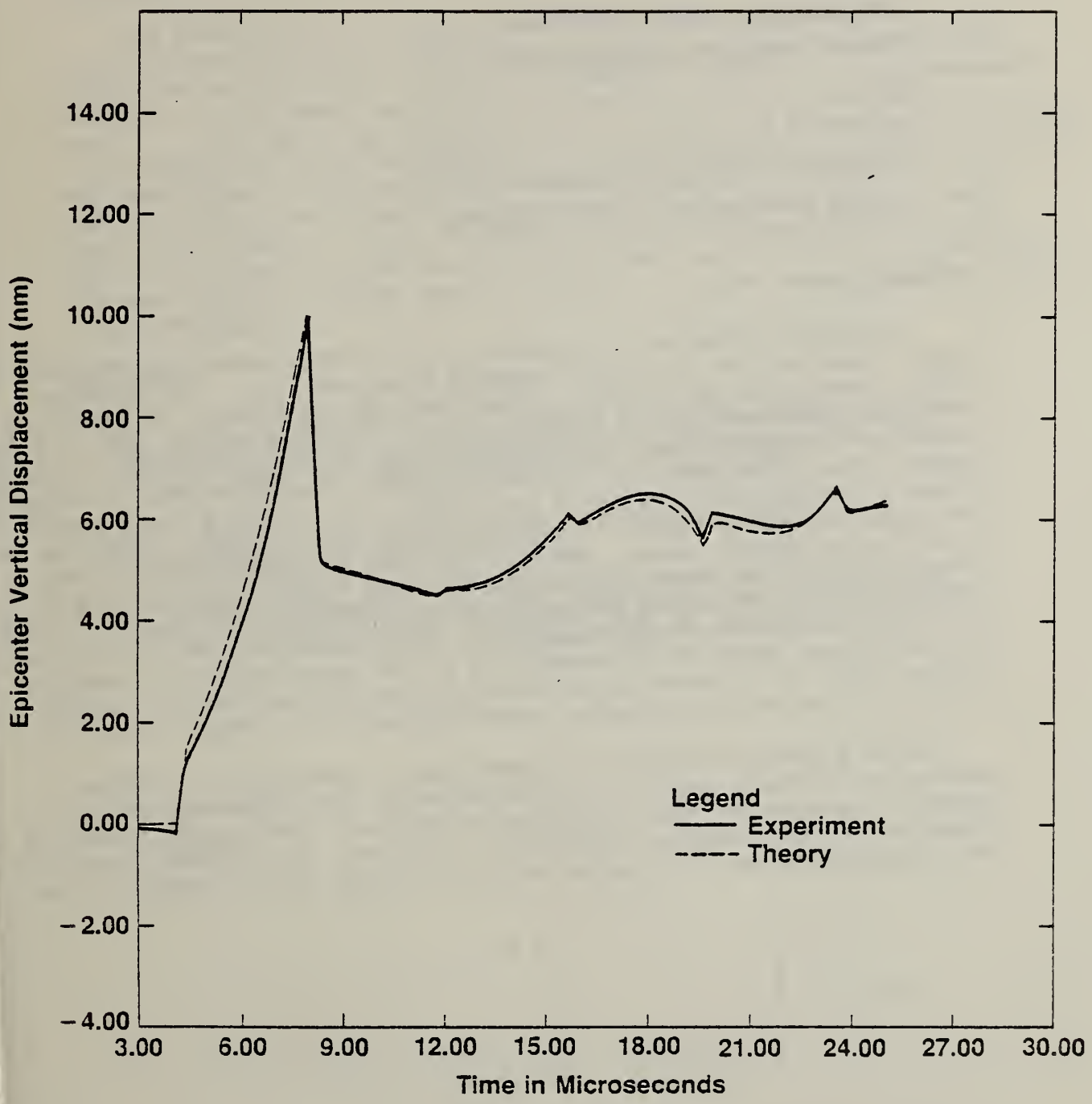

Figure 7 Comparison of theory and experiment for laser generated AE in 2024-T6 aluminum.

POINT SOURCE TIME DEPENDENCE IN THE DETERMINATION OF ACOUSTIC EMISSION GREEN'S FUNCTIONS

Alfred S. Carasso
Mathematical Analysis Division
Center for Applied Mathematics
and
Nelson N. Hsu
Mechanical Production Metrology Division
Center for Manufacturing Engineering

INTRODUCTION

In acoustic emission (AE) testing, it is often necessary to determine the Green's function for an elastic structure experimentally. This involves using a known point source with a prescribed time dependence, and detecting the signal generated by this source (ref. 1). In the idealized case of a Dirac δ-function time dependence, the detected signal is proportional to the exact dynamic Green's function. If a general arbitrary time dependence is prescribed, however, the detected signal is a convolution of the Green's function with the source time dependence. It should be noted that AE Green's functions are typically <u>not</u> smooth; rather, they exhibit sharp discontinuities in their time derivative, and these discontinuities carry information regarding the times of arrival of various components of the solution (see Figure 1). As a rule, the convolution process smooths out these sharp features, so that the detected signal bears little resemblance to the structure Green's function. In that case, an ill-posed deconvolution problem must be carefully solved in order to arrive at an accurate reconstruction of the Green's function.

While a Dirac δ-function time dependence is impossible to realize physically, a smooth (infinitely differentiable) time dependence of short duration, concentrated near $t = 0$, can be realized. Such a function may be viewed as an approximation to the Dirac δ-function. An important example is the inverse Gaussian distribution (ref. 2), defined for all values of t by

$$k(\sigma,t) = \begin{cases} 0 & \text{if } t < 0, \\ \dfrac{\sigma}{2\sqrt{\pi}\, t^{3}} \exp\left(-\dfrac{\sigma^{2}}{4t}\right), & t > 0, \end{cases}$$

where σ is a fixed positive constant. See Figure 2. The size of σ controls the "duration" of the time function $k(\sigma,t)$, and convolution with $k(\sigma,t)$ smooths out sharp features at an increasing rate, the larger σ is chosen. Compare Figures 1 and 3.

DECONVOLUTION

The above kernel is intimately related to heat conduction theory and deconvolution with such a kernel can be reduced to solving an appropriate initial value problem for a partial differential equation in two independent variables. This theory was previously developed by one of the authors (ref. 3). Applied to the acoustic emission problem, it offers the possibility of a powerful and reliable algorithm for reconstructing sharp features in the structure Green's function. Highly successful numerical simulations were carried out on some typical AE Green's functions in recent computer-based feasibility studies. Figure 4 shows the result of deconvolution of the function in Figure 3 using the above algorithm; this should be compared with the exact Green's function shown in Figure 1. Further work in this direction is contemplated.

REFERENCES

1. N. N. Hsu, "A Mechanical AE Simulator for System Calibration and Wave Form Analysis" 16th Meeting of the U. S. Acoustic Emission Working Group, Williamsburg, Virginia, October 1976.

2. M. T. Wasan, "On an Inverse Gaussian Process", Skandinavisk Aktuerietidskrift, pp. 69-96, 1968.

3. A. Carasso, "Determining Surface Temperatures from Interior Observations", SIAM J. Applied Mathematics 42, pp. 558-574 (1982).

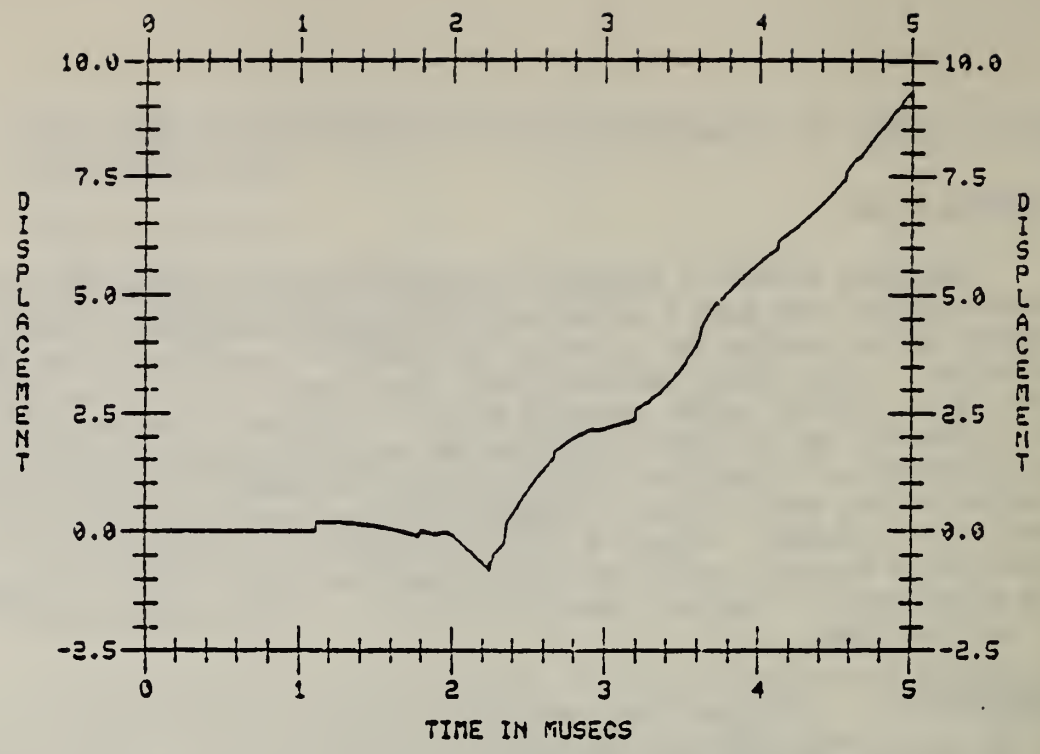

Figure 1. Exact dynamic Green's function for a structure.

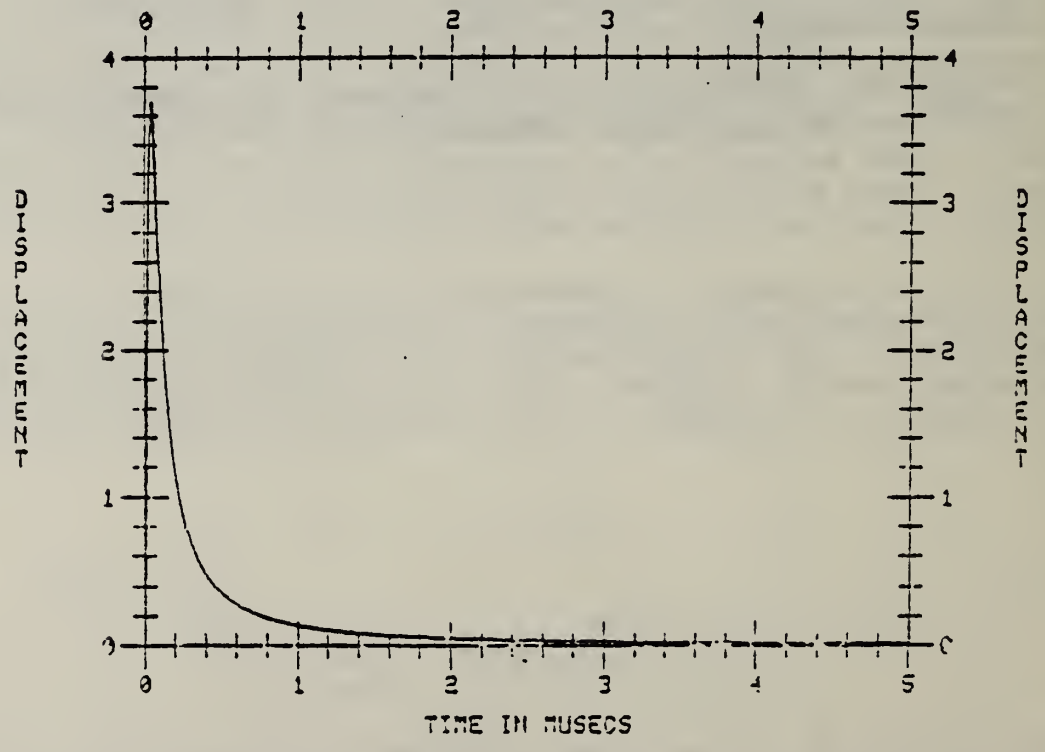

Figure 2. Inverse Gaussian time dependence with σ = 0.5.

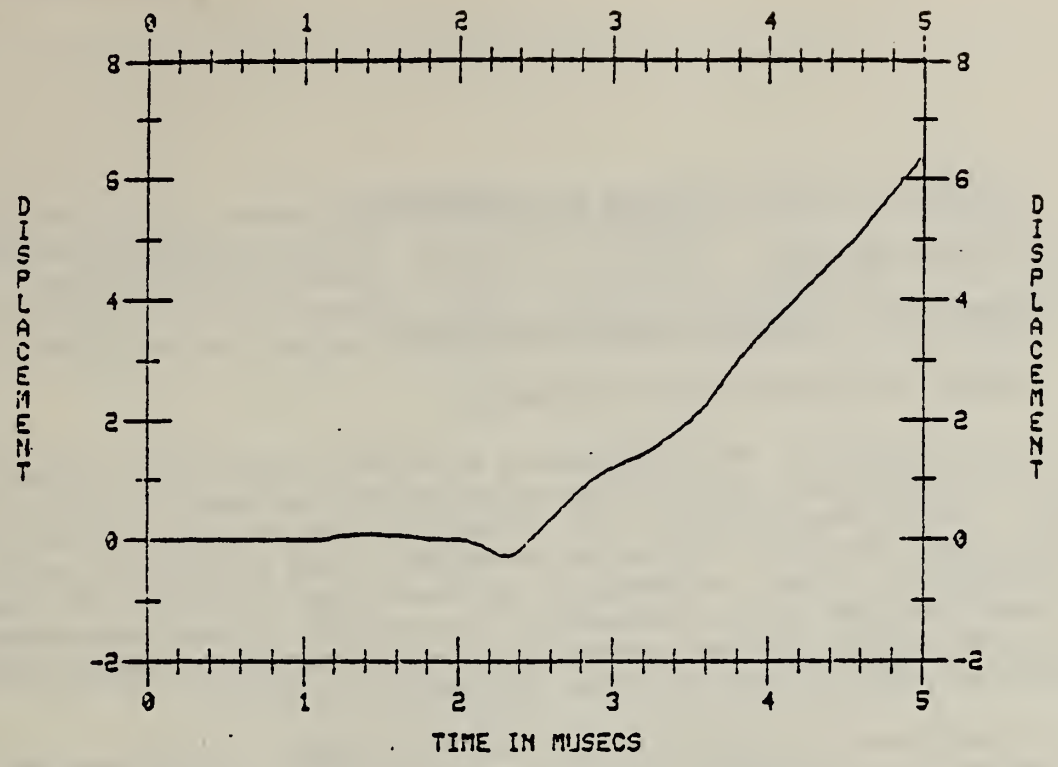

Figure 3. Convolution of Figures 1 and 2. Simulated detected Green's function with σ = 0.5.

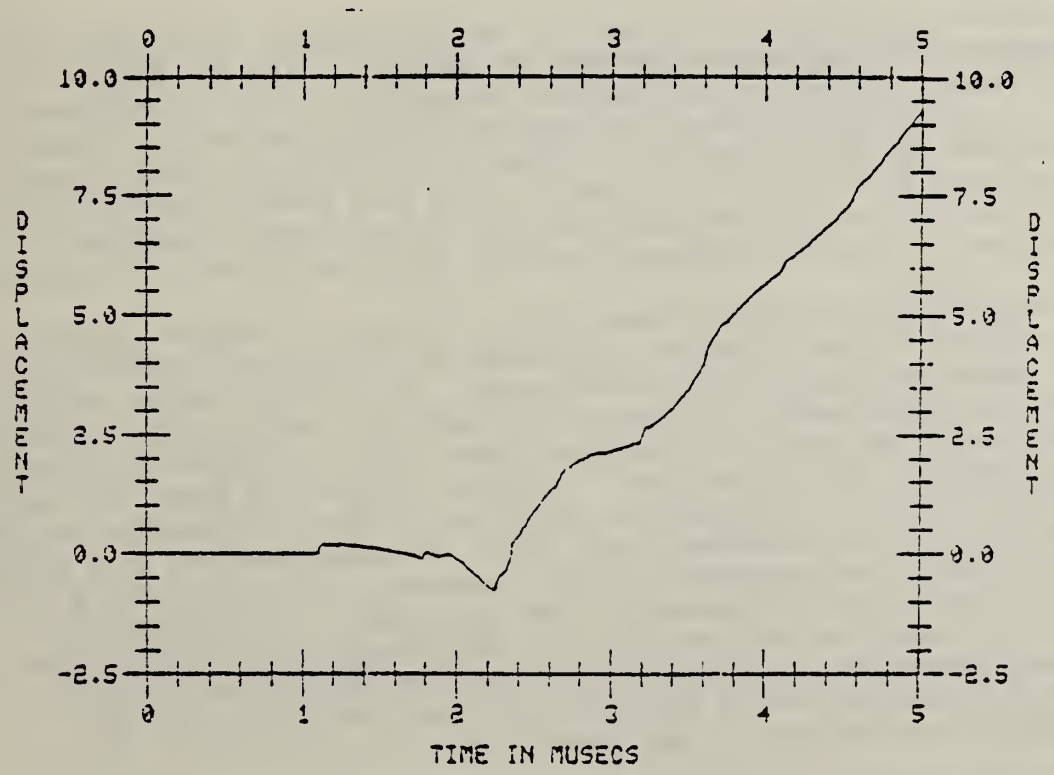

Figure 4. Deconvolution of Figure 3 using heat conduction theory.

CALIBRATION ACTIVITIES FOR AE TRANSDUCERS

F. Breckenridge

Mechanical Production Metrology Division

Center for Manufacturing Engineering

In January 1980, we implemented a calibration service for acoustic emission transducers using surface pulses on the surface of a 2100-kg steel block. A brief description of the calibration technique appears in the NDE annual report for 1982. Since the inception of the calibration service, 352 calibrations have been performed on the steel block facility. Of these, 97 were performed for paying customers of the service, 73 were experiments having to do with the calibration system, 155 were calibrations of experimental transducers, and 27 were for other laboratories at NBS.

As mentioned in the NDE annual report for 1982, a comparison was carried out between the reciprocity calibration implemented at the Nippon Steel Corporation in Japan and the NBS surface-pulse calibration. These results indicated very close agreement between the two methods, and they were presented to the Sixth International Acoustic Emission Symposium in Susono, Japan, November 1982.

Further comparisons have been carried out between the Nippon Steel reciprocity calibrations and the NBS calibrations. The new comparisons used six different transducers, of Japanese manufacture, some of which were of a special type designed to have low response to Rayleigh waves. Comparisons were made between the NBS surface-pulse type of calibration and the Japanese Rayleigh type of reciprocity calibration and also between the NBS through-pulse type of calibration and the Japanese longitudinal type of reciprocity calibration. Figures 1 through 4 show the excellent degree of the agreement.

The previously noted systematic bias between calibrations on the steel block done by surface pulse and those done by through pulse has been eliminated in our recent and more careful experiments. In the more recent through-pulse calibration experiments, the source is a capillary break on the bottom surface of the steel block, and the transducer under test is located on the epicenter of the source on the top surface. The force required to break the capillary is measured and used to calculate the magnitude of the through-pulse waveform at the location of the transducer under test. An experiment was done using the standard capacitive transducer as the transducer under test, and, within the limits of the estimated accuracy of the experiment, no discrepancy was indicated between the surface-pulse and the through-pulse calibrations. The agreement between the through-pulse calibration and the longitudinal reciprocity calibrations is taken as a further indication that the through-pulse calibration is not biased.

Computer software has been written to enable the through-pulse calibration to be used as a customer service.

The design of a secondary calibration system for users to transfer primary calibrations (performed at NBS) to other transducers is in the initial planning stage. Preliminary experiments indicate it should be feasible to use tone burst signals on a steel transfer plate, and to electrically drive an NBS conical transducer to produce the mechanical input for the calibration.

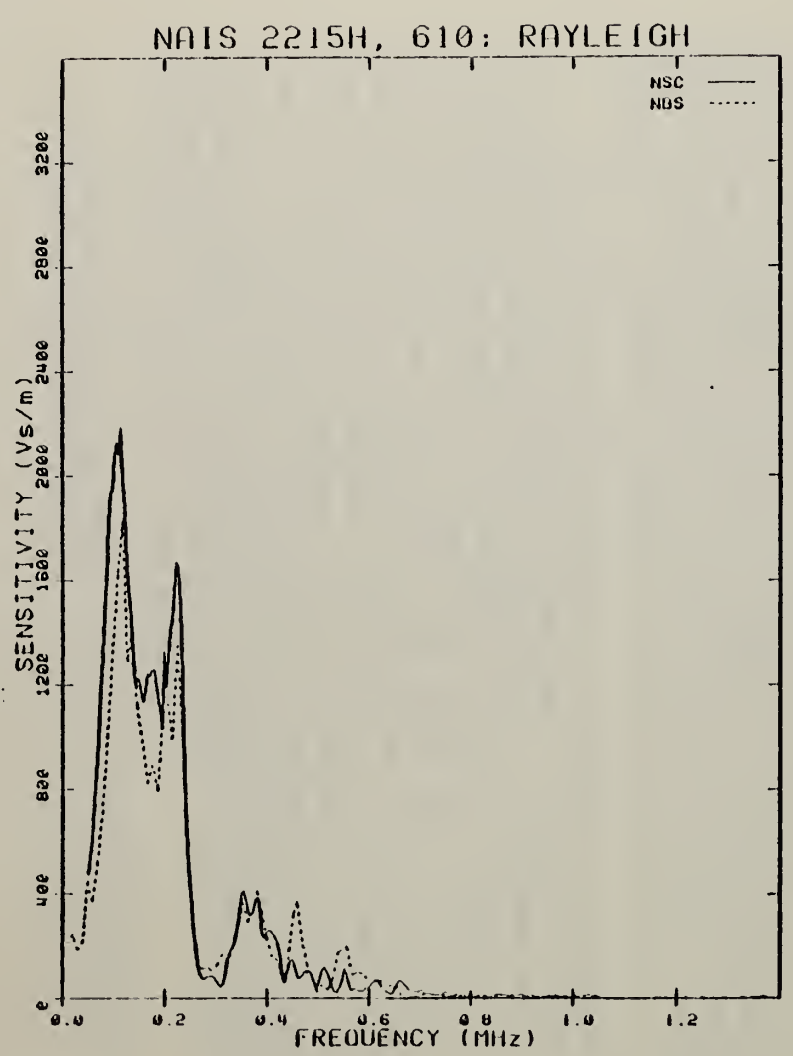

Figure 1. Comparison of the NBS surface-pulse calibration and the Nippon Steel Corporation Rayleigh reciprocity calibration performed on an acoustic emission transducer of Japanese manufacture.

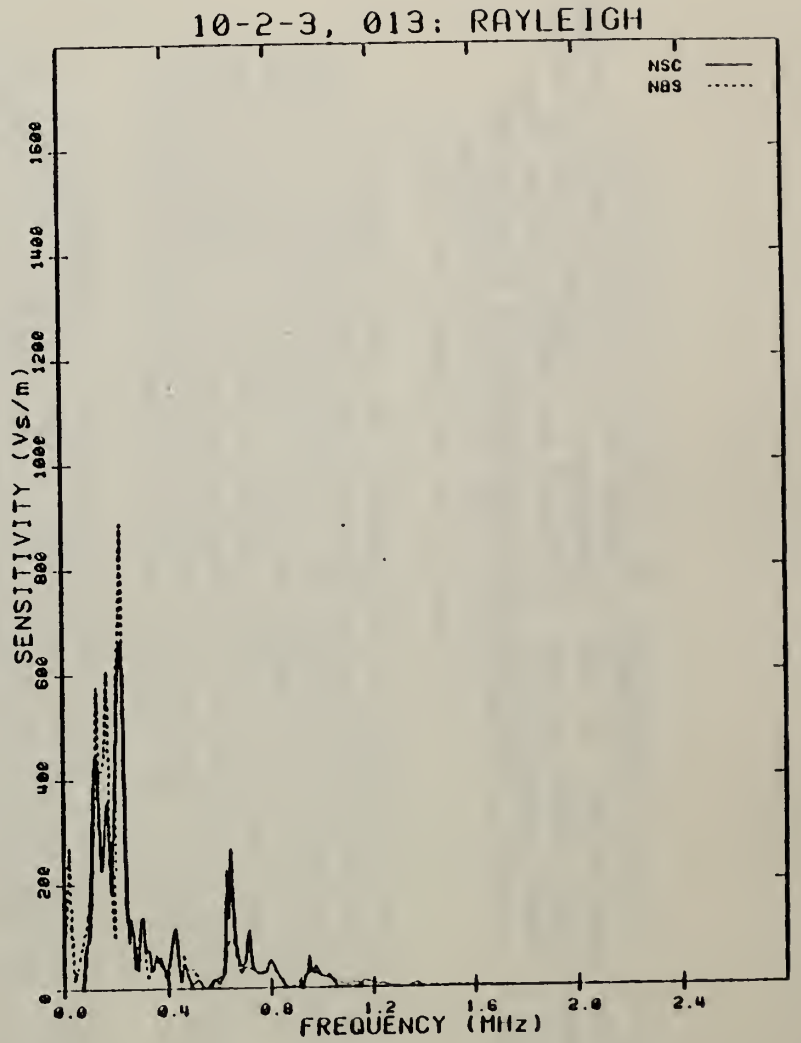

Figure 2. Comparison of the NBS surface-pulse calibration and the NSC Rayleigh reciprocity calibration performed on an experimental transducer designed to have low Rayleigh sensitivity.

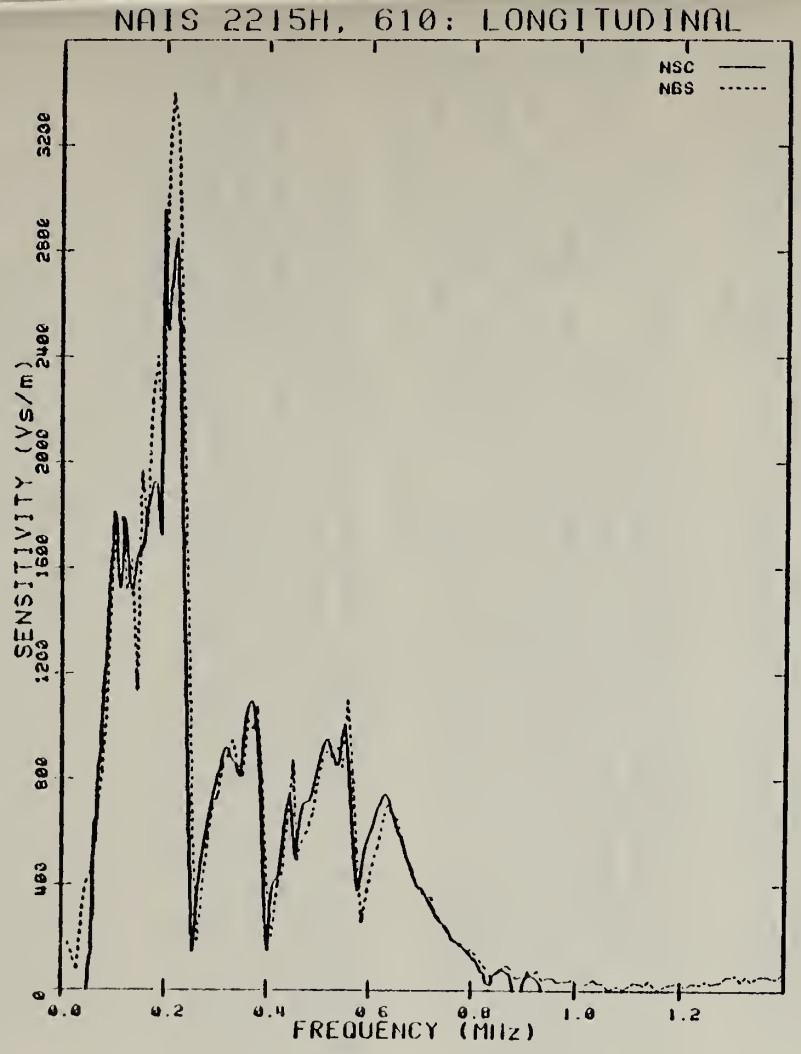

Figure 3. Comparison of the NBS through-pulse calibration and the NSC longitudinal reciprocity calibration performed on the transducer of Fig. 1.

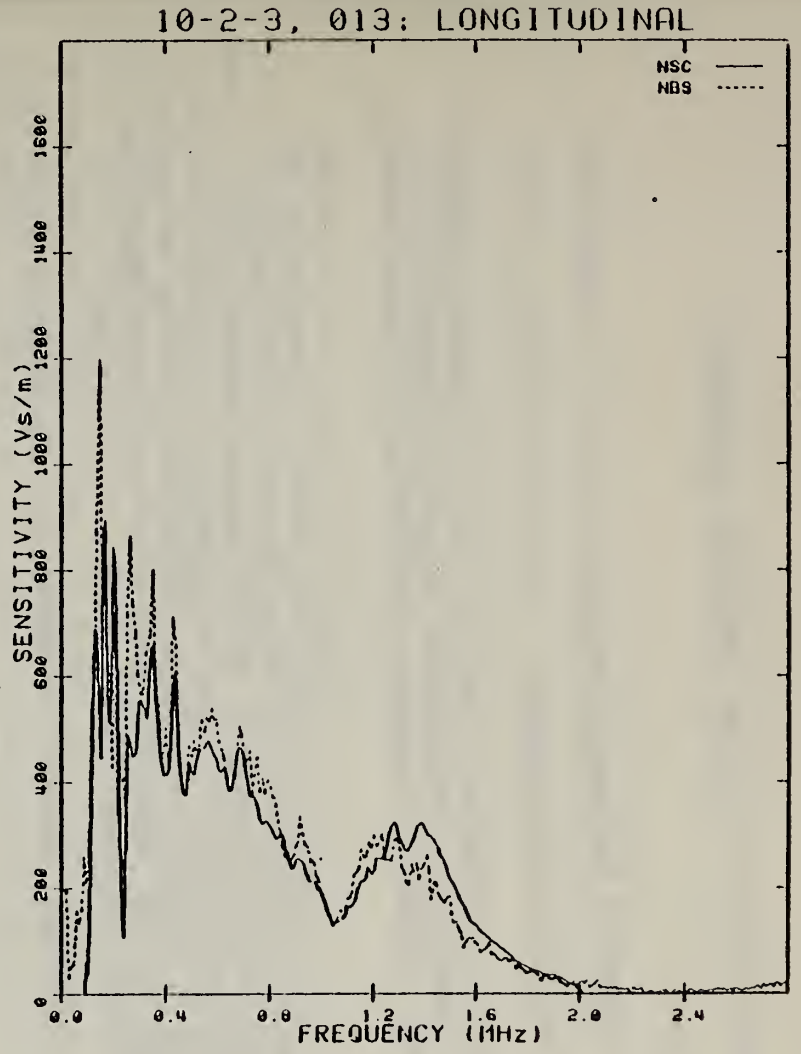

Figure 4. Comparison of the NBS through-pulse calibration and the NSC longitudinal reciprocity calibration performed on the transducer of Fig. 2.

MIL-STANDARD ON ACOUSTIC EMISSION TRANSDUCER CALIBRATION

Donald Eitzen

Mechanical Production Metrology Division

Center for Manufacturing Engineering

The Army Materials and Mechanics Research Center (AMMRC) has asked that NBS assist them in developing a MIL-document describing a method for the primary (and a later document on secondary) calibration of acoustic emission transducers.

In working on this objective, internal and archival literature on the NBS calibration method, the Nippon Steel Corp. method, the NBS Standard Transducer, the NBS Conical Transducer, and Simulated AE Sources were reviewed in preparation for the writing of a procedural document for the primary calibration of acoustic emission transducers. An outline for this procedural document has been developed. Portions of existing documentation nearly suitable for the procedural document have been identified.

Drafting of a "strawman" document has begun and is proceeding well.

IMPROVEMENTS TO THE NBS CONICAL TRANSDUCER FOR ACOUSTIC EMISSION MEASUREMENTS

Thomas M. Proctor

Mechanical Production Metrology Division

Center for Manufacturing Engineering

The original model of the NBS conical transducer, which received an IR-100 Award in 1981, had been shown to measure dynamic normal picometer displacements in the range from tens of kilohertz to above a megahertz thus making it an ideal transducer for acoustic emission measurements. The physical shape of the early model was approximately a cylinder 25 mm high and 37 mm in diameter (see Figure 13 of last year's report). Significant size reduction has been accomplished. The new version (Figure 1) has a backing that is filled with an absorptive mix of copper and tungsten powders and epoxy. The back wave from the active element is effectively dispersed by not only scattering as in the original models but also by absorption. The response of this version is shown in Figure 2.

Because the high fidelity of these devices depends in part on the direct contact of the small face of the active element, the problem of front electrode wear has presented itself. Older versions of this device which had silver plated electrodes have suffered from significant front electrode wear. We have been able to recondition these transducers by replacing the front electrode with evaporated nickel. Nickel not only forms a strong bond to the PZT element but also has much better wear characteristics than the silver electrodes frequently used on PZT elements.

Other protective layers have been developed. A few transducers have been made that have a very thin steel shim (0.17 mm) cemented to the tip of the conical element. Another method which has been successful is the use of very thin (0.17 mm) lead shim between the transducer tip and the working surface. These small shim pads are placed at the point where the transducer is to be placed. They are not cemented to the tip but are used only once and thrown away. A grease couplant is used on both faces of the shim. These protective layers do degrade the flat response characteristic somewhat but their performance is still quite good.

To satisfy requests from other laboratories and from the ASTM Acoustic Emission Subcommittee for a secondary standard, a Standard Reference Material project was undertaken for NBS to offer for sale standard AE transducers for comparison purposes. The transducer design to be used is one commonly known as the polyhedron version which was shown in Figure 14, and its response in Figure 15, of last year's report. First versions of this device will be offered for sale later this year.

The work begun last year on experimental measurements of the displacement of a plate due to stress waves generated by a point force step function has continued. The results of these experiments and a comparison with the plate theory is described in a paper which has been submitted by Breckenridge, Pao and Proctor. These results are for a number of different source/receiver geometries. The agreement is quite good; an example is given in Figure 3.

The NBS conical transducer is sensitive almost exclusively to motion normal to the surface. It produces virtually no signal due to tangential surface motion. However, much of the information that is contained in every acoustic emission event is carried by the tangential component. Thus we have undertaken the development of a transducer sensitive to tangential surface displacements as a complementary element to the vertically sensitive NBS conical transducer. Some progress in the development of a tangential transducer has taken place this year. Figure 4 shows a promising candidate for a high fidelity tangential transducer. Figures 5, 6 and 7 are, respectively, the theoretical horizontal displacement on an infinite half space, the time response of the transducer we are developing and the frequency response of this transducer as compared to the theoretical displacement wave form. The time response indicates some ringing after the main large spike. This shows up in the frequency response as minima at 800 and 1500 kHz. Work continues on improving this new AE transducer.

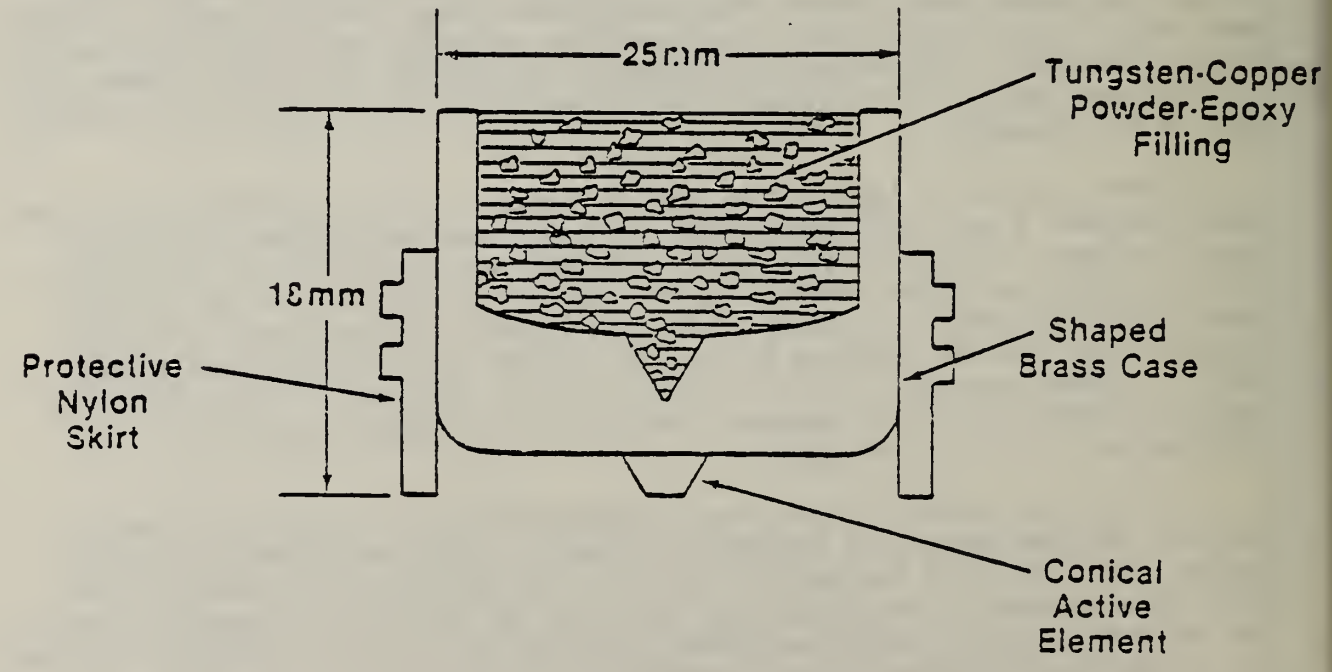

Figure 1. Small version of NBS conical transducer.

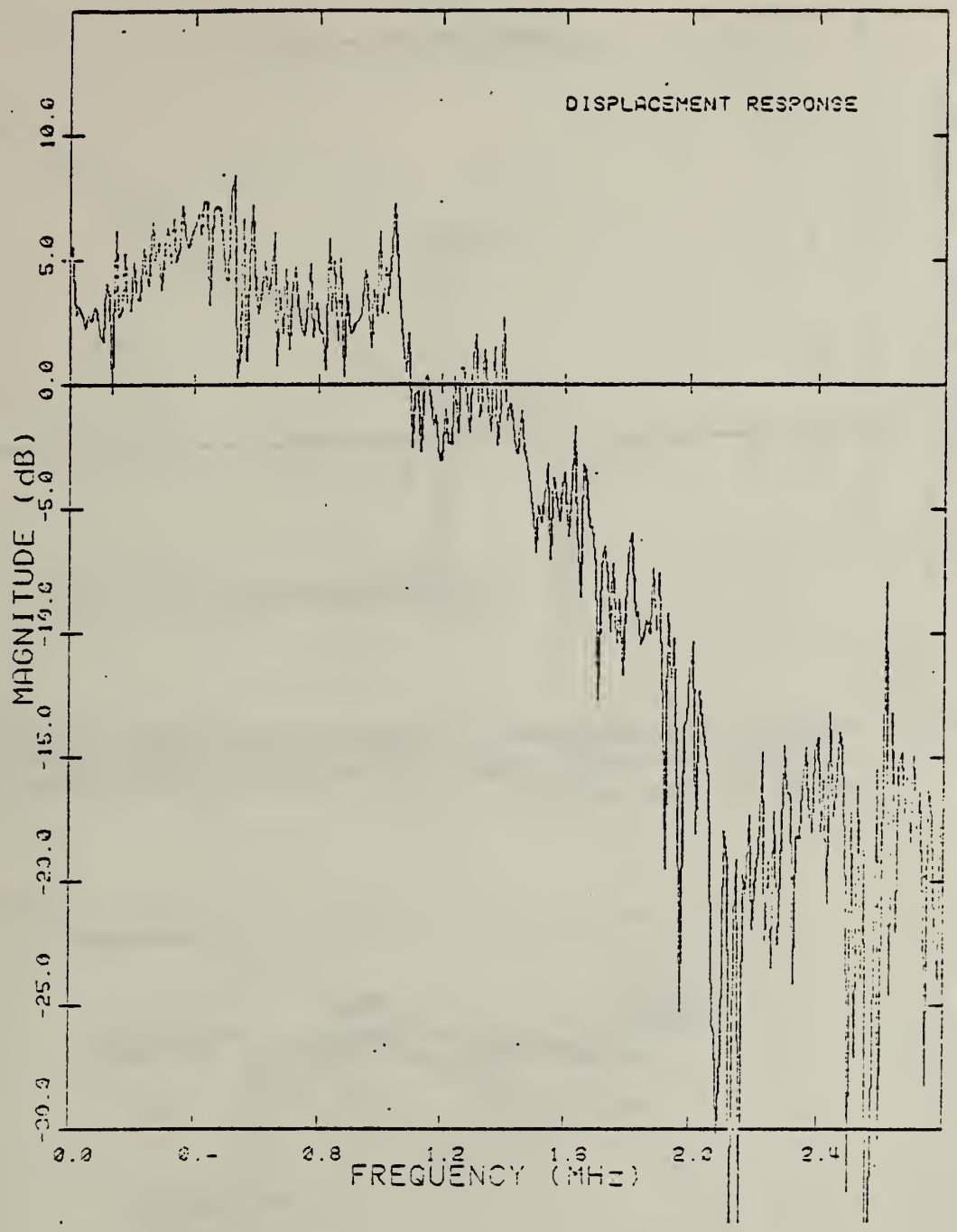

Figure 2. Frequency response of the NBS conical transducer model shown in Figure 1.

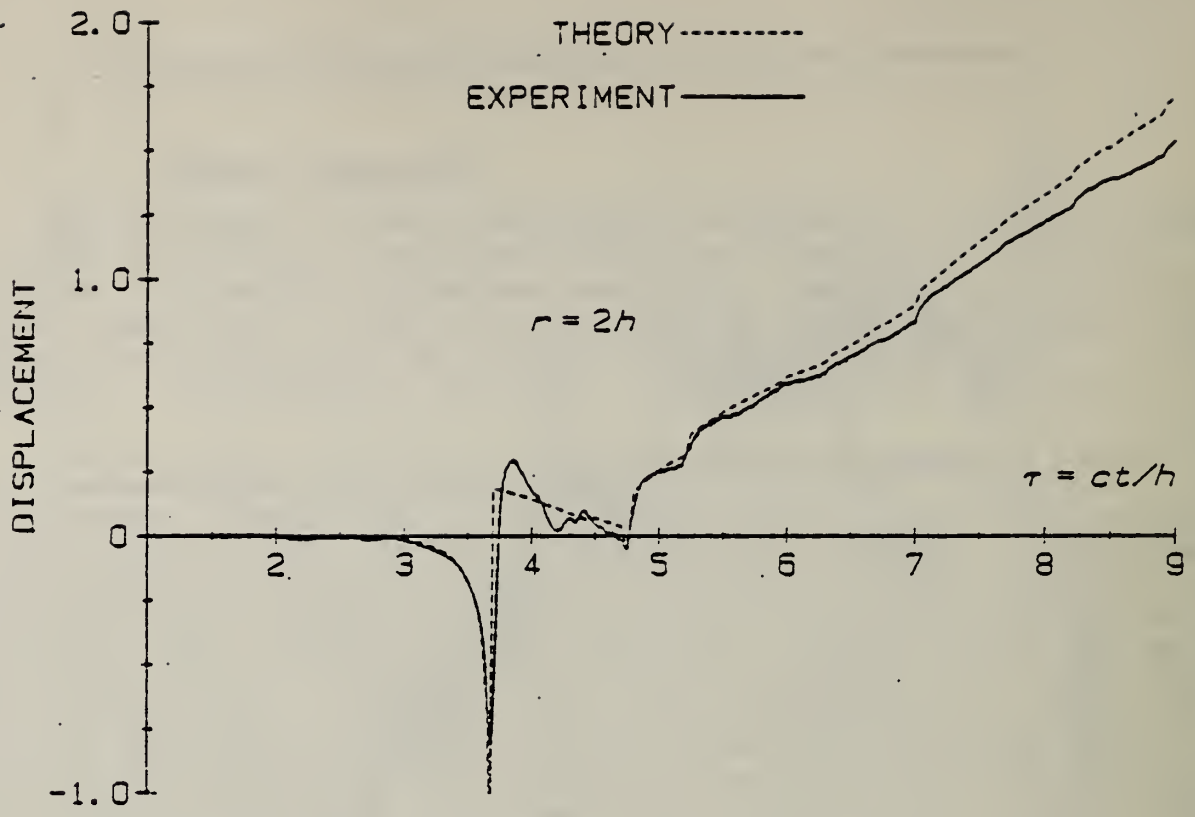

Figure 3. Measured and theoretically predicted surface displacements due to a point force step function on a plate two thicknesses away and on the same surface.

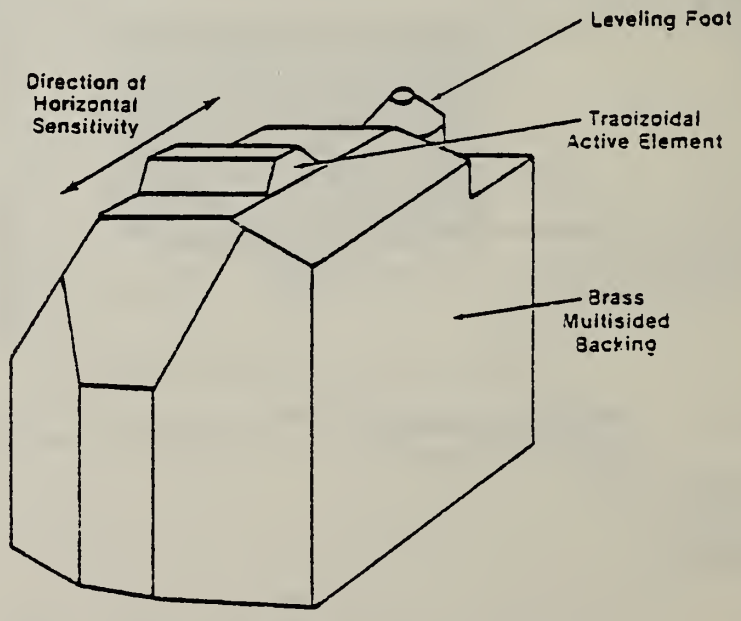

Figure 4. Horizontal displacement transducer (upside down).

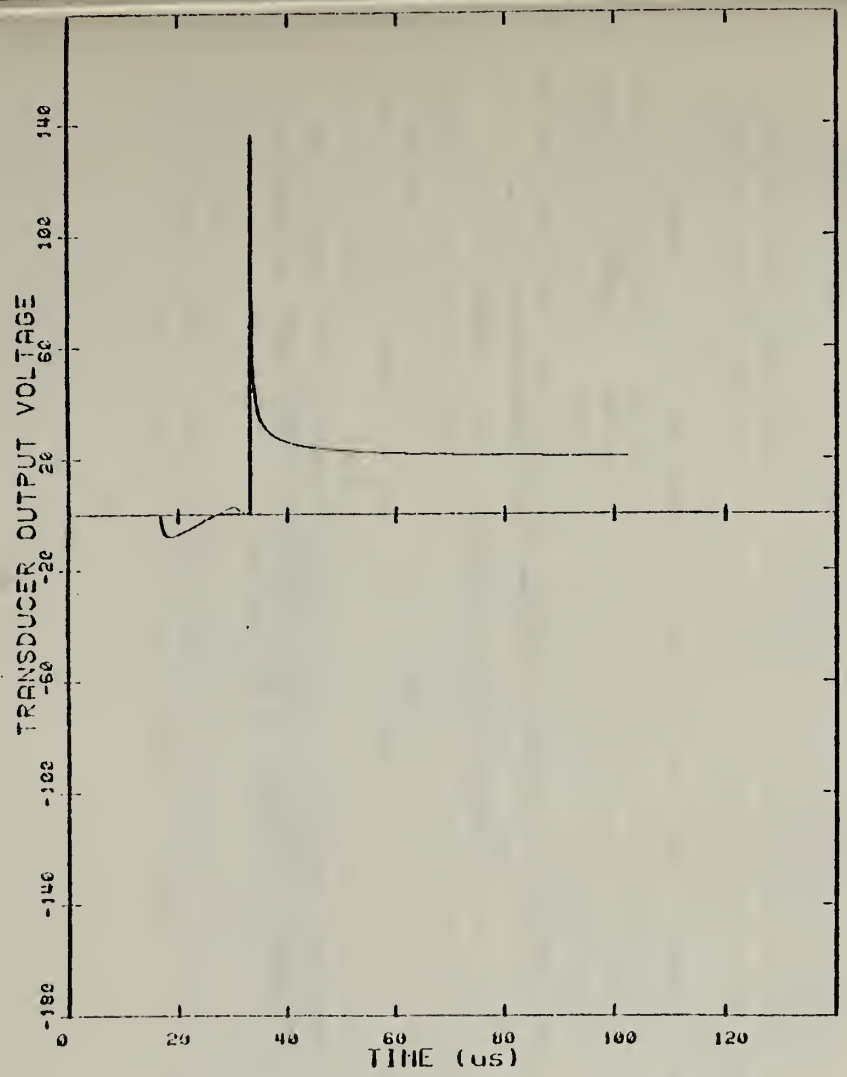

Figure 5. Theoretical horizontal displacement of the surface of a half space due to a point force step function.

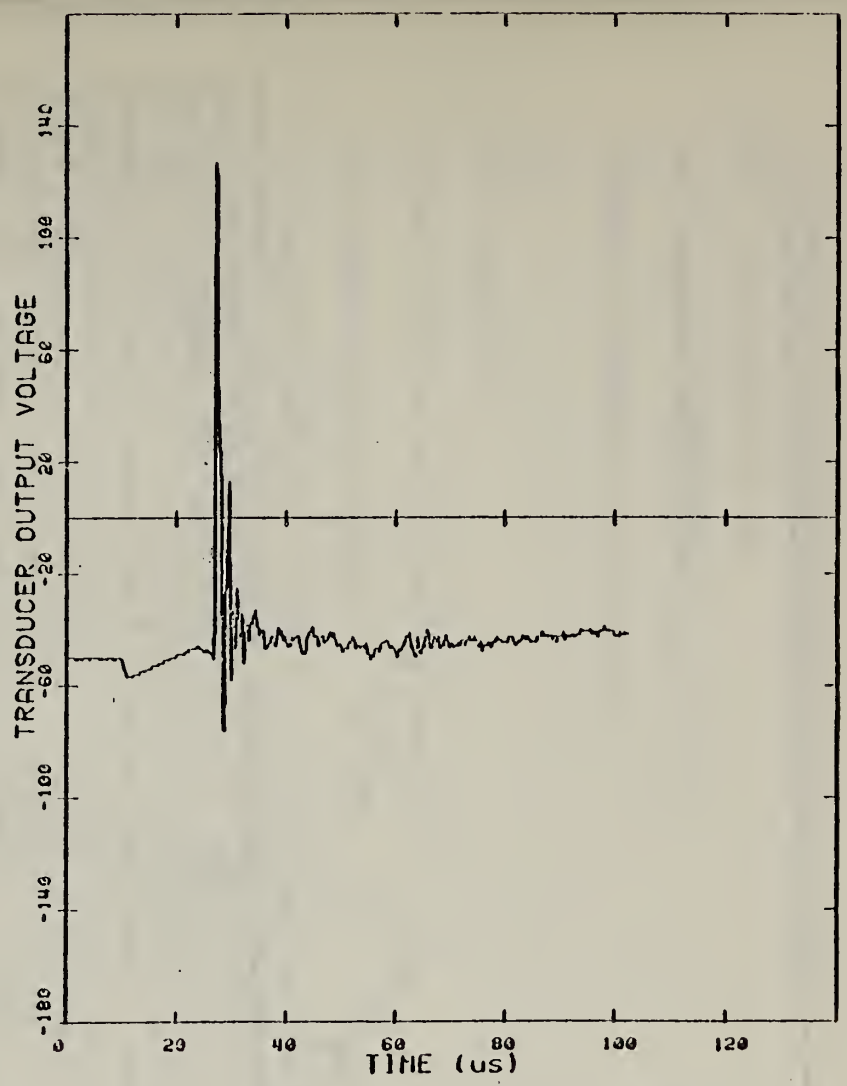

Figure 6. Waveform measured by the transsducer shown in Figure 4 (compare with the theoretical waveform in Figure 5).

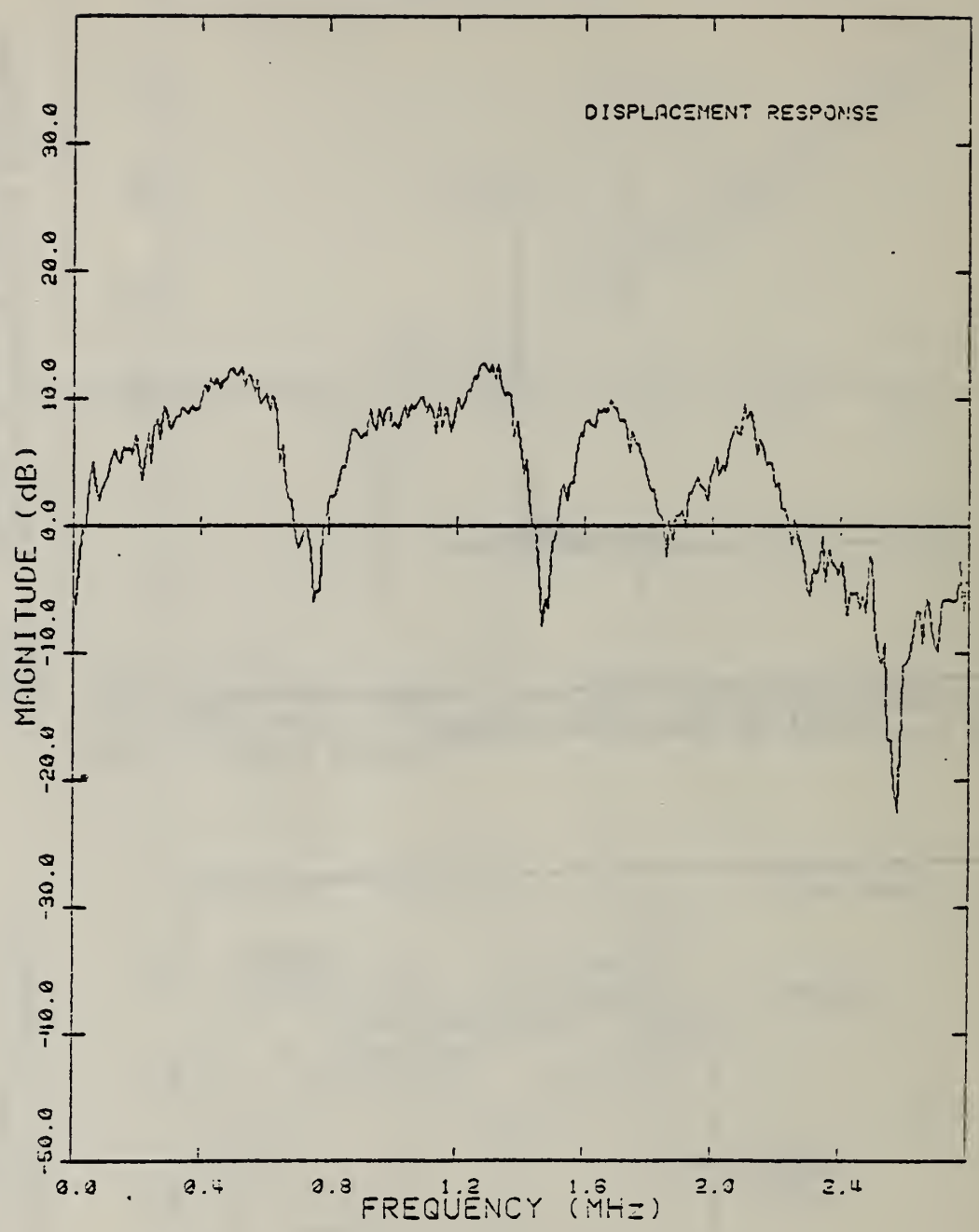

Figure 7. Frequency response of the tangential transducer determined by comparing Figures 6 and 5.

A COMPARISON OF SIMULATED ACOUSTIC EMISSION SOURCES

M. P. Jones and N. N. Hsu

Mechanical Production Metrology Division

Center for Manufacturing Engineering

and

R. E. Green, Jr.

Material Science and Engineering Department

The Johns Hopkins University

Although the phenomenon of acoustic emission has been the subject of an ever-increasing number of scientific investigations and technological applications for a number of years, it has not optimally fulfilled its promise as a nondestructive testing technique since the precise characteristics of the stress waves emitted from specific sources remain unknown. In order to assure that a selected, experimental, acoustic emission source-identification system can be successfully used to detect and record the unknown waveforms of acoustic emission signals which are characteristic of real structural or microstructural materials alterations, it must first be shown that the system is capable of faithful detection and recording of waveforms produced under carefully controlled experimental conditions which correspond to known theoretical waveform solutions.

One method of characterizing an acoustic emission system is to generate a stress wave possessing known features and propagate it through the structure being monitored. The distortion of the stress wave by the structure and/or the sensors can then be ascertained by systematically changing the structure or sensor while the source remains constant. Since it is impossible at the present time to have a real acoustic emission source which is precisely reproducible and which can be generated at will, simulated acoustic emission sources must be used. A prerequisite to utilization of any simulated source is that its characteristics be established and compared with real acoustic emission sources.

In the present work a well-characterized system was used to obtain the dynamic force-time function at the source. The system consisted of an aluminum plate with sensor at the epicenter; the sensor measured the vertical displacement of the surface of the plate. In this configuration, the experimental and theoretical surface displacement waveforms were found to be in excellent agreement when a glass capillary fracture was used to approximate a step-force unloading source. Furthermore, the step-force function was recovered from the detected signal using deconvolution techniques. Two other sources approximating a step-force unloading were also investigated. One of these was the fracture of a brittle pencil lead and the other was a new type of piezoelectric transducer developed at the

National Bureau of Standards. The rise time, the time needed for each source to unload the plate, was approximately 0.1 μs, 0.3 μs, and 0.5 μs for the glass capillary, the pencil lead, and the pulsed transducer, respectively. Three faster rise-time sources were developed using transient local heating to generate thermoelastic stress waves. One source used a 50-ns, 30-mJ Nd:YAG laser pulse. Another was produced when a 25-ns, 100-A current was passed through a junction consisting of an electrode and the plate. Finally, an electric spark was discharged directly onto the plate. A discussion of all these simulated sources and the associated surface displacement waveforms and their respective deconvolutions were reported at the Ultrasonics International 83 Conference at Dalhousie University, Halifax, Canada, July 1983.

A SIMPLE REAL-TIME AE SOURCE LOCATION SYSTEM

N.N. Hsu and M. Barsky

Mechanical Production Metrology Division

Center for Manufacturing Engineering

Flaw location by the acoustic emission (AE) technique has many advantages. It is a real-time, whole-field, passive monitoring technique; it can determine the location of an active flaw while the structure is under load; and it requires relatively few sensors attached to the structure for monitoring an area.

In an effort to optimize the effectiveness of the technique, we have performed detailed system error analysis and found:

(1) available source location systems require a computer,

(2) computation and display of source location are computer time shared with the acquisition and computation of other AE parameters during the AE test,

(3) AE source location cannot be very precise unless the details of individual waveforms of the detected AE are analyzed (the uncertainty of dispersive wave speed of AE propagating in a structure contributes large errors to the source location calculation), and

(4) the available computer based AE systems are not only expensive but also inefficient as far as source location is concerned.

From a systems engineering point of view and in many AE monitoring applications, it is the rapid display of the approximate location of an AE source that is of greatest importance. Rather than refine the numerical algorithm for computing the source location with time-of-arrival data of limited precision, we resolved to maximize the effectiveness with minimum cost. A prototype was designed, constructed and demonstrated. It consisted of the following features:

(1) It uses a simplified algorithm for converting delta-time to x-y coordinates.

(2) It monitors a square area with four sensors.

(3) It displays the location of an AE source in a 16x16 grid.

(4) It is self contained as a modular system.

(5) It was constructed with readily available low cost parts.

Details of the design were given at the June 83 AEWG Meeting and will be reported in the open literature.

ACOUSTIC EMISSION IMAGING

S. J. Norton and M. Linzer

Metallurgy Division

Center for Materials Science

During the past year, an examination was made of the problem of reconstructing a two-dimensional random source distribution from measurements of the emitted radiation recorded on the circumference of a circle surrounding the source region (ref. 1). An analytical inversion formula for the two-dimensional random source problem and the analogous solution to the three-dimensional inverse problem were derived. For tractability, the analysis was restricted to random sources that are spatially incoherent, i.e., where the radiation emitted from distinct points in the source distribution is statistically uncorrelated. Sources that can be reasonably modeled as random and spatially incoherent are common in nature. In optics, thermal or blackbody sources are notable cases. Acoustic emission, arising from cracking or other material transformations, sometimes satisfies these conditions. The importance of the latter example derives from the fact that acoustic emission is often an accurate indicator of the potential of a material to fail under stress. Mechanisms that give rise to acoustic emission sources consistent with the assumptions of a random and incoherent source model are distributed microcracking and martensitic transformations.

Devaney (refs. 2-4) has shown how the far-field correlation function of the radiated source field bears a multiple Fourier transform relationship to the incoherent source distribution. This relationship is mathematically analogous to the Born inversion procedure in inverse scattering, and is based on the usual assumption that the radiation is recorded in the far field of the source. In this study, closed-form inversion formulas were derived that are valid for the near field, i.e., no far-field approximations are employed. The derivation for the two-dimensional source consists of inverting an integral equation with the aid of a Green's function expansion in a set of basis functions suitable for the geometry of interest. An efficient method for performing numerical reconstructions of the source intensity using the fast Fourier transform algorithm was developed.

The three-dimensional generalization of the two-dimensional inversion formula was also derived. The 2-D problem consists of reconstructing a 2-D random source distribution from emitted radiation on a circular detecting array surrounding the source region. The analogous three-dimensional problem assumes a bounded 3-D source enclosed by a spherical detector array. This problem was solved by making use of Devaney's observation (refs. 2-4) that the inverse-scattering and inverse-source problems are mathematically similar when the source is random and spatially incoherent. Under these conditions, both problems reduce to solving integral equations of identical form. In the

corresponding 3-D inverse-scattering problem, a scattering region replaces the source region and the elements in the spherical array are used as spherical wave transmitters as well as receivers. Ball, Johnson and Stenger (ref. 5) have recently reported a near-field solution to the inverse-scattering problem in this spherical geometry. Their inverse-scattering solution was used to solve the corresponding 3-D inverse-source problem.

A backprojection approach to the inverse-source problem was also investigated. Although some approximations are made in generating the image, this technique is more efficient computationally and less restrictive with respect to source characteristics and transducer array geometry than the exact inverse-solution outlined above. In this approach, the signals recorded by transducers surrounding the source region are correlated pair-wise, filtered, and then backprojected into image space. This process of filtering and backprojection bears some similarity to image reconstruction algorithms used in medical x-ray tomography. The backprojection method may make it practical, for the first time, to image acoustic emission sources and to detect acoustic emission signals below the random electronic noise in the receiving system.

REFERENCES

1. S. J. Norton and M. Linzer, "Reconstructing Spatially-Incoherent Random Sources in the Near Field: Exact Inverse Formulas for Circular and Spherical Arrays", in preparation.

2. A. J. Devaney, "The Inverse Problem for Random Sources", J. Math. Phys. 20, pp 1687-1691 (1979).

3. A. J. Devaney, "Inverse Source and Scattering Problems in Optics", Optics in Four Dimensions - 1980, Chap. 15, pp 613-626 (Proceedings #65, Am. Inst. of Phys., New York, 1981).

4. A. J. Devaney, "A New Approach to Emission and Transmission CT", 1980 IEEE Ultrasonics Symposium Proceedings, pp 979-983, Cat. No. 80CH1602-2.

5. J. S. Ball, S. A. Johnson and F. Stenger, "Explicit Inversion of the Helmholtz Equation for Ultrasound Insonification and Spherical Detection", Acoustical Imaging, Vol. 9, pp 451-461 (Plenum Press, New York, 1980).

ACOUSTIC EMISSION (AE) STUDIES OF RAPID SOLIDIFICATION

R. B. Clough, H. N. G. Wadley and R. J. Schaefer

Metallurgy Division

Center for Materials Science

Rapid solidification is a new technique used for producing metallic glasses, which provide low loss transformer core material, and is also used to produce superior surface coatings and long wearing bearing surfaces. AE can be used to monitor rapid solidification surface modification to detect flaws produced during processing. It also promises to provide dynamic information on the solidification process itself, since a typical solidification time for a surface melt is on the order of 10 ms and stress waves can be monitored over considerably shorter times (~ 100 μs). Very little work has been done in this area and due to the potential of AE to shed light on this subject, NBS and DARPA are sponsoring research on AE monitoring of rapid solidification processing.

Two types of directed energy source are being used, an electron beam and a Nd-glass laser. The former can provide an energy pulse over 10 ms in duration and the latter can have a pulse duration of about 100 μs to 5 ms. Metallographic examination was made of resolidified electron beam surface melts of an Al/Cu (2219) alloy and a commercially pure (1100) aluminum. There are no cracks in the resolidified 1100 aluminum, and very little AE during resolidification. In contrast, there are numerous cracks in the 2219 aluminum alloy, and large amounts of AE. This indicates that AE monitoring of electron beam surface modification may be used for detecting cracking during processing. As a partial explanation for such cracking, and/or plastic deformation; a preliminary stress analysis of rapid surface solidification suggests that large tensile forces can be produced during cooling, which could generate cracking and/or plastic deformation. Cracks can be formed or run into the region directly outside of the melted layer, such as in the heat-affected zone of the substrate. This is shown in Fig. 1, which depicts a typical "mushy zone" microstructure in a resolidified layer of 2219 aluminum. A hot tear can be seen to run down into (or out from) the heat-affected zone of the substrate. Thus it is not surprising that the AE can be dependent on the heat treatment of the bulk material as is shown in Table I. This variation is presumably caused by differences in thermoelastic and plastic deformation and/or cracking during cooling in highly stressed regions both within and outside of the resolidified microstructure. To study such effects, it is essential to eliminate experimental variability due to inadequate measurement precision.

In order to minimize the variability in results produced by the measurement system, an improved specimen holder has been fabricated which minimizes ringdown and the influence of specimen geometry. This has been calibrated (Fig. 2) with a Nd-YAG laser, yielding the result that the measured AE energy (the sum of the squares of the signal voltages) is proportional to the absorbed energy. An identical proportionality holds true regardless of source type or

orientation, an advantage to using the energy approach. It is also possible to use this method to make absolute determinations of source strength; equivalent dipole moments are given for an Al/4% Cu alloy. This method, thus, is a quantitative acoustic emission method.

AE has also been monitored during the drilling of holes by a Nd-glass laser in 2024-T4 aluminum plate. Here the AE energy from the entire process is calculated and preliminary results indicate that AE energy increases monotonically with hole depth. This is an important result, since there can be a large variability in hole depth for a given set of laser control parameters, which may be due to material variability, surface condition, or instabilities inherent in deep penetration. From these initial results, AE shows promise for monitoring of laser drilling or surface modification, for feedback control of hole depth or depth of penetration.

TABLE I

Acoustic Emission After Beam Cut-off as Affected by Substrate Material Condition

Material and Condition	Rockwell B Hardness	AE Energy (Relative Units)		
		$qa \leq 1.5 \times 10^5$ W/m	$qa > 1.5 \times 10^5$ W/m	Total
2219-Solutionized	39	0.008	0.013	0.021
2219-T6	77	0.056	0.117	0.173

q = absorbed heat flux
a = melt radius

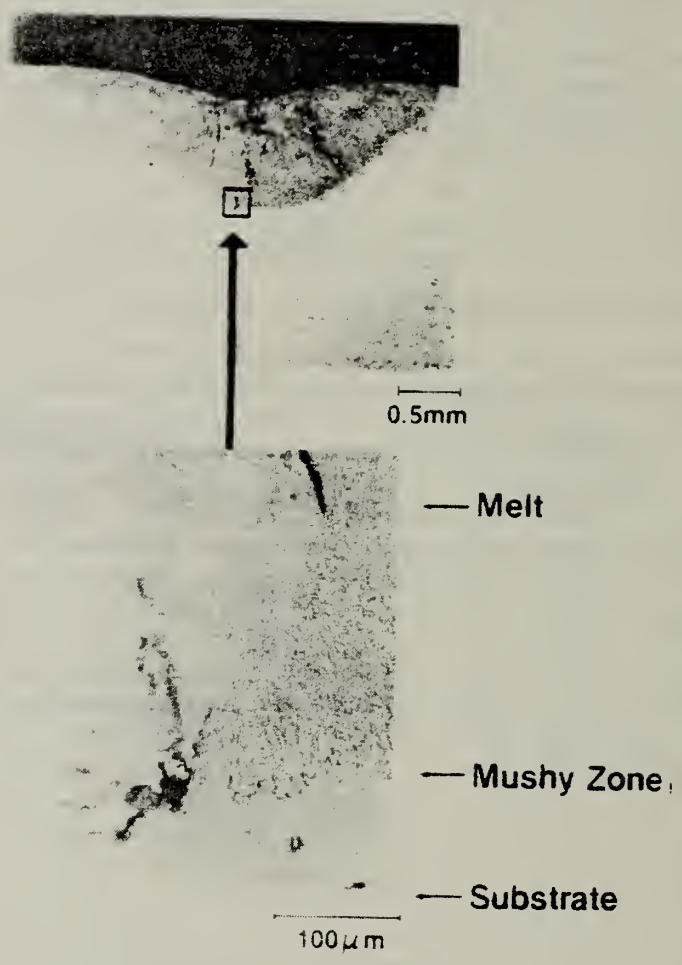

Figure 1 Optical micrographs of 2219 aluminum alloy surface melted at $\underline{q}a = 2.7 \times 10^5$ Wm^{-1} showing detailed microstructure of the region of the "mushy" zone at the bottom of the melt pool.

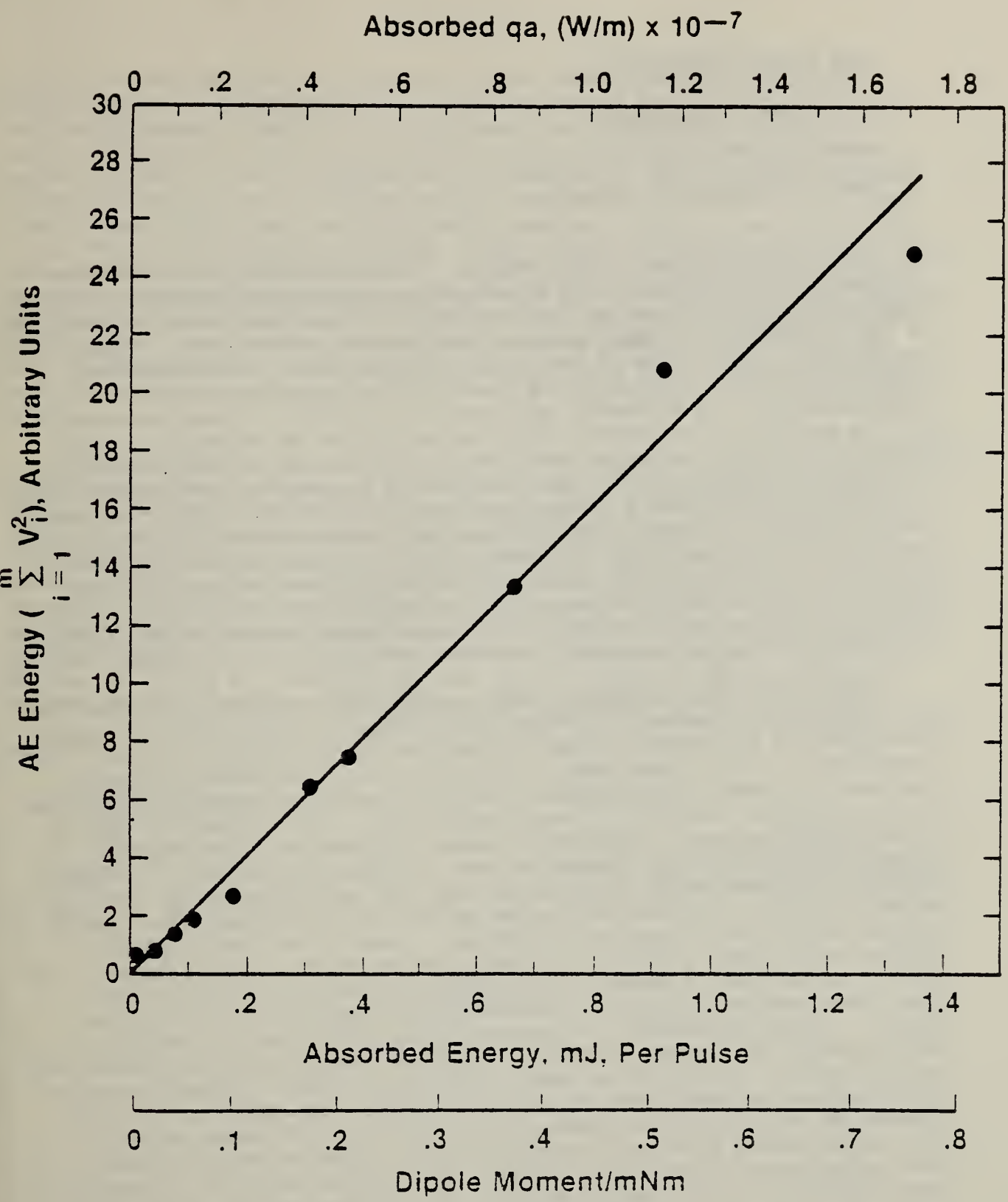

Figure 2 Relationship between input energy and acoustic emission energy in rapid solidification AE apparatus.

WEAR CONDITION MONITORING

A. W. Ruff, E. Whitenton
Metallurgy Division
Center for Materials Science

The principal thrust of this project is concerned with the application of acoustic emission monitoring to wear under laboratory conditions. The experiments are done under well-controlled and simple conditions so that some of the fundamentals of the phenomena involved can be identified. Actual application in the future to real field conditions will involve much more complex conditions. However it is hoped that by achieving some basic understanding of the phenomena, application in certain selected instances will be possible. The problem being studied is that of delamination wear under high stress, lubricated conditions. This wear process has been very extensively studied (ref. 1), and involves the progressive development of subsurface cracks as a result of the normal applied load and surface tractions due to friction. At some critical size, the crack propagates quickly to the surface and a wear particle is formed. These particles can be 10 μm thick and 100 μm wide and long, in the case of steels. Since all but the final stages occur below the specimen surface, a technique for monitoring crack growth, such as acoustic emission, would be extremely useful. Some studies of contact fatigue using acoustic emission have already been reported (ref. 2).

Studies have been carried out this year on a quenched O-2 tool steel that was intentionally treated to achieve low toughness. Studies on this same steel (ref. 3) have characterized the emission resulting from hardness indentations, so that some detail is known already. The wear test system involves a block-on-ring geometry. The ring is machined to have a small bump on the surface so that once in every revolution a load increment is applied to the block specimen. This load increment should cause an incremental advance in the subsurface cracks that are susceptible to growth. The signal detection electronics are synchronized with the load increment so that observation of acoustic emission pulses can be done at the optimum time. The AE system consists of a standard PZT detector, preamplifier, amplifier, and display oscilloscope. Built-in filtering restricts the system band pass from 100 kHz to 1.2 MHz. A number of experiments carried out on the O-2 tool steel have revealed pulses that correlate with some of the load increment events. The pulses display a ring-down characteristic that is probably determined by the specimen geometry. There are several possible explanations for the sporadic nature of the detected emission pulses: (1) small emission events may not be identified because of the noise level present, (2) crack advance may not occur to the same extent on each load increment pulse, (3) each crack advance event may produce basically different emission events. It is also necessary to positively identify the detected pulses as originating from subsurface cracks (even though they are synchronous with the load increment pulse). Subsurface metallography has been carried out on some of the specimens and cracks are found. However it has not been possible to identify the particular cracks that grow during the wear experiment. Metallographic subsurface studies are destructive to the specimen and preclude further wear

studies on the same block. Therefore another technique will be needed to monitor the crack growth during wear. It is planned to use ultrasonic pulse scattering methods to do this in a different test geometry, that of two crossed cylinders. A new test machine has been obtained and will be instrumented this year. The AE detector will be mounted on the stationary 12.7-mm diameter steel cylinder. The orthogonally mounted 12.7-mm diameter cylinder rotates under lubricated conditions and at contact pressures over five times larger than the block-on-ring system. These higher pressures should accelerate the wear and crack growth processes. An ultrasonic pulse transducer will be mounted on the end face of the stationary cylinder and should indicate changes in crack size (area) during the wear test. This additional source of information should overcome some of the interpretation problems experienced so far. These experiments will begin in FY84, and will be closely coordinated with other efforts on acoustic emission and ultrasonic pulse characterization at NBS.

A second thrust of the project concerns wear debris particle characterization using ferrographic techniques. Efforts this year are concentrating on the development of two standard reference materials for this method, and are funded by the Office of Standard Reference Materials. However, contact has also been maintained with other laboratories doing these measurements. Two methodologies have been developed by the Joint Oil Analysis Program laboratory, Pensacola, FL, and the Air Force Materials Laboratory, Ohio. Interlaboratory tests using these methods are being organized for the near future, and NBS will participate in these. Based on those results, one consensus method may develop for use by all DoD laboratories, and for possible standardization through the SAE committee. NBS input to this process will be provided.

REFERENCES

1. Delamination Wear, N. P. Suh, editor, (Elsevier Publ., 1977).

2. T. Yoshioka and T. Fujiwara, "A New Acoustic Emission Source Locating System for the Study of Rolling Contact Fatigue," Wear 81, 183-186 (1982).

3. Private communication, R. B. Clough (NBS).

EDDY CURRENT STANDARDS

A. J. McAlister

Metallurgy Division

Center for Materials Science

The eddy current method is widely used in both the ferrous and nonferrous metals industries for nondestructive detection of flaws such as cracks, inclusions, and variations in composition and microstructure in metals and metal parts via local changes in electrical conductivity. Primary conductivity standards are needed for reliable execution of this work but, to date, this need has been addressed by industry itself. The necessary range of conductivity for industrial testing is from 0.585 to 58.5 MSm^{-1} (1 to 100 percent IACS).

The properties desired in a primary conductivity standard are long term stability, durability, and low magnetic susceptibility. (In testing of high susceptibility steels, normal practice has been to apply a saturating magnetic field to reduce the differential permeability to a value near that of vacuum.) Hence, elemental metals and alloys of equilibrium phase composition, upon which stable nonconducting surface layers can be formed, are desirable. The surface properties are important not only for durability, but for reproducible lift-off behavior as well.

Our overall aim, the selection of metals and alloys and demonstration of their suitability for primary conductivity standards is now essentially complete. Pertinent results are summarized in the following table. Magnetic permeability is expressed as the difference in permeability in units of the vacuum value and one.

Target Conductivity (% IACS)	Material (wt.%)	Condition	Observed Conductivity (% IACS)	Magnetic Permeability (μ/μ_0-1) Max
101	OFHC Cu	annealed	101.9 ± 0.1	
		unannealed	99.5 ± 0.1	
85	1.3 Zn + Cu	as cast	81.1 ± 1.0	
75	2.4 Zn + Cu	900 °C HT	70.4 ± 1.0	$+ 1 \times 10^{-4}$
60	Al 1100 F	finished	60 ± 0.05	
48	Al 2024-O	finished	47 ± 0.10	
41.5	Al 6061-T	finished	41.5 ± 0.05	
29	Al 2024-T-351	finished	29 ± 0.10	
23	21 Zn, 2.5 Al + Cu	900 °C HT	20.5 ± 2.0	$+ 8 \times 10^{-5}$
23	3.0 Al + Cu			
17	7 Al + Cu	900 °C HT	15.0 ± 0.01	$- 6 \times 10^{-5}$
		as cast	15.0 ± 0.01	
12	1.5 Si + Cu	as cast	12.7 ± 0.01	$- 1 \times 10^{-4}$
7	3.0 Si + Cu	as cast	7.4 ± 0.02	$+ 2 \times 10^{-4}$
3.5	Ti, Grade 4	as received	1.9 ± 0.02	
1	6 Al, 4V + Ti	as received	0.97± 0.005	

The nonlinear spacing of target conductivities is necessitated by the nonlinear variation of probe coil impedance with sample conductivity. Commercial alloys in as-received condition proved suitable for the Al and Ti based standards. Observed conductivity variations over smooth surfaces of these materials are adequately small and appear to be random. Magnetic permeability is not a significant question with these materials, since transition metal impurities do not carry a local moment in either metal. High levels of transition metal impurity could result in the formation of ferromagnetic compounds in Al. However, as a practical matter, their occurrence would be revealed in calibration as an apparent change of conductivity with frequency. The higher conductivity and reduced conductivity variation of annealed vs unannealed Cu is due to the removal of cold work damage. Annealing did not improve either Ti or the Ti alloy.

The decision to focus on Cu-based alloys outside the Al and Ti ranges, and to prepare special melts, was not made lightly. As a practical matter, it is essential that the magnetic permeability of an eddy current conductivity standard be very close to the vacuum value. Only Cu-based alloys are potentially capable of meeting this criterion in the needed conductivity ranges. Special melts are indicated because current industrial practice is to add significant quantities of Fe, Co, and Mn (which can develop full magnetic moments or form magnetic precipitates in Cu) as grain refiners or to improve mechanical properties. Currently available Si-bronzes contain 0.8 w/o Fe; Cupronickels, 1.0 w/o Fe; brasses, 0.05 percent Fe. Yet the brasses, for example, must contain less than 0.03 percent Fe if Fe precipitation is to be avoided during stress relief. Cupronickels, otherwise attractive, were rejected because of the tendency of Ni to form superparamagnetic clusters in Cu.

Castings (alloy additive content indicated in weight percent) of 1.3 Zn, 2.4 Zn, and 21 Zn + 2.5 Al in Cu, and of 7 Al, 1.5 Si and 3.0 Si in Cu were made in-house. OFHC Cu and alloy additives of 99.995 purity or better were employed. Due to the higher vapor pressure of Zn, the brasses were formed by melting the components in sealed, He-filled vycor tubes; consequently, the ingots were slow cooled. The Al and Si bronzes were melted in graphite crucibles and quickly cooled. As the table shows, the brasses achieved target conductivity and good magnetic permeability ratios, but showed unacceptably large conductivity variation. This fault is due to porosity, probably arising from the slow cooling. It should not be regarded as a disqualifying defect, however, since with appropriate commercial foundry practice, using hot isostatic compaction if necessary, such porosity can be avoided or eliminated. The bronzes performed quite well, electrically and magnetically, in as-cast condition. Two ingots of 7 Al bronze were prepared, one homogenized at 900 °C, the other left as cast. No difference could be detected in their performance.

Magnetic susceptibility measurements were made in-house on five of the Cu-based alloys by the Thorpe-Stenftle method. Pieces were sawn from the interior of the ingots, etched, and stress relieved at 200 °C prior to magnetic measurements. As indicated in the table, levels of magnetic impurity in the starting materials are low enough to make standards quite satisfactorily from the magnetic standpoint. Such impurities are present however. Three of the samples were slightly paramagnetic; extremely pure alloys would be slightly diamagnetic.

One final alloy, 3 Al in Cu with target conductivity of 23 percent IACS, is being prepared and will be tested as the last phase of this project.

TRACEABILITY FOR EDDY-CURRENT NDE MEASUREMENTS

George M. Free

Electrical Measurements and Standards Division

Center for Absolute Physical Quantities

The eddy-current project to develop nonmagnetic electrical conductivity standards and to initiate a calibration service for electrical conductivity standards is nearing completion. Measurement systems for both dc and eddy-current measurements are in final form. The methodology of calibration has been established and documentation is being completed. Standard Reference Materials (SRMs) at various points in the range 1-100 percent IACS will be offered as the materials become available and we complete the required certifications. The calibration service for electrical conductivity standards will be announced sometime in 1984.

The electrical conductivity calibration service and the certification of electrical conductivity standard reference materials have a common factor: the instrumentation developed to measure electrical conductivity. The instrumentation consists of a direct-current measuring system by which the dc conductivity of metal samples is determined. These metal samples then become the primary conductivity standards at NBS. Using an eddy-current bridge developed at NBS comparison is made between the primary conductivity standards and either customer samples or SRMs to determine their electrical conductivities.

The dc measurement system has been modified so that four-point measurements can be made on small samples. The feasibility of using a four-point measurement in conjunction with the relations betwen conductivity, sample resistance, and sample thickness, i.e., the relationship developed by Van der Pauw, has been tested. Measurements were made on aluminum discs. These samples were 2.0 cm in diameter and varied in thickness from 0.15 cm to 0.6 cm. The resistance of the test samples can be measured with an accuracy of $\pm$ 0.01 percent of value. The initial measurements were difficult to make due to noise in the measurement system generated by thermal EMFs. To reduce this noise the oil bath in which the test samples are submerged must have better temperature stability and more uniform flow of oil past the contacts. A new temperature controlled oil bath has been purchased and is now being tested for temperature stability. The bath controls temperatures between 15°C and 30°C to approximately $\pm$ 0.002 C. Over periods of 20 minutes the stability is $\pm$ 0.001 C. Future measurements will be made in this bath. The accuracy of the dc measurement should be improved by an order of magnitude. This improvement is possible since resistivity is a function of sample thickness instead of sample cross-sectional area. The smaller metal standards will be macnined using techniques developed for making optical flats. The measurement of the thickness of the standards will also be improved.

Development work on the eddy-current bridge is focussed in two areas; simplifying the measurement and increasing the frequency range of the bridge. In the typical Maxwell inductance bridge there are two sets of balances that must be made, the primary circuit balance (which determines the values of R and L of the inductor) and the group circuit balance (which reduces the error due to stray capacitance). To simplify the measurement either the ground circuit can be eliminated or the number of balances between the two circuits can be reduced. Both approaches are being tested but at present elimination of the ground circuit is not possible. The present approach is to match components in the primary and ground circuits and use common inductive dividers to drive the components. Using this scheme the measurement had been greatly simplified. The main circuit is balanced, a slight adjustment is made to the ground circuit at the highest detector sensitivity, and then a final balance is made of the main circuit. In most cases three circuit adjustments are all that are necessary to obtain final balance.

To increase the frequency range of the bridge it was necessary to use new broadband operational amplifiers in the ground network. The bridge frequency range has been increased so that it now covers the range 100 Hz to 100 kHz. The final configuration of the ground circuit, to obtain minimum noise and drift and high phase accuracy over the frequency range, is being completed.

The errors in the eddy-current measurement due to lift-off and coil heating (which changes the resistance of the coil) have been reduced. A sample holder has been built which automatically varies coil-to-metal separation in increments of 0.1 μm. It is now possible to measure a standard with a number of known values of lift-off. These measurements with different lift-off settings become part of the calibration data. An algorithm has been written to determine, from the measurements on the standard and on the unknown being calibrated, what coil-to-metal separation is present in the measurement of the unknown. The separation is then varied until it is the same as the initial measurement of the standard sample. By interspersing measurements of the standard with measurements of the unknowns it is possible to determine changes in coil resistance due to coil heating. These changes are calculated and corrections are then applied to all measurements. Measurement repeatability is now at $\pm$ 0.005 percent of value.

The following summarizes the principal accomplishments during FY83: (1) The dc measurement circuit was modified to make measurements of resistance at the 10 microohm level. (2) A holder for small metal samples was constructed and the feasibility of making measurements using Van der Pauw's relationship was tested. The major sources of error in the new measurement were determined and steps are being taken to eliminate them. (3) The frequency range of the eddy current bridge was extended to cover the range of 100 Hz and 100 kHz. (4) Measurements with the eddy-current bridge have been simplified so that in most cases three adjustments of circuit parameters are all that are necessary to achieve final balance at the highest sensitivity. (5) A new sample holder has been constructed for eddy current measurement. Coil-to-metal separation distance can be varied by increments of less than 0.1 micrometer. (6) A new

calibration scheme has been devised which incorporates the capabilities of the sample holder. Measurement repeatability has been improved to + 0.005 percent of value. (7) A method has been devised to determine the frequency error in the calibration of the test coil. This has not been tested as yet. (8) A document on the measurement of electrical conductivity by eddy currents, written for ASTM, has passed the main committee ballot and will be published in the ASTM book of standards. (9) Documentation of the dc and eddy-current measurement systems will be completed for possible publication as a NBS Technical Note. (10) 100 SRMs of conductivity 100 percent IACS have been certified. These will be issued as electrical conductivity SRMs.

Plans for FY84 include (1) Calibration of all primary standards using the new dc method. (2) Determination of temperature coefficients of primary standards over a broader range of temepratures, i.e., 15-30°C. (3) Certification of a new SRM at the 1 percent IACS level. (4) Announcement of the calibration service for eddy current conductivity standards. (5) Determine those ferromagnetic materials for which SRMs would have the greatest impact. (6) Initial design of an eddy-current bridge for the calibration of ferromagnetic materials.

EDDY CURRENT COIL CHARACTERIZATION

F. R. Fickett

Electromagnetic Technology Division

Center for Electronics and Electrical Engineering

The overall goal of this program is the development of experimental techniques for accurate characterization of eddy current test coils and the determination of the effect of various mechanisms, such as heat or mechanical motion, on the coil signature. An important feature of this characterization is that it is made independent of the presence of a work piece. Such information is necessary in two areas of eddy current work, the field evaluation of commercial coils and the more esoteric problem of investigating the interaction between an eddy current coil and a defect. In the first instance, we would hope to develop a standard test method and a field-usable system for rapid evaluation of coil performance and, in the second, a technique for accurate mapping of the near-field of the coil. In this first year of the program we have concentrated our efforts on the investigation of techniques to evaluate the basic electrical parameters of prototype coils. Initial work evaluating various field mapping techniques has also been done.

ELECTRICAL CHARACTERIZATION STUDIES

Measurements of the basic electrical parameters have been made on a variety of coils by several techniques that showed promise of capability for precision measurement based on our preliminary study of the problem in FY 82. We have made measurements with: 1) a lock-in detector system; 2) a vector voltmeter; 3) a digital processing oscilloscope; and 4) a commercial digital LF impedance analyzer. The major source of imprecision in all these measurements is the determination of the phase between the current and voltage signals. Thus, part of our work has involved the investigation of low-inductance resistors and Rogowski coil devices. Calculations of inductance and distributed capacitance have been made for conventional resistors, folded-strip precision resistors, and a Rogowski coil. Inductances are on the order of 3 nH for the conventional resistors and about an order of magnitude lower for the other two. Capacitance values are in the nF range, not a problem for our work here.

The commercial LF impedance analyzer mentioned above should solve many of these problems, at least over a limited range of parameters, but at the time of this writing we have just taken delivery of the analyzer and are still in the initial stages of evaluation. However, it appears almost certain that this instrument will be the workhorse of the program in the next year. Preliminary frequency dependence curves for impedance and phase shift of a surface-type coil, both with and without a ferrite core are shown in Figs. 1-2. Data for an encircling coil are shown in Fig. 3. The data from which these were drawn should have a relative uncertainty of a part in ten thousand on impedance and a part in a thousand on phase angle. These claims are under evaluation.

Analysis of measurements made with the lock-in system led to that system being removed from consideration because of a lack of phase accuracy and stability, even when a precision phase option was incorporated. The vector

voltmeter technique was also discarded due to its lack of sensitivity at the relatively low frequencies used in most commercial eddy current applications.

The digital processing oscilloscope is used in the configuration indicated in Fig. 4. It offers the advantage of a waveform processing capability, waveform storage, and noise reduction by software processing of stored signals. The system does have a limited frequency range and uses discrete values which can contribute to zero-crossing errors. Lack of simultaneity of the separate channels is a potential source of error as are phase shifts in the input amplifiers. We have measured these shifts and incorporated the corrections into our data processing. The parameters of interest can be determined from the acquired waveform data by two methods: integration of the product of the coil voltage and a signal proportional to the current, or measurement of the time between zero crossings of the two signals. In either case, the ultimate accuracy of the measurement is determined by the total effective bit capacity of the instrument. Development of software to control the processing, to account for variations in dc levels, and to accurately determine the location of zero crossings has required a significant effort. Figure 5 shows processed 10 kHz data from this system for the same coil for which data are shown in Fig. 2. Those data give a phase angle of 86.54 degrees. Our measurements indicate that, with further refinement, we can expect to achieve an accuracy of 0.040 degrees and a precision of 0.01 degrees under rather ideal conditions and using 16 bit processing. This is well in excess of what would be required in most commercial applications, but the apparatus is also far more sophisticated than that available to most commercial operations. It is still more than an order of magnitude less accurate than the phase calibrator developed by the Electrosystems Division. We are refining the measurement and the data processing software. We are also looking at higher frequency digital oscilloscopes in hopes of extending the frequency range of our measurements without serious degradation of accuracy, but some tradeoff is inevitable.

At this writing, a selection of commercial coils has been ordered and is due to be delivered within a few weeks. The characterization of several of these and determination of the effect of temperature on the electrical parameters of at least one will be completed before the end of the year.

MAGNETIC CHARACTERIZATION STUDIES

Determination of the best method to use for measuring the field configuration in the near-field region of a typical coil is another aspect of the program. We have constructed a device that allows precise orientation of a subject coil in the vicinity of a detector. Measurements using conventional small-area Hall probes are underway and a detection system making use of a Superconducting Quantum Interference Device (SQUID) has been designed. Discussions are being held with M. Ma of the Electromagnetic Fields Division regarding the potential for using a TEM cell (ref. 1) for evaluation of the coils. This system offers some interesting possibilities, but it is more of a far-field device. However, it is still worth considering because of the large amount of information that can be obtained with a relatively easy-to-operate apparatus. Other techniques for microscopic measurement of ac and dc magnetic fields are also being investigated such as the application of high-permeability disk-reading heads and optical methods involving polarization by magnetic stress.

INTERACTIONS

We have been increasing our familiarity with the problems of eddy current NDE by attendance at the DARPA workshops and by interaction with industry, the military, and universities. These interactions have been most productive and have given us much information regarding the actual problems faced in the day-to-day application of standard eddy current probes in industry and the special problems associated with the more complex new probe designs.

Acknowledgment is due L. F. Goodrich, who assisted in much of the early work on this project and has continued to serve as a helpful source of information on aspects of instrumentation.

REFERENCES

1. M. T. Ma and G. H. Koepke, "A Method to Quantify the Radiation Characteristics of an Unknown Interference Source," NBS Tech Note 1059 (1982).

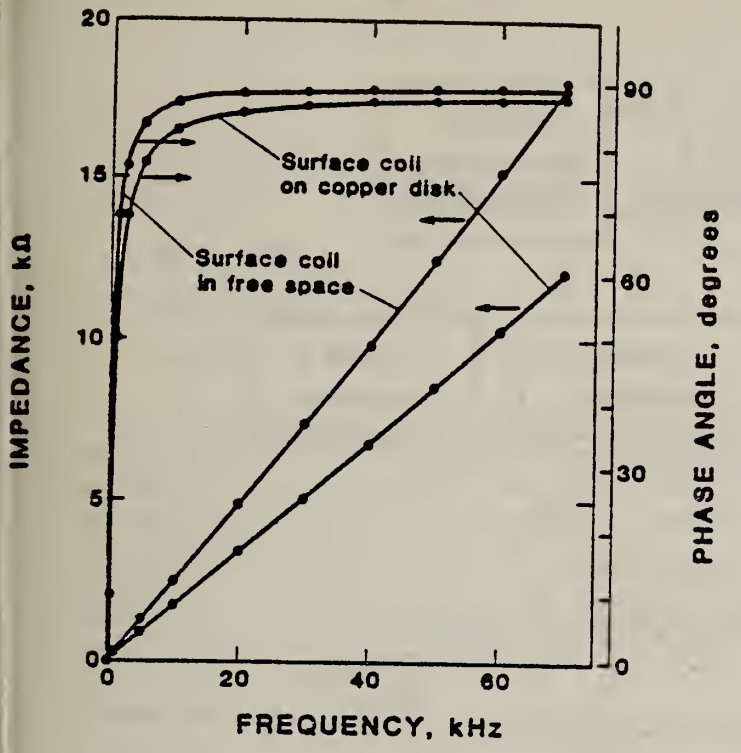

Figure 1. Impedance and phase shift of a surface-type coil measured as a function of frequency in free space and in contact with a high-conductivity copper sheet.

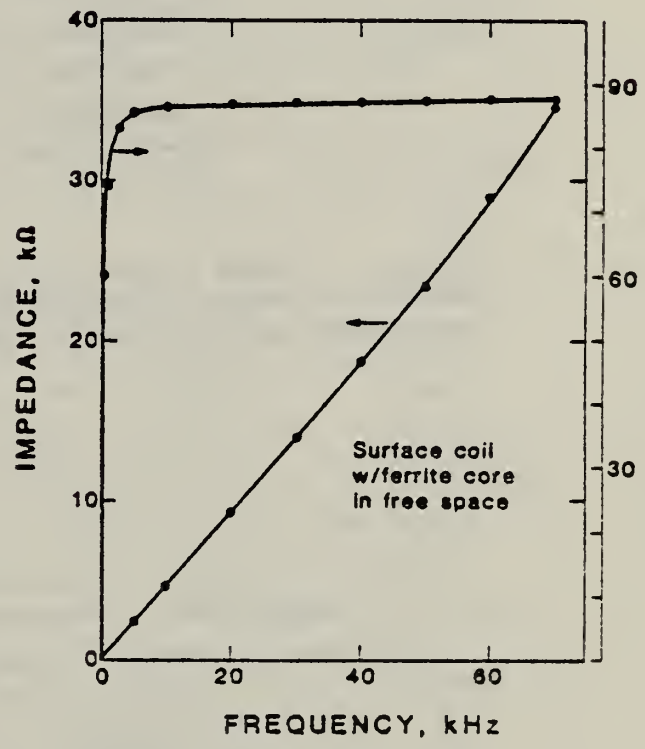

Figure 2. Free-space impedance and phase shift for a coil of the same type for which data are shown in Fig. 1, but with a ferrite core. Note the higher values on the impedance axis.

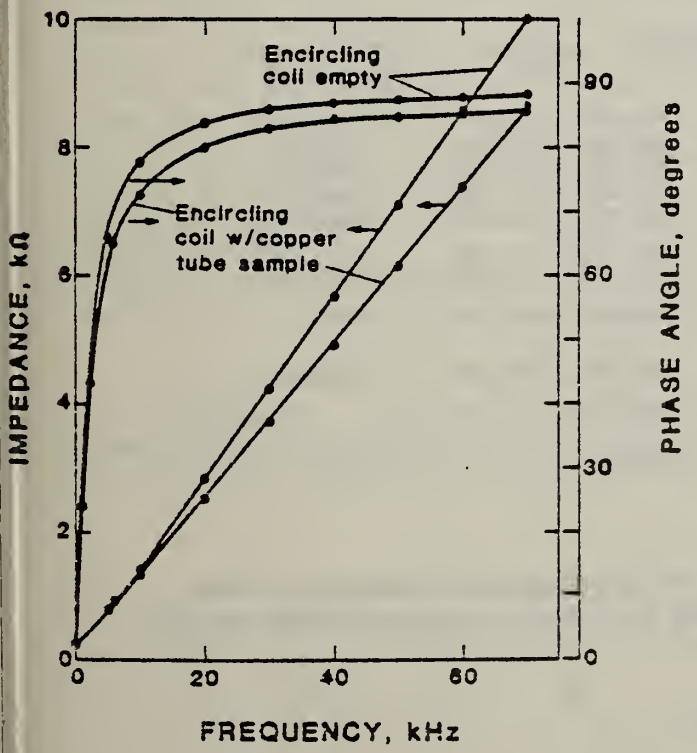

Figure 3. Impedance and phase shift data for a coil of the encircling type, both empty and containing a copper tube sample.

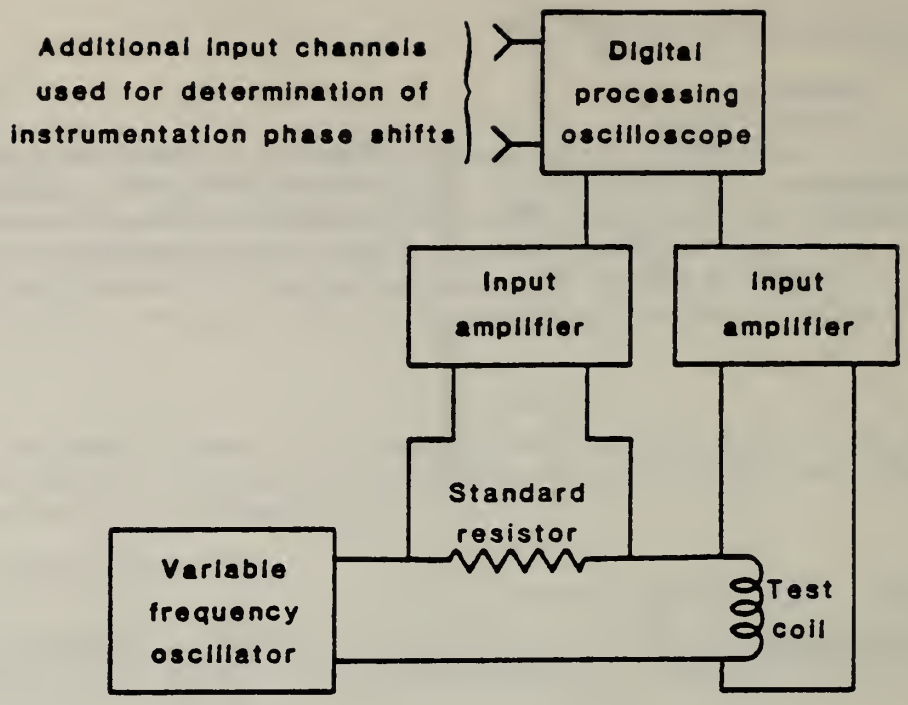

Figure 4. Block diagram of the digital processing oscilloscope system. Phase shifts due to the input amplifiers and the separate system channels are determined and corrected out with the processing software.

820729 Q1:Q2:Q3 0

K	freq Hz	Shift deg	angle deg	Resist ohm	Induct henry
1	10020.27	0.000	86.624	298.777	.080443
2	10020.22	0.000	86.614	298.669	.080181
3	10020.17	0.000	86.568	304.076	.080543
4	10020.22	0.000	86.595	301.181	.080403
5	10020.23	0.000	86.572	303.052	.080347
average	10020.22	0.000	86.595	301.151	.080383
upper	10020.27	0.000	86.624	304.076	.080543
lower	10020.17	0.000	86.568	298.669	.080181
pts/wave	494.45	pts shift	0.00		
Vrms	2.691	Irms	.000531		

Figure 5. Typical data from the digital processing oscilloscope system. These are taken at 10 kHz on the same coil for which data are shown in Fig. 2.

THEORETICAL MODELING IN EDDY CURRENT NDE

A. H. Kahn

Metallurgy Division

Center for Materials Science

The purpose of this project is to provide theoretical support for the development and improvement of electromagnetic methods of NDE. The principal activity in the past year has been the development of a theoretical model for the detection of a surface crack in metallic material by the interpretation of impedance signals in an excitation coil. Previous calculations of the magnetic field in the vicinity of a crack had either neglected the role of the dimensions of the exciting coil or had taken it into account in an approximate way. In this work, a model was developed and computational methods assembled which allow calculation of the impedance signal, taking into account coil dimensions, elevation and position, and crack dimensions. The model used gives the impedance per unit length of a pair of wires oriented parallel to a V-groove crack in the surface of a slab of metallic material. The calculations may also be performed for the same configurations, but without a crack, and the crack signal obtained by subtraction. The model is illustrated in Figure 1.

An example of the calculated fields in the absence of a crack is shown in Figure 2, where the complex Poynting vector (energy flux) is plotted as a function of position on the surface of the slab. For the case illustrated, the wire center separation and liftoff are both one skin-depth δ (= $2/\sigma\omega\mu$ where σ is the conductivity of the test material, ω is the angular frequency, and μ the permeability). (For aluminum at 100 MHz excitation, δ is 0.25 mm). In the figure, the real part of the Poynting vector, corresponding to dissipative loss, is marked by squares; the imaginary part, corresponding to inductively stored energy flux, is marked by circles. With a crack present the curves are modified, as may be seen in Figure 3, where the crack depth is 2.0δ and the opening is 0.5 (corresponding to 0.5 mm depth and 0.13 mm opening in the example for aluminum). In Figure 4, the coil is positioned at 0.8δ from the crack center. These curves give a physical picture of the electromagnetic fields and also show the quality of the level of approximation used. From the calculations which produce the fields over the surface of the metal it is also possible to obtain the impedance modification of the wires, which is the principal measured quantity in a testing situation. From a series of these calculations, the impedance was obtained for a scan of the coil over the region of the crack. The results are shown in Figure 5, where the phase and magnitude of the impedance of the wires, per unit length, are shown as a function of distance, P, from the crack.

The extension of these calculations to cover a range of frequencies is now in progress. The results will be compared with the experimental and theoretical investigations of Dr. C. M. Fortunko at NBS Boulder, and of Dr. B. A. Auld of Stanford University.

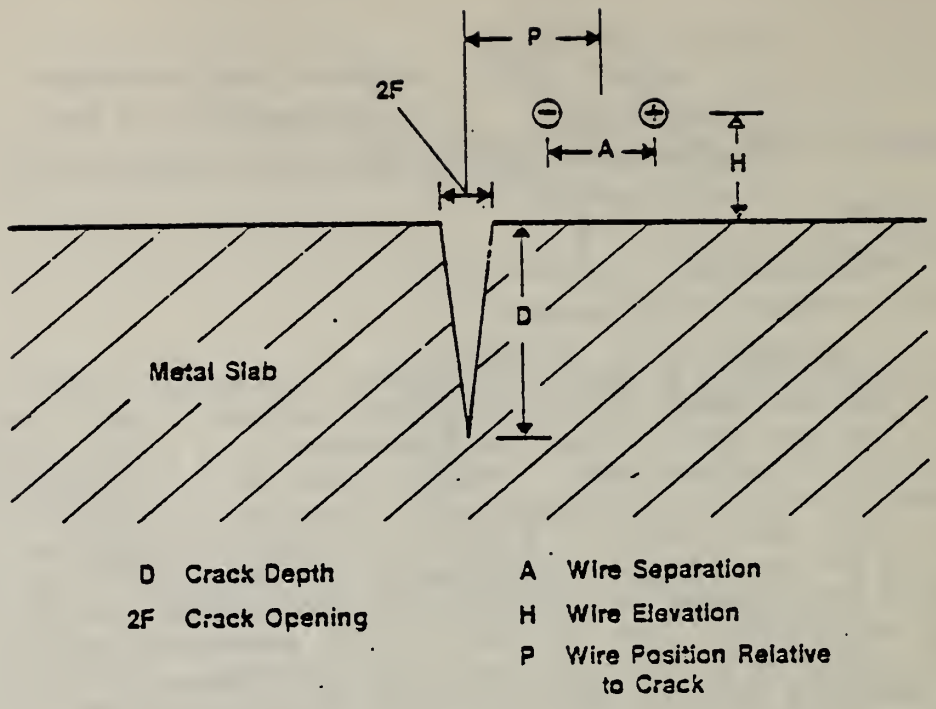

Figure 1 Schematic drawing and nomenclature for the model used for the calculation of eddy current crack signals.

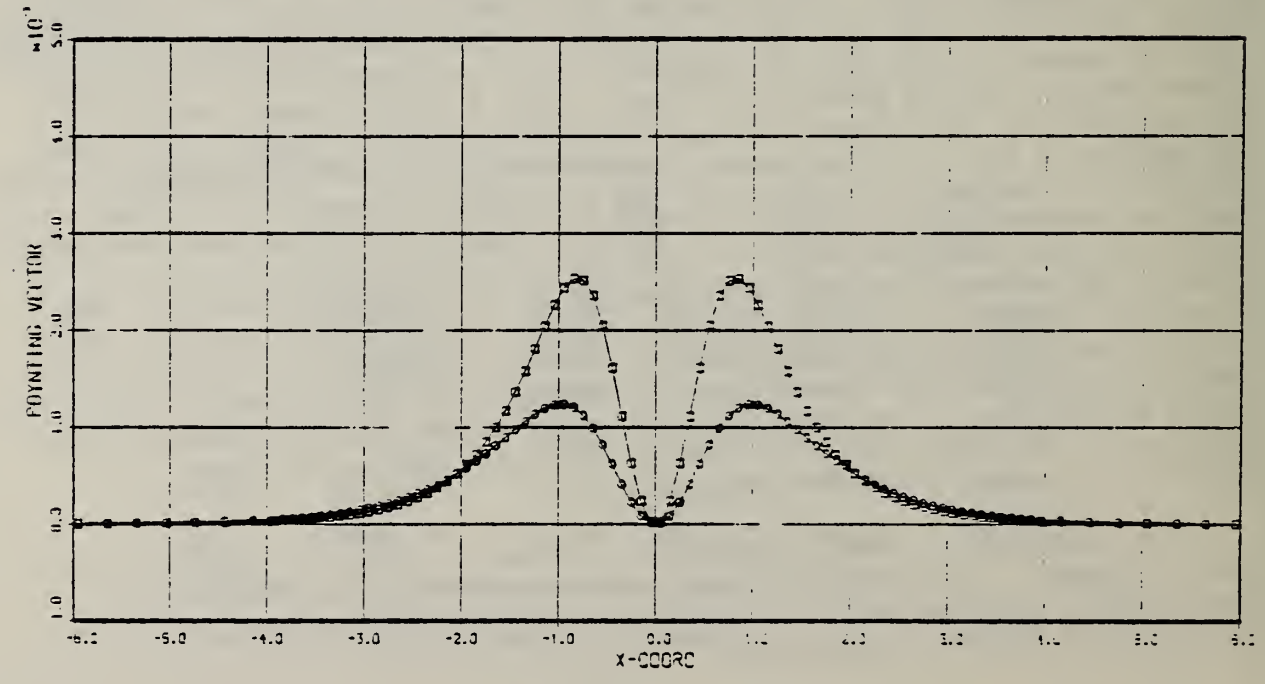

Figure 2 Poynting vector at the surface of a metal slab with no crack. Parameters are as described in the text. The real part (energy loss) is shown by squares; the imaginary part (energy stored) by circles.

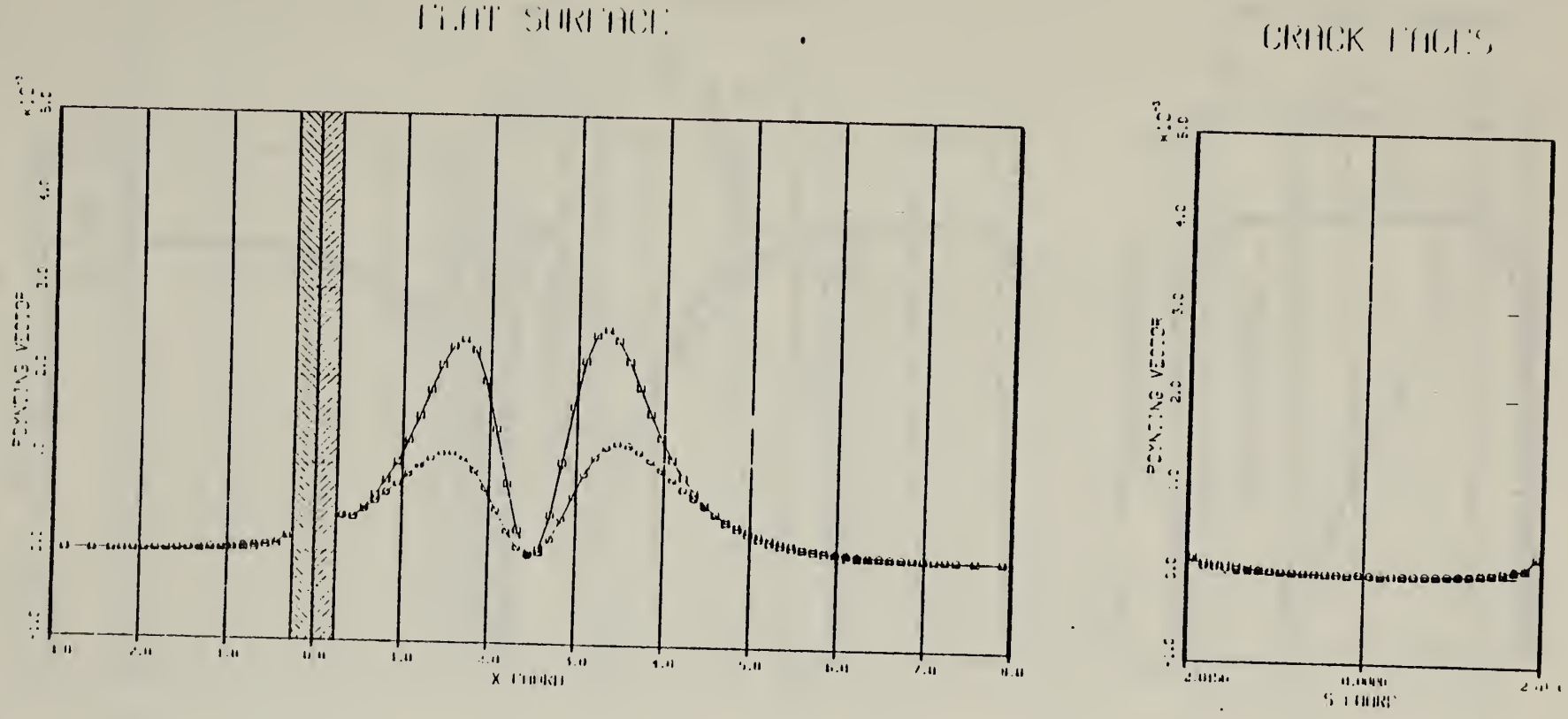

Figure 3 Poynting vector at the surface of a slab with a crack for the same geometry as in Fig. 2. The coil is centered at P = 2.5. The crack region is indicated by the cross-hatched area; the Poynting vector is plotted on the right for the crack, which is shown unfolded.

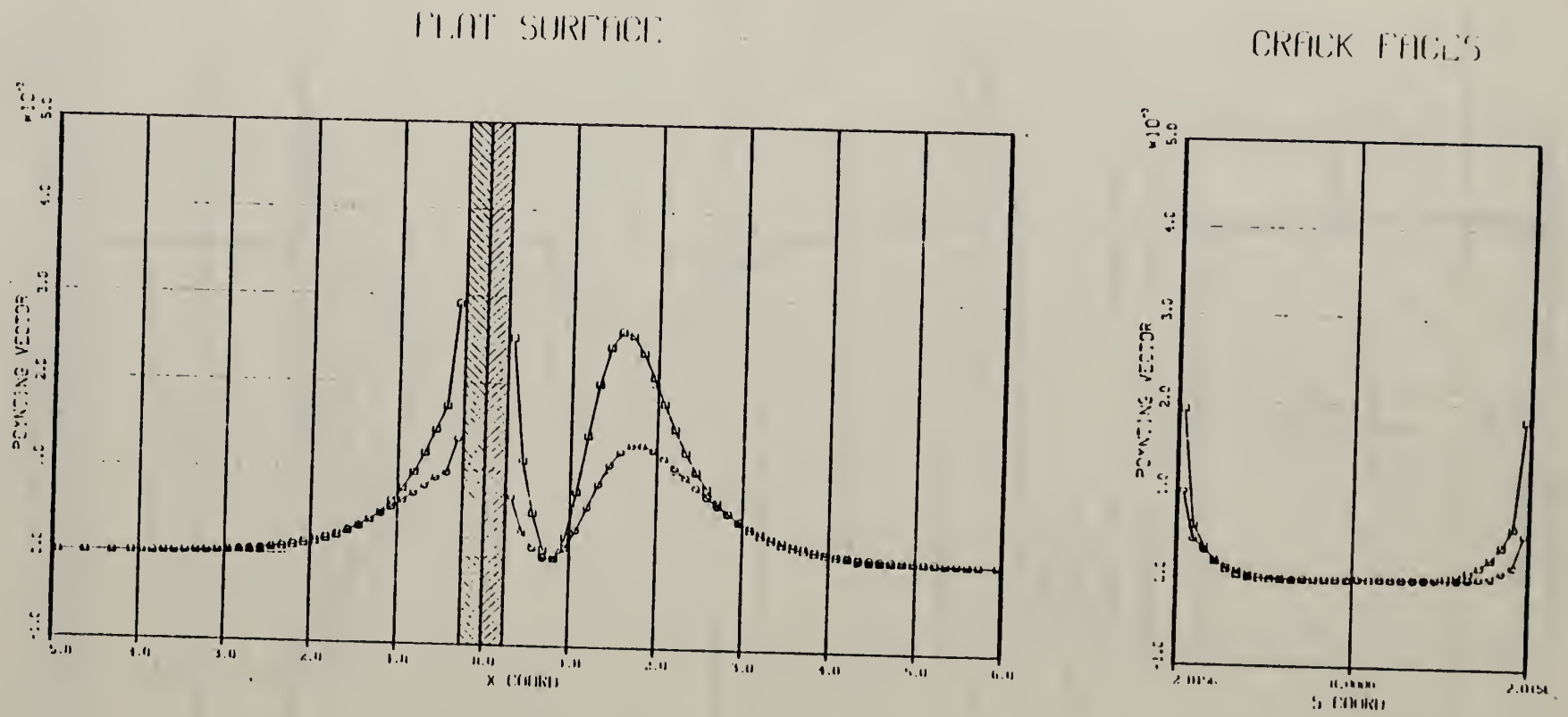

Figure 4 Poynting vector at the surface of a slab with a crack, for the same geometry as in Fig. 2 and Fig. 3. The coil is centered at P = 0.80.

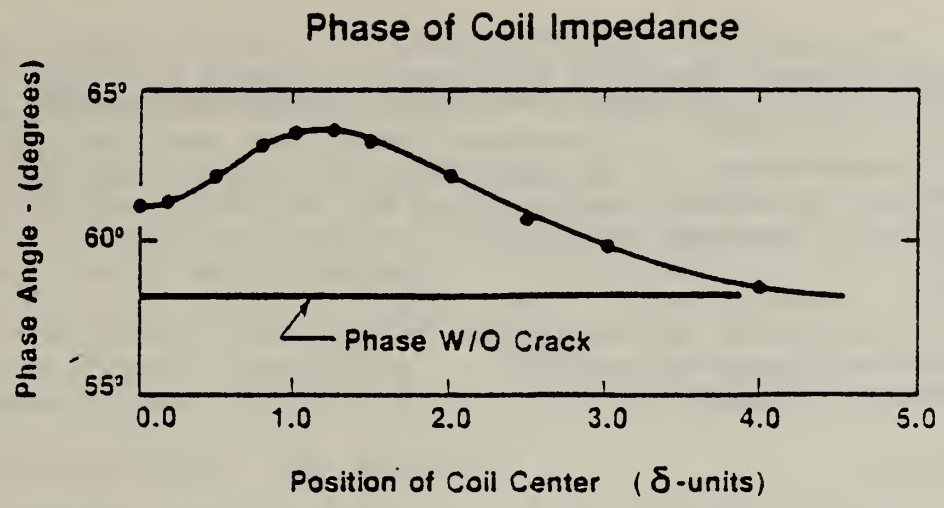

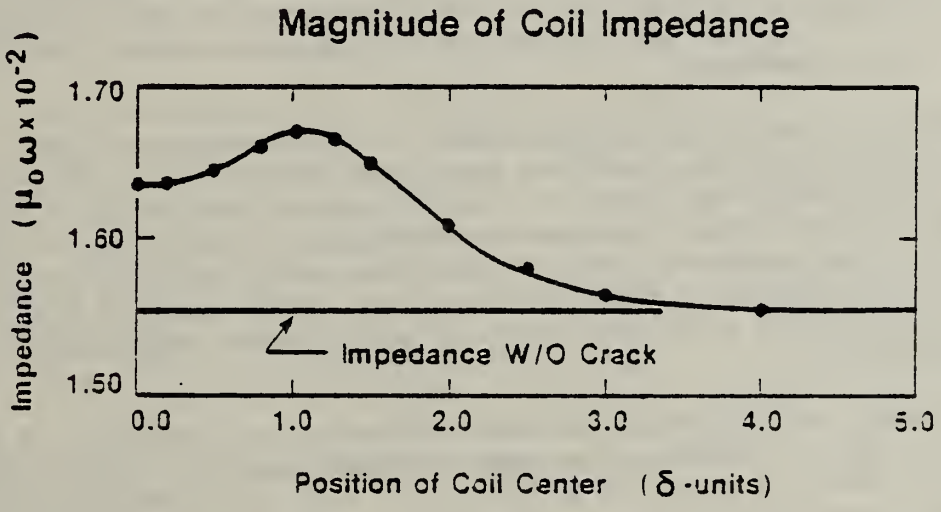

Figure 5 Computed phase and magnitude of coil impedance as a function of coil center position, P.

HIGH-FREQUENCY, BROADBAND EDDY-CURRENT PROBES FOR IMPROVED FLAW CHARACTERIZATION

C. M. Fortunko, J. C. Moulder, J. Gerlitz, and A. C. Bennett
Fracture and Deformation Division
Center for Materials Science

and

B. A. Auld and F. G. Muennemann
Edward L. Ginzton Laboratory
Stanford University

INTRODUCTION

Eddy current techniques for nondestructive evaluation have been used in industry for many years, but current practice is largely qualitative and empirical in nature. Flaw identification and sizing usually are based on comparisons of the observed flaw signal with an atlas of measurements on known flaws of the type expected. This approach has been dictated by the lack of a firm theoretical basis for inferring flaw characteristics from actual eddy current signals. In recent years, however, theoretical interest in the eddy current inversion problem has quickened, stimulated by the increased interest in quantitative NDE that the concepts of fitness-for-purpose and retirement-for-cause have engendered.

Progress in modeling the interaction of an eddy current probe with a flaw has been rapid during the last five years, advancing from early studies of idealized two-dimensional flaws in a uniform field (ref. 1) to recent detailed analyses of three-dimensional flaws interrogated by a nonuniform probe field (refs. 2,3). The advances in theory have led to the design of procedures for extracting flaw parameters from multiposition, multifrequency eddy current data and have created a need for critical experimental measurements to verify model predictions.

The present collaboration between NBS and Stanford University was begun last year in order to address the need for measurements of eddy current flaw responses to verify theoretical predictions. The work at Stanford has focused on theoretical modeling of flaw responses as a function of flaw parameters, probe geometry, material properties, and frequency of operation, as well as experimental measurements at very high (microwave) frequencies. The NBS effort has been directed towards developing and characterizing new high-frequency, broadband eddy-current probes. During FY82, a broadband probe design was developed and a prototype version was constructed and used to make measurements on a series of well characterized calibration specimens. The theoretical model and the results of these preliminary measurements are summarized in reference 3.

During FY83, NBS efforts emphasized further development and characterization of broadband eddy-current probes and new experimental measurements. Specific accomplishments this year included: 1) a coil-winding fixture was developed that improves considerably our ability to fabricate eddy-current sensor coils; 2) a computer model for the broadband probe was devised and used to optimize and characterize the probes; 3) two new eddy-current probes were developed covering the frequency range of 100 kHz to 1 MHz and 20 to 80 MHz; 4) the eddy-current apparatus was improved by interfacing it to a digital voltmeter controlled by a hand-held computer; 5) a series of measurements were made on an Inconel 718 calibration specimen supplied by Rockwell International to verify and characterize the high-frequency probe response. Progress in these areas is described below.

BROADBAND EDDY-CURRENT PROBE DEVELOPMENT

A novel coil-winding fixture was developed to facilitate the fabrication and matching of flat, spiral-wound, pancake coils for eddy current probes. The fixture considerably reduces the amount of time required for fabricating a coil and produces flat, uniform coils reproducibly from smaller gauge wire than it was possible to use with previous manual techniques. The fixture has made it possible to produce coils of sufficiently high impedance (10-50 ohms) that transformers are no longer required to match the coil impedance to the input impedance of the four-port hybrid, resulting in a significant simplification of the hybrid design. The possibility of patenting this coil-winding fixture is currently being explored.

A significant improvement was made in the design of the four-port hybrid used as the inductance bridge for the broadband eddy-current probe. By optimizing the inductance of the balun transformer, it was possible to minimize the inherent imbalance signal while maintaining sensitivity to flaw signals. Optimization was accomplished through the use of extensive computer simulations described below. A circuit diagram of the improved broadband eddy-current probe is shown in Figure 1 . Using the new design, a new high-frequency eddy-current probe was constructed for operation in the 20 to 80 MHz band. This new probe is particularly well suited for detecting very small flaws in highly resistive materials such as Inconel 718. In addition to the new high-frequency eddy-current probe, a new four-port hybrid was constructed for use with commercial eddy-current probes in the 100 kHz to 1 MHz frequency range.

In order to efficiently design and characterize broadband eddy-current probes, it is advantageous to have a model of the probe circuit that can predict the response of the probe to changes in such circuit parameters as coil impedance, component values, or frequency of operation. Unfortunately, the circuit is too complex for an analytical approach to be tractable, so that numerical modeling is required. Although there are several commercial circuit analysis programs available for laboratory minicomputers, these programs invariably use a form of nodal network analysis not readily adapted to transformer circuits. So an effort was undertaken to develop a simplified circuit model that could be solved with standard numerical techniques.

The lumped-parameter circuit model that was developed is shown in Figure 2 . Several simplifying assumptions were made in order to make the problem more tractable. Using Kirchoff's law to write the loop equations for the 4 currents shown in the figure yields the following complex matrix equation:

$$\begin{bmatrix} (Z_1 + Z_2 + Z_3 + R_0) & j\omega M_3 & j\omega(M_2 + M_3) & (Z_3 + R_0) \\ j\omega M_3 & (Z_1' + Z_2 + Z_3) & Z_3 & j\omega(M_2 + M_3) \\ j\omega(M_2 + M_3) & Z_3 & (Z_2 + Z_3 + R_0) & (R_0 + j\omega M_3) \\ (Z_3 + R_0) & j\omega(M_2 + M_3) & (R_0 + j\omega M_3) & (Z_2 + Z_3 + 2R_0) \end{bmatrix}^{-1} \begin{bmatrix} 0 \\ 0 \\ V_0 \\ V_0 \end{bmatrix} = \begin{bmatrix} I_1 \\ I_2 \\ I_3 \\ I_4 \end{bmatrix} \quad (1)$$

This equation is readily solved with standard methods for the four unknown currents, given the appropriate values for the impedance matrix and input voltage, V_0. The output voltage of the probe may then be found from the expression

$$V_1 = (I_1 + I_4)R_0 \quad (2)$$

A computer program was developed to solve Equation 1 by Gauss-Jordan elimination. Inputs required for the program are the measured impedances of actual circuit components and the input voltage. By holding the impedance of one coil fixed while varying the impedance of the other coil and solving Equations 1 and 2 iteratively, the probe response to a simulated flaw may be determined. The results of two such simulations are shown in Figure 3 .

EXPERIMENTAL MEASUREMENTS

In order to verify and characterize the performance of the new high-frequency eddy-current probe, a series of measurements were undertaken on a calibration specimen of Inconel 718. Each measurement was repeated 15 times to provide adequate data for statistical analysis. In addition, it was hoped that the data would prove useful for verification of theoretical predictions in the important region of $a/\delta = 0.5$ to 1.5, where a is the flaw depth and δ is the skin depth.

The experimental apparatus used for these measurements was essentially the same as that used last year. In order to improve the precision of the measurements, a digital voltmeter controlled by a hand-held computer was used to monitor the analog output of the vector voltmeter. The use of the hand-held computer also facilitated data analysis.

The calibration specimen used in the experiments consisted of an Inconel 718 bar, 13 x 75 x 300 mm, with a number of slots electro-discharge machined into one surface. Three flaws were chosen for the measurements; the flaw dimensions are given in Table I. The specimen was prepared by the Rocketdyne Division of Rockwell International and loaned to NBS for this study by Mr. J. L. Nummelin.

As discussed in last year's report, the new broadband eddy-current probe does not include any provision for nulling the bridge circuit. Thus, the probe has an inherent imbalance signal, even when placed over unflawed metal. When the probe is placed over a flaw, the output signal is the sum of this bridge imbalance and the actual flaw signal. In order to determine the flaw signal, it is therefore necessary to independently determine the bridge imbalance so that it may be subtracted from the composite signal. The following procedure was developed for making measurements on the Inconel specimen. The composite signal is obtained by centering one of the eddy-current sensor coils over a flaw using fiducial marks on the probe and the specimen. The probe is firmly clamped in place and measurements taken at the target frequencies. The probe is then removed from the flaw, repositioned in a good area adjacent to the flaw, and reclamped. Measurements are then taken at the same frequencies to obtain the bridge imbalance signal. The entire procedure was repeated 15 times in order to establish the reproducibility of the measurements. The liftoff signal was determined in separate experiments by inserting a series of spacers under one of the eddy-current coils and measuring the output of the probe at the target frequencies.

The data for each frequency were analyzed by averaging the 15 bridge imbalance measurements to obtain an average bridge imbalance signal. This average bridge imbalance was then subtracted vectorially from each of the composite "flaw plus imbalance" signals to obtain 15 independent measurements of the flaw signal. These 15 flaw signals were averaged to yield the average flaw signal. All averages were computed by separately averaging the in-phase and quadrature components of each signal.

The results of this series of measurements are shown in Table II, together with the liftoff phase angle. The results clearly show the ability of the probe to detect very small flaws in highly resistive material, such as Inconel 718. Unfortunately, the depth-to-width ratio is too close to unity for these flaws for a meaningful comparison with theoretical predictions, as is evidenced by small angles between the liftoff phases and the observed flaw signals.

THEORETICAL MODELING

As mentioned in the introduction, there has been rapid progress recently in theoretical modeling of two- and three- dimensional flaws interrogated by non-uniform probe fields. All such models require as an input a detailed description of the probe magnetic field distribution in both phase and amplitude. Such a field distribution is highly dependent on a number of parameters which are independent of the physical and electrical characteristics of the probe, e.g., conductivity of the test piece, probe liftoff, operation frequency, etc. For this reason, much of the theoretical effort during FY83 was directed to the development of a rationalized calibration scheme, together with analyses which allow the computation of probe fields under different circumstances. This procedure requires only the distribution of the probe's tangential magnetic field on a single liftoff plane, measured (or calculated) in air, to compute magnetic field distributions for any

liftoff and test sample conductivity. Such a procedure is also very valuable in the probe calibration effort, since it provides a basis for reproducible measurements which can be made on a variety of different samples.

Fourier methods were used to perform this calculation. First, the tangential magnetic field is transformed to the two-dimensional Fourier domain; each spatial frequency component of this transformed field is then multiplied by a propagation factor of the form

$$\exp[-k\ (z_2-z_1)] \tag{3}$$

where k is the magnitude of the spatial frequency, and z_1 and z_2 are respectively the measured and desired liftoffs. To accommodate samples having different conductivities, one also multiplies by a reflection factor, $(1 - \Gamma)$, which is given by

$$\Gamma(k) = \omega\mu[\omega^2\mu\varepsilon - k^2]^{-1/2}. \tag{4}$$

For most metals, this can be expressed in terms of the skin depth, δ, as

$$\Gamma(k) = [2/i\delta]\ [1 + k^2\delta^2]^{1/2}. \tag{5}$$

The resulting field distribution is the spatial transform of the original field, but in a new reference plane and in the presence of a conducting plane. A two-dimensional inverse Fourier transform is then performed to recover the actual field.

A preliminary test has been performed on this numerical procedure. The magnetic field distributions for horizontal and vertical dipoles were calculated, using an analytic formula for the spatial-transform field, for a given distance from the point dipole source. These were then transformed, using the above procedure, to a different plane, and the result compared to the value calculated directly from the analytic formula. These were in very good agreement, showing only numerical round-off errors. The comparison for the full transformation procedure is presently underway.

One limitation with this theory is that the transformed liftoff distance, z_2, must be larger than the measurement liftoff z_1. It is therefore most advantageous to make calibration measurements as close to the probe as possible.

FUTURE STUDIES

From the results of this year's work, several areas that would be fruitful for future work have been identified. First, in order to facilitate the comparison of experimental measurements with theoretical predictions, it will be necessary to make measurements on flaws with much higher depth-to-width ratios, perhaps actual fatigue cracks. Second, a means to calibrate the probes is required so that the actual flaw impedance may be determined from measured flaw signals. Third, since eddy current inversion protocols involve multiposition, as well as multifrequency, data, it is

necessary to systematically study the probe response for various probe-flaw configurations to understand in detail the probe behavior in the scanning mode.

REFERENCES

1. A. Kahn, R. Spal, and A. Feldman, "Eddy Current Losses Due to a Surface Crack in Conducting Material," J. Appl. Phys. 48, pp. 4454-4459 (1977).

2. B. A. Auld, F. G. Muennemann, M. Riaziat, and D. K. Winslow, "Analytical Methods in Eddy Current NDE," in Review of Progress in Quantitative Nondestructive Evaluation, (D. O. Thompson and D. E. Chimenti, eds.), pp. 363-368 (Plenum, 1982).

3. F. G. Muennemann, B. A. Auld, C. M. Fortunko, and S. A. Padget, "Inversion of Eddy Current Signals in a Nonuniform Probe Field," to be published.

Table I. Flaw dimensions for rectangular E.D.M. notches in Inconel 718 specimen.*

Flaw Number	Length mm (in)	Depth mm (in)	Width mm (in)
A - 1	6.396 (0.2518)	0.1245 (0.0049)	0.0914 (0.0036)
A - 4	2.619 (0.1031)	0.1270 (0.0050)	0.0940 (0.0037)
A - 7	1.298 (0.0511)	0.1168 (0.0046)	0.0965 (0.0038)

* Measurements made by A. Smith, Rocketdyne Metrology Lab.

Table II. Average flaw signals for three rectangular E.D.M. notches in an Inconel 718 specimen. Flaw dimensions are given in Table I.

Frequency (MHz)	Flaw Number	Average Flaw Signal		
		Magnitude (mV)	Phase (deg.)	Angle to liftoff (deg.)
20	A-1	0.044	66.3	5
	A-4	0.045	70.6	0
	A-7	0.029	74.0	-3
25	A-1	0.032	167.7	3
	A-4	0.041	164.6	6
	A-7	0.030	165.3	6
30	A-1	0.053	164.9	5
	A-4	0.063	161.2	9
	A-7	0.046	162.1	8
35	A-1	0.061	169.5	-7
	A-4	0.086	154.0	8
	A-7	0.067	153.6	8
40	A-1	0.187	150.8	-3
	A-4	0.227	140.5	7
	A-7	0.158	142.9	5

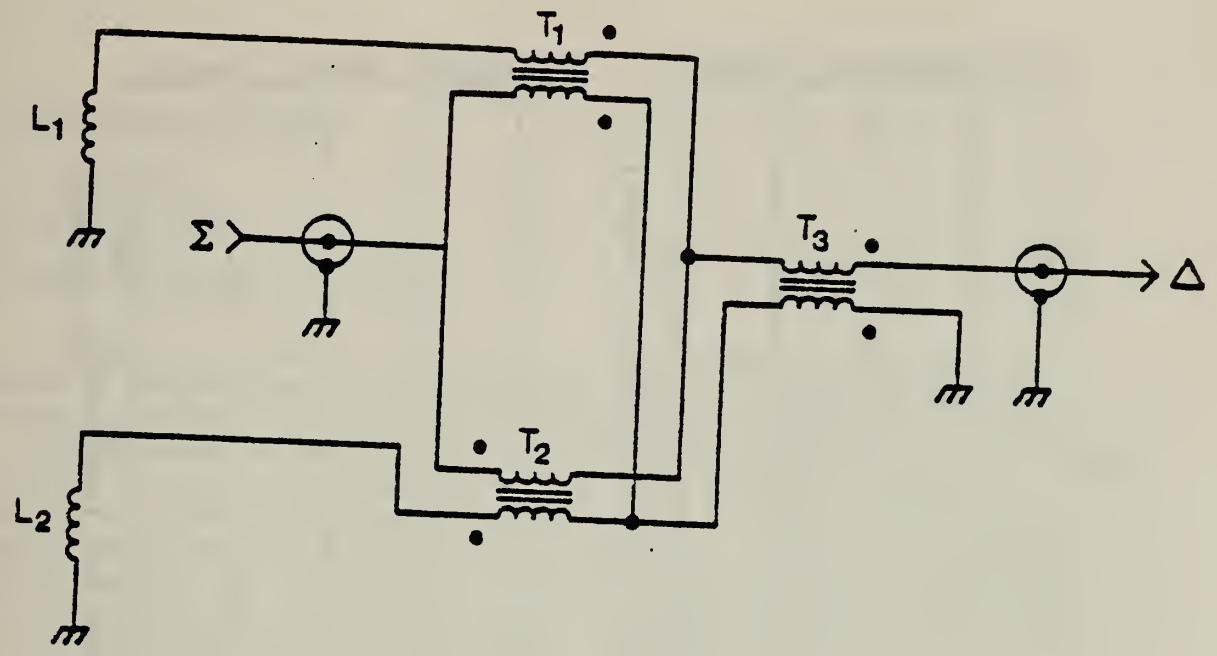

Figure 1 . Improved broadband eddy-current probe design. L_1 and L_2 are the eddy-current coils; T_1 and T_2 are identical transformers precision-wound on ferrite cores; and T_3 is the balun transformer, also wound on a ferrite core. Excitation voltage is supplied to the Σ-port and the eddy-current signal is extracted from the Δ-port.

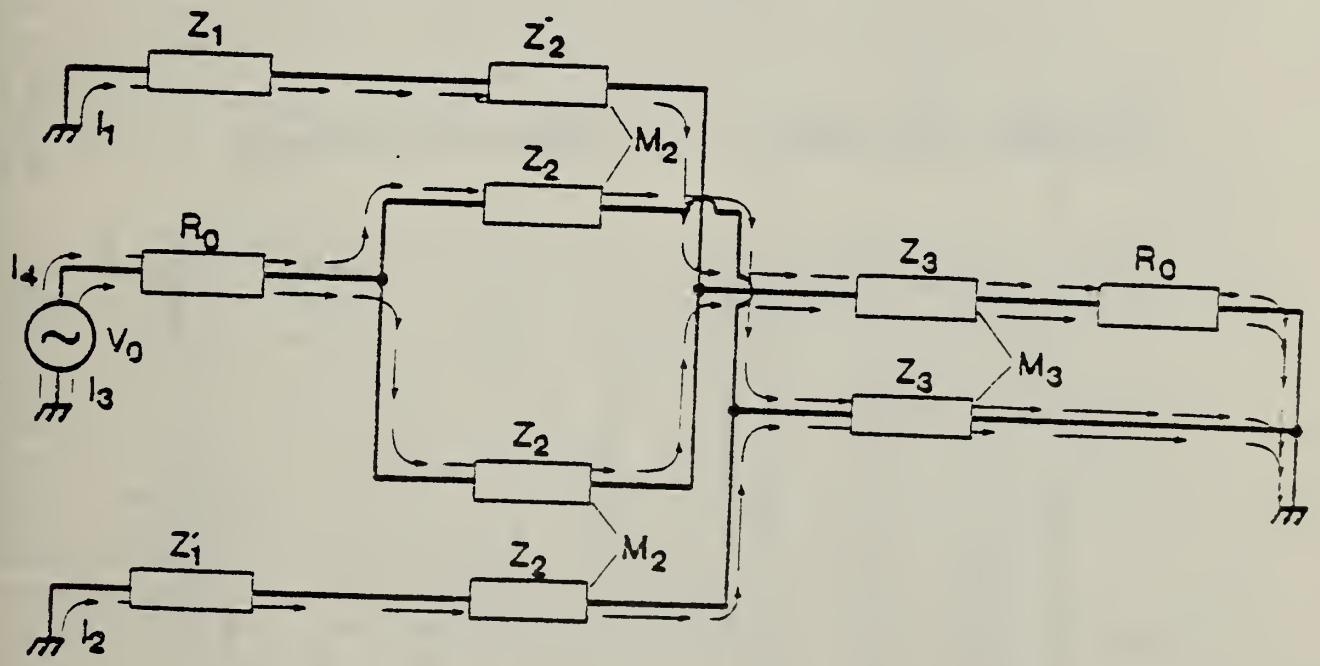

Figure 2 . Lumped-parameter circuit model for the broadband eddy-current probe shown in the preceeding figure.

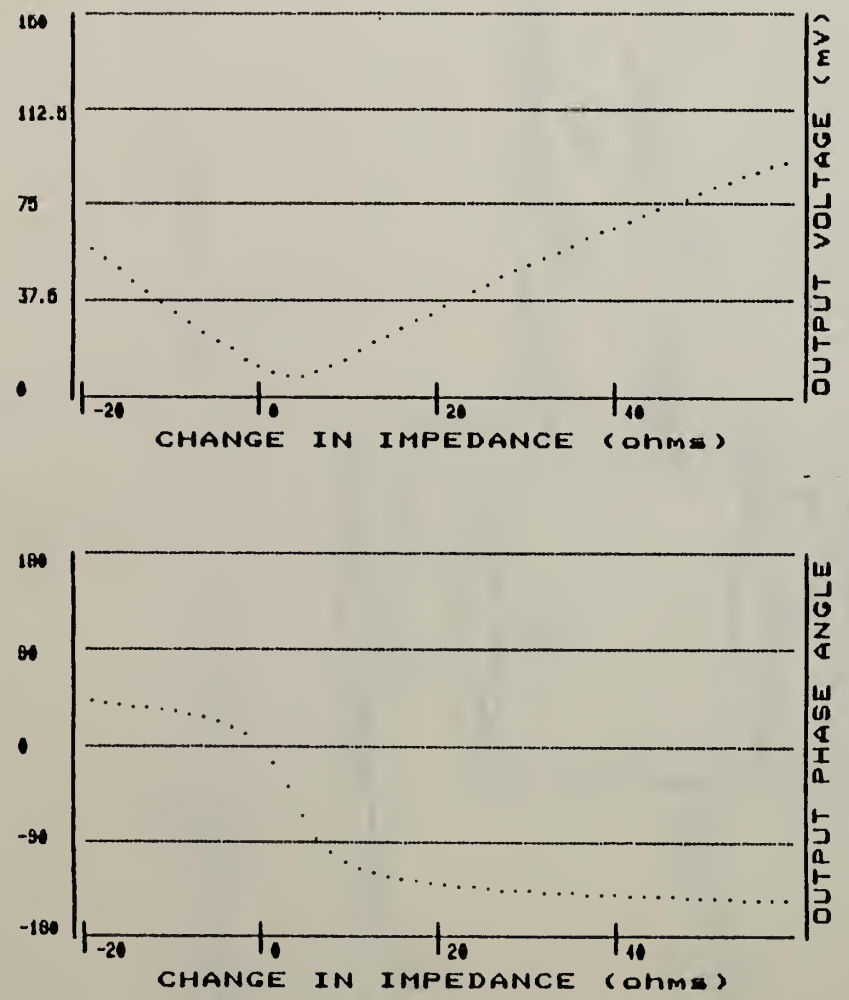

(A)

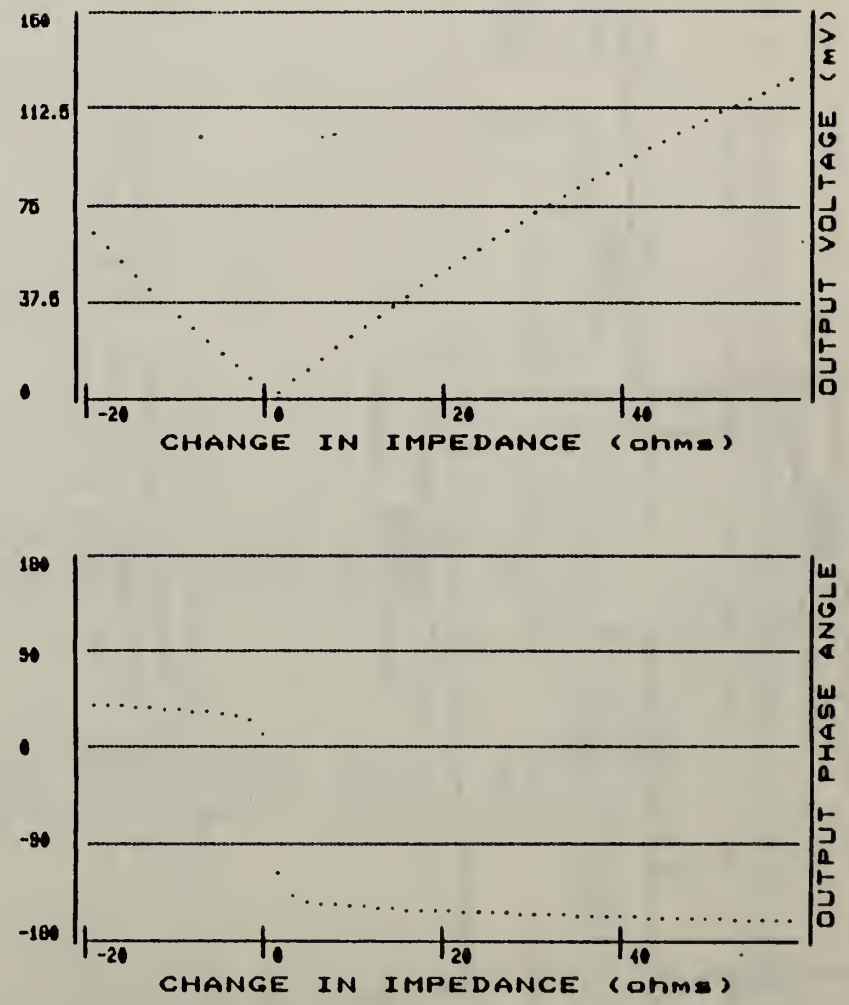

(B)

Figure 3 . Results from computer simulations of broadband eddy-current probes. (A) Results obtained using original design parameters. (B) Improved response obtained after optimizing design parameters. Sensitivity of the probes is proportional to the slopes of the response curves.

ELECTROCHEMICAL NOISE

Ugo Bertocci

Metallurgy Division

Center for Materials Science

Localized corrosion is a serious practical problem caused by the breakdown of the passive film, and affects most corrosion-resistant materials. Its detection is often difficult, particularly at an early stage. Electrochemical noise analysis, that is, the analysis of the random fluctuations in electrochemical cells, has shown promise to become a method for observing film breakdown, since there is correlation between the amplitude of the noise and the magnitude of the localized corrosion. The method might have applications for monitoring the onset of localized corrosion and for the study of the stability of protective films. At the present time little is known on the sensitivity of the method or on its applicability to different corroding systems.

Over the past year, a study has been made of the breakdown of the passive film on aluminum in neutral solutions. The stability of the film was checked by measuring the fluctuations of the passive current in the absence and in the presence of chloride ions at different potentials. The results obtained are quantitatively similar to those obtained for Fe-Cr alloys, since breakdown was detected only where Cl^- ions were present. This indicates that this method can be applied for the monitoring of passivity breakdown also in the case of Al. Current transients during the induction period were recorded, together with their amplitude spectra. The amplitude of the transient is quite small, of the order 10 to 30 nA, and the slope of the spectra is consistent with repassivation times of the order of one second.

The relationship between noise amplitude and degree of localization of anodic attack has been investigated. The correlation between localized attack and the NDE method of measuring electrochemical noise levels, and the independence, on the other hand, of noise amplitude or the rate of anodic dissolution was confirmed by measurements during the transpassive dissolution of glassy Fe-Ni-Cr alloy, which has no tendency to pitting; very low current noise was observed even when the anodic dissolution proceeded rapidly at more than 1 mA/cm^2. An alloy of the same composition but in crystalline form, which is subject to localized attack, showed a much higher level of current noise. In the course of this research, characterization of the electrode behavior by measurement of the ac impedance was carried out employing white noise as input signal with excellent results. These measurements, giving both the real and imaginary parts of the electrode impedance, were taken both in passive and in transpassive conditions, and ranged from 24 mHz to 5 kHz, showing that white noise is a convenient means for ac impedance measurements.

OPTICAL NDE: LIGHT SCATTERING

G.S. White

Inorganic Materials Division

Center for Materials Science

Light scattering measurements have been made upon grooves with trapezoidal cross sections in order to determine if the observed scattering could be described by a simple Fraunhofer calculation and to compare the observed scattering with that from grooves of simple cross section (shallow rectangular and V-shaped).

The simple Fraunhofer approach which worked well for describing scattering from the shallow rectangular groove (ref. 1) has not been amenable to expansion to the trapezoidal case. The calculated scattering has consistently been more complex than the observed scattering, although the envelope of the calculated scattering has approximated what is observed. It appears that the model used is too local for it to provide realistic scattering. Because the narrow two trapezoids have dimension A = 50 μm, a = 20.2 μm, h = 21 μm, and A = 68.9 μm, a = 21 μm, h = 27 μm, where A and a are the top and bottom widths of the trapezoid, respectively, and h is the depth, these two grooves lie in or near the resonance domain. In this region where the dimensions of interest are about the same as the wavelength being used, a local theory would be expected to be inadequate. The vector theory of Maystre (ref. 2), developed for the resonance domain, describes the observed scattering much more closely although discrepancies remain. As shown last year in the work with the V-shaped grooves (ref. 3), most of the discrepancy can be attributed to variations in the precise shape of the trapezoid cross section over the region of illumination. This is a combination of the Gaussian cross section of the incident beam and the departure from ideal uniform groove shape of the trapezoid. The latter is caused, not only by variations in A, a, and h across the illuminated area but also by metal displaced during the grooving process and left piled up along the length of the groove. As has been shown, this metal residue does not alter the number or spacing of the diffraction peaks but can change dramatically the relative peak heights.

Comparison of the scattering from the trapezoidal V-shaped grooves and shallow rectangular grooves produced clear differences. The scattering from the shallow rectangular groove was identical to that from an ideal single slit. Scattering from the V-groove produced a much different pattern with large narrow maxima at small angles, small maxima next and intermediate height, broad maxima at the largest angles. These large angle, large maxima must result from a combination of diffraction effects with specular scattering from the angled walls of the groove. However, because scattering in the resonance domain must be treated by fitting solutions to Maxwell's equations across the entire region of interest, it is clear that assigning specific scattering features to specific features of the groove is impossible. The trapezoidal groove produced scattering which appeared to be a combination of the other two patterns, due possibly to the fact that the trapezoidal shape contains flat regions corresponding to the rectangular groove and slanted

walls corresponding to the V-groove. Most interesting, however, is that these patterns seemed to scale with groove size. That is, a narrow trapezoid produced a scattering pattern clearly more closely related to that from a large trapezoid than to that from a narrow V-groove. Since the narrow grooves are in the resonance domain while the wider grooves are approaching the geometric scattering region, this scaling feature is somewhat surprising and is not yet understood.

REFERENCES

1. G.S. White and A. Feldman, "Diffraction from a Shallow Rectangular Groove," Appl. Opt. 20, No. 14, pp. 2585-2589 (July 1981).

2. D. Maystre, "Scattering from Perfectly Conducting Rough Surfaces in the Resonance Domain," IEEE Trans. Antennas and Propagation, submitted for publication.

3. G.S. White and J.F. Marchiando, "Scattering from a V-Shaped Groove in the Resonance Domain," Appl. Opt., 22, No. 15, 2308-2312 (Aug. 1, 1983).

OPTICAL MEASUREMENT OF SURFACE ROUGHNESS

E.C. Teague, T.V. Vorburger, F.E. Scire, D.E. Gilsinn, and M.J. McLay

Mechanical Production Metrology Division
Center for Manufacturing Engineering

There have been, over the last ten years, increasing efforts in the U. S. and the rest of the world to use light scattering rather than the traditional stylus instrument for nondestructive evaluation of manufactured parts. The theory of light scattering from surfaces whose irregularity heights are comparable to and larger than the wavelength of the light is more difficult and much less developed than that for highly polished surfaces. Light scattering has therefore been used primarily for comparison measurements of surface roughness. Our work has been directed towards building the experimental capability and theoretical expertise to investigate the behavior of light scattering measurements in terms of their use for both comparator and absolute determinations of surface roughness.

Our apparatus for performing angular distribution measurements, Detector Array for Laser Light Angular Scattering (DALLAS), has been described in previous ONDE annual reports. During the past year we have been analyzing the first sets of data and seeking to interpret the measured angular scattering distributions in terms of surface roughness properties, as determined by stylus measurements, and in terms of theoretical models of the electromagnetic scattering processes. Towards this end we are performing both direct and inverse scattering calculations.

In the direct scattering approach, the optical angular distributions and stylus roughness profiles are measured for the same rough surface. Typical angular distributions for lapped stainless steel surfaces are shown in Figure 1. The corresponding stylus profiles of these surfaces are shown in Figure 2. A theoretically predicted angular distribution is then calculated by substituting the digitized stylus profile into the integrand of an optical phase integral calculation based upon a simplified Kirchhoff solution for the scattering of electromagnetic waves, ref 1. Although the calculation involves only elementary scalar theory for optical scattering, the agreement between experiment and calculation is fairly reasonable.

Figure 3 shows one comparison. The data, solid line, which show scattered light intensity vs. scattering angle, were taken for a highly two dimensional specimen with a roughness of 0.20 μm, as measured with a stylus instrument. The angle of incidence was +30 degrees. Theoretical intensity values were calculated for the 87 angles that correspond to the angles of the detectors for DALLAS. Each calculated intensity value was obtained by averaging over seven closely spaced scattering angles within the angle subtended by the detectors of DALLAS and ten surface profiles.

The calculations in Figure 3 were performed after we had first attempted to obtain agreement between theoretically predicted and measured angular distributions for surfaces that were slightly three-dimensional in nature, i.e., surfaces with randomly shaped grooves that had a dominant direction but with some directional randomness. We have not yet been successful in obtaining a procedure to account for the directional randomness of these surfaces.

Agreement between theory and experiment for the inverse approach has not been as good as for the direct calculations. Here we attempt to calculate the rms roughness parameter Rq and the autocorrelation length T of the scattering surface. The calculation proceeds by assuming that the surface may be described by a statistical model characterized by these two parameters; a Gaussian height distribution function and an exp(-x/T) autocorrelation function are assumed. A two-parameter non-linear least squares fit between the measured and theoretical angular distributions is then calculated. Figure 4 shows the relatively poor agreement between the data and the calculated results which have been obtained with this model of this surface. The results, therefore, strongly suggest that the model is inappropriate for this surface. This is borne out by the fact that the autocorrelation function for this surface, as computed from stylus profile measurements (see Figures 5 and 6), is quite different from the exponential form assumed in the model.

Our plans for future work are to explore the use of more complex models of the surface topography, to explore alternative means for solving the inverse problem and to compare the direct scattering results obtained with different models for the electromagnetic scattering processes. Specific models to be compared are the Beckmann-Spizzichino model (used in the work described in this report), Maystre-Meecham projection distance approximation, Rayleigh model and possibly the geometric optics slope model for the larger roughnesses. Our work this year has clearly shown that, for scattering from rough surfaces, attempts to practically solve the inverse scattering problem must iteratively improve upon both the direct scattering model and the algorithm used for obtaining its inverse.

REFERENCES

1. P. Beckmann and A. Spizzichino, The Scattering of Electromagnetic Waves from Rough Surfaces (Pergamon, New York, 1963).

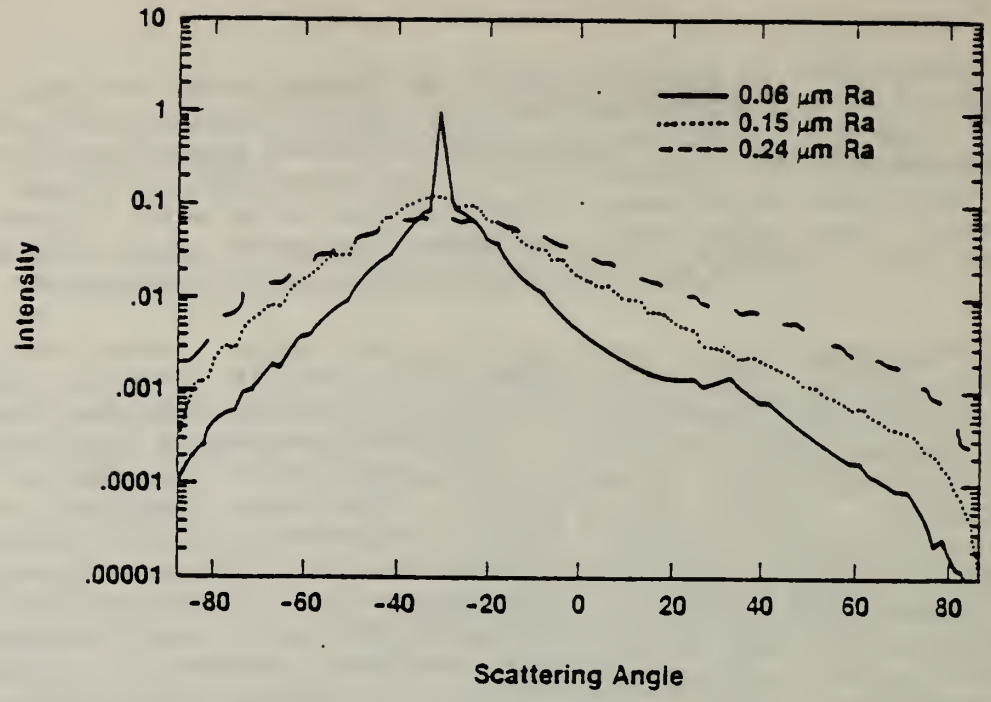

Figure 1. Angular scattering data for three lapped stainless steel specimens. The angular distributions are normalized so that each has the same total intensity. The total intensity is obtained by summing the signals from all the detectors. Note that the intensities are plotted on a logarithmic scale.

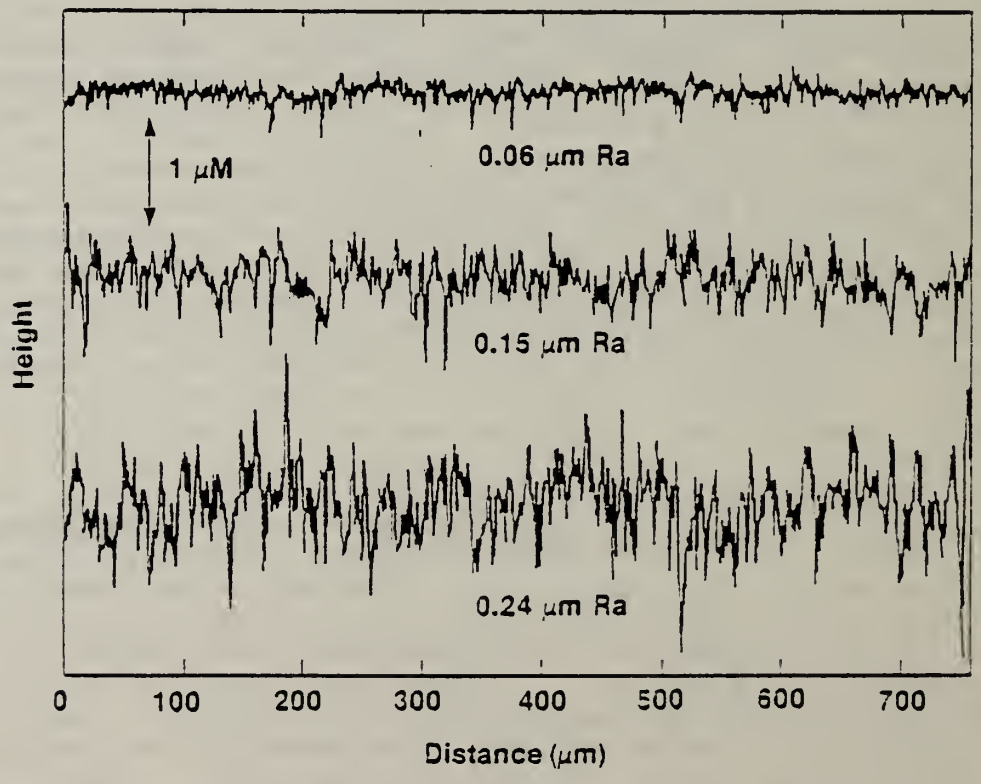

Figure 2. Stylus profiles of the surfaces used for the angular scattering measurements shown in Figure 1.

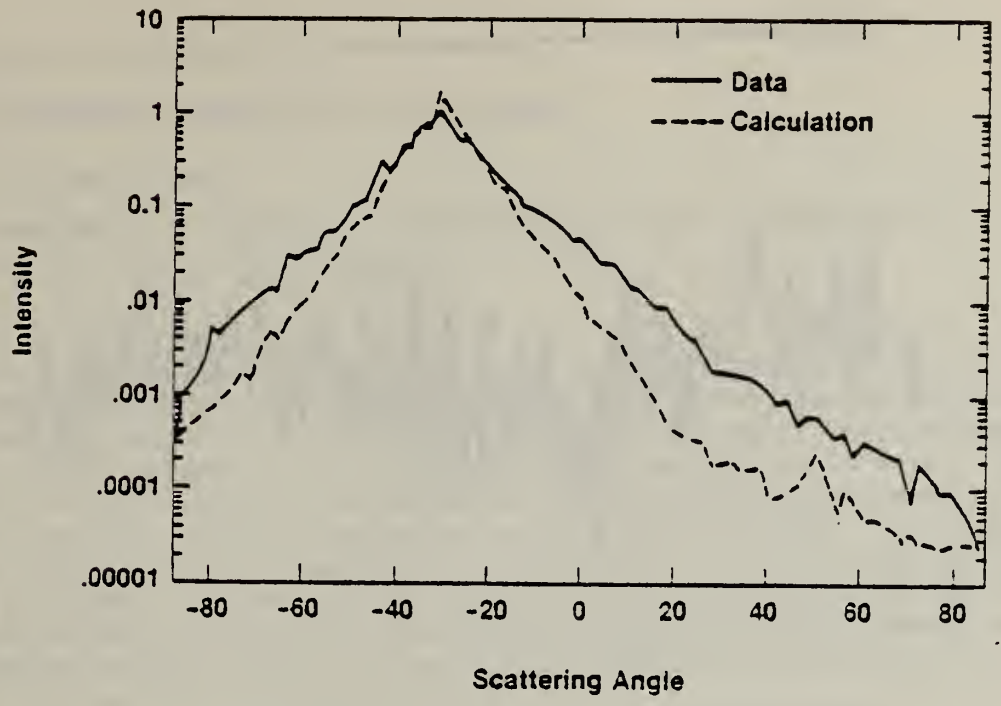

Figure 3. Comparison between theory and experiment for direct scattering calculation. The scattering surface had a roughness of 0.20 micrometers, as measured with a stylus instrument, and was a highly two-dimensional surface with a profile and an autocorrelation function as shown in Figures 5 and 6, respectively. The distributions were normalized in the same way as those in Figure 1.

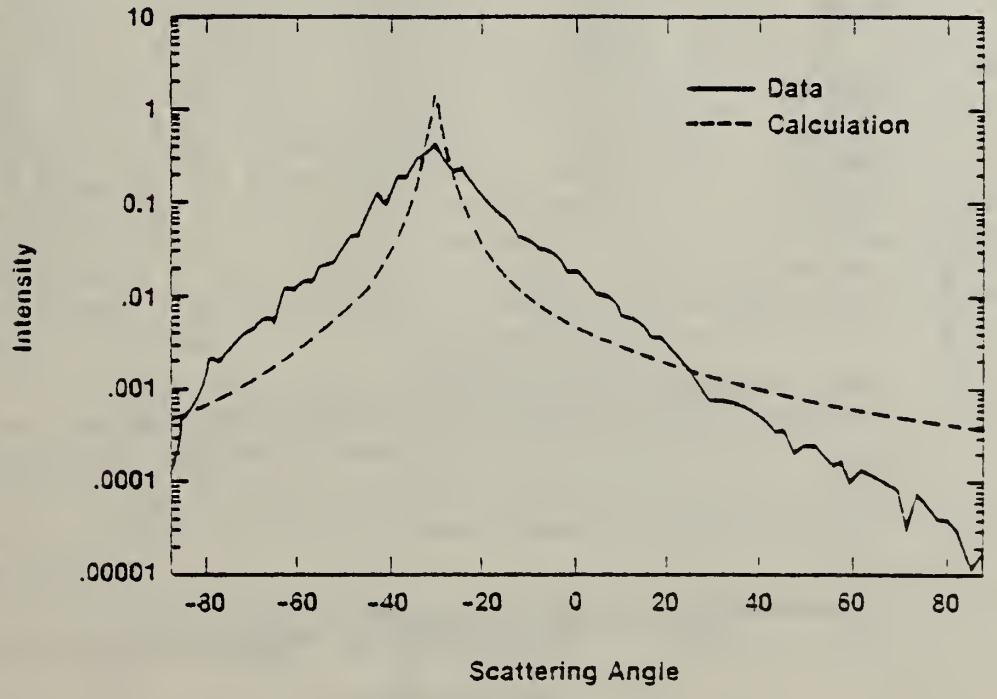

Figure 4. Comparison between theory and experiment for inverse calculation, optimized two-parameter fit. The specimen surface was the same one used for the direct calculations shown in Figure 3.

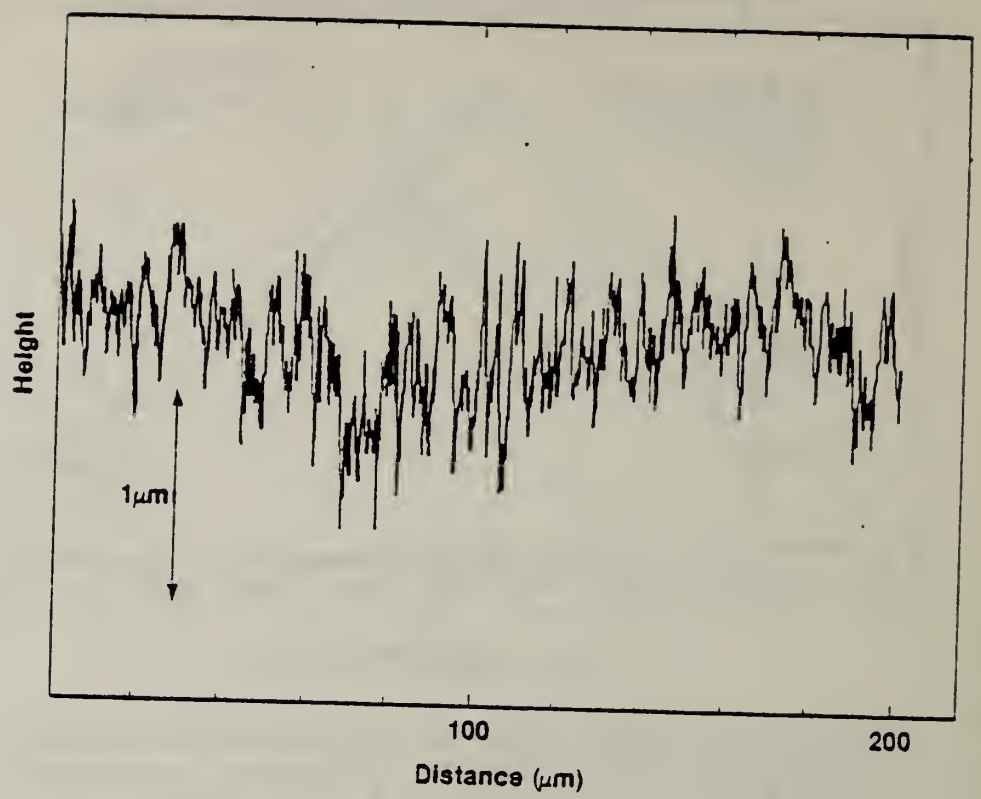

Figure 5. Stylus profile of surface used for calculations of Figures 3 and 4.

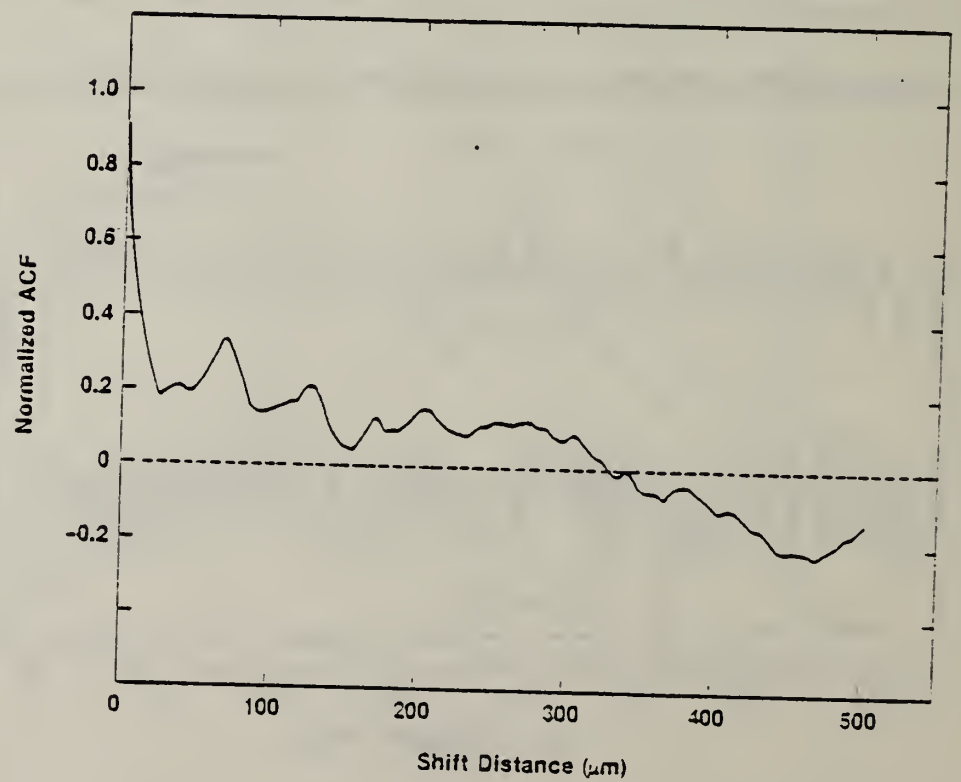

Figure 6. Autocorrelation function for the surface used for the direct and inverse calculations shown in Figures 3 and 4.

HOLOGRAPHIC NONDESTRUCTIVE EVALUATION

Charles M. Vest

Department of Mechanical Engineering and Applied Mechanics

The University of Michigan

During this year our exploration of the applications of optical holography to nondestructive evaluation was continued. This program was initiated a few years ago by preparing an extensive evaluative review of the technical literature of holographic nondestructive evaluation. Based largely on the results of that review a number of experimental investigations have been carried out in the areas of quantitative nondestructive evaluation and flaw detectability. During the past year we emphasized three areas. The first area was the use of moire techniques to enhance flaw detectability; the second area was development of a real-time technique for simultaneously measuring displacement and tilt in the neighborhood of a point on an object surface; the third area was updating of the evaluative literature review.

Two-exposure holographic interferometry produces a fringe pattern indicative of the surface displacement of an object. In its application to nondestructive evaluation, the presence of a flaw can be noted by comparing the fringe pattern produced by the flawed object with that produced by a nominally identical object with no flaw. Often, the defect may include only a small perturbation of the pattern and, therefore, it may be difficult to detect. Moire phenomena can be used to detect small perturbations in periodic patterns. If we superimpose a transparency of the interference fringe pattern of a flawed object upon the inteference pattern of a similar, but flaw-free, object, a moire pattern can be formed that is indicative of the presence of the flaw. In a typical interferogram, the fringe pattern varies over the surface of the object, so the application of moire techniques to flaw detection is less straightforward than application of these techniques to error detection in gratings that have constant periods. In particular, the clamping and stressing of the test and the flaw-free objects must be nearly identical if ambiguous or confusing moire patterns are to be avoided. In holographic nondestructive evaluation this is difficult to achieve. However, a practical testing scheme should present a clear indication of the flaw, unencumbered by extraneous moire fringes. For this reason we studied three techniques for improving moire detections of flaws in such interferograms (ref. 1):

1. Introducing a small relative magnification of the transparencies of the interferograms of the flawed and flaw-free components in order to compensate for small differences in stress level.

2. Forming a moire pattern by superimposing two transparencies of a single interferogram of the flawed component that differ only by a small relative magnification.

3. Utilizing digital image processing to form and enhance the moire patterns of techniques 1 and 2 above.

The goal of the application of each of these techniques us to produce a clear display of a flaw. In fact, our goal was to produce a closed moire fringe roughly outlining the flaw. The interferograms used were all formed by pressurizing an aluminum disk, which had blind-drilled holes or slots in its rear surface. The first experiments were done using superposition of photographic transparencies of the fringe patterns. Introduction of the relative magnification was very cumbersome to achieve. This led to the introduction of digital-image processing. A single interferogram of the flawed object was digitized and stored in a computer. A second magnified image of this interferogram was formed computationally. These two images were then multiplied and enhanced by the computer to produce the moire pattern. An example is shown in Figure 1. The flaw is clearly indicated by a light region on the left-hand side of the disk. We believe that the application of digital-image processing to forming and enhancing moire patterns has great potential and may be useful in industrial applications of NDT.

In recognition of interest in monitoring of small surface motions, we investigated a technique in which real-time holographic interferometry was performed with two very thin, parallel, closely-spaced object illumination beams in order to produce a time-varying irradiance which, when incident on a photodetector, gives a signal whose analysis indicates both the normal displacement and tilt at a point on an object surface (ref. 2). Figure 2 is a schematic diagram of the experimental system. P and Q are points on the object surface. The imaging system is composed of lenses L_1 and L_2. The hologram is recorded in plane H, and the points P and Q are imaged onto detector D. The output signal from the photodector has a function of time and is shown in Figure 3. A detailed analysis of the interference and detection process led to the interpretation of such signals. In essence, the fine structure of this signal indicates the normal displacement. (In this particular example a shift of one fringe corresponds to a displacement of 0.3 μm.) The zero crossings of the modulation of this signal indicate the tilt of the object. (In this particular example each pair of zero crossings corresponds to a tilt of 0.16 mrad.) It is hoped that this technique will be useful for monitoring motions due to transient phonomena such as stress wave propagation in solids.

REFERENCES

1. X.Youren, C. M. Vest and E. J. Delp, "Digital and Optical Moire Detection of Flaws Applied to Holographic Nondestructive Testing," Optics Letters 8, No. 8, pp. 452-454 (Aug. 1983).

2. Y. Xu and C. M. Vest, "Holographic Technique for Simultaneous Measurement of Displacement and Tilt," Applied Optics 22, No. 14, pp. 2137-2140 (July 15, 1983).

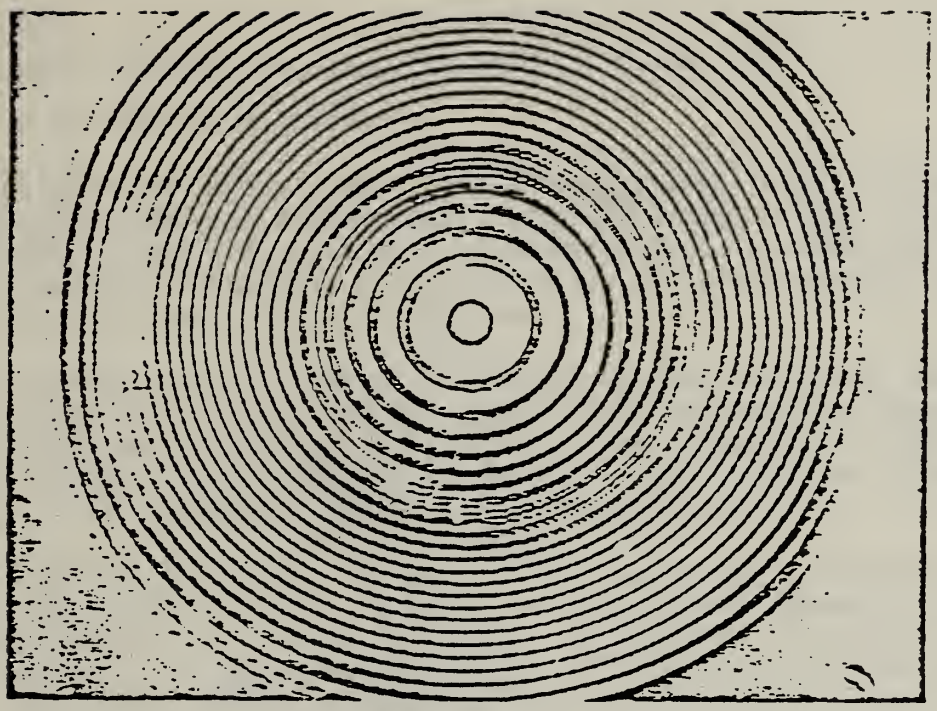

Fig. 1. Digitally-formed moire pattern. A flaw is indicated by the light region on the left side of the disk.

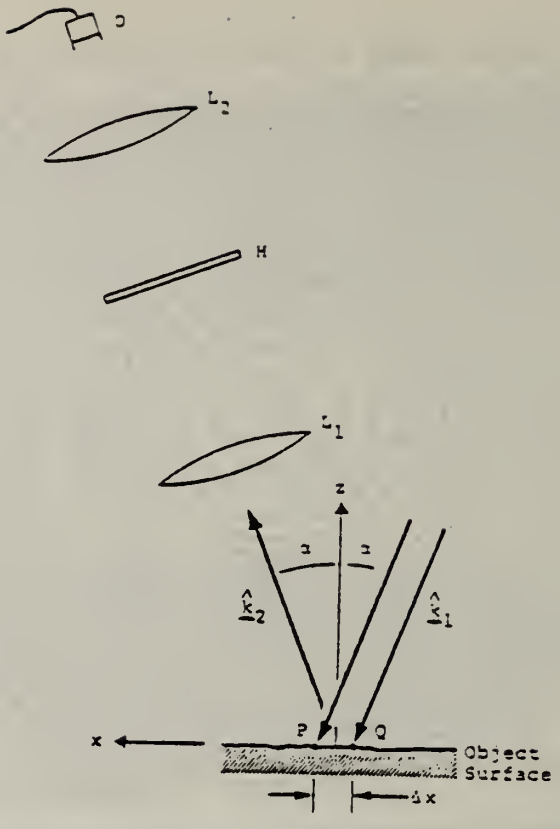

Fig. 2. System for real-time monitoring of surface displacement and tilt.

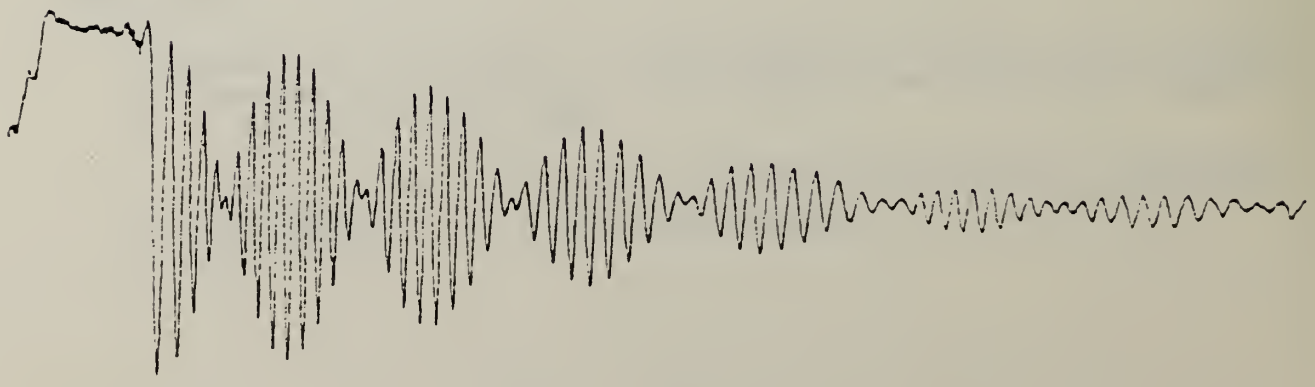

Fig. 3. Typical output signal of system shown in Fig. 2.

INFRARED METHODS OF NONDESTRUCTIVE TESTING

J. Cohen

Radiometric Physics Division

Center for Radiation Research

The purposes of this project, initiated last year, are 1) to develop expertise and maintain an awareness of infrared methods of NDT, especially thermography, as they are practiced in industry; 2) to evaluate the current and future needs for standards and traceability for these methods; and 3) to assess the Bureau's role in this area.

An intensive study of thermal imaging, including theory and system engineering was made, and a need for performance standards for thermal imaging systems was identified and brought to the attention of ASTM. As a result, a task force within ASTM subcommittee E7.10 has been formed, dedicated to the development of the performance standards.

NBS Technical Note 1177, "Elements of Thermography for Nondestructive Testing", was issued. This is intended to be a tutorial report in thermography, especially as it relates to NDT. It includes a treatment of performance measures, which likely will serve as a basis for an ASTM standard. Further, this investigator has begun to provide consultation service.

NDE OF BUILDING MATERIALS

James R. Clifton and Mary E. McKnight

Building Materials Division

Center for Building Technology

The determination of the engineering properties, quality, and uniformity of building materials is necessary to reliably predict service lives of materials in-place in both buildings under construction and in existing buildings. The technical feasibility of using NDE methods in the inspection of in-place materials is being assessed by laboratory and field studies. During the past year the use of NDE in improving quality assurance programs for building materials was explored. The state-of-the-art of quality assurance (QA)/quality control (QC) of building materials was addressed in a Federal Workshop (ref. 1). The most troubling quality problems with materials appear to be those resulting from on-site construction activities, as contrasted with fabricated components. The economic loss due to lack of QA/QC in the construction industry appears to amount to billions of dollars yearly. NDE methods which can be used in the quality acceptance of building materials were described in two publications (refs. 2 and 3). In another publication (ref. 4), results of research on the detection of cracks in concrete were presented. Future activities will be directed toward identifying improvements in the QA/QC NDE inspection of building materials which can be obtained by computer applications.

The development of an NDE method using scanning infrared thermography to evaluate the state of degradation of organically coated metal substrates was continued during the past year in a project sponsored by the Center for Building Technology. Information contained in the thermograms was quantified by digitizing the signal, associating degradation (ref. 5), i.e., blistering and corrosion, with gray level, and determining the fraction of area represented by each gray level. Further work to obtain size and location maps of the deteriorated areas is planned for next year.

REFERENCES

1. Federal Workshop on Quality Assurance of Building Materials, October 1982, NBS.

2. J.R. Clifton and N.J. Carino, "Nondestructive Evaluation Methods for Quality Acceptance of Installed Building Materials", J. Res. NBS, 87 (5), pp. 407-436 (1982).

3. J.R. Clifton, "Nondestructive Evaluation Methods for Quality Acceptance of Building Materials", Proceedings of 31st Defense Conference on Nondestructive Testing, pp. 95-109 (Nov. 1982).

4. L.I. Knab, G.V. Blessing, and J.R. Clifton, "Laboratory Evaluation of Ultrasonics for Crack Detection in Concrete", ACI Journal, 80 (1), pp. 17-27 (1983).

5. M.E. McKnight and J.W. Martin, "Nondestructive Corrosion Detection Under Organic Films Using Infrared Thermography", Proceedings of the 14th National SAMPE Technical Conference (Oct. 1982).

MICROHARDNESS REFERENCE MATERIAL STANDARD

David S. Lashmore

Metallurgy Division

Center for Materials Science

The Electrodeposition Group has developed two microhardness standards under contract with the Office of Standard Reference Materials. We hope that we can make 200 of these standards available to the public through OSRM by October 1983. The hardness ranges of these standards are 125 and 550 KHN and they will be certified at loads of 25, 50 and 100 grams. Preliminary results indicate that it may be possible to certify the standards to within $\pm$ 5 percent at all loads with both Knoop and Vickers indentors.

The standards were made using electroforming technology which yields an extremely uniform microstructure, and hence a uniform hardness. A comparison between a commercial standard and an electroformed standard is shown in Fig. 1 which shows the hardness variation with position.

Significant efforts in the packaging have resulted in a standard whose top and bottom faces are parallel to within 0.115 degrees and whose top face is metallographically polished flat. This packaging allows the standard to be used without an auxiliary leveling stage on the hardness tester. The standards have also been designed to withstand prolonged use in a corrosion laboratory environment.

Development of the certification procedures for these standards is now in the last stages. The procedure is in conformity with ASTM E92, B578, E384, but it has been necessary to go beyond the ASTM specifications to ensure that: (a) the load actually applied by the indentor is the load specified; (b) there is no impact (kinetic) loading or other artifact introduced by the testing machine; and (c) the optical measurement of the hardness impression is accurate. One of the problems that came up during the certification process is illustrated in Fig. 2a. In this load-time trace from a commercial hardness tester one can observe both an artifact at 10g, and some impact loading amounting to approximately 3 grams. The slope of the load-time curve is much too steep in this machine. It turns out that these phenomena are both independent of the applied load and independent of the cycle time, which is adjustable on this particular model. This error in loading might, in turn, produce errors as high as 12 percent at 25g. As we are aiming at $\pm$ 5 percent accuracy for the standards, clearly this machine is unsuitable. A much improved load-time characteristic is shown in Fig. 2b. Note the more gradual slope as the load is slowly increased, and the much reduced impact loading.

Vibration can introduce significant errors into the hardness measurement. An example of vibrational 'noise' is shown in Fig. 3a. Load errors can be extreme if someone 'taps' on the table, Fig. 3b, or slightly less if acoustic noise is present (e.g., a vacuum pump). In order to minimize these types of errors we have mounted the hardness tester on a heavy granite block and, in turn, mounted the block on a thick rubber pad.

Another source of error is introduced by using the low power (0.65 NA) objective lens normally supplied with the hardness tester to measure the hardness impression. This effect is illustrated in Table I.

A summary of the errors made in the complete measuring process is shown in Table 2. It would seem possible to certify the hardness numbers (both Vickers and Knoop) at 25, 50 and 100 grams at ± 5 percent accuracy and, for most cases, still maintain a factor of 2 for safety.

TABLE 1: COMPARISON OF 0.65 NA LENS WITH 0.95 NA LENS

	0.65 NA		0.95 NA	
Position	Vickers	Knoop	Vickers	Knoop
1	612.8	626.4	593.3	590.8
2	607.9	619.0	598.1	584.1
3	607.9	611.8	598.1	597.7
4	612.8	622.7	593.3	601.2
5	607.9	622.7	603.0	608.2
6	598.1	626.4	598.1	604.7
7	617.8	608.2	588.6	594.2
8	603.0	604.7	593.3	594.2
9	607.9	597.7	570.3	594.2
10	612.8	601.2	593.3	597.7
11	593.3	615.4	593.3	597.7
12	607.9	615.4	607.9	608.2
13	622.9	619.0	593.3	594.2
Average	608.6	614.6	594.1	597.4

Note that when measured with the 0.95NA, Vickers and Knoop agree almost exactly, so that any deviation between one measurement and another is certainly a result of standard non-uniformity.

TABLE 2: POSSIBLE MARGINS FOR ERROR IN CERTIFICATION PROCESS

	DEVICE B (0.95 NA)	DEVICE A (0.65 NA)
Measuring process	± 2.5%	± 4.0%
Vibration effects	± 0.5%	± 1.0%
Loading impact	± 0.5%	± 25.0%

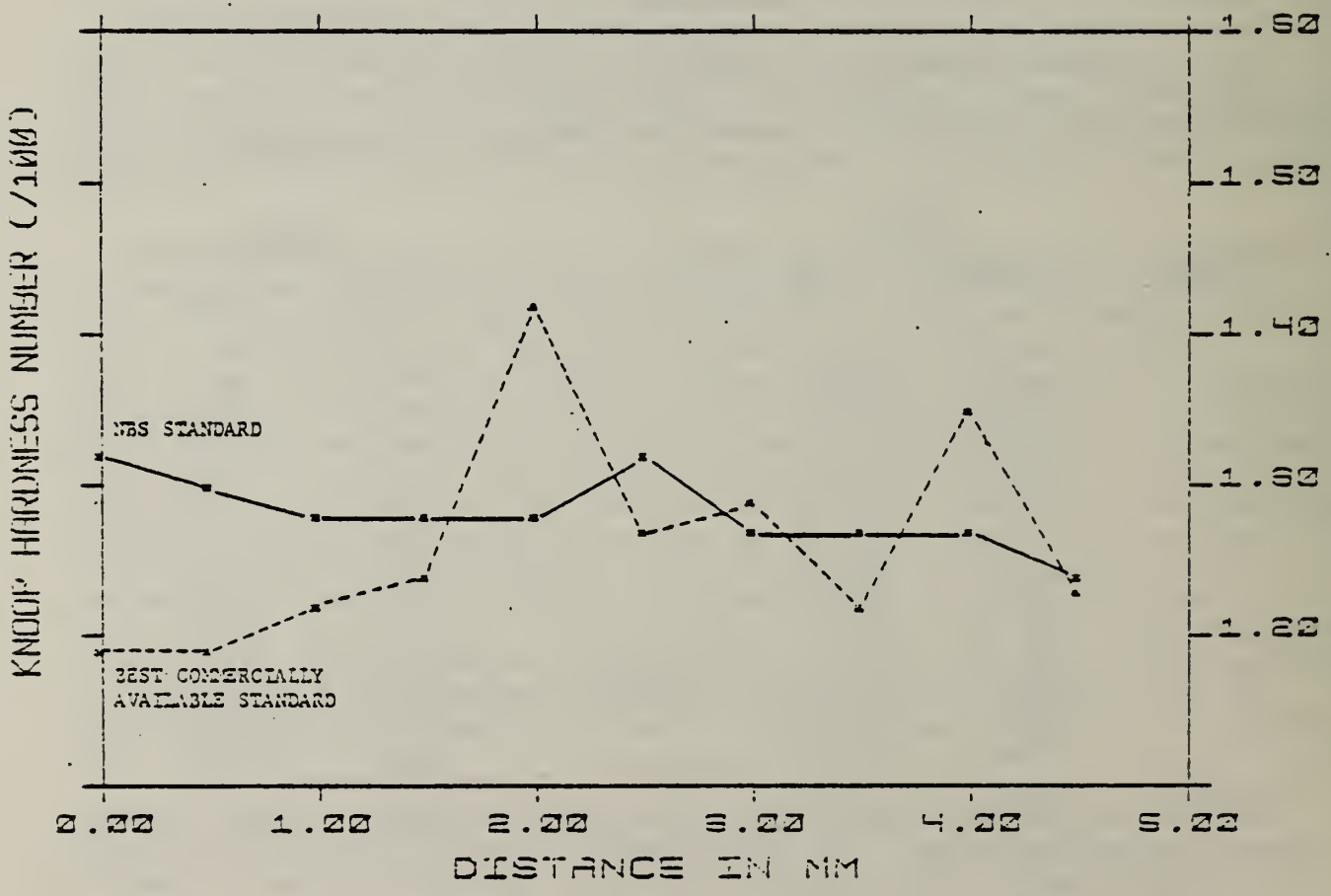

Fig. 1. Variation of microhardness with position on the substrate comparing the electroformed NBS standard with the best commercially available standard.

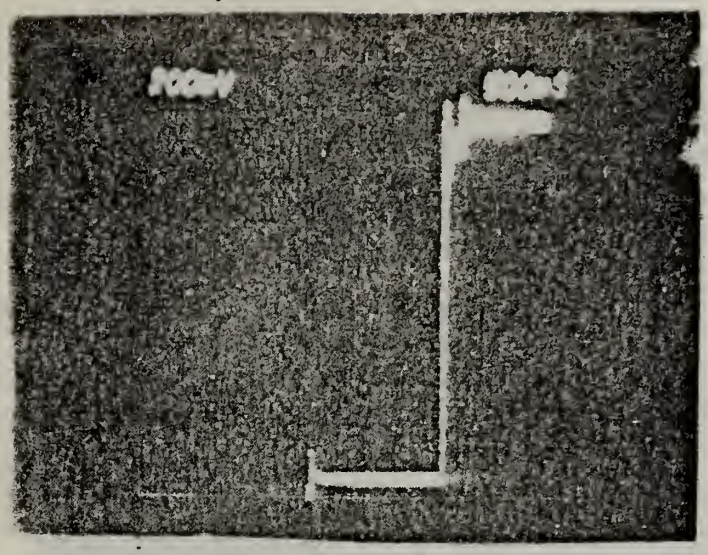

Fig. 2a. Load-time trace:Device A w/ 0.65 NA;
50 g load at approx. 45 sec. dwell

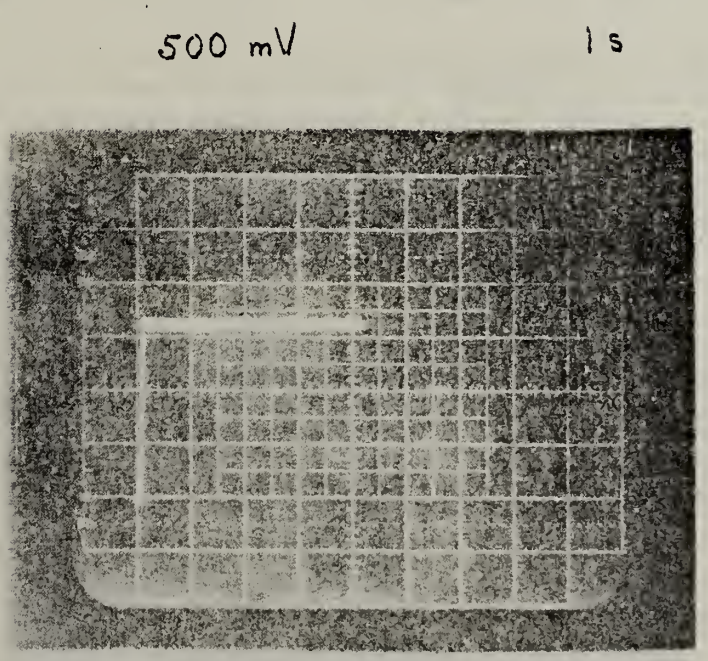

Fig. 2b. Load-time trace: Device B w/ 0.65 NA;
50 g load at approx. 45 sec. dwell

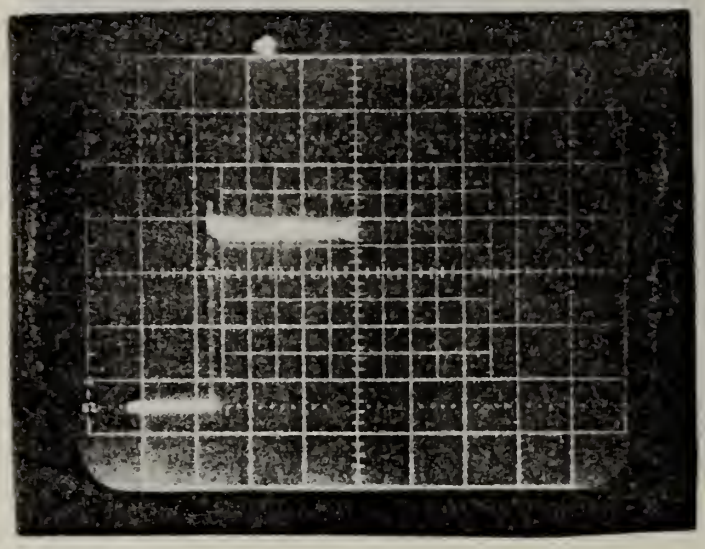

Fig. 3a. Vibrational 'noise' incurred during normal operation of Device A.

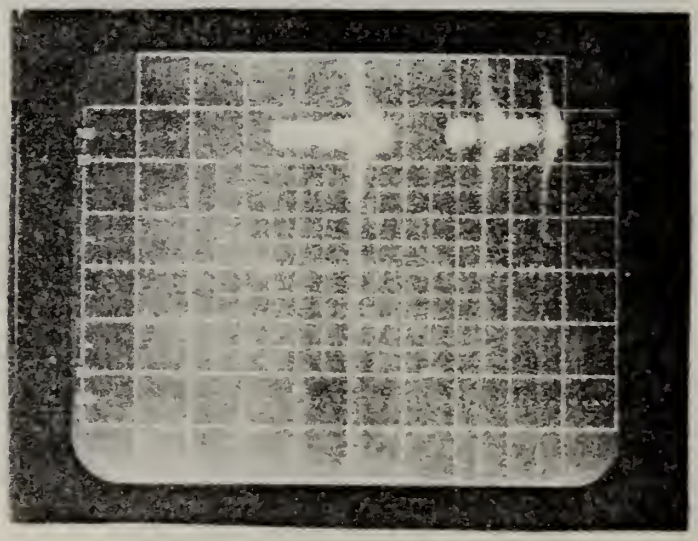

Fig. 3b. Vibrational 'noise' incurred when table mounting is tapped.

NONDESTRUCTIVE EVALUATION OF NONUNIFORMITIES IN 2024 ALUMINUM ALLOY PLATE - RELATIONSHIP TO PROCESSING

L. K. Ives, L. J. Swartzendruber, W. J. Boettinger, M. Rosen, S. D. Ridder, F. S. Biancaniello, R. C . Reno, S. Fick, D. B. Ballard and R. Mehrabian

Metallurgy Division

Center for Materials Science

This task was initiated at the National Bureau of Standards at the request of the National Aeronautics and Space Administration shortly after the announcement in August 1979 by the Reynolds Metal Company tnat about 31 million pounds of aluminum were suspected of containing "soft" spots due to a possible malfunction in the water cooling system at one manufacturing plant. Some of these "soft" spots were reported to be as much as 45 percent below the strength specifications used for the purchase of the aluminum by aircraft manufacturers and suppliers.

The initial concern of this task was the 2219-T87 aluminum alloy used extensively on the space shuttle. The results of our investigations on this alloy were used by the sponsoring agency to ensure that the testing necessary to prove structural integrity had been accomplished prior to launch. The results also had the fortunate effect of expediting the space shuttle launch by eliminating a large amount of unnecessary testing.

Following the effort on 2219 attention was focused on 2024, an alloy which is widely used in the construction of commercial aircraft. Because our results established that better nondestructive evaluation techniques are needed for quickly judging the strength of an aluminum plate throughout its thickness rather than simply on the surface as given by hardness and electrical conductivity, investigation of the feasibility of using an ultrasonic technique as an alternative were carried out on both the 2219 and 2024 alloys.

The goal of this task, which is now essentially complete, was to develop specific relationships between processing variables used during ingot casting, mechanical properties, and NDE responses. The detailed blend of metallurgical examination of the alloy with its NDE response was necessary not only to attack the specific problem at hand but also to gain a fundamental knowledge of the features of metallurgical microstructures which cause changes in NDE parameters.

The investigation included the following:

1. Studies on as-received material. This included a 15.24 cm (6 in) thick plate of 2024-T851, a 0.635 cm (1/4 in.) thick plate of 2024-F, and a direct chill cast ingot for 2024, all obtained from industry.

2. Investigation of the phases and inclusions present in cast 2024 aluminum alloy with the aim of determining the degree of micro- and macro-segregation and identifying the inclusions present in the as-cast ingots.

3. Determination of a set of C-curves which can predict the mechanical and NDE properties for any type of quench following the solution heat treatment. Two tempers, T851 and T351, were investigated.

4. Transmission electron microscope studies of the stable and metastable phases present and an attempt to relate the observed microstructural changes to the measured changes in mechanical properties and NDE measurements.

5. A study of the ultrasonic wave propagation as a function of thermomechanical treatment of the alloy with the objective of establishing a correlation between ultrasonic data and mechanical properties and of providing an additional NDE method to improve the characterization of the material.

6. A nondestructive evaluation of the age hardening sequence by means of dynamic eddy-current conductivity measurements.

7. Use of heat flow modelling to calculate almost all conceivable heat flow conditions anticipated during the quench of 2024 aluminum alloy plate from the solution heat treatment temperature of 495°C. The calculated time-temperature data were then coupled to the C-curves and the variations in properties across different thickness plates for the "worst case" heat flow conditions were predicted.

Predictable macrosegregation was obtained in laboratory ingots of 2024 aluminum alloy. It was found that macrosegregation of copper and other alloying additions in direct chill cast ingots of 2024 aluminum alloy cannot be completely eliminated by chill face scalping and subsequent thermomechanical treatment. Although good scalping practice should maintain compositions within specified limits with no deterioration in mechanical properties, the macrosegragation remaining in the finished plate product will contribute to the scatter observed in NDE measurements. Further, because of the large copper content variation near the chill face, surface hardness and eddy-current conductivity measurements are necessarily very sensitive to scalping depth in their ability to evaluate the condition of finished alloy plates.

A large number of samples were taken from a 0.635 cm thick plate of 2024 aluminum alloy in the F temper and processed to the T851, T351 or T4 temper. During processing to these tempers, the quench following solution heat treatment was varied, giving a series of samples with a wide range of microstructures and hence mechanical properties. Two types of "pre-aging" treatment, labelled sequence A and sequence B, were used.

The hardness, eddy-current conductivity, yield strength, ultimate tensile strength, elongation, and area reduction of these samples were measured. The accumulated data were used to establish a set of statistically significant C-curves from which the alloy properties can be predicted for any time-temperature cycle of the quench following heat treatment. The C-curves can also be used to generate correlations between mechanical and NDE properties. The ultimate tensile strength vs. hardness and vs. conductivity determined for 2024-T351 are shown in Figures 1 and 2. Based on such calculations and measurements it was concluded that eddy-current conductivity alone cannot be used as a reliable predictor of the mechanical properties of 2024-T351 or 2024-T851. It must be combined with other information such as hardness and yield strength measurements on the same lot (same ingot or plate) of material.

The C-curves were combined with time-temperature data from a computerized heat flow model to predict the variations in properties across plates of different thickness for both sequence A and sequence B type "pre-aging" heat treatments. It was found that the ultimate tensile strength falls below specification for the "worst case" quench conditions for rather thin plates (~ 1 cm thick).

TEM studies were carried out on a large number of specimens in a 120 kV instrument equipped to operate in scanning transmission (STEM) mode as well as in the conventional transmission mode. The instrument was equipped with an x-ray energy dispersive spectrometer. A major objective was to identify those microstructural changes that were responsible for the mechanical and physical properties delineated in the C-curve representations. Although the microstructure as a function of "pre-aging" treatment is complex, it appears that "pre-aging" induced precipitates can contribute to the strength and are subject to overaging during further heat treatment. This provides a mechanism for the loss of strength which can account for the fact that the strength of the T851 temper is actually reduced below that of the T351 temper given the same "pre-aging" heat treatment (rather that being raised as occurs for properly quenched material).

The objective of the ultrasonic studies was to determine the extent to which a correlation exists between the mechanical and ultrasonic properties. For this purpose, the absolute, rather than the relative, values of the sound velocity and ultrasonic attenuation are required. The absolute values of sound velocity and ultrasonic attenuation were determined to within $\pm$ 1 ms^{-1} and $\pm$ 0.02 dB, respectively. A parabolic relationship was found between hardness and sound-wave velocity, whereas ultrasonic attenuation decreases with increasing hardness.

Detailed results of the project have been published in a final report (ref. 1).

REFERENCES

1. "Processing/Microstructure/Property Relationships in 2024 Aluminum Alloy Plates", NBISR 83-2669, U. S. Department of Commerce, N.B.S., January 1983.

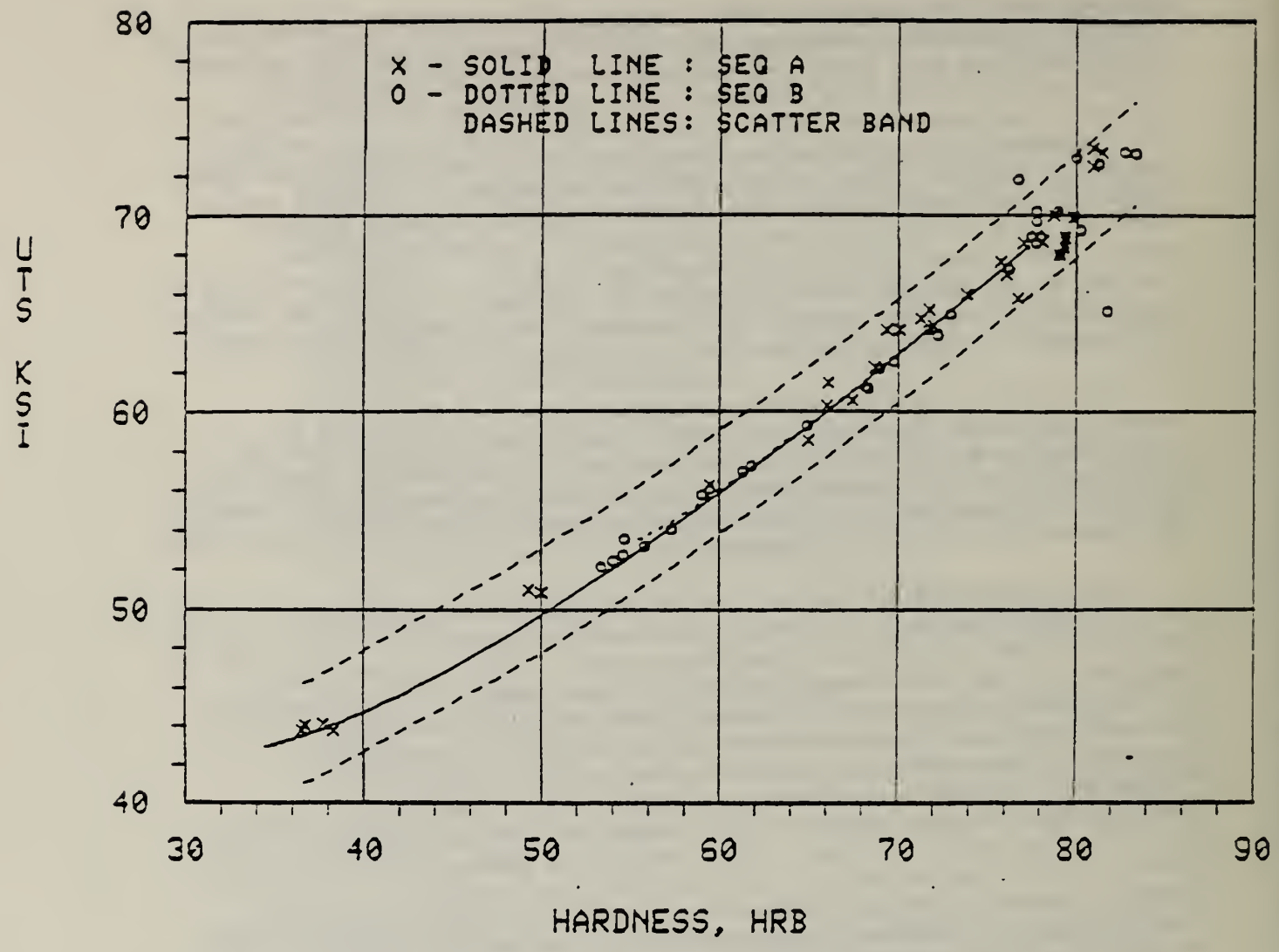

Figure 1. Comparison of ultimate tensile strength vs. hardness data for 2024-T351 with the correlations predicted by the C-curves. The dashed lines are the scatter band (~95% confidence level) obtained from a least squares quadratic fit to the data. The solid and dotted lines were calculated from the C-curves.

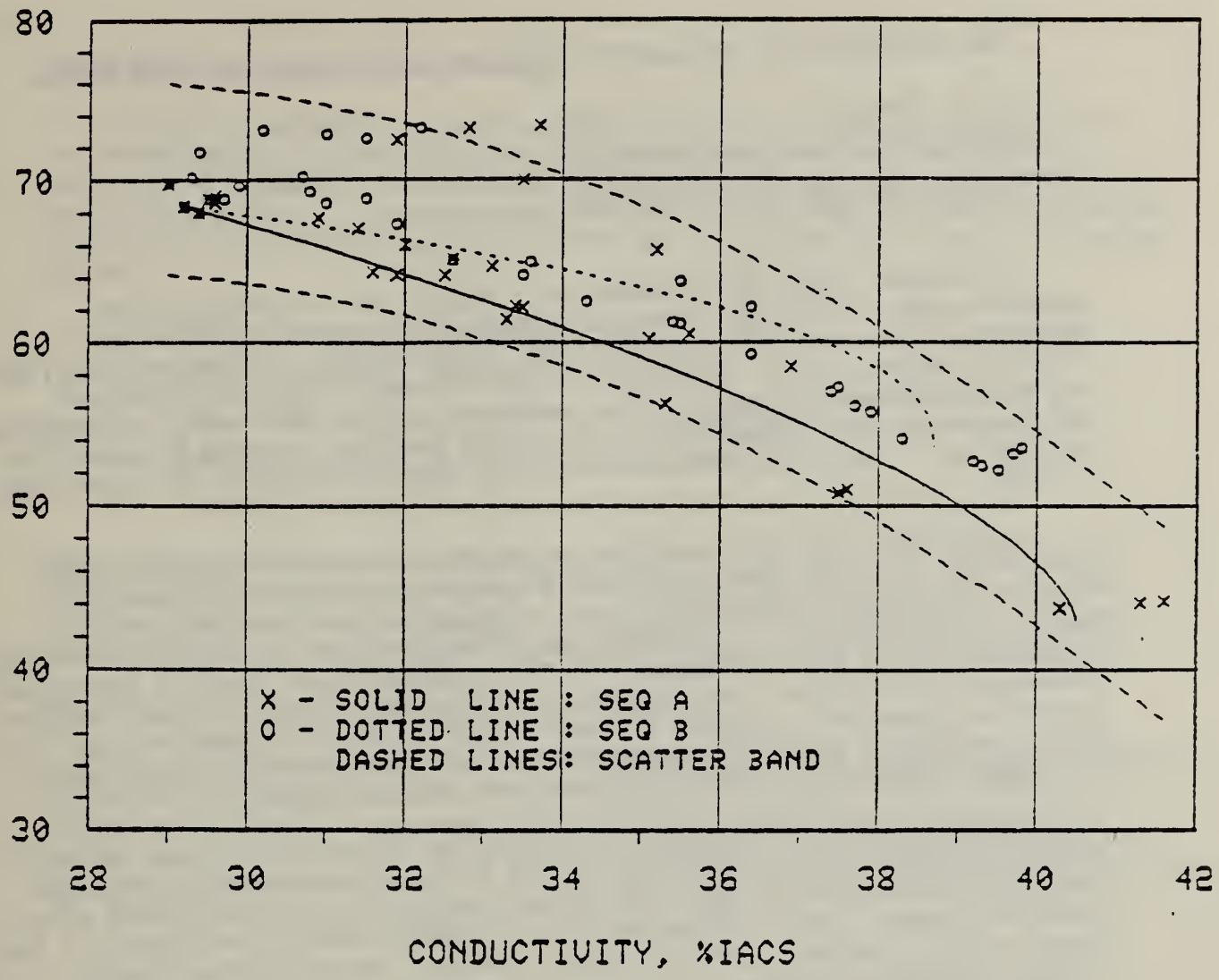

Figure 2. Comparison of ultimate tensile strength vs. conductivity data for 2024-T351 the correlations predicted by the C-curves. The dashed lines are the scatter band (~95% confidence level) obtained from a least squares quadratic fit to the data. The solid and dotted lines were calculated from the C-curves.

NDE DATA ANALYSIS, RELIABILITY MODELING, AND ON-LINE DECISION-MAKING

J. T. Fong

Mathematical Analysis Division

Center for Applied Mathematics

In October 1982, NBS responded to a request by an industry-based research group to conduct a two-year study on the analysis and reliability modeling of five sets of flaw-sizing and location data. The request resulted from the recognition by the Pressure Vessel Research Committee (PVRC) of the Welding Research Council that a computer-assisted data analysis methodology has been under development at NBS since 1978 and that it would be beneficial to collaborate in applying that methodology to some specific NDE data generated by PVRC.

Since 1965, PVRC has supported an industry cooperative program on NDE reliability by having twelve plate-weld specimens containing intentional flaws fabricated and inspected by several teams using either existing or improved NDE methods. To calibrate the efficacy of the ad-hoc flaw fabrication procedure, one of the specimens, PVRC 251J, was sectioned after it completed a round-robin NDE program. More importantly, the sectioning data were expected to provide an "absolute" estimate of the reliability of NDE procedures used for 251J as well as a qualitative assessment of all round-robin NDE tests where the actual location and sizing of flaws were not available.

Specimen 251J was fabricated by welding two 11-in. thick plates of ASTM A-533-65, Grade B, low-alloy steel (80,000 psi tensile strength), using the submerged arc welding process. The 36-in. long by 1-1/4-in. wide butt weld, as shown in Figures 1 and 2, contained 15 intentional flaws of four types (5 long cracks of 2-in. nominal length, 5 cross cracks of 3/4 in. nominal length, 3 long slags, and 2 short slags).

The NBS-PVRC joint project on the analysis of PVRC round-robin NDE data calls for the development of specific computer software for, and the application of NBS-developed graphics and analysis software to, the following sets of data on specimen 251J:

Set 1 Sectioning Data (Yukawa, 1983) vs. Assumed Geometry of Intended Flaws.

Set 2 Ultrasonic Test Data (5-team, 1968), using an existing PVRC procedure.

Set 3 Ultrasonic Test Data (3-team, 1970), using a "new" PVRC procedure.

Set 4 Ultrasonic Test Data (4-team, 1971), using the "new" procedure on cladding.

Set 5 Radiographic Test Data (6-team, 1976).

This summary report describes the progress made during the first ten months of the project.

ENGINEERING DATA ANALYSIS METHODOLOGY

To assist engineers in meeting their information needs for both crisis and normal modes of work, credible and affordable sources of engineering data such as handbooks and databases exist with varying scopes of coverage and depths of analysis. A computer-assisted methodology had been developed where the process of analyzing any engineering data is broken down into five distinct phases:

1. Data structure and representation.
2. Data completeness and quality check.
3. Data simplification for parametric studies.
4. Data analysis and variability modeling.
5. Critical evaluation of assumptions and results of analysis.

This conceptual scheme is being implemented for two specific applications, namely, (a) the round-robin NDE data of specimen 251J, and (b) the elastic, yield strength, ultimate strength, creep, and fatigue properties of a class of steels with corresponding microstructural data during mechanical testing.

ANALYSIS OF 251J SECTIONING DATA - Interim Report

Dr. S. Yukawa of the General Electric Materials & Processes Laboratory made available, on behalf of PVRC, a large number of drawings and micrograph-like images of 15 flaws of specimen 251J as observed and intrepreted following sectioning. A summary of the sectioning data (ref. 2) is reproduced in Table 1. Pictures of the flaws in either projected or sectioning forms were received by NBS for digitizing and 3-dimensional representation.

As shown in Figures 3 and 4, the manual drawings of the projections of one such crack, flaw H, revealed a lot of geometric information which may or may not be detected or relevant to a specific application. Of the 13 sections provided for this flaw, two typical ones appear in Figures 5 and 6 as test problems for exercising the digitizing software initially developed by David Redmiles of the NDE Mathematical Analysis Division. Using Dataplot, another NBS-developed software (ref. 3), the digitized images of the two sections are displayed in Figures 7 and 8. A 3-dimensional representation of the two sections in a perspective view is given in Figure 9. New software is being developed to connect those sections to form a continuous solid body for viewing at arbitrary angles to facilitate a comparison with ultrasonic test data at different beam angles.

QUALITY CHECK FOR NDE DATA AND THE CONCEPT OF A QUALITY INDEX

In collaboration with H. Berger of Industrial Quality, Inc., Gaithersburg, MD, a list of thirteen criteria for checking the quality of radiographic data, and a system of weights on those criteria to arrive at a measure known as the "data quality index", were developed. A graphical display of the index in the form of a rosette is given in Figure 10. Eighteen criteria for ultrasonic data are being developed together with Berger and D. Eitzen of the NBS

Mechanical Production Metrology Division. Details of both lists are given in ref 1.

PVRC 251J FLAW FABRICATION RELIABILITY - Interim Report

To demonstrate the value of an erstwhile variance decomposition technique (ref. 4), we chose one parameter, the maximum flaw dimensions as revealed by sectioning and normalized by the intended length, as a sample parameter for reliability analysis. As shown in ref. 5 and Figure 11, there are 15 data points for the normalized maximum dimensions that range from 1.0 to 2.9 with a mean of 1.89 and a standard deviation (SD) before analysis equal to 0.53. Because of the replications in the 15-data structure, it is possible to obtain additional information by applying the so-called one-way analysis of variance (ref. 5) such that the flaw fabrication procedure can now be characterized by an SD equal to 0.60. Using this new information and the condition that we allow the actual maximum dimension to exceed the intended by no more than 50 percent, the reliability of the fabrication procedure is now estimated at 25 percent.

INTERNATIONAL NDE RELIABILITY SYMPOSIUM

In June 1983, more than a hundred NDE scientists and engineers from Europe, Japan, and North America met in Portland, Oregon to review and discuss the use of round robin NDE of flawed specimens for estimating inspection reliability (ref.6). The symposium, which was chaired by the writer, was organized by the American Society of Mechanical Engineers (ASME), the American Society for Nondestructive Testing, the U. S. Pressure Vessel Research Committee, and NBS. Among the co-sponsors were the Japan PVRC, the Plate Inspection Steering Committee of the Commission of European Communities, the U. S. Nuclear Regulatory Commission, the U. S. Department of Energy, the Electric Power Research Institute, and others.

The symposium reviewed the history of an international round robin NDE program that was spearheaded by the U.S. PVRC more than ten years ago, summarized the technical accomplishments of all participating laboratories and companies including work in progress, discussed data analysis methodologies including one developed at NBS, and examined open problems at panel sessions on future directions in NDE research. A significant finding of the symposium was that research in NDE measurements and parametric studies in round robin testing have led to systematic improvements in inspection procedures and a more sound basis for decision-making in both the industrial and the regulatory sectors.

NDE DATABASE FOR ON-LINE ENGINEERING DECISION SUPPORT

Looking beyond the analysis and modeling of NDE data for reliability estimation, we began a computer software effort to integrate the NBS-PVRC database on NDE with five additional engineering databases to demonstrate the feasibility of bringing credible and up-to-date information on line to engineers for crisis decision-making (ref. 7). The five additional databases are:

(a) Materials Property Database.
(b) Design Loads and Stress Analysis Software Package Access Database.
(c) Inservice Inspection and Failure Database.

(d) Human Factor Database.
(e) Case Studies, Economics, and Directory of Experts for Critical Review.

This demonstration project is sponsored by the ASME Committee on Research Needs and is administered by a task force of 20 members with the writer as its chairman. The first on-line demonstration of the project is scheduled for June 1984.

REFERENCES

1. J. T. Fong, "A Data Analysis Methodology as Applied to the PVRC Round Robin NDE Test Program," Proc. International Symposium on NDE Reliability, Portland, Oregon, June 1983,in preparation.

2. S. Yukawa, "Sectioning of PVRC NDE Specimen 251-J," Progress Reports to PVRC dated Jan. 15, 1981 and May 25, 1983.

3. J. J. Filliben, "Dataplot - An Interactive High-Level Language for Graphics, Nonlinear Fitting, Data Analysis, and Mathematics," Computer Graphics 15, No. 3, pp. 199-213 (1981).

4. H. E. Daniels, "The Estimation of Components of Variance", J. Royal Statistical Soc. Supplement 6, No. 2, 186-197 (1939).

5. J. T. Fong, "Analysis of Sectioning Data of PVRC-J for Estimating Flaw Fabrication Reliability," to appear in Proc. International Symposium on NDE Reliability, Portland, Oregon, June 1983, in preparation.

6. J. T. Fong, S. H. Bush, and O. F. Hedden, eds., A Symposium Preview on NDE Reliability through Round Robin Testing, a 193-page document prepared for the pre-registants of an international symposium on NDE reliability, Portland, Oregon, June 19-21, 1983.

7. J. T. Fong, "Computer Software Needs of Materials Property Data Bases for Selected Engineering Applications," to appear in An On-Line Materials Property Data Base, Proc. of a symposium sponsored by ASME Pressure Vessels & Piping Division and the Metal Properties Council, Inc., Sheraton Boston Hotel, Nov. 15, 1983, during the 1983 Winter Annual Meeting of the Am Soc of Mechanical Engineers.

Table 1. Sectioning Results for PVRC Specimen 251J

Flaw	Type*	Actual Dimensions**			Intended Dimensions		
		X	Y	Z	X	Y	Z
A	CC	26.1-26.5	2.4-4.2	1.0-1.3	25.5-26.3	3.0	1.0
B	LS	26.3-26.4	16.1-18.1	0.6-1.1	26.3	16.0-18.0	1.0
C	LC	25.9-26.6	29.7-33.4	0.7-1.2	26.3	30.0-32.0	1.0
D	LC	25.1-25.6	2.2-5.5	2.4-3.1	25.0	2.0-4.0	2.75
E	CC	25.3-25.5	17.1-19.0	2.8-3.2	25.0-25.8	17.0	2.75
F	SS	25.1-25.2	30.6-31.8	1.9-2.7	25.0	30.6-31.4	2.75
G	LS	26.2-26.4	2.2-4.8	4.6-5.4	26.3	2.0-4.0	5.5
H	LC	25.7-26.4	16.1-21.9	5.0-5.7	26.3	16.0-18.0	5.5
I	CC	26.0-26.4	30.2-31.9	5.2-5.7	25.5-26.3	31.0	5.5
J	CC	25.1-25.8	3.1-4.6	7.7-8.2	25.0-25.8	3.0	8.3
K	SS	25.1-25.5	17.1-18.1	8.0-8.3	25.0-25.8	17.0	8.3
L	LC	25.1-25.7	29.1-33.9	7.6-8.2	25.0	30.0-32.0	8.3
M	LC	25.7-26.3	1.0-5.0	9.3-10.0	26.3	2.0-4.0	10.0
N	CC	25.8-26.3	16.7-18.7	9.3-9.8	25.5-26.3	17.0	10.0
O	LS	26.0-26.2	29.8-32.2	9.6-10.2	26.3	30.0-32.0	10.0

*Type of Flaw: CC = Cross Crack
LS = Long Slag
LC = Long Crack
SS = Short Slag

** Dimensions: Coordinates of the flaw extremities; coordinate system as per Figs. 1 and 2; dimensions in inches as per ref. 2.

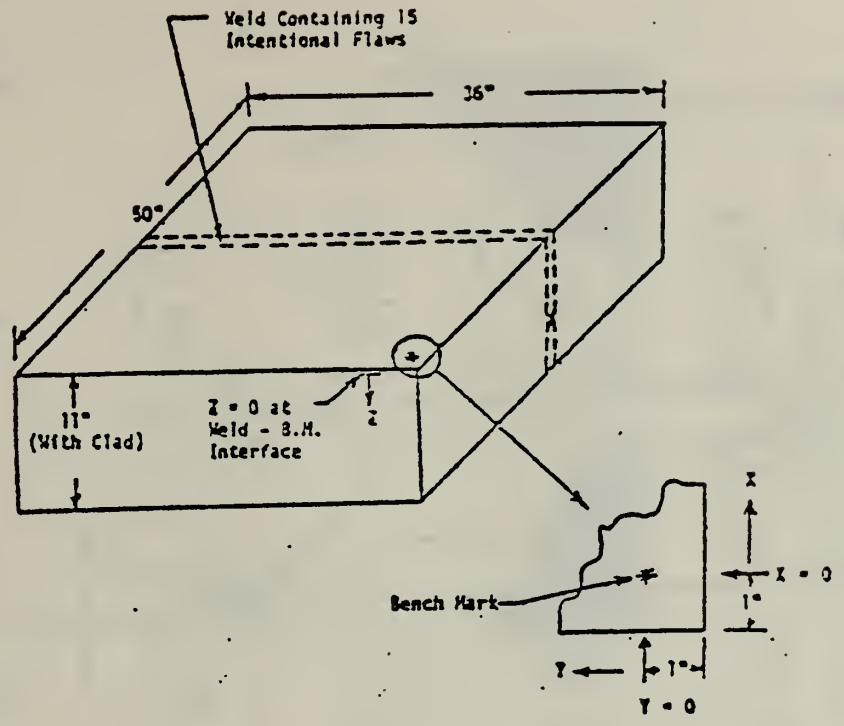

Figure 1. Dimensions of Specimen 251J.

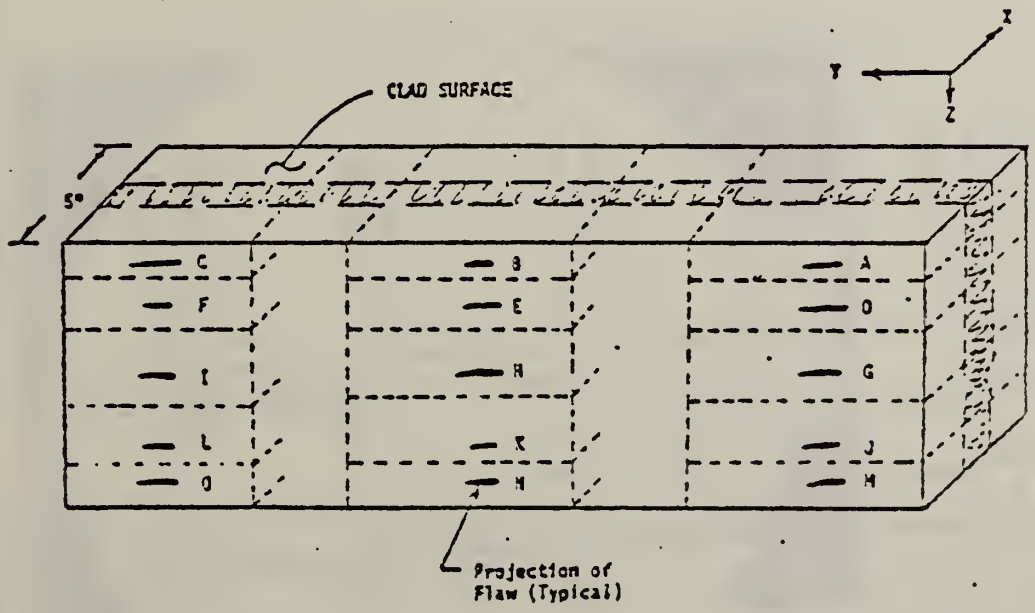

Figure 2. Principal sectioning cuts.

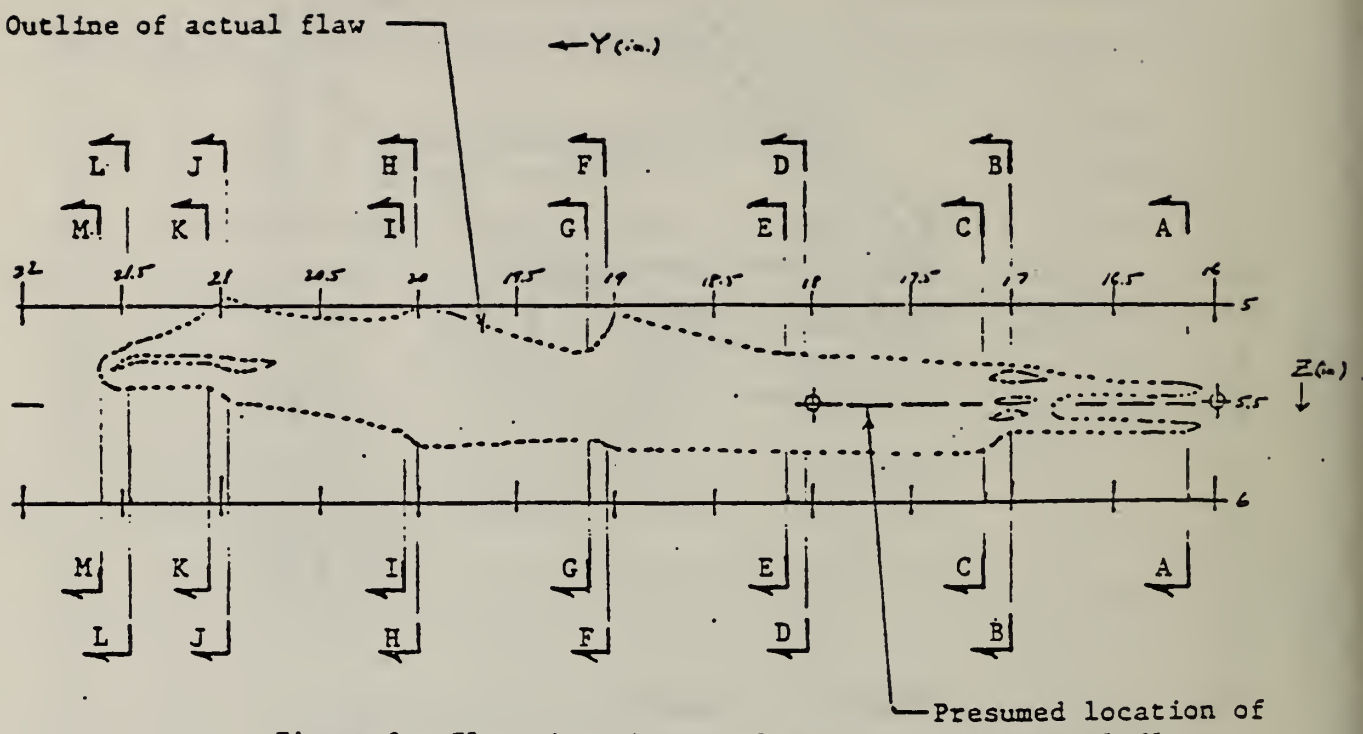

Figure 3. Elevation view of Flaw H.

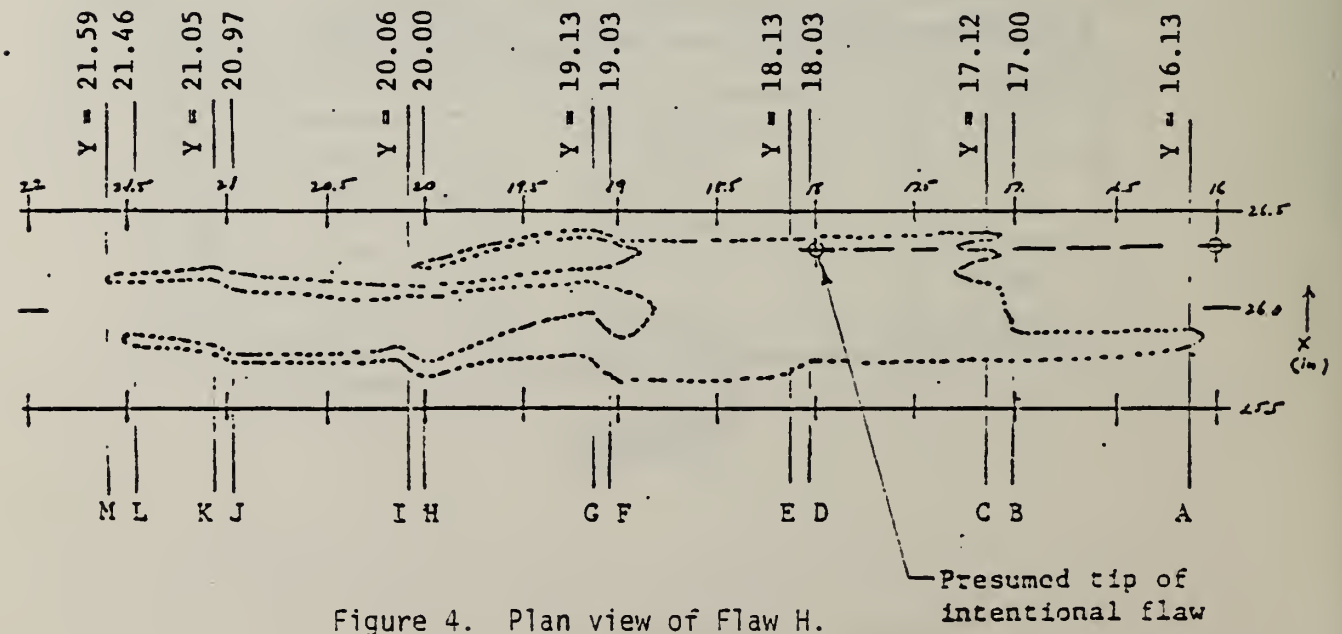

Figure 4. Plan view of Flaw H.

Figure 5. Section C-C of Flaw H.

Figure 6. Section D-D of Flaw H.

Figure 7. Digitized image of Section C-C of Flaw H.

Figure 8. Digitized image of Section D-D of Flaw H.

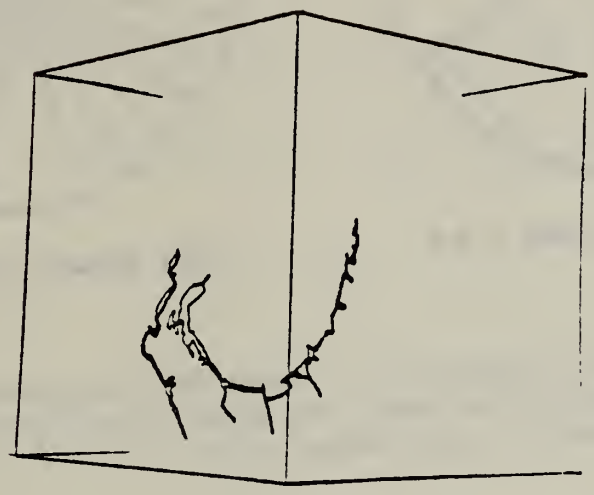

Figure 9. Three-dimensional representation of Flaw H between Sections A-A and D-D, as viewed from a perspective. (The separate element at the upper left corner of Section D-D has been omitted for clarity.)

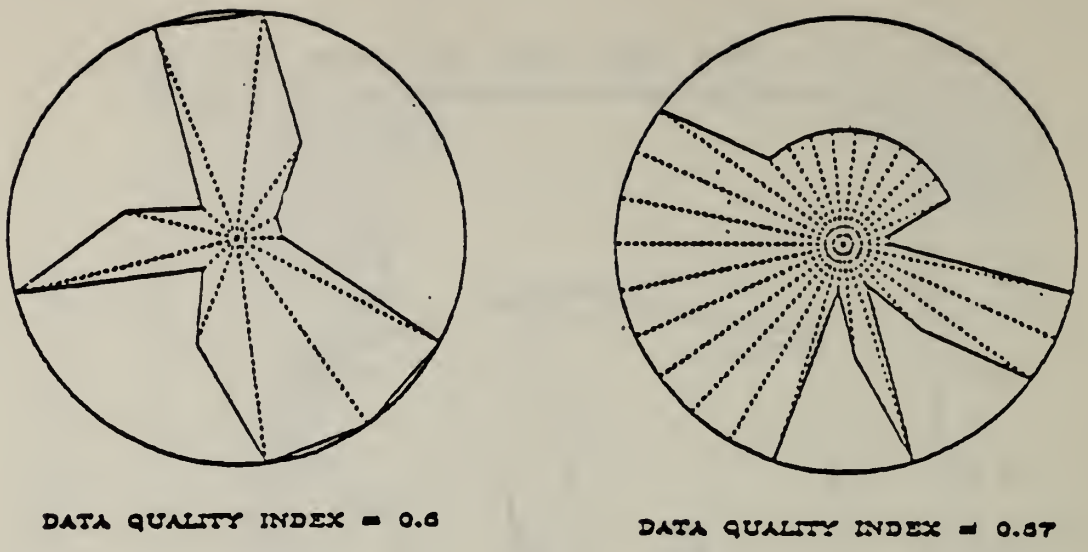

Figure 10. Data quality index for a 13-criterion radiographic data check list, shown before (left) and after (right) some of the criteria are weighted by a data source.

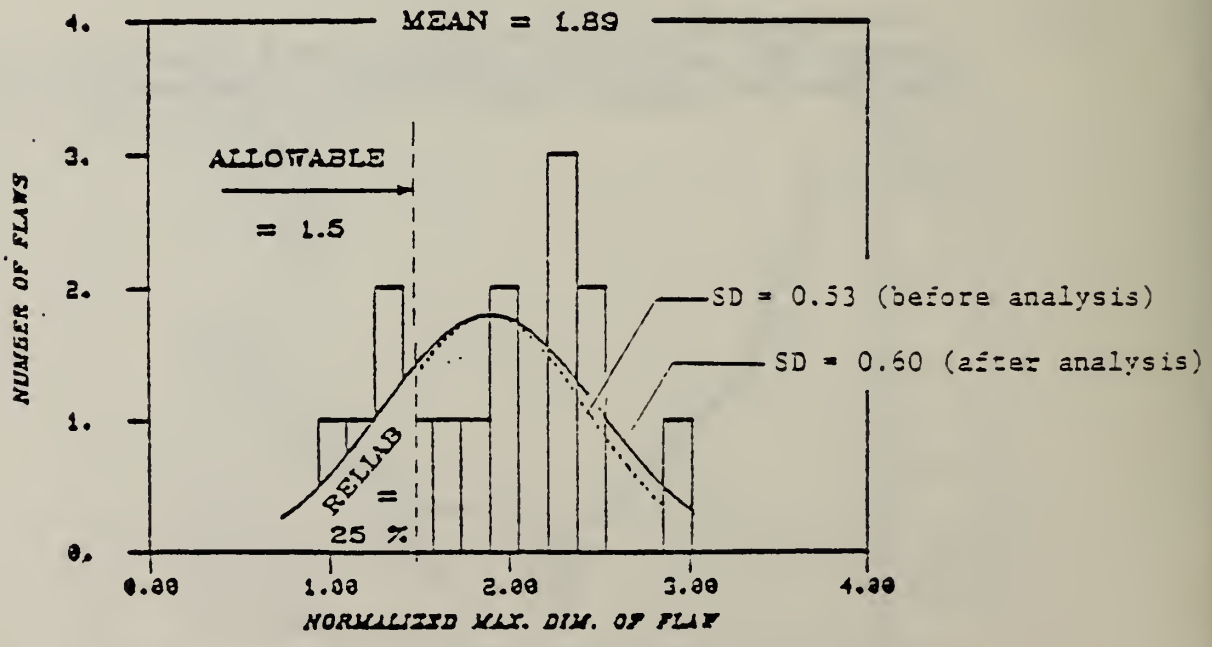

Figure 11. Reliability of the flaw fabrication procedure for one parameter (flaw length) based upon a one-way analysis of variance.

APPENDICES

A. Conferences Sponsored or Co-Sponsored

Eighth International Symposium on Ultrasonic Imaging and Tissue Characterization, June 5-8, 1983, Washington, D. C.

International Symposium on Reliability of Nondestructive Evaluation through Round Robin Testing, June 19-21, 1983, Portland, Oregon.

Gordon Research Conference on Nondestructive Evaluation, August 21-26, 1983, Andover, New Hampshire.

NDE in Materials Processing Meeting, ASM Metals Congress, October 3-5, 1983, Philadelphia, Pennsylvania.

B. NDE Seminars at NBS

Dr. Allan Rosencwaig, Therma-Wave, Inc., Fremont, CA

"Thermal Wave Detection and Imaging"

March 21, 1983

Dr. Fred E. Stanke, Stanford University, Stanford, CA

"Elastic Wave Propagation in Polycrystalline Materials"

April 11, 1983

Dr. James E. Gubernatis, Los Alamos Scientific Laboratory, Los Alamos, N. M.

"The Role of Elastic Wave Scattering Theory in Ultrasonic Nondestructive Evaluation"

April 15, 1983

Dr. L. S. Fu, Ohio State University, Columbus, OH

"Ultrasonic Evaluation of Mechanical Properties"

June 23, 1983

Professor Dr. Paul Hoeller, Director, Fraunhofer Institut fur Zerstorungsfreie Prufverfahren, Saarbrucken, W. Germany

"Nondestructive Testing for Materials Characterization and Stress Analysis"

September 12, 1983

C. Invited Talks by ONDE Staff

"Nondestructive Evaluation for Materials Characterization," L. Mordfin, IAEA Seminar on Nondestructive Testing Technology -- Current Development and Future Trends, Singapore, March 11, 1983.

"New Directions in the National Bureau of Standards' NDE Program," H. T. Yolken, 14th Symposium on Nondestructive Evaluation, San Antonio, TX., April 20, 1983.

"The Role of NDE in Manufacturing Science," H. T. Yolken, 1983 Conference and Workshops on Mission Assurance: Industry/AF Space Division/NASA, Los Angeles, CA., June 15, 1983.

"Reliability of Industrial NDE," H. T. Yolken, Review of Progress in Quantitative NDE Sponsored by the Center for Advanced NDE at the Ames Laboratory (USDOE) with cooperation from the Air Force Wright Aeronautical Labs., the Naval Sea Systems Command, and DARPA, Santa Cruz, CA., August 8, 1983.

"Developments in Sensor Technology for Microstructure Monitoring and Process Control," H. T. Yolken, (co-authored by R. Mehrabian), ASM Metals Congress, Philadelphia, PA., October 3, 1983.

D. NDE Program Publications

H. Berger and L. Mordfin, Comparison of Common Nondestructive Evaluation Methods, Quality Progress 16, No. 2, p. 17 (Feb., 1983).

G. V. Blessing, An Assessment of Ultrasonic Reference Block Calibration Methodology, NBSIR 83-2710 (June, 1983).

G. V. Blessing and D. G. Eitzen, Variables Affecting Ultrasonic Reference Block Calibration, 1982 Paper Summaries, ASNT National Conferences, 287-291 (1982).

D. A. Bracher, D. A. Garrett and C. O. Heller, Theory and Design of Instrumentation for Bridge Investigation, Failure Prevention in Ground Transportation Systems, NBS SP 621, 143-150 (Oct., 1982).

G. Birnbaum, H. Berger and D. G. Eitzen, Traceable NDE Standards, Can. Soc. NDT J 4, 47-49 (Jan., 1983).

J. C. Chang, F. Nadeau, M. Rosen and R. Mehrabian, Crystallization Kinetics Study of $Cu_{50}Zr_{50}$ by Means of Ultrasonic Measurements and Microhardness, Scripta Met 16, p. 1073 (1982).

J. R. Clifton and N. J. Carino, Nondestructive Evaluation Methods for Quality Acceptance of Installed Building Materials, J. Res. NBS 87, No. 5, 407-436 (1982).

J. R. Clifton, Nondestructive Evaluation Methods for Quality Acceptance of Building Materials, Proc. 31st Defense Conf. on Nondestructive Testing, 95-109 (Nov., 1982).

R. B. Clough, ed., Quantitative NDE in the Nuclear Industry (Proc. 5th Intl. Conf. on NDE in the Nuclear Industry, ASM, 1983).

R. B. Clough and H. N. G. Wadley, Indentation Loading Studies of Acoustic Emission from Temper and Hydrogen Embrittled A5 33 B Steel, Metallurgical Transactions 13A, 1965-1975 (Nov., 1982).

J. Cohen, Elements of Thermography for Nondestructive Testing, NBS TN 1177 (May, 1983).

S. K. Datta, C. M. Fortunko and R. B. King, Sizing of Surface Cracks in a Plate using SH Waves, Review of Progress in Quantitative Nondestructive Evaluation 1, 227-231 (Plenum, NY, 1982).

D. Eitzen, F. Breckenridge, R. Clough, N. Hsu, T. Proctor, C. Stockton and H. Wadley, Fundamental Developments in Acoustic Emission Measurements: The NBS Program, Quantitative NDE in the Nuclear Industry, R. B. Clough, ed., 315-325 (ASM, 1983).

D. G. Eitzen and J. R. Quinn, Electric Power Research Institute/National Bureau of Standards Joint Program on Acoustic Emission, Nondestructive Evaluation Program: Progress in 1982, G. J. Dau, et al, eds., Report NP-2728-SR, pp. 40-1 to 40-16 (EPRI, Feb., 1983).

D. L. Hunston, Cure Monitoring of Thermosetting Polymers by an Ultrasonic Technique, Review of Progress in Quantitative Nondestructive Evaluation 2, 1711-1730 (Plenum, NY, 1983).

D. L. Hunston, Relationship Between Mechanical Properties and Performance of Inks as the Basis of Quality Control Techniques, NBSIR 83-2691 (April, 1983).

N. N. Hsu, S. F. Fick and T. M. Proctor, Recent Developments in the Design of Piezoelectric Ultrasonic Transducers for Nondestructive Evaluation, 1982 Paper Summaries, ASNT National Conferences, p. 54 (1982).

N. N. Hsu, T. M. Proctor, Jr., and G. V. Blessing, An Analytical Approach to Reference Samples for Ultrasonic Residual Stress Measurement, J. Testing and Evaluation 10, No. 5, 230-234 (Sept., 1982).

L. K. Ives, L. J. Swartzendruber, W. J. Boettinger, M. Rosen, S. D. Ridder, F. S. Biancaniello and R. Mehrabian, Relationship between Process Variables and NDE in 2024 Aluminum Alloy Plate, 1982 Paper Summaries, ASNT National Conferences, 480-481 (1982).

A. H. Kahn, Impedance Changes Produced by a Crack in a Plane Surface, Review of Progress in Quantitative Nondestructive Evaluation 1, 369-373 (Plenum, NY, 1982).

R. B. King and C. M. Fortunko, Determination of In-Plane Residual Stress States in Plates using Horizontally Polarized Shear Waves, J. Appl. Phys. 54, No. 6, 3027-3035 (1983).

L. I. Knab, G. V. Blessing and J. R. Clifton, Laboratory Evaluation of Ultrasonics for Crack Detection in Concrete, ACI J. 80, No. 1, 17-27 (1983).

R. D. Kriz, Monitoring Elastic Stiffness Degradation in Graphite/Epoxy Composites, 1982 Paper Summaries, ASNT National Conferences, 160-164 (1982).

M. Linzer, ed., Ultrasonic Imaging 5 (1983).

M. Linzer and S. J. Norton, Ultrasonic Tissue Characterization, Ann. Rev. Biophys. Bioeng. 11, 303-329 (1982).

M. E. McKnight and J. W. Martin, Nondestructive Corrosion Detection Under Organic Films using Infrared Thermography, Proc. 14th Natl. SAMPE Tech. Conf. (Oct., 1982).

L. Mordfin, ed., NDE Publications: 1981, NBSIR 83-2741 (May, 1983).

S. J. Norton, Generation of Separate Density and Compressibility Images in Tissue, Ultrasonic Imaging 5, No. 3, 240-252 (1983).

S. J. Norton and M. Linzer, Correcting for Ray Refraction in Velocity and Attenuation Tomography: A Perturbation Approach, Ultrasonic Imaging 4, No. 3, 201-233 (July, 1982).

C. L. Oehl and L. J. Swartzendruber, On the Optimum Applied Field for Magnetic Particle Inspection using Direct Current, J. Nondestructive Evaluation 3, p. 125 (1983).

R. L. Parker, Ultrasonic Measurement of Solid/Liquid Interface Position During Solidifcation and Melting of Metals, Physics in the Steel Industry (AIP Conf. Proc. No. 84), 254-271 (1982).

T. M. Proctor, Jr., Introduction to Papers Presented at the Symposium on Ultrasonic Measurement of Stress, J. Testing and Evaluation 10, No. 5, 199-201 (Sept., 1982).

T. M. Proctor, Jr., Some Details on the NBS Conical Transducer, J. Acoustic Emission 1, No. 3, 173-178 (Sept., 1982).

M. Rosen, S. Fick, E. Horowitz and R. Mehrabian, An Ultrasonic Investigation of Precipitation Hardening Phenomena in 2219 Aluminum Alloy, Review of Progress in Quantitative Nondestructive Evaluation 1, 625-628 (Plenum, N. Y., 1982).

S. Ruthberg, Leak Testing of Hermetically Sealed Electronic Components, 1982 Paper Summaries, ASNT National Conferences, 431-436 (1982).

R. A. Schrack, J. W. Behrens, A. D. Carlson, C. D. Bowman and R. D. Johnson, Recent Developments in Resonance Neutron Radiography, Quantitative NDE in the Nuclear Industry, R. B. Clough, ed., 158-163 (ASM, 1983).

C. Tschiegg, M. Greenspan and D. Eitzen, Ultrasonic Continuous-Wave Beam-Power Measurements; International Comparison, J. Res. NBS 88, No. 2 (Mar. - Apr., 1983).

H. N. G. Wadley, C. K. Stockton, J. A. Simmons, M. Rosen and S. D. Ridder, Quantitative Acoustic Emission Studies for Materials Processing, Review of Progress in Quantitative Nondestructive Evaluation 1, 421-431 (Plenum, N. Y., 1982).

G. S. White and J. F. Marchiando, Scattering from a V-Shaped Groove in the Resonance Domain, Appl. Opt. 22, No. 15, 2308-2312 (Aug. 1, 1983).

Y. Xu and C. M. Vest, Holographic Technique for Simultaneous Measurement of Displacement and Tilt, Appl. Opt. 22, No. 14, 2137-2140 (July 15, 1983).

H. T. Yolken, ed., Technical Activities 1982 Office of Nondestructive Evaluation, NBSIR 82-2617 (Dec., 1982).

X. Youren, C. M. Vest and E. J. Delp, Digital and Optical Moire Detection of Flaws Applied to Holographic Nondestructive Testing, Optics Letters 8, No. 8, 452-454 (Aug., 1983).

E. Awards

Acoustical Society of America Gold Medal

Mr. Martin (Moe) Greenspan was awarded the Gold Medal of the Acoustical Society of America in the Spring of 1983. This award, the Society's highest, is given annually to a member who has made major contributions in the field of acoustics. Mr. Greenspan was cited "for wide ranging and superlative contributions to experimental and theoretical physical acoustics, including induced cavitation in liquids and sound propagation in solids, liquids, and gases."

Engineer of the Year

Dr. Nelson N. Hsu of the Mechanical Production Metrology Division, a principal investigator for acoustic emission in the NDE Program, was named Engineer of the Year for his contributions to the science and technology of experimental mechanics. The award was given by the National Society of Professional Engineers on February 24, 1983, during Engineers Week in Washington, D. C.

ASTM Awards of Merit

Mr. Daniel Polansky of the Radiation Physics Division, a principal investigator for radiography in the NDE Program, received the ASTM Award of Merit and designation as a fellow of the Society in June, 1983. He was cited for his years of outstanding service to ASTM in the development of Committee E-7 on Nondestructive Testing and the standards it produced.

Dr. Jeffrey T. Fong of the Mathematical Analysis Division was also a 1983 recipient of the ASTM Award of Merit. Dr. Fong, who has provided mathematical and analytical support to the NDE Program for several years, was recognized for his leadership and dedicated service in fatigue research.

ASM Fellow

Dr. A. William Ruff of the Metallurgy Division, principal investigator for wear-debris analysis in the NDE Program, was elected a Fellow of the American Society for Metals in October, 1983 in recognition of distinguished contributions in the field of metals and materials.

ISHM Best Paper Award

Mr. Stanley Ruthberg of the Semiconductor Materials and Processes Division, a longtime principal investigator for leak testing in the NDE Program, received an award in November, 1983, for the best paper presented at the International Society for Hybrid Microelectronics Annual Symposium last year. Ruthberg's paper, "Hermetic Testing of Large Hybrid Packages," discussed the special problems posed by hermeticity tests for microelectronics packages having volumes on the order of tens of cubic centimeters.

NTA Award

Mr. Jimmy James, a cooperative student in the Mechanical Production Metrology Division, won first place in a regional paper competition for undergraduates in Albuquerque, N. M. This cash award was presented by the National Technical Association for his paper on measuring residual stresses by ultrasonic methods. The paper was based on work performed at NBS under the direction of Dr. G. V. Blessing and supported by ONDE.

F. Technical and Professional Committee Participation and Leadership

Participants in the NDE Program and the staff of ONDE have continued their participation and leadership in standards committee and professional society activities relating to NDE. The following appointments or elections to leadership positions occurred during the past year.

G. V. Blessing	Chairman, Washington Area Chapter IEEE Sonics/Ultrasonics
D. G. Eitzen	Chairman, ASTM E7.06.02 on Aluminum Ultrasonic Reference Blocks
L. Mordfin	Chairman, ISO/TC 135/SC 3 on Acoustic NDT Methods, for the Sept. 15, 1983 meeting.

NBS-114A (REV. 2-8C)

U.S. DEPT. OF COMM. BIBLIOGRAPHIC DATA SHEET (See instructions)	1. PUBLICATION OR REPORT NO. NBSIR 84-2815	2. Performing Organ. Report No.	3. Publication Date January 1984

4. TITLE AND SUBTITLE

Technical Activities 1983
Office of Nondestructive Evaluation

5. AUTHOR(S)

Leonard Mordfin, editor

6. PERFORMING ORGANIZATION (If joint or other than NBS, see instructions)	7. Contract/Grant No.
NATIONAL BUREAU OF STANDARDS DEPARTMENT OF COMMERCE WASHINGTON, D.C. 20234	8. Type of Report & Period Covered Annual, FY 83

9. SPONSORING ORGANIZATION NAME AND COMPLETE ADDRESS (Street, City, State, ZIP)

10. SUPPLEMENTARY NOTES

☐ Document describes a computer program; SF-185, FIPS Software Summary, is attached.

11. ABSTRACT (A 200-word or less factual summary of most significant information. If document includes a significant bibliography or literature survey, mention it here)

A review of the Nondestructive Evaluation Program at NBS, for FY 1983, is presented in this annual report.

12. KEY WORDS (Six to twelve entries; alphabetical order; capitalize only proper names; and separate key words by semicolons)

Acoustic emission; calibration; eddy currents; magnetics; neutron methods; nondestructive evaluation; optics; penetrants; radiography; standards; thermal testing; ultrasonics

13. AVAILABILITY	14. NO. OF PRINTED PAGES
☒ Unlimited ☐ For Official Distribution. Do Not Release to NTIS ☐ Order From Superintendent of Documents, U.S. Government Printing Office, Washington, D.C. 20402. ☒ Order From National Technical Information Service (NTIS), Springfield, VA. 22161	202 15. Price $19.00

USCOMM-DC 6043-P80